REINFORCEMENT OF BALLASTED RAILWAY TRACKS USING 3D-GEOCOMPOSITE

Chandr Toshan Rampat, BEng.

Thesis submitted to the University of Nottingham for the degree of Masters of Philosophy

February 2018

Declaration of Originality

Title of Thesis: Reinforcement of Ballasted Railway Tracks using 3D-Geocomposite

I declare that the thesis hereby submitted for the degree of Masters of Philosophy at the University of Nottingham is my own work except as cited in the references and has not been previously submitted for any degree.

Name: **Chandr Toshan Rampat**

Signature:

Date: 10/01/2018

ABSTRACT

Recent growth in high-speed traffic, due to increased commercialism and modernisation, has driven the conventional ballasted track to its limit. The design of railway tracks has not significantly evolved for hundreds of years. Most attention has been paid to the superstructures, and less consideration was given to the substructure. Researchers have indicated that the major portion of maintenance budget is spent on the substructure. The development of a high-speed railway demands a more stable, durable and longitudinally homogenous substructure with higher strength, higher rigidity, and reduced strain. Track deterioration is directly influenced by the applied pressure distribution combined with high frequency, the entire track modulus, and the type of ballast material used. In this context, high-speed traffic increases the need to improve ballasted tracks structurally. The reinforcement of railway tracks has proven to be advantageous, but each specific reinforcement technique comes with its respective benefits. In this research two common materials, bitumen and rubber geocell, are combined to form a new reinforcing geocomposite where the weakness of one material is compensated by the strength of the other. Bitumen, being a visco-elastic material, has proven to have vibrational damping properties and can also consolidate ballast owing to its highly adhesive nature. Geocell confines the ballast and helps to increase shear strength, bending resistance, tensile strength and bearing capacity by allowing more excellent load distribution and improved frictional characteristics. Current codes are non-scientific, and a proper understanding of the phenomenon at the wheel-rail interface is needed. Using theories derived from contact mechanics, a load-time graph was plotted so that the load from different train speeds that acts on

the ballast at each time step could be obtained for a range of different track profiles. A finite element model was set up to understand the change in mechanics of the model when speed was raised, and a parametric study was conducted to verify if components can be changed to account for higher speeds. The results were then used to perform a Discrete Element Analysis on the ballast since extremely high-frequency cyclic loading experimental tests are very limited. Ballast was modelled by agglomerating spheres to mimic the behaviour of breakage. The geocell was a clump of small spheres, while bitumen was modelled as visco-elastic spheres and settlement was observed for each reinforcement scheme. Experimental tests were also performed on a single geocell to check the damping ratio and the increase in bearing capacity. A small cyclic compressive test using a tensile machine was performed to check the optimum geometry of geocells and the increase in lateral confinement. A large box test was also performed in order to validate DEM results and to check the benefits of implementing the reinforcement. It was concluded that bitumen decreased settlement but did not contribute in reducing the lateral vibration or lateral load. Geocell served to enhance the properties of ballast by deducing the lateral force but settlement was much significant since interlocking between ballast was reduced. While geocell amplified the settlement and movement of ballast, bitumen decreased the damping properties of ballast.

ACKNOWLEDGEMENTS

I would like to express my sincere gratitude to my supervisors *Dr.Adbullahi Ali Mohamed* and *Dr. Sandy Sien Ti Kok* for their motivation, immense knowledge, and continuous support of my research. Their guidance helped me throughout my research endeavour and during the writing of this thesis.

Besides my supervisors, I would like to thank my internal assessor, *Dr Wael Elleithy,* for his insightful comments and encouragement, but also for the hard interrogation, which incented me to widen my research from various perspectives.

My sincere thanks also go to *Mr. Kumar Bathumalai* and *Mr.Khairul Razdi* who provided me access to the powerful university cluster and to several workstations simultaneously during off peak times. Without their precious support, it would not be possible for me to conduct this research in such a short period.

In particular, I am grateful to *Miss Shameena Bonomally* for proofreading my thesis and helping me in building samples for laboratory testing.

Last but not the least, I would like to thank my parents for their moral, motivational and financial support.

Table of ContentsAbstract _____ **i**

Acknowledgements _____ **iii**

List of Figures _____ **x**

List of Tables _____ **xix**

Chapter 1: Introduction _____ **1**

1.1 Background 1

1.2 Problem Statement 6

1.3 Aim 10

1.4 Research Objectives 10

1.5 Thesis Outline 10

Chapter 2: Track structure and Loading _____ **13**

2.1 Introduction 13

2.2 Forces 13

2.2.1 Wheel Load 13

2.2.2 Lateral load 17

2.3 Wheel-Rail-Subgrade Interface 19

2.3.1 Ballast Degradation Mechanism 22

2.4 Track Modulus 25

2.4.1 Track stiffness 25

2.4.2 Optimal Stiffness 28

2.4.3 Damping 29

2.5 Vibration 31

2.6 Critical Speed 33

2.7 Conclusion 38

Chapter 3: Track Reinforcement Design _____ 40

3.1 Introduction 40

3.2 Track requirements 40

3.3 Ballast Reinforcement 41

3.3.1 Geosynthetic reinforcement 41

3.3.2 Geocell confinement 44

3.3.3 Bitumen Stabilisation 49

3.4 Testing Methodology 52

3.4.1 Testing Methodology Flowchart 55

3.5 Reinforcement Design 56

3.5.1 Combining reinforcements 56

3.5.2 Installation procedure 59

3.6 Conclusion 62

Chapter 4: Finite Element Modelling of rail profiles _____ 63

4.1 Introduction 63

4.2 Background 63

4.3 Model 65

4.3.1 Step 1: Static 3D Contact model 66

4.3.2 Step 2: Creating rail profile 70

4.3.3 Step 3: Calculating reaction forces 74

4.4 Parametric study 79

4.5 Validation 81

4.5.1 Contact model 81

4.5.2 Ansys model 85

4.6 Limitation of models 87

4.7 Results and Discussion 88

4.7.1 Effect of Corrugation 88

4.7.2 Effect on Dynamic Amplification Factor 101

4.7.3 Effect of Speed and Load 106

4.7.4 Effect of Pad Stiffness 108

4.7.5 Effect of Creepage 110

4.8 Conclusion 111

Chapter 5: Discrete Element Modelling of Reinforced Ballast __114

5.1 Introduction 114

5.2 Modelling Ballast 114

5.3 Discrete Element Modelling 117

5.3.1 DEM Simulation 119

5.3.2 Force 120

5.3.3 Parametric study 122

5.4 Validation of model 127

5.5 Limitation of model 129

5.6 Results and discussion 130

5.6.1 Effect of reinforcement 131
5.6.2 Effect of load and speed on reinforcement 132
5.6.3 Effect of Geocell geometry 134
5.6.4 Long-term effects 135
5.7 Conclusion 136
Chapter 6: Experimental testing _____138
6.1 Introduction 138
6.2 Test 1: Vibrating table test 139
6.2.1 Preparation of sample 139
6.2.2 Testing 143
6.2.3 Results and discussion 146
6.2.4 Conclusion of test 1 152
6.3 Test 2: ERUDITE 152
6.3.1 Results and Discussion 155
6.3.2 Conclusion of test 2 159
6.4 Test 3: Cyclic-Compressive Test 159
6.4.1 Preparation of sample 5-10 160
6.4.2 Testing 163
6.4.3 Results and discussion 165
6.4.4 Conclusion of test 3 170
6.5 Test 4: Large scale Box-Test 171
6.5.1 Results and Discussion 177

6.5.2 Conclusion of test 4 187

6.6 Limitation of the experiments 187

6.7 Conclusion 187

Chapter 7: Conclusion _____190

7.1.1 Finite Element Analysis 190

7.1.2 Discrete Element Analysis..... 191

7.1.3 Experimental Testing 192

7.1.4 Overall conclusion 194

7.1.5 Future Works 194

References _____196

Appendices_____215

A.1: Ballast Specification..... 215

A.2: DAF Formule..... 216

A.3: CONTACT Code 217

A.4: Contact result for C1 50kN 20ms..... 220

A.5: Subsurface stress for DX1 222

A.6: Ansys Input data..... 223

A.7: Case 4 DEM 227

A.7.1 Code for case 4..... 227

A.7.2 DEM compared with experiment..... 236

A.8: Vibrating table results..... 238

A.9: Cyclic-Compressive test results..... 243

A.10 Large scale box test results 248

A.10.1 Box Cyclic-compression results 248

A.10.2 Accelerometers results 256

LIST OF FIGURES

Figure 2.1: Conventional, Heavy Haul and HSR Q_{tot} with speed 14

Figure 2.2: Q-Forces of 225kN axle loads 15

Figure 2.3: Design dynamic factors due to increase in speed 16

Figure 2.4: Lateral forces and moment 18

Figure 2.5: Wheel load distribution 20

Figure 2.6: Track structure, pressure distribution, track deterioration and depth of influence 20

Figure 2.7: Track interaction diagram 22

Figure 2.8: Influence of rail pad stiffness on vibration in the ballast 25

Figure 2.9: Dynamic Amplification vs Speed due to moving load 34

Figure 2.10: Critical velocity effects and a dynamic portion representing freely propagating Rayleigh waves 35

Figure 2.11: Dynamic signature of train ICE2 with different damping rates 37

Figure 3.1: Location of geosynthetic for required function 43

Figure 3.2: Geocell cross section..... 46

Figure 3.3: Geocell filled with gravel..... 46

Figure 3.4: Methodology flowchart at its simplest..... 55

Figure 3.5: Geocell Confinement 56

Figure 3.6: Ballast-Bitumen Adhesion 56

Figure 3.7: Bituminous Geocomposite..... 58

Figure 3.8: Expected Load Path 58

Figure 3.9: Placement of geocell during ballast cleaning..... 60

Figure 3.10: Sample detailed Design 61

Figure 4.1: Contact distance for One time step 66

Figure 4.2: Schematizing the contact forces 67
Figure 4.3: One discretised contact region 69
Figure 4.4: Plan view of contact areas added together to form profile at t=1 70
Figure 4.5: Plan view of contact areas added together to form profile at t=2 70
Figure 4.6: Plan view of contact areas added together to form profile at t=3 71
Figure 4.7: Load time Graph for Input 73
Figure 4.8: Resultant force from superposed graph in time-domain 73
Figure 4.9: Transient loading 74
Figure 4.10: Ansys 16.0 transient structural module 76
Figure 4.11: Detailed Geometry used for simulation 78
Figure 4.12: Ansys 16.0 Explicit Dynamics 86
Figure 4.13: Simply supported beam case 1 86
Figure 4.14: Simply supported beam case 2 87
Figure 4.15: 3D corrugated contact Profile 90
Figure 4.16: 2D corrugated contact Profile 90
Figure 4.17: Stress profile of a corrugated rail at Contact Area 92
Figure 4.18: Stress Contour of a corrugated rail at Contact Area 92
Figure 4.19: 3D Smooth contact profile 93
Figure 4.20: 2D Smooth contact profile 93
Figure 4.21: Stress profile of a smooth rail at Contact Area 94
Figure 4.22: Stress contour of a smooth rail at Contact Area 95
Figure 4.23: Corrugation quantification 96
Figure 4.24: Corrugation profile 1 97

Figure 4.25: Corrugation profile 2 98
Figure 4.26: Corrugation profile 3 99
Figure 4.27: Corrugation profile 4 100
Figure 4.28: Corrugation profile 5 100
Figure 4.29: Variation of DAF at 20m/s..... 104
Figure 4.30: Static analysis vs Contact Analysis..... 105
Figure 4.31: Explicit dynamics results for C5 300kN 80ms EXP 106
Figure 4.32: The stress fluctuation in the wheel-rail contact at different speed and wheel load. 107
Figure 4.33: Effect of Pad Stiffness..... 109
Figure 4.34: Effect of creepage..... 111
Figure 5.1: Model of a single geocell and agglomerated spheres 117
Figure 5.2: Elastic interaction. Normal and shear springs 118
Figure 5.3: Simulation Area..... 119
Figure 5.4: DEM Model of Simulation area showing large spheres and one geocell in Yade-DEM..... 120
Figure 5.5: Force-Time graph for 10 iterations..... 122
Figure 5.6: Force-Time graph for 1 Wheel Cycle..... 122
Figure 5.7: DEM Simulation in Yade-DEM 124
Figure 5.8: Plan view of simulation geometry.....123
Figure 5.9: 10mm particles 124
Figure 5.10: Comparison between DEM and Experiment 127
Figure 5.11: Effect of Reinforcement 131
Figure 5.12: Effect of load on reinforcement..... 132
Figure 5.13: Effect of Speed..... 133
Figure 5.14: Effect of Geocell Geometry..... 134

Figure 6.1: Sample details(a) 139
Figure 6.2: Sample details(b) 139
Figure 6.3: Scaled Ballast 141
Figure 6.4: Samples for Test 1,2 and 3 142
Figure 6.5: Sample 1 142
Figure 6.6: Sample 2 142
Figure 6.7: Sample 3 143
Figure 6.8: Sample 4 143
Figure 6.9: Shaking table test setup(a) 145
Figure 6.10: Shaking table test setup(b) 145
Figure 6.11: Acceleration of sample 1 in XYZ direction 147
Figure 6.12: Displacement of all samples in X-direction 148
Figure 6.13: Acceleration of all samples in X-direction 149
Figure 6.14: a_T and a_B description 151
Figure 6.15: ERUDITE equipment 154
Figure 6.16: Relationship between F_r, F_1, F_2 and Q 155
Figure 6.17: Resonant frequency of samples 158
Figure 6.18: Box for cyclic compressive test for samples 5-10 160
Figure 6.19: Samples under applied load 161
Figure 6.20: Sample 6 162
Figure 6.21: Sample 7 162
Figure 6.22: Sample 8 162
Figure 6.23: Sample 9 163
Figure 6.24: Sample 10 163
Figure 6.25: Unbounded sample test for sample 1-4 164
Figure 6.26: Cyclic Box test for sample 5-10 164

Figure 6.27: Force-extension graph for 1st Cycle for samples 1-4 167
Figure 6.28: Settlement of samples 1-4 167
Figure 6.29: Lateral Load during Cyclic loading 169
Figure 6.30: Railway Test Facility 172
Figure 6.31: Large-Scale box test 174
Figure 6.32: Box test setup 175
Figure 6.33: Accelerometer location 175
Figure 6.34: Box 1 176
Figure 6.35: Box 2 176
Figure 6.36: Box 3 177
Figure 6.37: Accelerometers axis 178
Figure 6.38: Loading frequency comparison 179
Figure 6.39: Settlement vs frequency 179
Figure 6.40: Comparison of reinforcement settlement..... 180
Figure 6.41: Final settlement under high and low frequencies..... 181
Figure 6.42: Accelerometer 1 results for reinforcement schemes..... 182
Figure 6.43: Peak accelerometer 1 results..... 183
Figure 6.44: Peak accelerometer 2 results..... 184
Figure 6.45: Acceleration comparison at 2hz loading 185
Figure 6.46: Acceleration comparison at 20hz loading 186
Figure A.1: Comparison between DEM and Experiment for 2Hz loading for Control 236
Figure A.2: Comparison between DEM and Experiment for 12Hz loading for control..... 236
Figure A.3: Comparison between DEM and Experiment for 2Hz loading for Reinforced..... 237

Figure A.4: Comparison between DEM and Experiment for 2Hz loading for reinforced 237
Figure A.5: Vibrating table Results for sample 1..... 238
Figure A.6: Vibrating table Results for sample 2..... 239
Figure A.7: Vibrating table Results for sample 3..... 240
Figure A.8: Vibrating table Results for sample 4..... 241
Figure A.9: Vibrating table Results for table only..... 242
Figure A.10: Cyclic compressive test results for sample 1..... 243
Figure A.11: Cyclic compressive test results for sample 2..... 243
Figure A.12: Cyclic compressive test results for sample 4..... 244
Figure A.13: Cyclic compressive test results for sample 3..... 244
Figure A.14: Cyclic compressive test results for sample 6..... 245
Figure A.15: Cyclic compressive test results for sample 5..... 245
Figure A.16: Cyclic compressive test results for sample 7..... 246
Figure A.17:Cyclic compressive test results for sample 8 246
Figure A.18: Cyclic compressive test results for sample 10..... 247
Figure A.19: Cyclic compressive test results for sample 9..... 247
Figure A.20: Box test results for control at 2Hz..... 248
Figure A.21: Box test results for control at 6Hz..... 248
Figure A.22: Box test results for control at 12Hz 249
Figure A.23: Box test results for control at 15Hz 249
Figure A.25: Box test results for sample reinforced with geocell at 2Hz 250
Figure A.24: Box test results for control at 20Hz 250
Figure A.26: Box test results for sample reinforced with geocell at 6Hz 251
Figure A.27: Box test results for sample reinforced with geocell at 12Hz 251

Figure A.28: Box test results for sample reinforced with geocell at 15Hz 252
Figure A.29: Box test results for sample reinforced with geocell at 20Hz 252
Figure A.30: Box test results for sample reinforced with geocell and bitumen at 2Hz 253
Figure A.31: Box test results for sample reinforced with geocell and bitumen at 6Hz 253
Figure A.32: Box test results for sample reinforced with geocell and bitumen at 12Hz 254
Figure A.33: Box test results for sample reinforced with geocell and bitumen at 15Hz 254
Figure A.34: Box test results for sample reinforced with geocell and bitumen at 20Hz 255
Figure A.35: Accelerometer 1 results for control at 2Hz 256
Figure A.36: Accelerometer 2 results for control at 2Hz 256
Figure A.37: Accelerometer 1 results for control at 6Hz 257
Figure A.38: Accelerometer 2 results for control at 6Hz 257
Figure A.39: Accelerometer 1 results for control at 12Hz..... 257
Figure A.40: Accelerometer 2 results for control at 12Hz..... 257
Figure A.41: Accelerometer 1 results for control at 15Hz..... 257
Figure A.42: Accelerometer 2 results for control at 15Hz..... 257
Figure A.43: Accelerometer 1 results for control at 20Hz..... 257
Figure A.44: Accelerometer 2 results for control at 20Hz..... 257
Figure A.45: Accelerometer 1 results for geocell reinforcement at 2Hz. 257
Figure A.46: Accelerometer 2 results for geocell reinforcement at 2Hz. 257

Figure A.47: Accelerometer 1 results for geocell reinforcement at 6Hz. 257
Figure A.48: Accelerometer 2 results for geocell reinforcement at 6Hz. 257
Figure A.49: Accelerometer 1 results for geocell reinforcement at12Hz 257
Figure A.50: Accelerometer 2 results for geocell reinforcement at12Hz 257
Figure A.51: Accelerometer 2 results for geocell reinforcement at 15Hz257
Figure A.52: Accelerometer 2 results for geocell reinforcement at 15Hz257
Figure A.53: Accelerometer 1 results for geocell reinforcement at20Hz 257
Figure A.54: Accelerometer 2 results for geocell reinforcement at 20Hz257
Figure A.55: Accelerometer 1 results for geocell and bitumen reinforcement at 2Hz 257
Figure A.56: Accelerometer 2 results for geocell and bitumen reinforcement at 2Hz 257
Figure A.57: Accelerometer 1 results for geocell and bitumen reinforcement at 6Hz 257
Figure A.58: Accelerometer 2 results for geocell and bitumen reinforcement at 6Hz 257
Figure A.59: Accelerometer 1 results for geocell and bitumen reinforcement at 12Hz 257
Figure A.60: Accelerometer 2 results for geocell and bitumen reinforcement at 12Hz 257
Figure A.61: Accelerometer 1 results for geocell and bitumen reinforcement at 15Hz 257
Figure A.62: Accelerometer 2 results for geocell and bitumen reinforcement at 15Hz 257
Figure A.63: Accelerometer 1 results for geocell and bitumen reinforcement at 20Hz 257

Figure A.64: Accelerometer 2 results for geocell and bitumen reinforcement at 20Hz 257

LIST OF TABLES

Table 3.1: Good track requirements apart from structural needs..... 41

Table 3.2: Summary of important parameters to consider for geocells... 49

Table 3.3: Reinforcement materials Properties..... 56

Table 4.1: Load applied at contact regions DXn over 7 time-steps..... 72

Table 4.2: Properties of materials used in CONTACT and ANSYS 75

Table 4.3: Parameters used by the programs when solving 77

Table 4.4: Cases category description..... 79

Table 4.5: Ansys Case Scenarios..... 80

Table 4.6: Stresses for different rail profile 84

Table 4.7: Analytical results vs FEM results 87

Table 4.8: B-Values for surface equation..... 89

Table 4.9: Results for discretised contact region of corrugated profile.... 91

Table 4.10: Results for discretised contact region of corrugated profile .. 94

Table 4.11: Corrugation description..... 97

Table 4.12: Results from ANSYS 102

Table 4.13: Explicit Dynamics setting for Case 8 111

Table 5.1: DEM parameters..... 123

Table 5.2: Case Scenarios for DEM..... 125

Table 5.3: Case Scenarios for DEM..... 125

Table 5.4: DEM results compared with experimental results 128

Table 5.5: DEM results for 215 Cycles showing settlement in mm 130

Table 5.6: Results after 1000 wheel cycles..... 135

Table 6.1: Samples and configurations 142

Table 6.2: Maximum acceleration of all samples 150

Table 6.3: Damping ratio of all samples..... 151

Table 6.4: ERUDITE Setting..... 154

Table 6.5: ERUDITE Results 155

Table 6.6: Damping calculation from ERUDITE..... 157

Table 6.7: Sample Configuration for samples 5-10 162

Table 6.8: Compression test results for samples 1-10..... 165

Table 6.9: Large-scale Box test sample details 176

Table 6.10: Large-scale box test results..... 177

Table 6.11: Summary of experiments..... 188

Table A.14: Damping ratio of all samples 242

Table A.1: Ballast specification.....215

Table A.2: DAF formulae adopted from Steenbergen(2013)..... 216

Table A.3: Subsurface stress for DX1 for C1 50kN 20ms 222

Table A.4: 50 kN processed loads from CONTACT for Ansys Input 223

Table A.5: 100 kN processed loads from CONTACT for Ansys Input 223

Table A.6: 150 kN processed loads from CONTACT for Ansys Input 223

Table A.7: 200 kN processed loads from CONTACT for Ansys Input 224

Table A.8: 250 kN processed loads from CONTACT for Ansys Input 224

Table A.9: 300 kN processed loads from CONTACT for Ansys Input 224

Table A.10: 50 kN processed loads from CONTACT for Ansys Input 225

Table A.11: 100 kN processed loads from CONTACT for Ansys Input ... 225

Table A.12: 150 kN processed loads from CONTACT for Ansys Input ... 225

Table A.13: 200 kN processed loads from CONTACT for Ansys Input ... 226

Table A.14: 250 kN processed loads from CONTACT for Ansys Input ... 226

Table A.15: 300 kN processed loads from CONTACT for Ansys Input ... 226

CHAPTER 1: INTRODUCTION

1.1 BACKGROUND

Advances made in railway track design have played a significant role in improving the performance, safety and quality of service of conventional ballasted tracks. Many tracks in developing countries, being remnants from the colonial period, are over 100 years old but, owing to extensive maintenance, are still operative today. Although some components have been replaced over the years, the substructure has basically remained unchanged (Berggren 2009). In most countries, railway companies, unlike road traffic and inland waterway shipping ones, have to carry the full cost of the infrastructure. These companies are unprofitable and require governmental financial subsidy due to the declining number of train passengers and increasing operational costs. In order to generate sufficient competition with respect to automobiles and planes, fast passenger rail services are necessary. In an age of mobility and modernity, the High-Speed Rail (HSR) is a viable and gratifying alternative to private cars and aeroplane travel. Conventional passenger train tracks should be upgraded to allow for speeds similar to that of HSR lines, defined by the European Union as lines that can upkeep operational speeds of at least 250 km/h (Feigenbaum 2013), and a cruise speed of 300km/h (Esveld 2001).

Rail transport has entered an era of high-speed traffic where swiftness, energy efficiency, safety and comfort are key strengths that give vitality to the transportation mode. According to Chen (2014), a successful HSR project should bring along socio-economic and environmental benefits by increasing the number of passengers and reducing delays through the decongestion of

highways, and the enhancement of urban and regional industrial competitiveness. Generally, faster and heavier vehicles demand more energy, and this results in higher carbon costs. However, a report published by Network Rail UK (2009) stated that per-passenger-km, an HSR emits 15% less Green House Gases than conventional rails on similar types of electric rail services. It is anticipated that in the near future, the HSR will be the prime choice for travel distances of 300km to 1500km in both the Asian and European continent (Wei 2014). In Asia, the Southeast Asian rail link that will connect Beijing to Singapore is expected to increase demands on rail components, and services globally (Mohamed et al. 2015). Moreover, Europe's high-speed network, which consists of more than 6,600 km of operational line, will extend to 20,000 km within the next decade, thereby bringing major European capitals and metropolitan regions closer in terms of travelling time (Carol et al. 2011). The HSR industry is expanding exponentially, and many countries including the USA, India and Australia have already shown interest in high-speed lines.

Even though construction costs, which include signalling systems, tele/radio communication links, acoustic barriers, fencing, and stations, are independent of speed within the high-speed range of 250–500 km/h (Fröidh 2014), the HSR substructure is, in itself, very expensive to build. Despite being investments that take decades to realise a return, HSR lines have proved to be profitable in the long run. Indeed, the French 'TGV Sud-Est' business plan achieves 15% financially for SNCF (Société nationale des chemins de fer) and 30% socio-economically. The German ICE network more than doubled its passengers to 23 million and accounted for 28% of the total long-distance passenger

revenues in Germany within only 5 years of its opening (Leheis 2012). Deutsche Bahn estimates that around 12% of the ICE Network traffic has been diverted from road and air (Vickerman 1997). Moreover, the earliest HSR route, between Tokyo and Osaka, cost less than $8M/km and enabled the repayment of loans in only 7 years. The profits generated were used to cross-subsidise local trains, encouraging the government to continue building HSR throughout Japan.

New lines cost at least $16M/km to construct. Clearly, the higher the construction cost, the more difficult it is to break even. In Europe, the cheapest rail line annual operating cost is more than $50,000 per seat (Feigenbaum 2013). In 2015, a ‘MAGLEV’ test train, powered by strong electromagnetic forces achieved a world record speed of 603 km/h. The magnetic levitation technology, which exists since 1905, causes the vehicle to hover above the track and advance forward at very high speeds, opposing only air as resistance. However, as in the case of the MAGLEV Beijing–Shanghai line project, plans for using magnetic levitation have often been abandoned in favour conventional wheel-on-rail high-speed systems (Nimbalkar 2015). MAGLEV trains, being incompatible with existing rail networks, have special infrastructure requirements, which imply high construction costs. Fast-moving vehicles, propelled by powerful motors on conventional tracks, also have their own limitations; the trains damage the ballasted tracks severely, rendering their commercial application infeasible (Raoul 1997).

Remarkably, high-speed rails built by France and Japan on the traditional ballasted track, have been successful in contributing to increased traffic capacity (Feigenbaum 2013). These lines represent good results but, in most cases, require notable maintenance (20,000–68,000 $/km) to guarantee adequate operating conditions (Kuo & Huang 2009). Frequent maintenance and routine checks counteract the progressive pulverisation of ballast, differential settlement, pumping, high ballast lateral movement and track buckling which often result in reduced drainage, derailment risk, speed restrictions and poor ride quality. The Japanese high-speed line, Shinkansen, is maintained and tampered 2-3 times yearly while tamping is usually done once every 4-5 years (Lichtberger 2005) for a standard passenger train track. Furthermore, ballast degradation was witnessed after only 5 years of operation as compared to the conventional 15-20 year period (Hussaini 2013). According to the Chinese Railway (CR), about 75% of the daily maintenance work on track structures is performed on the ballast component (Zhai et al. 2004). This is because more than 50% of the total deformation of the track originates from the breakage of sharp corners in ballast, which decreases the mechanical interlocking mechanisms between the particles (Lackenby 2006). Geometrical track defects occur due to differential ballast settlement after a high number of loading cycles. The higher the standard deviation of the track, the higher the impact loads which would further degrade the quality of the track. At this point, possible track maintenance options include ballast cleaning or renewal. It is to be noted that maintenance work on ballast contributes to 67% of the total capital spending. However, freshly crushed particles were also found to

generate more fines than used particles. In practice, owing to “ballast memory”, the track returns to its pre-maintenance profile very soon (Cossio et al. 2012b) and the deterioration process restarts (Guler 2013).

Such maintenance schemes cause regular traffic disruptions (Judge 2002; Ebrahimi & Keene 2011). During realignment maintenance (tamping), ballast breakage occurs, producing 70% of fine particles defined as particles passing the 14mm sieve (Minsili et al. 2012). See Appendix A.1 for the particle distribution used in railway tracks. These fines block drainage networks (Judge 2006; Neupane & Members 2007; Indraratna 2010). More water is retained by the fouled layers, resulting in track instability, alignment problems (Rahman 2013) and an increase in ground-borne vibration during train passing owing to the building-up of pore water pressure (Esmaeili et al. 2014). Furthermore, saturated samples show larger permanent and resilient strains (Boyce et al. 1976), and the infiltration of fines from the subgrade and sub-ballast increases in the presence of water (Lim 2004). These frequent and extensive maintenance operations do not decrease the risk of accident in practice (Fu et al. 2012). In some cases of stone-blowing, the resulting track quality was found to be even worse than it was before maintenance (Fair & Anderson 2003). Traditionally, the cost of replacing ballast, and maintaining it, will continue to increase in the future unless railway foundations are re-engineered using innovative design concepts.

From this background, it follows that the development of innovative structural solutions for high-speed tracks, that reduce the total life-cycle costs, is a key

issue in improving the operational profits of future investments in this sector. In the case where massive investments are not feasible, it is worth evaluating possible upgrades of conventional tracks. Teixeira et al. (2010) evaluated the possibility of using a bituminous sub-ballast sublayer in the Spanish high-speed lines. The scheme confirmed to have a beneficial effect on the structure, and this acted as an incentive for the Spanish Railways to build a 3km trial line in order to evaluate the possibilities that the reinforcement scheme has to offer. Moreover, Wong et al. (2002) investigated main parameters, including passenger number, train velocity, operational and maintenance costs, and energy efficiency, and concluded that high-speed trains can successfully be operated on the Beijing to Shanghai conventional rail networks. Different countries have developed alternative systems for their high-speed networks. Japan has an independent high-speed line which adopts standard gauge tracks while in France and China, high-speed trains run on existing narrow gauge ones. South Korea entered the same league by achieving a speed of over 420 km/h on a conventional track. Several other countries use a system of tilting trains to allow operation on conventional lines, and it is worth evaluating the possibility of possible upgrades of the existing lines for high-speed applications.

1.2 PROBLEM STATEMENT

In the railway sector, design standards are often non-scientific and inconsistent (Powrie n.d.), and past experience still play a significant role in the designing process. However, high-speed lines are a recent technology, and empiricism may not extrapolate to these higher speed lines. The design of old tracks did not account for “long-term performance”; only static instantaneous loading

and load-bearing were considered (Steenbergen 2013). In the long-term, dynamic responses, cyclic loading, and their interaction need to be considered. Elastic and plastic movements of the track substructure can lead to voiding issues within the ballast and hence superstructure movements. A high degree of vibration, for instance, increases track damage and thus, the possibility of safety issues and maintenance requirements. Dynamic loads that cause further deterioration of the track need to be understood in order to propose a rational reinforcement schemes. Different quality and profile of the tracks will lead to varying patterns of loading. Therefore, it is essential to identify the key parameters that govern the nature of the dynamic loads.

Furthermore, railway vibration, which travels as far as 200m from the line (Zicha 1989), combined with noise pollution, is a growing global concern. Studies conducted in 1604 railway track sections based in nine countries throughout the globe reported that on approximately 50% of projects, ground vibration limits are exceeded in 44% of the time, and noise is beyond usual restrictions in 31% of assessments. These situations require mitigation measures, including modification of the track structure (Ferreira & López-Pita 2015). Moreover, if the speed of a train increases continually along a particular track, a point would eventually be reached whereby a Rayleigh ground wave would start to develop in the formation and the subgrade. A typical analogy is that of an aircraft approaching the sound barrier, thereby producing a sonic boom. The magnitude of ground vibration is heavily influenced by the dynamic characteristics of the ground, such as frequency content and damping values. In relatively soft subgrades, the velocity of the Rayleigh wave falls within the

speed of conventional trains, and hence the phenomenon can cause serious resonance issues for the operational running and safety of the train. In order to reduce the vibration, further research needs to be conducted. Excessive vibration can damage both the train and surrounding structures. Countermeasures to isolate, mitigate and absorb these effects need to be developed (Wang & Zeng 2004). Laboratory tests on ballast under high-frequency vibration and impact loading are still very limited.

Since the wheel-rail interface is the source of vibration (Connolly et al. 2015), it is essential that the contact area is analysed in detail. Rail corrugation is one of the factors that need to be investigated in order to decrease vibration. Measures such as using continuously welded rails to reduce dynamic loads have resulted in increasing the operational speed and axle load (Esmaeili et al. 2015). Other solutions have been proposed; including rail dampers or lubrication, but corrugation was not entirely eliminated. Since it is unwise to attempt to reduce the vibration at the source (rolling contact between rail and wheel), alternative methods need to be investigated. Furthermore, Oyarzabal et al. (2011) carried out Finite Element Analysis on different types of track and concluded that ballasted track performed better than slab track, in terms of growth of corrugation. It is worth evaluating the possibilities that a ballasted track can offer in order to reduce corrugation. It should be noted that according to Larsson and Gunnarsson (2001), a 24% increase in maintenance cost should be expected if axle load were to be increased by 20%.

Appropriate improvements to the ballasted track can reduce maintenance needs and satisfy the requirement for high-speed and freight traffic without increasing the construction cost (reconstruction is about 5 times more expensive than building a new formation; 30€ million/km for the TGV (Kidd 2007)). Stabilisation of the rail track bed, using geosynthetic materials and viscoelastic materials such as bitumen, has been technologically established over many years. Generally, each manufacturer of geosynthetic uses a different design method, highlighting the benefits of using the particular product. Such diversity results in a fundamental lack of understanding of the mechanisms involved in this type of problem, requiring further investigation. Often, improvement of one characteristic leads to deterioration of other ones. For instance, increasing the stiffness of the track by densification can increase the bearing capacity of the subgrade, but this method has proven to increase dynamic loads violently. It is, therefore, essential to consider the static and dynamic loads separately. Increasing the resilience of the track can reduce the dynamic impacts, but the track is prone to larger deflection. Therefore, the correct behaviour and relation between static and dynamic load need to be identified, and a proper stabilisation scheme needs to be proposed, so as to counteract both effects (bearing capacity and vibration) at the same time. Other factors such as problems of high maintenance costs, noise and uncomfortable rides are also needed to be considered when proposing a stabilisation scheme.

1.3 AIM

This research focuses on improving the substructure of a conventional track by incorporating 3D-geocomposite materials for high-speed applications.

1.4 RESEARCH OBJECTIVES

1. Identify how reinforcement can be used to improve railway tracks and propose a theoretical concept based on past research.
2. Use numerical simulations to understand the change in mechanics when speed increases, and the generation and behaviour of dynamic loads when the speed increases and track quality (rail profile) changes.
3. Perform numerical simulation on reinforced ballast to model the behaviour and degradation under stresses induced by traffic loading using the 3D Discrete Element Method (DEM) and perform a parametric study to optimise reinforcement,
4. Perform appropriate scaled experimental testing on a range of different samples to assess the efficiency and accuracy of the proposed reinforcement schemes and validate the DEM tests,
5. Perform large experimental testing by modelling the critical region of a track to assess the benefits of incorporating reinforcement.

1.5 THESIS OUTLINE

This thesis consists of seven chapters, which present information regarding the formulation of the numerical models and experiments used in this study, the development of this research and obtained results. A brief outline of this thesis is given below:

Chapter 1 details background information pertaining to the need for improvement of ballasted tracks and shows why the world needs to converge towards HSR. It also gives a brief description of the engineering problems that currently exist in the railway industry and the objectives that need to be completed to achieve the aim of the research.

Chapter 2 contains a literature review of the mechanical and dynamic behaviour of ballast. A description of ballast functions, forces generated on the granular layers and details about the properties of geocomposite materials are presented. The parameters that need to be considered in upgrading the current ballasted tracks are identified in this chapter.

Chapter 3 contains the design philosophy of the reinforcement and the need for the specific function of the geosynthetic. A brief method of implementing the reinforcement is also presented. Justifications on the use of these materials to modify the parameters that have been identified in Chapter 2 are also presented in this chapter.

Chapter 4 describes the numerical simulation formulation used in this study and presents the results of using the developed model in conducting a parametric study. A discussion of the main findings and parameters that need to be considered for the DEM simulation is presented. These results will be used in the succeeding chapter. Emphasis is drawn on the stiffness of the track that needs to be brought about by the ballast rather than by the pads. Stresses caused by non-linear track profiles as speed increases have also been investigated.

In Chapter 5, a simple procedure to generate clumps which resemble real ballast particles is introduced and a DEM analysis, using the open-source package YADE-DEM, is performed on ballast to determine settlement and ballast movement when reinforcement is placed. The effects of wheel load, geocell geometry, and speed of the train on ballast is discussed.

Chapter 6 details a cyclic compressive test on a single geocell that is constructed using rubber, polyurethane, ballast and bitumen, performed to determine the ultimate bearing capacity of the different reinforcement schemes. A shaking table test is also conducted to determine the vibrational damping properties of the cells. The behaviour of the assembly is then compared with the results obtained from DEM for validation of the latter. The lateral pressure is also determined in a small box test, and a large-scale test is performed to simulate the critical region of a track.

Chapter 7 summarises the major contributions of this research and presents suggestions for future research.

CHAPTER 2: TRACK STRUCTURE AND LOADING

2.1 INTRODUCTION

Since the number of high-speed trains running on conventional tracks is not widespread, a proper understanding of the behaviour of the interaction between the track and the vehicle is essential. It is essential that the mechanics and the dynamics of a ballasted railway track are understood before attempting any structural improvement. The forces that are exerted by the wheel on the ballast and the process of degradation of ballast which is the primary cause of settlement is detailed in this chapter. Several track parameters that can be modified to improve the track have been identified. As stated in the problem definition, vibration due to the increase in train speed and wheel load is a global concern. The cause of such disruption also needs to be understood so that appropriate measures can be taken in order to reduce vibrational effects caused at the rail-wheel interface and at the sub-structure.

2.2 FORCES

2.2.1 WHEEL LOAD

The wheel load, $Q_{tot,}$ is a combination of a quasi-static load, Q_{stat}, which involves the self-weight of the running train and that of the superstructure, and a dynamic component, Q_{dyn}, which depends on the train velocity, track irregularity, wheel unevenness and track stiffness variations. The dead wheel load can be taken as the vehicle weight, and is assumed to have a trapezoidal pressure distribution. The static load ranges from about 50kN to 500kN for light rail trains and heavy freight trains respectively (Selig & Waters 1994). As per standard design (BS), the static axle loads are limited to 25.5 Tonnes in

the UK, but a typical high-speed passenger coach weighs approximately 16 Tonnes. Still, for the design of a railway track, the actual stresses used in calculations are much higher since the dynamic and lateral forces imposed are highly dependent on the track condition. Esveld & Steenbergen (2005) proposed a formula for the determination of the dynamic load. From Figure 2.1 it can be seen the dynamic component is highly influenced by speed and wheel loads. The total force, Q_{tot} of a 170/2 kN wheel load train is the same as a 350/2 kN wheel load train moving at a third of the speed.

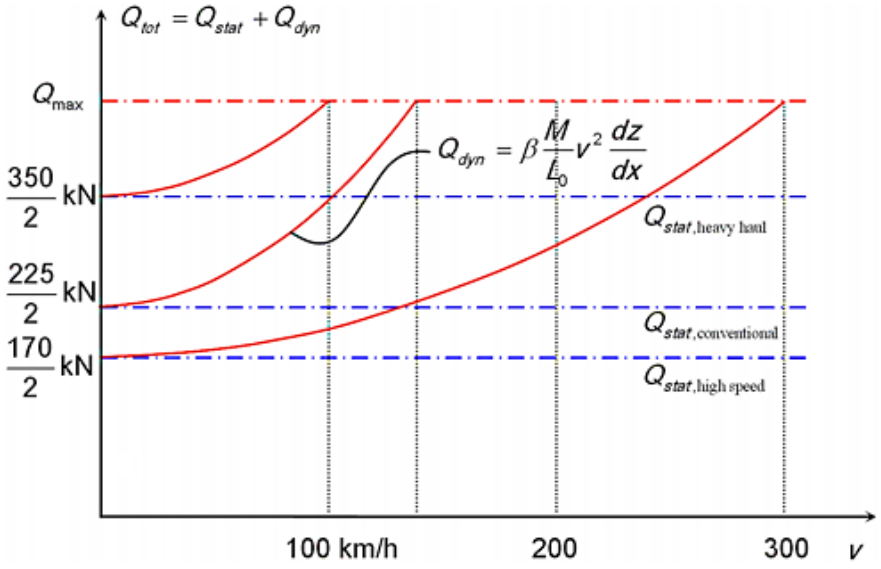


Figure 2.1: Conventional, Heavy Haul and HSR Q_{tot} with speed(Esveld 2001)

In Figure 2.2, can be seen that the same train exerts a higher stress when its speed and the standard deviation of the track are increased. Higher standard deviation in the tracks implies that the linearity and the quality of the track is not good. High-speed trains require standard deviation of less than 1mm (Chandra & Agarwal 2007). The dynamic load is more influential than the static wheel load, causing impact forces and rail vibration due to speed and rail non-linearity. According to Berggren (2009), roughness of the rail contributes to

high-frequency forces while rail imperfections(joints and welds) lead to impact forces. Thompson & Wu (2000) further confirmed, by numerical analysis, that the dynamic component is minimal when the root mean square level of roughness is below 15 µm. When the latter is above 25 µm, slipping between the wheel and rail occurs, leading to impact loads. Yang et al. (2009) carried in-situ measurements on three sites in the UK, using a geophone coupled with video recording. It was found that the static load generated from slow trains is approximately one-half of that arising from fast trains, per sleeper. At speeds of 120 km/h and 260 km/h, the percentage increase in static load was 67% and 145% respectively.

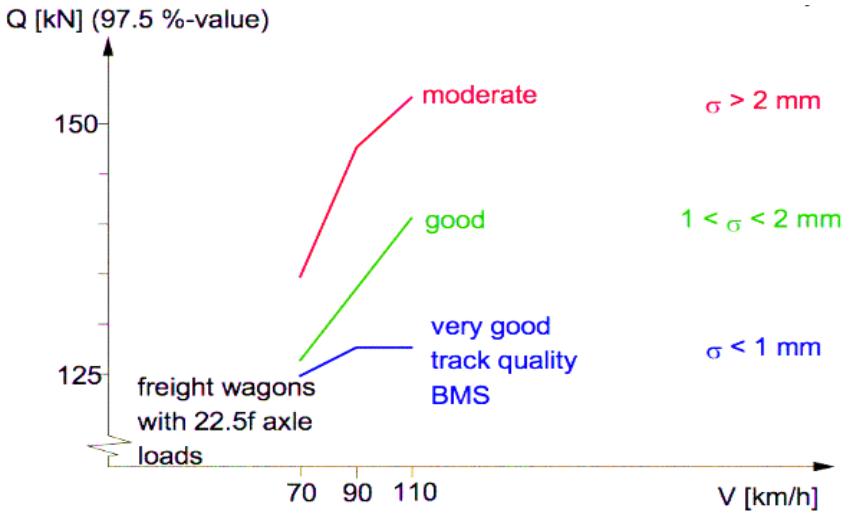


Figure 2.2: Q-Forces of 225kN axle loads(Esveld 2001)

Currently, there are no standard methods for determining the dynamic properties of a track. Instead, engineers assume the dynamic responses based on the static loads. In design codes, the static wheel load is factored by an incremental amount, called the Dynamic Amplification Factor (DAF). An impact factor of 50% was first used and has incrementally increased to today's 200%

level. A 200% increase above static load indicates that the design load is three times the static load, and corresponds to an impact factor of three. Yoon et al. (2013) conducted field measurements under train speeds of 100-300 km/h on the Yeonjae Bridge in South Korea and concluded that the DAF decreased with heavier trains even though deflection was larger. At high speeds, 300 km/h, the limiting values were exceeded, and calculation showed that the DAF varied considerably. Different codes calculate their impact factor using different parameters. The impact factors of the same train resulting from the use of different design formulae were investigated by Dyk et al (2014) and is shown in Figure 2.3. Note: 1mph = 1.609km/h

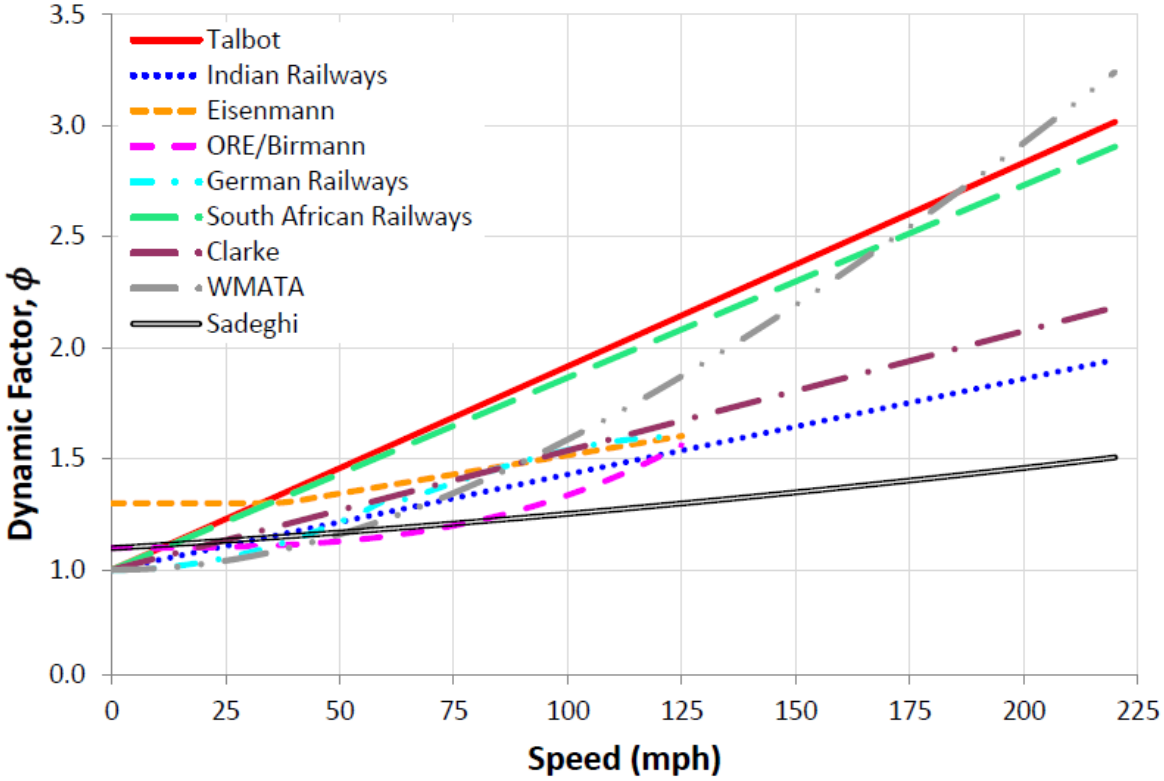


Figure 2.3: Design dynamic factors due to increase in speed(Dyk et al 2014)

Not every method considers all the parameters involved. The table in Appendix A.2 shows the formulae used in design manuals; most of them consider train speed and wheel load. Many of the dynamic factors can be used to predict the load amplification, due to speed, only in specific operating applications because they have been established over many years in particular regions of the world. Furthermore, the classical methods available in engineering codes of practice, for evaluating dynamic impact factors, do not cover the possibility of resonance. The latter may lead to liquefaction of soft ground at the critical speed. Although other research is currently being conducted in order to understand the behaviour of ballast under high impact loads generated from wheel unevenness, from the above background, it is mandatory to consider railway problems as dynamic problems rather than static ones (Indraratna et al. 2010). It is therefore mandatory to relate how track quality and speed affects the DAF since ballast is considered to be elasto-plastic, and degrades under high dynamic loads.

2.2.2 LATERAL LOAD

Unlike vertical loadings, the horizontal mode is less understood (Zicha 1989), and the total lateral force cannot be predicted with great reliability. The total lateral force is a function of the lateral force exerted by the wheels on the outer rails. The lateral deflection of the rail is resisted by the friction between the rail component and ballast. The displacement is also influenced by weight, dimension and spacing of sleepers, grain-size distribution in the ballast bed, quality of ballast outside the sleeper, and consolidation of the ballast bed. Not only should the train be capable of running at high speed, but the track must

be able to support such high velocities on curved sections where it needs to resist centrifugal force. Any lateral sliding due to such vertical load action is difficult to observe(Siew et al. 2015). As shown in Figure 2.4, the lateral stability of the track/ballast interface is mainly caused tilting trains cornering at high speed, side-winds and dynamic loads such as hunting. Manda (2014) recorded the increase in dynamic load factors of passenger trains travelling at different speeds on tangent and curved sections of the track, and noticed an increase of 1.2 and 1.6 respectively. The dynamic factor on the curved tracks was found to be in the range of 2-3. Field measurements on a high-speed line, conducted by Chebli et al. (2008), indicated that the lateral force was 20% that of the vertical load.

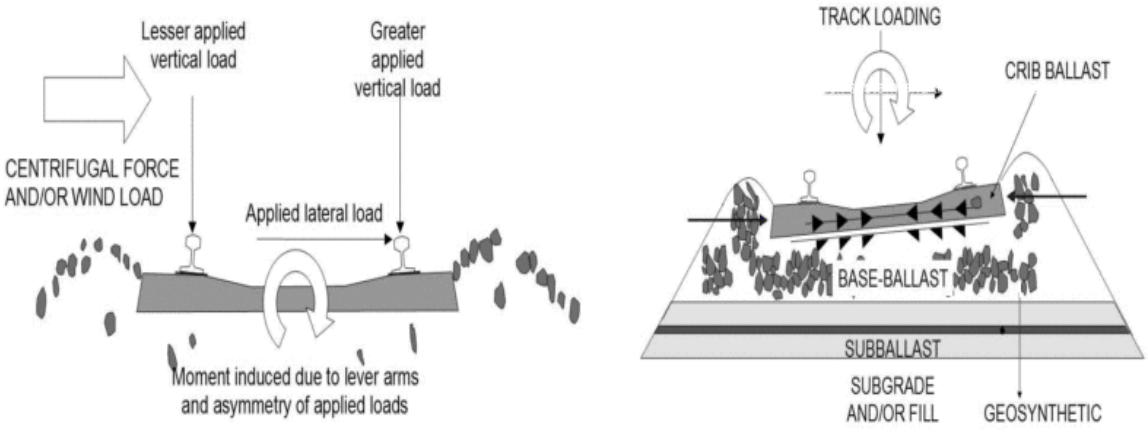


Figure 2.4: Lateral forces and moment(Powrie n.d.)

The conventional ballasted track lacks lateral confinement, and despite the current knowledge of rock fill mechanics, high lateral movement is expected. It is therefore essential to attempt to increase the lateral stability of the track.

2.3 WHEEL-RAIL-SUBGRADE INTERFACE

The load, arising from the contact interaction between the wheels and the rails, eventually needs to be transmitted to the subgrade. This non-linear distribution of the stress schematically illustrated through Figure 2.5 and Figure 2.6, is dependent mainly on material parameters, load characteristics and geometry as shown in Figure 2.7. The 'steel wheels on steel rail' technology, of the modern HSR, has not changed since its introduction in the 19th century. Ballasted tracks have low construction costs, short construction and maintenance times, and offer the possibility for further improvement by allowing for feasible and practical changes in geometry, including super-elevation. Many ingenious technological enhancements were required so as to allow trains to run at speeds over 200 km/h. When modelling the mechanics of the problem, the conventional railway track is regarded as a panel comprising of a pair of rails and sleepers, floating on a granular material. The 2 degrees of freedom per rail depend on the cant, level alignment and gauge of the track. These degrees of freedom arise from the wheel and lateral loads. Figure 2.5 shows how each component distribute the load. The wheel loads are transferred via high stresses at the steel wheel to steel rail contact which can be up to 1 GPa until it reaches 50 kPa at the subgrade. The stress between the sleeper and the ballast, considered as the primary load bearing stratum, is about 300 kPa. From this context, the highest concentration of stress is at the contact region between the wheel and the rails, and since non-linearity can play a considerable role in amplifying this load, it is important to try to reduce the stress at this region.

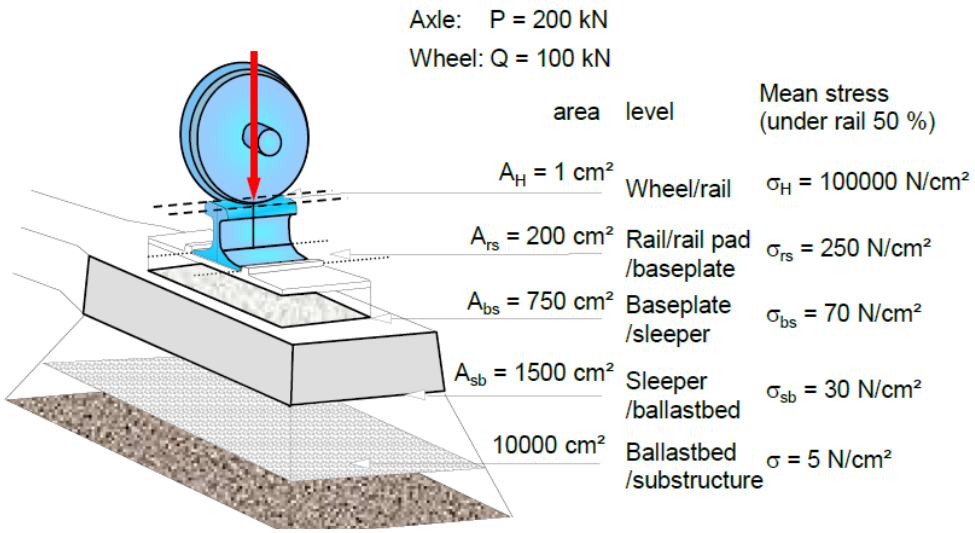


Figure 2.5: Wheel load distribution(Esveld 2001)

In design, a uniform trapezoidal pressure distribution is usually assumed in order to calculate the bearing capacity and bending stresses in the sleeper (Cossio et al. 2012a). However, a set of pressure distribution has been proposed by many researchers since the distribution to be used differ by application. Talbot (1953) was one of the researchers and proposed that the pressure distribution in the ballast under the sleeper would be shaped like bulbs as shown in Figure 2.6.

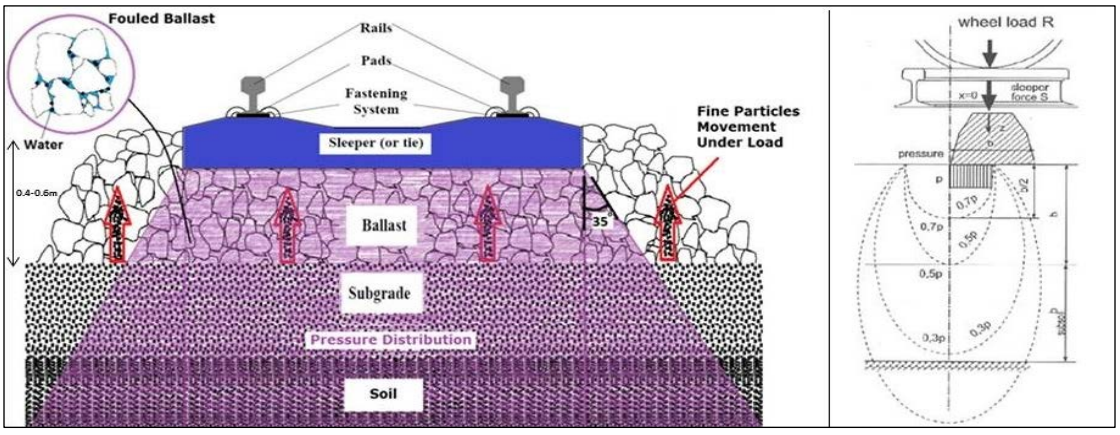


Figure 2.6: Track structure, pressure distribution, track deterioration and depth of influence (Chandra & Agarwal 2007; Lichtberger 2005; Esveld 2001)

There is a direct link between the level of pressure onto the ballast and the rate of deterioration of the track. Decreasing the average pressure on the ballast will lead to a lower rate of degradation. To achieve this, one can use a heavier rail-profile, which spreads the load over more sleepers, decreases the distance between the sleepers, or increases the bearing surface of the sleepers themselves by making them longer or broader. Several attempts have been made with broader sleepers and slab sleepers, but these were not successful. Several researchers have tried to alter this stress distribution in order to minimise track deterioration. Selig & Waters (1994) conducted parametric studies by altering the geometry of the track. Increasing sleeper distance from 250mm to 910mm increased the load underneath the sleeper by four, while a 40% reduction in the load under the sleeper occurred when the moment of inertia of the rail was increased from 1610 cm^4 to 6240 cm^4. A stiffer rail will have less elastic and bending properties, and the stress transmitted from the rail to the sleeper and further to the ballast and subgrade is thus higher. The pressure distribution in the sleeper-ballast interface depends mainly on the void ratio in the ballast, which is time-dependent since it is influenced by factors such as traffic loading, train speed and maintenance frequency. Figure 2.7 shows some of the parameters that affect the total settlement.

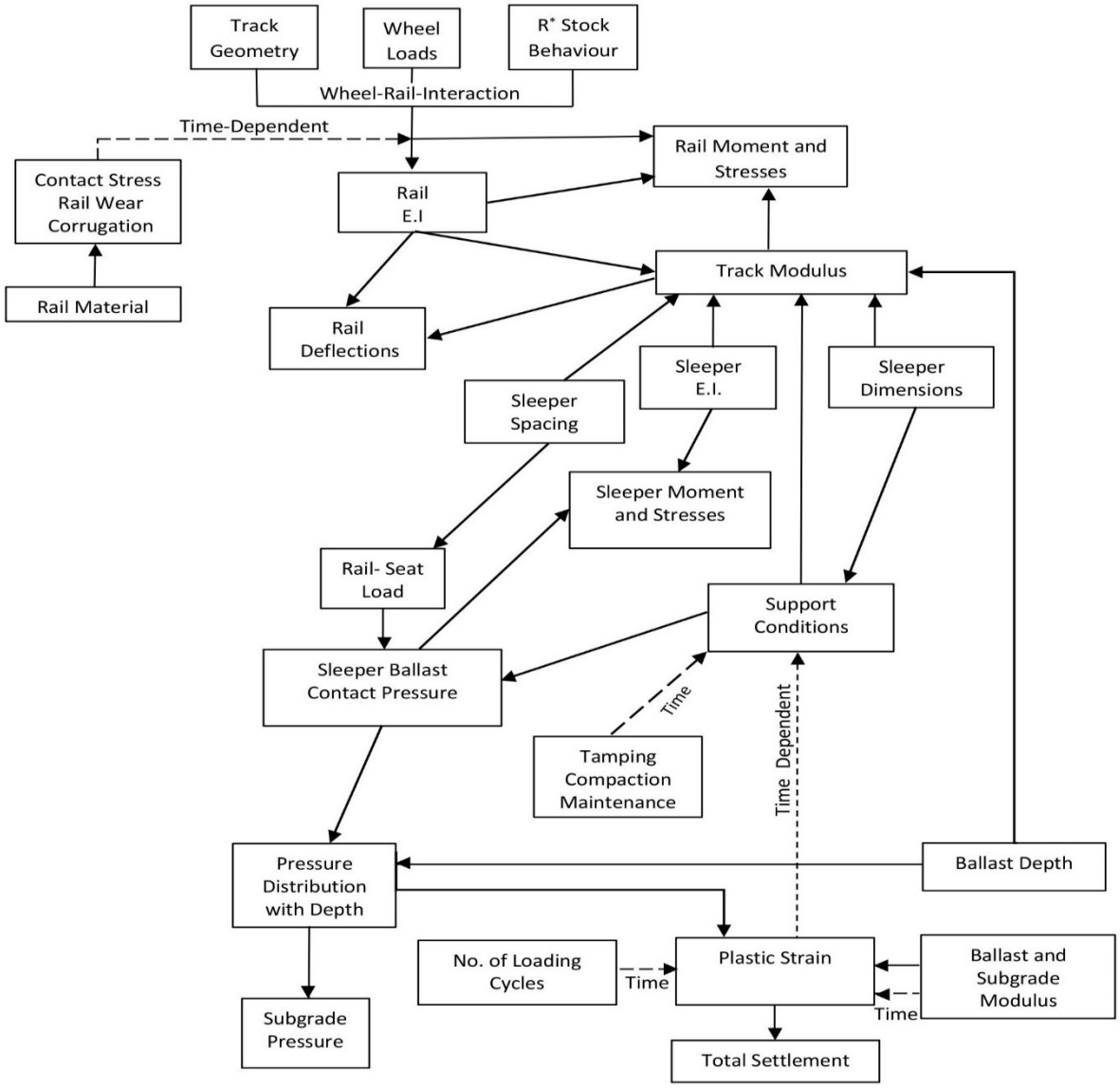


Figure 2.7: Track interaction diagram (Boyle 1980)

2.3.1 BALLAST DEGRADATION MECHANISM

Selig & Waters (1994) showed that among all the track components, the ballast layer contributes the highest (up to 50–70%) in track settlement. The granular layer settlement is the summation of the deformations of the individual track layers used to transmit the loads to the subsidiary layers. In-situ measurements, carried out by Chebli et al. (2008), on the Northern French

high-speed network, confirmed that majority of the dynamic loads are reduced by components under the sleeper, especially the ballast layer. Sensors placed above the sleeper recorded a peak positive acceleration of around 8 m/s^2, and negative acceleration amplitudes of about half of that of the positive ones (around 4 m/s^2). Sensors just below the ballast recorded lower amplitudes (around -1 to 2 m/s^2) at different depths. The subgrade did not reduce the acceleration as compared to a reduction factor of 4 obtained from above to the bottom of ballast layer.

Particle breakage was found to be intensified by increases in load frequency, confining pressure and maximum cycle load. (Sun et al. 2010; Nimbalkar 2015). The rate of permanent strain under cyclic loading decreases significantly with the decrease in the number of load applications. Owing to the lack of lateral resistance, the sleeper sinks deeper into the ballast due to the lateral and longitudinal movement of the sleeper. The load spreading ability of a material can be described by its resilient stiffness (the reciprocal value of stiffness is flexibility or resilience), which is determined from the recoverable strains during unloading. Materials of low stiffness do not spread loads well. The secant modulus has been widely adopted as the basic parameter to describe resilient strain behaviour. The secant modulus simplifies an unloading stress-strain curve by considering the endpoints of the curve only. (This approach is used in Chapter 6-test 3) In order to characterize materials more in detail, it is increasingly common to present the resilient deformation behaviour in terms of volumetric and shear deformations. There is a continuous volume reduction characterized by a permanent, and a resilient component.

The primary factors influencing the resilient strain response are the mean normal stress and the ratio of deviatoric stress to normal stress. On the conventional track, the ballast bed provides approximately half of the resilience needed to absorb dynamic forces; the other half is provided by the subgrade. If pads are present, ballast takes up to 20%. This stiffness of the overall track structure can be of the order of 100KN/mm, per sleeper which makes the rail deflect by approximately 1mm under a 200kN axle load.

Furthermore, cyclic loading at speeds higher than 300 km/h causes important track vibrations which are gradually amplified in a repeated manner and since classic ballast has not yet been optimised for such high-frequency vibration, there is an significant increase in track deterioration rates and maintenance costs (Ferreira & López-Pita 2015; Lichtberger 2011; Paixao et al. 2015). As ballast operations are a key life-cycle cost (Ebrahimi & Keene 2011), and excessive vibrations increase the need for maintenance in order to ensure track geometry. The accelerations need to be monitored, and the values should be limited in order to avoid track instability according to Eurocode standards. The combination of stresses (short period) in the ballast, and vibrations, which are transmitted to the substructure, play a decisive role in the deterioration process.

Figure 2.8 shows that, for speeds of 250km/h, the vibrations measured by Puzavac et al. (2012) are 30mm/s. In order to avoid quick deterioration of the ballast material, and thus track geometry deterioration, it is suggested that maximum allowable movement of the ballast per unit second should not

exceed 15 to 18mm. In addition, it can be seen that the use pads of stiffness 20 to 60kN/mm decreased vibration. Even if a less stiff pad can decrease vibration, larger deflections should be expected. In this context, a parametric study on track stiffness, frequency of loading and track geometry are essential, to find the optimum link between vibration and settlement.

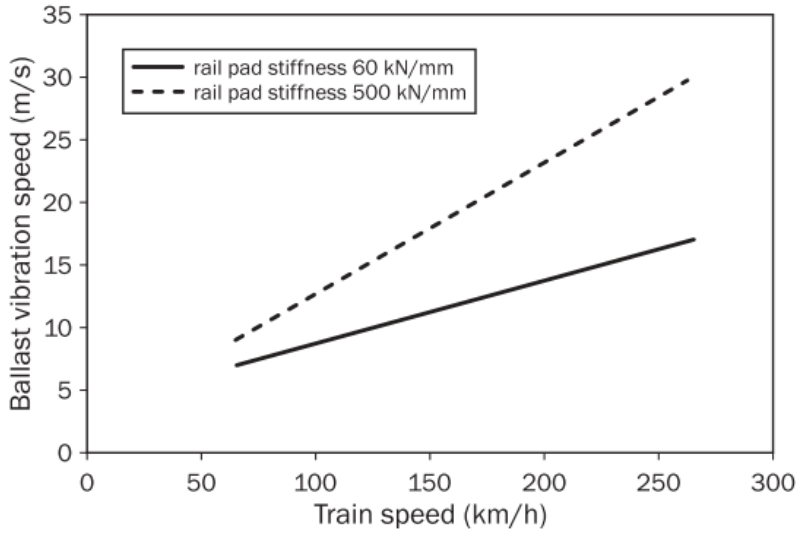


Figure 2.8: Influence of rail pad stiffness on vibration in the ballast (Puzavac et al. 2012)

2.4 TRACK MODULUS

2.4.1 TRACK STIFFNESS

The rail-wheel interaction flowchart in Figure 2.7, shows that the rate of track deterioration is mainly influenced by the track modulus or track stiffness. Compared to the superstructure, the substructure is influenced by more variables which are difficult to define (Selig & Waters 1994). Track stiffness is a basic parameter which influences the bearing capacity of the track, the dynamic behaviour of passing vehicles and the quality of track geometry. There

are many definitions for the vertical track stiffness (k), but in its simplest form, it is the ratio between track load (F) and track deflection (z) as a function of time(t), where the force can be either axle load or wheel load:

$$k(t) = \frac{F(t)}{z(t)} \qquad \text{Eqn(1)}$$

In general, a high track stiffness provides sufficient track resistance to applied loads and results in decreased track deflection, thereby reducing track settlement. However, Prud'homme (1967) demonstrated that a very high track stiffness speeds up deterioration since dynamic forces in the wheel-rail interface, as well as on sleepers and ballast, which may cause wear and fatigue of track components owing to wheel stresses which are concentrated within a small area, generating corrugation.

Fortin (1882) showed that a large reduction in track stiffness could produce an increase in the resistance to forward movement of the vehicles. A low stiffness allows elastic movements during wheel passage and will decrease the vertical strength of the structure. Consequently, larger displacement and larger bending moments will be observed. Additionally, a decrease in the track stiffness could increase the settlement of the track and the fatigue of its elements. Furthermore, Lin et al. (2009) stability of the ballast layer is also affected by the track stiffness.

Additionally, if stiffness varies radically over track sections, track deterioration and vibrations are amplified. Yang et al. (2009) calculated values for the track modulus from data obtained using geophones measuring dynamic displacements of the track during standard train service and showed that the

track modulus varies from 72% to 101% along a track. This is because the different sections of a track do not undergo the same amount of deflection under the same load due to the presence of slacks and voids in the track structure. The track deflection is disproportionately higher during the initial stages of loading. The void ratio decreases after the initial load, and, thereafter, any further deflection per unit load becomes smaller. This relationship is highly non-linear. Hence the track stiffness varies with frequency, dynamic amplitude, applied preload and position along the track.

A common method for analysing the frequency characteristics of railway tracks is to calculate the track receptance (reciprocal of track stiffness as a function of time). When known, these frequencies can be dampened accordingly. For a running train, each track property variation, in either material or geometry represents a transition. A stiffness difference increases the dynamic loading on the track as a consequence of the increased dynamic loading, and differential settlements. Therefore, track geometry deterioration and potentially vibration problems may emerge. Differential settlements trigger additional train vibrations which cause the dynamic loading to become larger the next time the train passes the stiffness transition. Accordingly, the differential settlements grow further, and the mechanism described repeats itself (Puzavac et al. 2012). Hence the length of the transition should be sufficiently large to reduce dynamic amplification.

Geometry degradation, as well as noise and vibration, have been identified as problems that need to be reduced. This could be possible by modifying track

vertical stiffness to obtain a more homogeneous value along the track (Sol-Sánchez et al. 2015). However, one should be careful with this approach as dynamic interaction is frequency dependent, not only on stiffness but also on mass and damping (See Section 2.3.2). In general, enhancing the resilience can have a positive effect on the dynamic forces.

2.4.2 Optimal Stiffness

Since the standard deviation of dynamic load is directly proportional to track stiffness, it is of practical interest to ensure an optimal stiffness value. Each track component has its own stiffness. Research, so far, did not manage to solve the problem of quantifying the total track stiffness based on individually explored sections. The modification of the stiffness of components such as rail, sleepers or ballast can cause the deterioration of the stability and resistance of the track (Sol-Sánchez et al. 2015). Ferreira & López-Pita (2015) stated that the optimal value of vertical stiffness should be around 50-78kN/mm, while according to available literature, the optimum track stiffness range from 80-130kN/mm and is dependent on the type of traffic.

According to Sol-Sánchez et al. (2015), the dynamic properties of a track can be enhanced by improving the elasticity of superstructures and by increasing the bearing capacity of the layers underneath the ballast. Use of softer ballast or rubber pads can minimize track wave velocities and hence reduce ground vibration by providing an optimal value of stiffness. A classic method to modify stiffness is to install a ballast mat underneath the ballast bed. This is performed for mitigating the propagation of ground vibration, or in zones of the track with significant longitudinal stiffness variations. Track resiliency can also be

augmented through the insertion of high-damping materials. López-Pita (2015) did numerical simulations on different track design solutions. It was concluded that the insertion of a pad of stiffness 70kN/mm^2, between the rail and the sleeper, filters out high-frequency vibrations under the sleeper, and reduces settlement (Sol-Sánchez et al. 2014). Substituting ballast by a bituminous layer reduced accelerations by approximately 18% for train speeds of 300 km/h and 24% for speeds of 350 km/h. From the analysis, instantaneous responses to train passage revealed reductions in track vibrations for all solutions except for the case of ballast mats. This only reduced vibrations on the track substructure but amplified accelerations (by 25–35%) and displacements above the subballast layer, which is clearly undesirable. The most significant reduction in acceleration was accomplished by placing under-sleeper pads.

2.4.3 DAMPING

Dynamic stiffness accounts for inertial effects as a function of frequency. The primary source of damping in structures is energy dissipation between components. The stiffness of mechanical structures is determined by structural deformations. It is shown that in many typical vibration control situations, the effects of changing stiffness (natural frequencies) and damping are interrelated, and can be expressed as criteria for decreasing vibrational effects. These are useful for guidance during solving vibration control problems, making the problem-solving process more flexible since the effects of changing stiffness and/or damping become transparent.

The damping capacity of ballast generally depends on two effects: the interparticle friction and the distribution of particle sizes. When the friction between the particles is high, a coarse-grained ballast, a relatively large amount of energy is dissipated at the particle contacts, causing the ballast to have a high damping capacity. The second effect stems from the fact that a wide particle size distribution excludes a dominant appearance by large particles that may act as resonators. Accordingly, a ballast material with a random distribution of various particle sizes has a better damping capacity than a ballast material which consists of identical particles of a relatively large size.

Fan et al. (2009) developed and tested different damping materials. The bitumen and water-based damping coating reduced vibration in the broader frequency range (63–1000Hz) and reduced noise inside the carriage by 5–8 dBA. The damping materials reduce low-frequency vibration of carriages less efficiently. Loaded trains running at subcritical speeds (See Section 2.5.1) inhibit two types of damping: Material damping and radiation damping (Steenbergen 2013). Research has proved that it is more efficient to damp and attenuate waves at the source itself and using a material with high damping ratios is more practical than damping waves themselves. Methods that are commonly used for solving these vibration control problems are to modify the stiffness or the fundamental natural frequency of the specified components and their damping (Rivin 2007).

An increase in stiffness results in a reduction in deformation of the component (See Section 2.4.1). These effects usually lead to damping reduction in the stiffened component/subsystem, since energy dissipation constituting the damping effect results from deformations of, and relative displacements (motions) between, the components. Thus expensive modifications, aimed to enhance stiffness, may, at the same time, fail in controlling vibrations due to the reduction of damping. Zhai et al. (2004) stated if the shear stiffness and shear damping are increased, stronger attenuation effects between neighbouring ballasts will diminish the vibration levels.

According to Snowdon (1958), an excellent anti-vibrational material should possess a high damping factor which does not increase significantly with frequency, and should be free from any major increase in dynamic modulus with frequency. Sorbothane is a polyurethane material with a very high damping coefficient. It combines shock absorption, good memory and has a long fatigue life. (Further details about the material is provided in Section 6.2.1)

2.5 VIBRATION

For many years, engineers and scientists have been concerned with the control of unwanted structural vibration and noise. When a railway track is excited to generalized dynamic loading, the railway track deforms and then vibrates for a certain duration. The primary aims of attempting to control vibration have been to avoid possible damage due to excessive and repeated motion, or to reduce acoustic radiation into areas surrounding the structure. Noise, or pressure waves, are generated by vibrating structures. Attempts in reducing

noise are often related to reducing vibration. On railway tracks, vibration waves that are transmitted are generated by dynamic loads at the wheel-rail interface due to the presence of irregularities caused by several phenomena such as differential settlements (Sol-Sánchez et al. 2015). The most critical conditions occur when the predominant frequency of ground vibration coincides with the natural frequency. An especially large increase in vibration level(more than 70 dB (Krylov 1996), as compared to conventional trains) may occur if train speeds exceed the velocity of Rayleigh surface waves in the ground.

The discomfort of passengers due to excessive train to body vibrations can be overcome by adjusting the train's suspension system to reduce the train to body vibration at high speeds. The ground-borne propagation problem is expected to be solved by decreasing the vibration of trackbed, which is the source of ground-borne noise and vibration. When reviewing the energy dissipation in a trackbed, it can be found that it is the kinetic energy, which is initially created from the train vibration that causes the trackbed (ballast) vibration. Some energy is dissipated due to the particle friction from ballast vibration, while the other energy is radiating to the subgrade in the form of waves. The percentage of energy dissipated by the trackbed is dependent on the stiffness, damping capacity, and vibration frequency of the trackbed (Su 2005). Furthermore, the dynamic subgrade-structure interaction is also dependent on properties of the soil such as its shear modulus and on the frequency and amplitude of the dynamic loading. When train speed increases linearly, the dynamic response of the ground increases exponentially

(Katzenbach n.d.). Currently, there is no requirement in existing code or standards that limit the acceleration levels of ballast in high-speed tracks. The vibrational effects need further investigation.

2.6 CRITICAL SPEED

It is known that a beam attached to sleepers on an elastic foundation should theoretically have a point where the dynamic amplification factor is highest (Connolly et al. 2015). The highest mechanical loads occur at critical speed, and large track vibration may occur hence the allowable speed has to be lower than the critical speed (Lichtberger 2005). As operational speeds increase, chances that the speed of the train matches this 'critical velocity' at a particular site also increases. For tracks of good quality, the critical speed lies far beyond the operating speed, but poor soil may have Rayleigh wave velocity of 40-50 m/s (Madshus & Kaynia 2000).

Finite element analysis carried by Esveld (2001) suggests that at half the critical speed of a train, the dynamic load increases by less than 10% of static, so at 260km/h the dynamic load is approximately equal to the static load. At 260km/h, Dahlberg (2004) suggests that the dynamic load increases by around 2.45 times that of the static load. According to Esveld (2001), the critical speed is approximately, as shown in Figure 2.9, the velocity that is situated on or near the velocity ratio when the latter is 1. Velocity ratio, ɑ, is described as train velocity/Rayleigh wave velocity and, β is the damping ratio. According to Esveld (2001), Eqn(2) and Eqn(3) can be derived for the critical speed V_c assuming a moving load on the surface of an elastic solid.

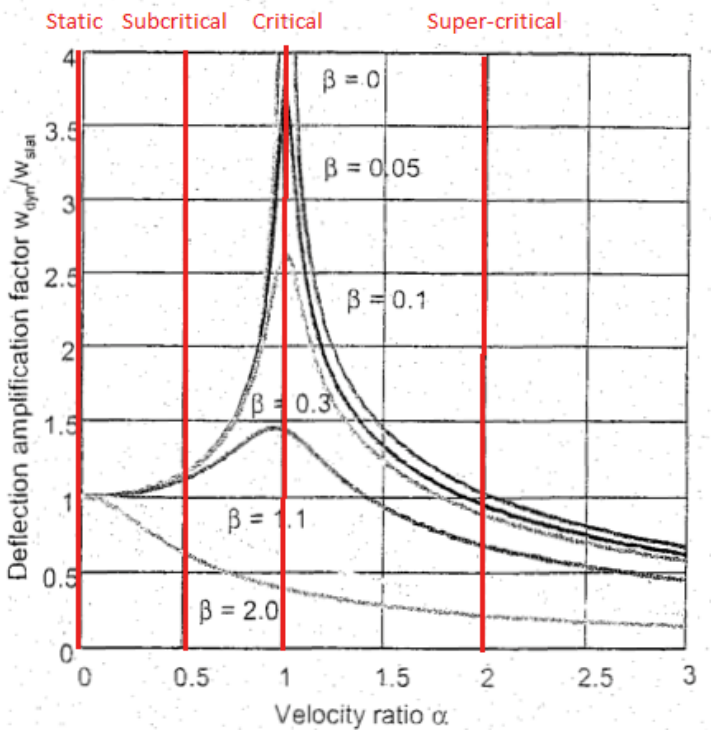


Figure 2.9: Dynamic Amplification vs Speed due to moving load (Esveld 2001)

Where:

$$V_{cr}^2 = \frac{2}{m}\sqrt{kEI} \qquad \text{Eqn(2)}$$

In which:

m = rail mass per length,

k = track stiffness,

EI = bending stiffness,

and

$$\frac{Qdyn}{Qstat} = \frac{1}{\sqrt{\left|1 - \left[\frac{V}{Vcr}\right]^2\right|}} \qquad \text{Eqn(3)}$$

According to Eqn(3), the higher the damping, the smaller the dynamic amplification factor(Manda 2014). However, Lichtberger (2005) contradicts the formula stating that the calculation for critical speed is inaccurate, because E and I are unknown for the entire track grid, because the requirement that

ballast bed is a zero-mass and permanently coupled to the track grid is not fulfilled entirely because the requirements of pure elasticity are not applicable.

Colaço et al. (2015), assuming linearity of the system, showed that the critical speed is both dependent on the ground layers and on the track–ground mechanical properties by using finite element analysis. Otherwise, the critical speed is not only function of the properties of the system but also depends on the magnitude of the loading and concluded that the higher the stiffness, the higher the critical speed will be.

In order to prove the critical speed, Madshus & Kaynia (2000) carried out field tests in Sweden soft soil site. The displacement responses were plotted in Figure 2.10. This confirms that when the ratio of the normalised speed or velocity ratio is 1, the displacements that were recorded were maximum.

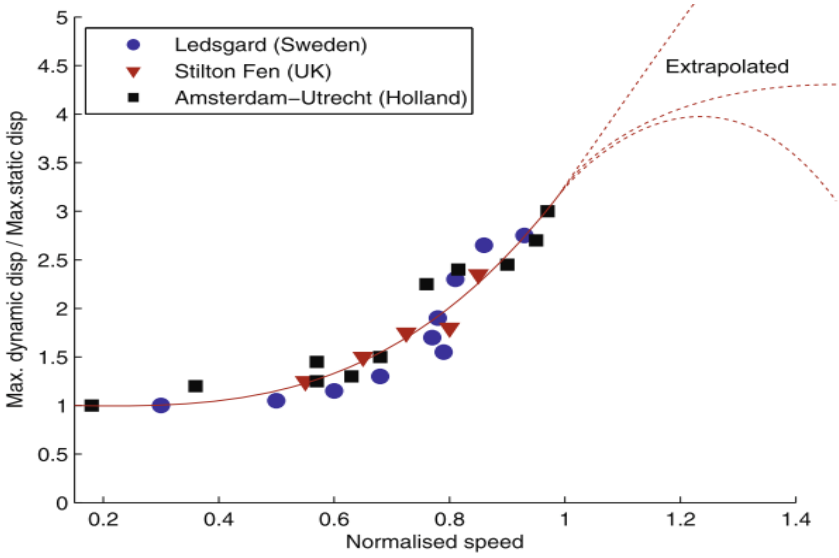


Figure 2.10: Critical velocity effects and a dynamic portion representing freely propagating Rayleigh waves (Madshus & Kaynia 2000)

Above that value, numerical models were used to extrapolate the graphs, and this is still an active area of research. Moreover, it is shown that the critical speed and the amount of dynamic amplification also depend on a coincidence between characteristic wavelengths for the site and the distances between bogies and axles in the train. Costa et al. (2015) who performed FEM–BEM numerical simulation further confirmed that with the increase in unsprung mass of the train, larger vibration levels should be expected. However, changes in wheel/bogie spacing and semi-sprung mass are found to have a minimal effect on vibration generation.

This is further confirmed by Goicolea et al. (2002) that each train has its own dynamic signature according to Eurocode 1 for actions which cover the be necessities for dynamics analysis adequately using the finite element method. Colaço et al. (2015) who performed a parametric study to determine the relationship between train properties and ground vibration propagation found no clear trend between them. Therefore, it is uncertain which parameters governing the vibration levels. Figure 2.11 shows that the larger the damping, the lower the impact force and it can be concluded that damping is one of the important factors that need to be considered.

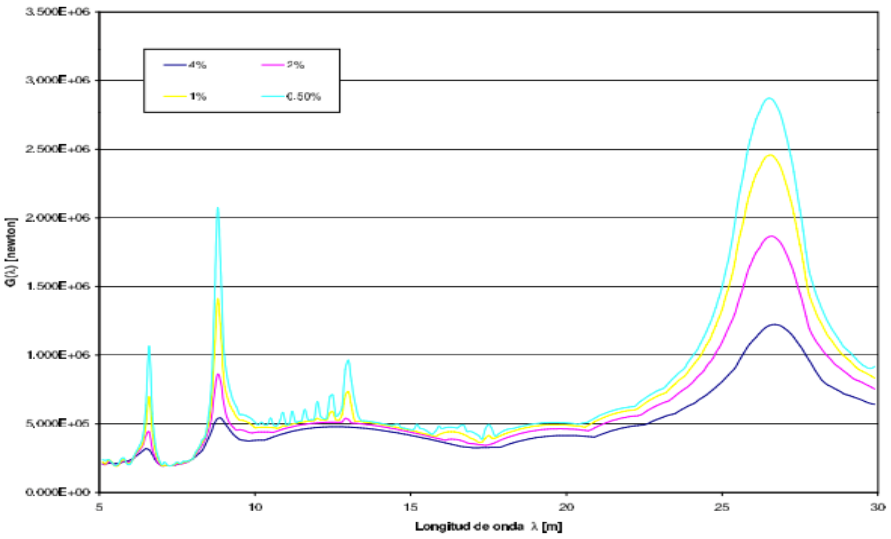


Figure 2.11: Dynamic signature of train ICE2 with different damping rates (Goicolea et al. 2002)

Madshus & Kaynia (2000) noted that for higher train speeds, displacements of the rail are both upwards and downwards. The displacement pattern is non-symmetrical in time with hardly any displacements ahead of the train but with a “tail'' of free oscillation following the train. Wavelength is proportional to the train circulation speed, v. However, to pass the point of critical speed would lead to large amplification, which are unacceptable for railway practice, this being the reason that present railway operations are all sub-critical (Esveld 1997). The combined vehicle/track system is complex and has many natural frequencies. When one of the excitation frequencies corresponds to a natural frequency of the system there is a particularly strong vibration. A strong vibration also occurs if an excitation frequency or natural frequency of the system corresponds to the sleeper passing frequency. However, natural frequencies of the system are independent of running speed, which complicates the relationship between critical speed and natural frequency of

the system. As the speed rises, a coincidence of frequencies may occur, and the vibrations will reach a peak and then diminish. Thus, vibrations do not increase steadily with speed and a speed reduction may sometimes make the vibrations worse.

2.7 CONCLUSION

Dynamic amplification factor can be used to assess the percentage increase in design load due to train speed and the geometry of the rails. All current codes for calculating DAF consider train speed and wheel load, and geometry of the track has a significant effect on the degree of incrimination. From the literature, it can be observed that it is difficult to provide a unique solution that would enhance the properties of a track since the behaviour of trains varies depending on ground conditions and train type. Each train and track has its own dynamic signature and a range of parametric study needs to be performed on a variety of rail pads (because they contribute to 20% of settlement reduction), train speed and rail geometry. Therefore, each type of improvement brought to the track can only be appropriate for a specific type of system. Furthermore, owing to the lack of lateral resistance, the sleeper sinks deeper into the ballast due to the lateral and longitudinal movement of the sleeper. The primary factors influencing the resilient strain response are the mean normal stress and the ratio of deviator stress to normal stress, both being closely related to the degree of confinement. The pressure distribution in the sleeper-ballast interface depends mainly on the void ratio in the ballast, which is time-dependent since it is influenced by factors such as traffic loading, train speed and maintenance frequency. Distribution of voids for different track

section causes stiffness variation, consequently leading to dynamic impacts and further change in stiffness. It is uncertain which parameters govern the vibration levels but the linking factor between vibration and track settlement is track stiffness which varies according to frequency of loading, dynamic amplitude, applied preload and position along the track. Different options of reinforcement that can both provide an optimum vertical stiffness and decrease the amount of vibration have been investigated in Chapter 3. From the study of the mechanics of a track, an optimum track will be considered as one that has very little settlement, excellent resistance to corrugation(non-linearity), uniform stiffness, provides good vibrational damping properties and has high critical speed limits.

CHAPTER 3: TRACK REINFORCEMENT DESIGN

3.1 INTRODUCTION

In this Chapter, optimisation of the track is attempted. From chapter 2, an optimal track should have little settlement, good resistance to corrugation (non-linearity), uniform stiffness, and provides good vibrational damping properties. Current techniques that are being used in practice are analysed, and a new design is proposed. A possible method of implementation is, furthermore, described. The methodology that will be adopted for testing the efficiency and benefits of the reinforcement is described. The design mainly focuses on reinforcement of ballast since this is where the highest settlement/damping occurs.

3.2 TRACK REQUIREMENTS

Exceptionally well-designed vehicles can operate at high speeds on ballasted lines since with increasing speed, the superstructure requirements do not change significantly; for example, modifications brought to train control system would only affect the operating pattern. This is not the case for the substructure. Structural enhancement is mandatory if subgrade improvement is not considered since a high-speed track requires an increase of 2 to 4 times in the elastic modulus of the subgrade. Table 3.1 includes other requirements, apart from structural requirements, of a ballasted substructure that would be classified as a very good track, and that would be appropriate for high-speed trains. These requirements are indirectly related to the quality of the track. In addition to the parameters described in Chapter 2, these requirements will also be considered where possible.

Table 3.1: Good track requirements apart from structural needs (Pimentel et al. 2009; J.Bathurst 2009; Lichtberger 2005)

Requirement	Description
Separation	Prevent intermixing of different soils under the repeated loading and water
Filtration	Retains soil while allowing passing of water
Drainage	Allow passage of water through the plane of the geosynthetic material without build-up of pore water pressure
Isolation	Prevents fluid from passing from one side of geosynthetic to the other
Planar Reinforcement	Resists soil extension strain with confinement provided by tensile strength of the geosynthetic
Ground-borne vibration	Provide the necessary dynamic resiliency, energy absorption, vibration attenuation, and noise absorption
Lateral spreading	Provide confining pressure and deviatoric stress amplitude which can contribute to track buckling
Subgrade settlement	Bearing Capacity by load distribution
Abrasion resistance	Withstand the impact and wear forces of moving aggregate

3.3 BALLAST REINFORCEMENT

3.3.1 GEOSYNTHETIC REINFORCEMENT

Geosynthetics have been used in the field of engineering for more than half a century and can be considered to be cost effective tools which can assist professionals in the construction, rehabilitation and maintenance of all forms of geotechnical work. The use of geogrids to enhance the performance of roadbed sections has become much more widespread, particularly during the last 10 years. Initial cost savings on the order of $30,000 per linear mile of track can generally be achieved by installing a geogrid within the sub-ballast layer (Penman & Priest 2009). This measure contributes to a decrease in

maintenance by reducing the roadbed thickness and differential settlement. In past research (Mishra & Hasan 2014; Han & Thakur 2012; Cook et al. 2015; DiMaggio & Cribbs 1996; Lu & McDowell 2008), a variety of geosynthetic materials were used to examine the effects of parameters of geosynthetic materials, including stiffness, aperture size of geogrids and rib profile on track settlement. The following physical properties (non-structural and non-geometric) of geotextiles are needed during implementation:

- Abrasion and impact resistance: When ballast is placed, it is dropped about one metre onto the geotextile. No evidence can be obtained to suggest that geotextiles meeting an abrasion criterion would not be suitable to resist the loads. It is suggested that a minimum strength of 0.5 N/tex is required. tex is the linear mass density of fibres.
- Elongation: A track geotextile should be able to elongate. Based on a comparison of failed and satisfactory in-track geotextile performance a minimum 60% elongation at failure in a grab test conforming to ASTMD-4632.
- Chemical Resistant: Track geotextiles must be degradation resistant to such chemicals.

The application of geosynthetic within railway construction can be subdivided into different types based on their application which are illustrated in Figure 3.1.

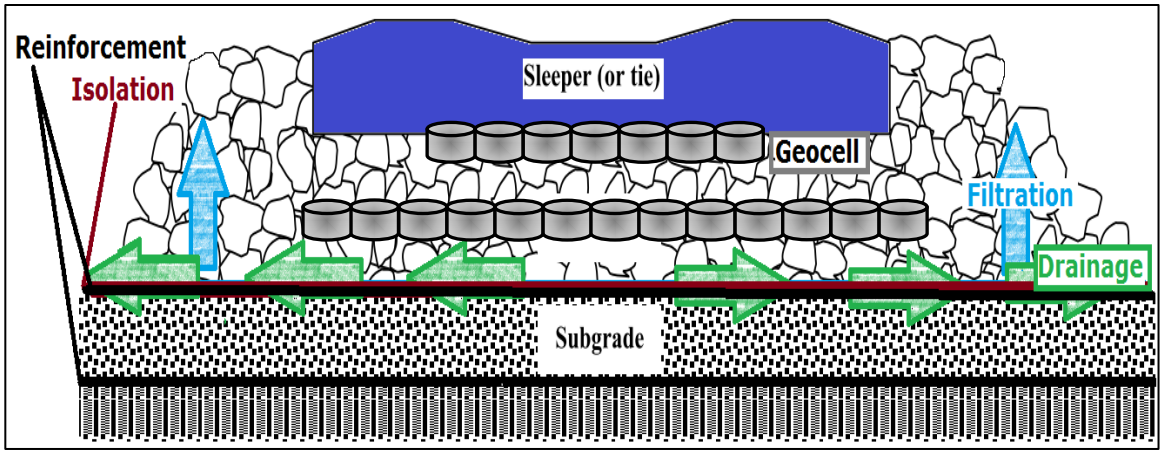


Figure 3.1: Location of geosynthetic for required function

However, no single geosynthetic can fulfil all the requirements of a good quality track on its own, and the use of a dual layer can result in slipping (Ferreira & López-Pita 2015; Lichtberger 2011). Model track tests reveal that geogrid effectively arrests the lateral strains in ballast, thus reducing the extent of ballast settlement and minimizing the particle breakage. However, the effect of geogrid decreases with vertical distance from its placement position. Nevertheless, reinforcements that are placed close enough to sleepers causes tamping difficulties, while the processes of separation, isolation and filtration require that the geosynthetics be placed deep, near the sub-ballast or subgrade. Observations of geotextile installation demonstrated that geotextiles should be installed at a depth of not less than 300 mm, below the tie base and that tamping should not be permitted until that depth of ballast was in place (Raymond 1999).

It was also observed that installing geotextiles to facilitate drainage is one of the most important factors but, according to Hamnett & Heeler, (1943) geotextile does not filter out clay under dynamic loading and the tensile

resistance of a geogrid is mobilized at a high degree of strain. Thus a planar geosynthetic material does not efficiently reduce vertical settlement and cannot contribute to the rigidity of the track (Leshchinsky & Ling 2013). Woodward et al. (2012) further stated that single geogrids have limited effect in changing the behaviour of ballast due to vibration and the use of combined geocomposite was more common and efficient.

3.3.2 GEOCELL CONFINEMENT

Stress ratio is the ratio of deviatoric stress, q, to confining stress, σ_3. Lackenby et al. (2007) who carried out a series of triaxial tests found out that at an optimum range of confining pressure, degradation of ballast was minimised. In-situ lateral confining pressure results from particle interlock, sleeper resistance, residual compaction stresses, and overburden pressure, and is considerably smaller than the wheel load-generated cyclic vertical sleeper-ballast interface pressures. This can result in a significant rearrangement of particles and the subsequent occurrence of ballast degradation, track settlement and lateral spreading. In the case of geocells, once filled, each cell acts in conjunction with adjacent cells to form a stabilised composite mattress that disperses load and resists lateral movement and shear failure.

Therefore, one potential method of enhancing the substructure is by manipulating the level of ballast confinement and thus, lateral strength (Esmaeili et al. 2015). Christie et al. (2007) performed a parametric study on a range of large-scale cyclic Triaxial tests on ballast. The resilient stress-strain behaviour showed that confining pressure has a significant effect on the behaviour and strength of ballast. It was suggested that in-situ lateral

pressures should be increased to counteract the axle loads. Field measurements conducted by Woodward et al. (2011) showed that for a 300mm wide ballast shoulder width the maximum lateral resistance measured was 2.15kN and for a 600mm wide shoulder it reached 2.317 kN; these contributed around 30 and 32 per cent of the maximum lateral resistance of the unloaded sleeper. Mcdowel et al. (2015) stated that to restrain the lateral movement of ballast under high frequency cyclic loads (corresponding to trains having speeds higher than 146 km/h) after 1000 cycles, side restraints should be applied to increase the confining pressure.

When the confining pressure is raised, the particles close to the movable sidewalls become compacted, and dilation is reduced. Sitharam & Sireesh (2006) conducted a study on different configurations of geogrid (planar reinforcement) and geocell (3D reinforcement). It was observed that the beneficial effect of the base geogrid layer becomes negligible with increasing height of the geocell mattress beyond the influence of the depth of the sleeper. Strain measurements in the base geogrid layer indicate that it is more effective with the limited heights of the geocell mattress.

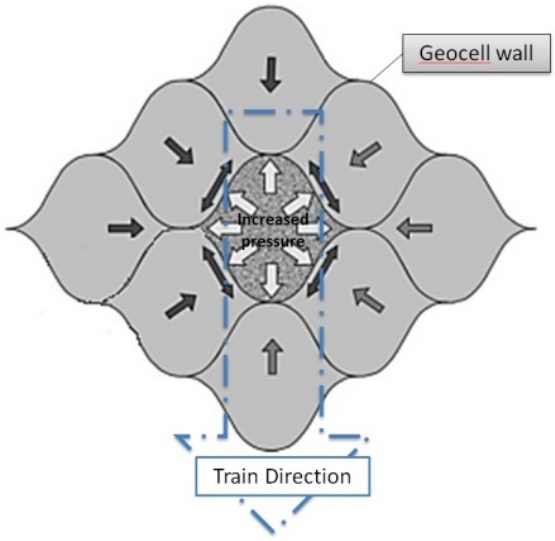




Figure 3.2: Geocell cross section (Kennedy 2011) Figure 3.3: Geocell filled with gravel (Kennedy 2011)

Unlike planar geotextile, 3D reinforcing elements made up of plastic, rubber or other polymers offers all-round confinement to the encapsulated material and behaves more effectively as a retardant for the effects of dynamic loading than planar reinforcement. Researchers (Tafreshi & Dawson 2010; J. Han, X. Yang 2007) found that geocell filled with granular materials were more effective under dynamic loading than cells that were completely filled with sand. Leshchinsky (2012, 2013) conducted finite element analysis as well as laboratory testing to examine the effect of geocell confinement under both cyclic and monotonic loading. The settlement was minimised because the confining mechanism distributed the load more uniformly. This statement was further acknowledged by Hegde & Sitharam (2014) who specified that the matressing effect that is provided to the subgrade can reduce settlement by 78% and increase bearing capacity by 4.5 times. Thallak et al. (2007) reinforced clay by using geocells and found that subgrade reaction coefficient

improved by 3000% and deformation can be reduced by 44%. Indraratna et al. (2015) claim that by reinforcing ballast with geocells, the allowable train speed can be increased by approximately 5–25%. According to Zhang et al. (2006), inclusion of 3D-reinforcement increases the internal friction angle of the encapsulated material as well as provide cohesion due to the stress imposed on the walls of the geocells. Furthermore, it was noticed that ground-borne vibration did not increase during the passing of a train when geocells were introduced (Esmaeili et al. 2014). Hushmand (1983) confirmed that confining pressure can increase the damping ratio in some cases since more energy is dissipated. From this context, it can be broadly said that inclusion of geocell into a railway ballasted track can increase the bearing capacity and lateral confinement, and decrease vibration. In the next section, the specification of the geocells that brought these improvements has been examined.

3.3.2.1 Specifications

Currently, no standards exist in relation to lateral ballast confinement in rail tracks and the effect of track confining pressure on substructure performance under cyclic loading has not been examined in depth. The optimum depth of a 3D geocell is 0.1 times that of the sleeper width. Leshchinsky (2012) conducted cyclic tests at a frequency of 5Hz and monotonic test on a ballast embankment and found that most significant spreading occurred in the middle portion of the embankment. Wesseloo et al. (2009) concluded that strength provided by geocell decreases with the increase in number and size of individual cells. Rea & Mitchell (1978) stated that the optimum dimensions of the cell were relative

to the loading plate. Pokharel et al. (2010) investigated the effects of providing geocell reinforcement of sand. The reinforcement that provided the highest stiffness under static load was confined and circular in shaped, and was dependent on the elastic modulus of the geocell material. On the other hand, unconfined geocell offered a higher bearing capacity than multiple geocells. Dual Layer geocells are even more effective (Leshchinsky 2011). However use of dual layer geosynthetic has proven to cause slipping (Cope et al. 2001). From the static tests conducted by Leshchinsky (2011), it was deduced that perforated geocell were less effective than unperforated ones. The shorter geocells offered larger bearing capacity since the longer ones, started to behave like beam structures and started bending rather than providing a tensioned membrane effect. It should be noted that, it is inappropriate to conduct static tests for railway application since frequency of loading has to be considered in tests. Geocell made up of materials such as aluminium involve very high cost, and handling is challenging (Pokharel et al. 2010). Geocells made up of materials such as rubber or geotextiles are more commonly used. Vertical confinement mechanism is provided through friction between the walls and the infill. Using all the information gathered in this section, some of the important parameters that do influence the behaviour and performance of geocells have been summaries in Table 3.2.

Table 3.2: Summary of important parameters to consider for geocells

Materials	**Geometry**	**Combination**	**Relative Dimension**	**Texture**
Tensile strength	Length	Number of layers	Sleeper	Perforated
Damping	Circular diameter	Number of cells	Depth	Roughness of wall

3.3.3 BITUMEN STABILISATION

The technique of reinforcement using bitumen, which solved problems such as pumping and excessive settlement, was pioneered by Ayres of British rail and has proven to be effective for more than 8 years on Richards Bay Coal Line under a total traffic of 353 gross million tons. Hampel et al. (1975) and Hall & Giles (1991) also effectively sprayed bitumen to consolidate ballast where about 4-6 litter per m^2 was required so as to fill all the voids and avoid bleeding. Crushed stones were then spread over the hot bitumen to fill all the voids and form an impermeable surface. According to Raymond (2002), by 1982, around 290km of railway, including high speed lines, was already treated with sprayed bitumen. A track with good structural integrity and stiffness has higher capacity for diffusing load. Bitumen also prevent fines degradation and prevent loss and intermixing of material. The adhesive nature of bitumen provide cohesion, damping and waterproofness. In the following section, the components that can be modified by bitumen and that are most influential to a track are detailed.

A similar technique involves the injection of Rigid-polyurethane foam (RPF), to granular materials. After injection and solidification of RPF in the ballast matrix, it improved strength by occupying pore space and cementing the particles together (Chandra & Agarwal 2007, Keene et al. 2010). In other words, the three-dimensional movement of the ballast was restricted, and issues such as ballast migration and subsequent voiding development were prevented. However, Rigid-polyurethane foam (RPF) is expensive and could be replaced by another visco-elastic material (Lee et al. 2014; Teixeira et al. 2010; Chen et al. 2015; Di Mino et al. 2012). The adhesive, waterproof, thermoplastic, durable, modifiable and recyclable characteristics make bitumen an ideal construction and engineering material (Etzkowitz & Zhou 2008).

Non-uniform stiffness along a track or transition problem is directly related to ballast movement, and hence techniques that attempt to increase the formation/subgrade strength will often not solve the problem, even if the track stiffness increases. Swedish high-speed network shows that rigid structures can accommodate design speed of 325 km/h, while ballasted track would allow approximately 40% slower speeds(Fröidh 2014). Generally, construction of slab track is more expensive than a ballasted track, but its high geometric stability allows a significant reduction in track maintenance. Bitumen aims to provide the same properties of a slab track, by adhering the ballasts together. This measure will result in the increase of the stiffness and the dynamic stability of the structure (Katzenbach n.d.). Woodward et al. (2012) proposed similar solutions which was termed geopavement where the ballast was transformed into a pavement-like structure using 3D-geocomposite. The

technique was found to be very effective in other regions as well, such as South Africa, until the waterproofness was lost during tamping. Therefore unlike XITRACK, which is an improved version of geopavement, (Balfour Beatty 2015), the use of bitumen as an adhesive is reasonable, and waterproofness is not expected to be lost very easily.

Apart from increasing the stiffness of the track, the ability to reduce track vibration forms an important aspect of polyurethane track reinforcement techniques. Most common damping materials displaying viscoelastic behaviour are polymers such as plastics and rubbers. A material is termed viscoelastic if it can simultaneously store and (through viscous forces) dissipate mechanical energy. Fang et al. (2013) proved that the usage of asphalt layer in vibration control results in smoother rides and tougher railway substructures. Chinese Railway successfully used various damping agents, namely bituminous materials, to enhance the travel environment of passengers (Fan et al. 2008). Bitumen dissipates energy by rebounding thus reducing tension, fatigue and cracking. Cracking leads to poor subgrade drainage and high deflection.

Additionally, according to Raymond (2002), large deformation settlement failure with granular material layer may occur due to seasonal softening of subgrade by heavy rainstorms. Liu & Xiao (2010) carried out field measurement in order to study the effect of water content in the substructure when used by high-speed trains. They noticed that in dry conditions, the dynamic loads did not impair the stability of the subgrade. In wet conditions, on the other hand, sudden elastic deformation of the subgrade and a significant

decrease in resilient modulus was observed. Gill (1991) highlighted the need for a good drainage and lateral resistance. Maintenance costs were reduced by 30% in 1926 where bitumen was sprayed. Suiker (1997) studied the effect of saturation on granular response and determined that loading frequency concerns only saturated materials due to the flow of pore water. When ballast is fouled, drainage can be blocked, and viscous effects may become important. The effect of moisture on resilient modulus depends on the degree of saturation. At low degrees of saturation, the moisture content has a negligible effect on resilient modulus. However, the resilient modulus decreases considerably for high degrees of saturation, especially as the aggregate approaches complete saturation. Too much water content in the substructure can cause series of different problems; therefore, drainage is of vital importance. As for most of the substructure issues, drainage should be adequately made when building the track. The first requirement to achieve substructure drainage is to keep the ballast clean enough to be able to drain the water as fast as it enters.

From this context, the use of bitumen to reinforce ballast is expected to increase the stiffness and waterproofing properties of the track. Ground vibration is also expected to decrease because of the visco-elastic nature of bitumen. The rigid structure will, therefore, allow higher speed trains to run.

3.4 TESTING METHODOLOGY

It is important to investigate the behaviour of ballast, geocell and bitumen under real field conditions as well as differences in loading characteristic that the structure will be subjected to when being used for high-speed trains. The current analyses and design approaches for using geocell are all empirical

(Hegde & Sitharam 2015; J. Han, X. Yang 2007) compared to geogrids where the BS8006(1995) and limit state design are used as design guides. Bitumen can be modified and applied to meet the requirements of specific applications. For this research, only one type of bitumen will be used. For geocells, the geometry and configuration will be tested. Many other parameters used in design processes cannot be estimated with absolute accuracy since they have an inherent variability. Further details about testing and reasoning have been given in the specific chapters. A flowchart, as shown in Figure 3.4. illustrates the methodology that was adopted in order to successfully complete the project. The parts are successively initiated once all the criteria of the previous parts have been achieved. The approach undertaken to achieve the aim of this research consists of 3 components.

Part 1 consists of finding the appropriate parameters and solid evidence that the type of reinforcement is practical and it would improve the stability and properties of the ballasted track. This has been carried out in Chapter 2 and Chapter 3, where the dynamics of the trains has been analysed, and appropriate measures have been proposed respectively. The design of the reinforcement as well as the specification of the materials in terms of geometry and properties have also been described.

Part 2 consists of finding the loads and the properties that cause a static wheel load to become a sinusoidal load at the wheel-rail interface and how the mechanics of the problem will change with the increase in speed and dynamic forces. Proper investigation, at a very small scale, needs to be carried out about this behaviour using numerical methods. Once the nature and origin of

the loads have been confirmed, it is important to attempt a parametric study, which includes pads and rail geometry, in order to verify if the track can be improved at the superstructure level.

A discrete element analysis will then be performed using the results that have been obtained from the Finite Element Analysis. If the results of the DEM prove to have beneficial effect, then Part 3 can be initiated, or else another reinforcement scheme needs to be proposed. Numerical parametric study can be found in Chapter 4 and 5.

The objectives of **Part 3** can be achieved by performing experimental testing, in order to improve the understanding of the interaction of ballast with both geocell and bitumen reinforcements. Preliminary tests such as cyclic compressive tests, ERUDITE and finally a shaking table test were used to determine the optimum geometry of geocells, stiffness changes, damping properties and appropriate properties of the reinforcement. A large-scale test can then be performed in order to validate the results obtained from the DEM. Experimental testing was performed in Chapter 6.

3.4.1 TESTING METHODOLOGY FLOWCHART

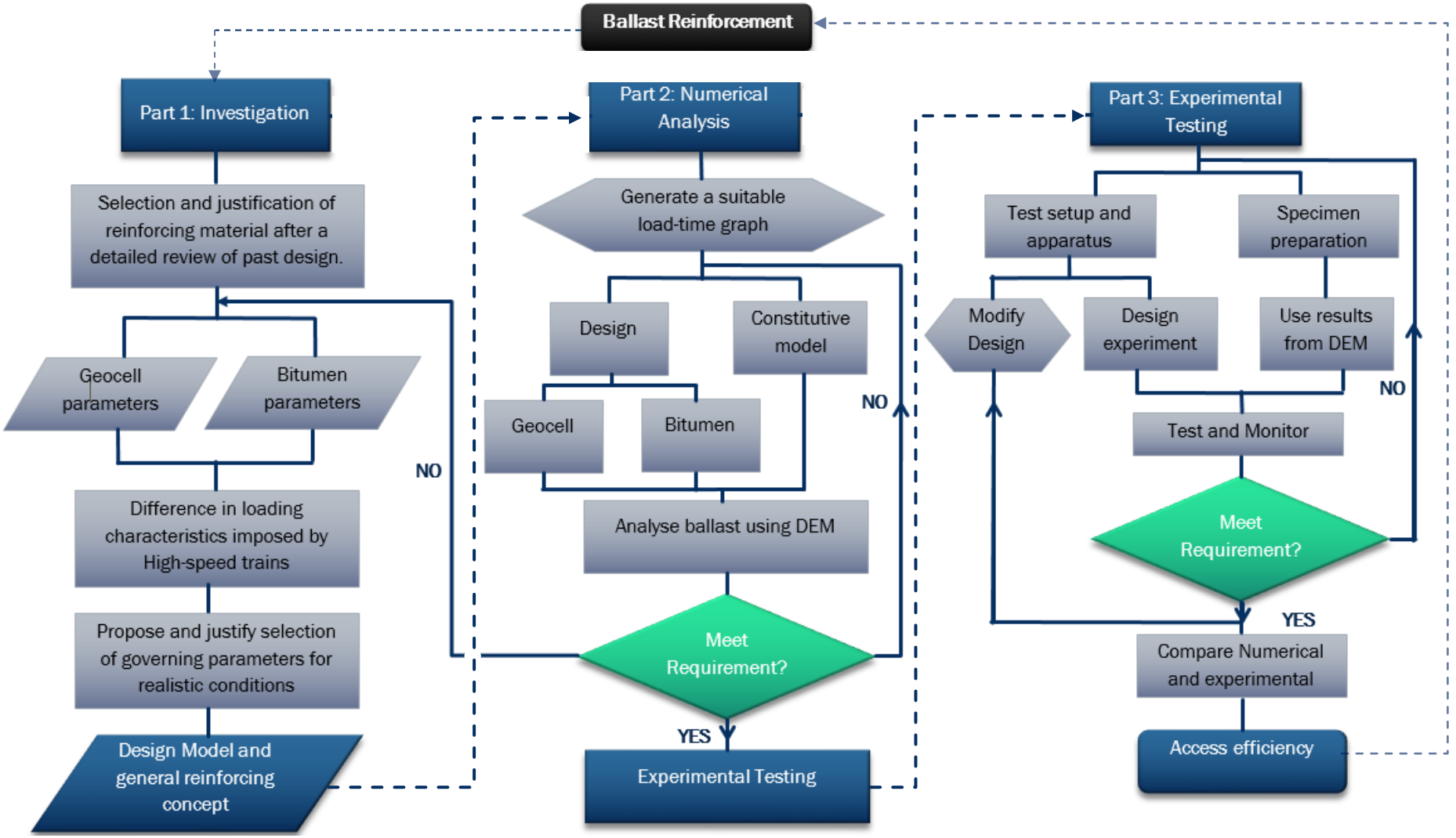


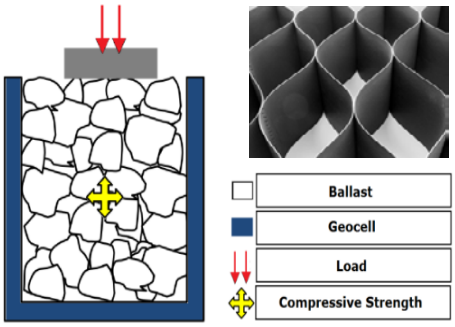
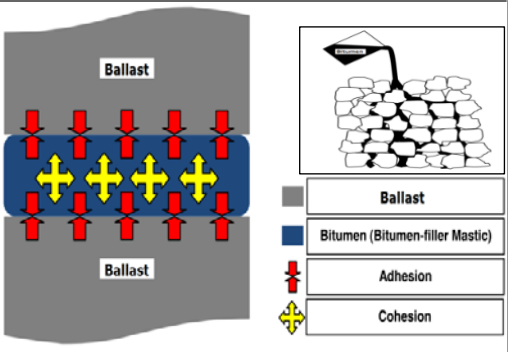
Figure 3.4: Methodology flowchart at its simplest

3.5 REINFORCEMENT DESIGN

3.5.1 COMBINING REINFORCEMENTS

In addition to structural improvement, the requirements listed in Table 3.1 also need to be fulfilled. The concept behind the use of a geocomposite material is the combination of different features of several materials so that applications are addressed in an optimal manner. Table 3.3 summarises the strengths of geocell and bitumen. The combination and possible incompatibility issues is discussed in this section. In Table 3.3, the strength of each reinforcement and mechanism of both geocell and bitumen is highlighted. The information presented is a summary form of section 3.3.1-3.3.3.

Table 3.3: Reinforcement materials Properties

Property	Geocell	Bitumen
Illustration	 Figure 3.5: Geocell Confinement	 Figure 3.6: Ballast-Bitumen Adhesion
Strength	Compressive	Tensile
Reinforcing Mechanism	Provides lateral confinement through geocell-ballast interface friction under loading (Dash & Shivadas 2012)	Provide vertical and lateral resistance through adhesion (Woodward et al. 2011)
Vibration	Does not increase vibration	Visco-elactic and damping material, can reduce internal vibration and noise (Fan et al. 2009)
Drainage	Allows vertical Drainage	Provides isolation and retention preventing ballast fouling

Void	Creates void	Decreases void, hence ballast movement
Settlement	Decreases settlement under dynamic and monotonic load and allows load distribution (Pokharel et al. 2010)	High resilience, and recovery properties. Increased stiffness.
Rigidity	Increased shear strength bending resistance, tensile strength (Singh & S 2015)	Increased rigidity through adhesion of discrete granular elements upon solidification

As mentioned in earlier sections, incorporating high damping materials in ballast can increase the resilience of a track. Incorporating a rubber geocell with a high damping ratio together with bitumen enhances the properties of the mixture since rubber increases the complex modulus of asphalt. Furthermore, the lateral confinement provided by the geocell will reduce strain and prevent cracking of bitumen under extremely high forces provided that the tensile strength of the geosynthetic material is very high. Previous studies where rubber and bitumen was used together include a study conducted by Sol-Sánchez et al. (2014) who demonstrated the effectiveness of using tire cord mesh to reinforce desirable properties of asphalt. Sanders (2001) carried out a survey of 185 organisations within Britain to find out the usability and benefits of geosynthetic materials in reinforcing asphalt. He concluded that the geosynthetic indeed reinforced asphalt. It was also noticed that placing the reinforcement between the roadbase and bindercourse was more effective in inhibiting cracking than when the reinforcement was placed between the binder course and the surfacing. Furthermore, Wang & Zeng (2004) conducted numerical simulations on different types of materials as High-Speed train foundations. From these results, it was concluded that rubber-modified asphalt concrete is more efficient in damping out vibrations (18% reduction) from

dynamic loading compared to other paving materials. Its rubber component adds resilience to the asphalt and increases its resistance against compression and crack propagation.

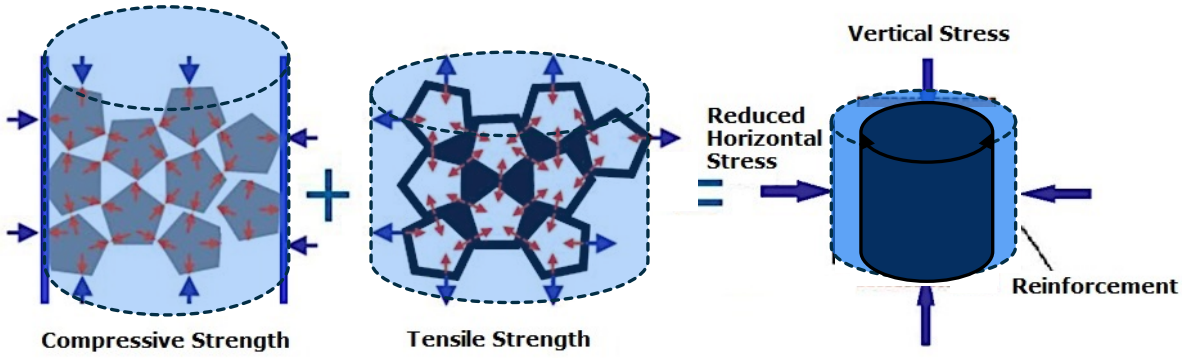


Figure 3.7: Bituminous Geocomposite(Balfour Beatty 2015)

It is proposed that bitumen reinforcement can prevent degradation if a sufficiently strong adherence is provided, increase rigidity if lateral strain is reduced and diminish vibration. Figure 3.7 shows the inside of each geocell. Bitumen fills in the voids in each cell, providing huge damping capabilities. The cells are squeezed by their neighbours, the particles surface break and the particles re-orientate themselves. When bitumen is added, this behaviour is expected to be reduced. The strain that the track will undergo in either the lateral or vertical direction is thus expected to be minimised.

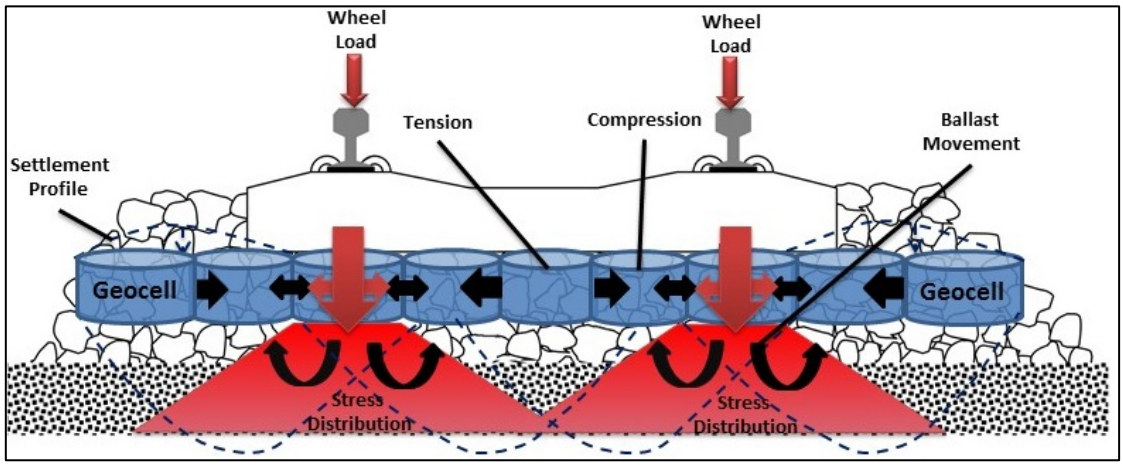


Figure 3.8: Expected Load Path (Chandra & Agarwal 2007)

As shown in Figure 3.8, geocells affect the stress distribution of the vertical stresses to the soft subgrade material. The effect of a geocell layer on the load transfer mechanisms was verified by tests conducted by Meyer (2010). It was found that geocells directly beneath the wheel path were in tension while the outside geocell experienced compressive stresses. The wheel load is converted into horizontal stresses which is counterbalanced by the compressive strength of neighbouring cell while the bitumen provides tensile strength through adhesion as shown in Figure 3.7, and provides damping owing to is viscoelastic nature. The difference in extensibility between the ballast and geosynthetic wall membrane causes the mobilisation of stresses at the soil-reinforcement interface, and as the amount of strain increases, there is a gradual increase in the level of confinement. Therefore, the settlement profile is expected to be similar to that of a rigid foundation.

3.5.2 INSTALLATION PROCEDURE

A particular problem that exists when upgrading an existing structure is the need for excavation and complete removal of the superstructure before building a new formation. This cannot be economically justified. Installation of the geocell can be done when maintenance such as ballast cleaning, or ballast renewal is being done. The ballast cleaner is a self-contained unit and progresses about 0.1m/sec. Figure 3.9 illustrates the basic principle for the installation (at its simplest) of the geocomposite. Substructure improvement is often costly. There are few techniques that can be used without removing the superstructure. Besides, Tensar International Corporation is currently developing techniques for installation of geogrid. Geocell installation may also be possible with minor modifications in the procedures (Penman & Priest 2009). It should be noted that emergency tamping would destroy the reinforcement

which can be effective for up to 7 years (Hall & Giles 1991). Therefore, it is important that the track is brought to a high geometric standard before attempting the procedure.

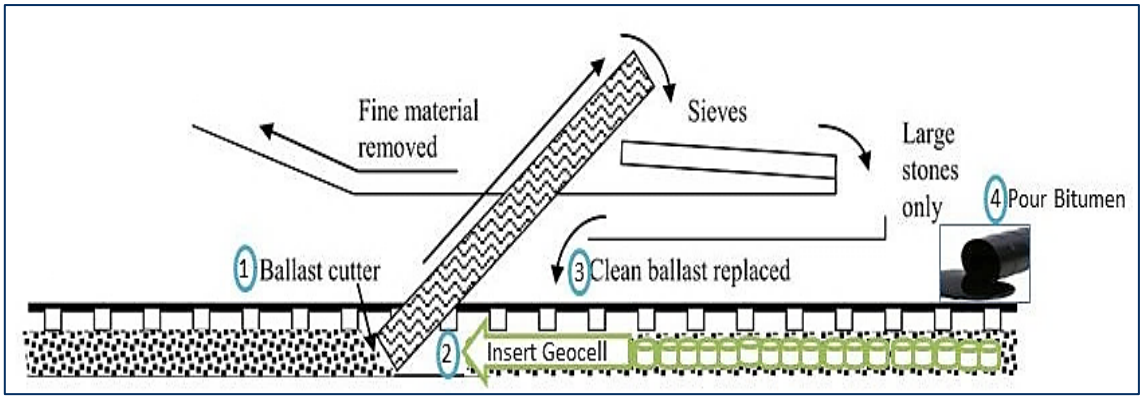
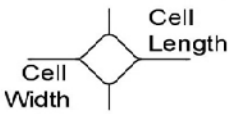


Figure 3.9: Placement of geocell during ballast cleaning (Chandra & Agarwal 2007)

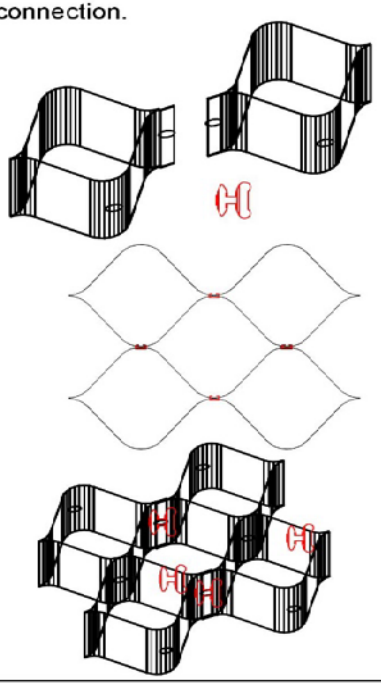
After the geocell has been placed at the required depth, the modified bitumen can be injected, and allowed to cure. A detailed sample drawing of the reinforcement is shown in Figure 3.10.

Cell Size

NOMINAL CELL AREA IN (CM^2)	CELL EXPANSION RANGE MINIMUM LENGTH IN (CM)	MINIMUM WIDTH IN (CM)	MAXIMUM LENGTH IN (CM)	MAXIMUM WIDTH IN (CM)
44.8	8.02	9.2	9.65	11.07



Alternatively, the cells can be connected with Atra keys at each interleaf and end to end connection.



Material Specifications

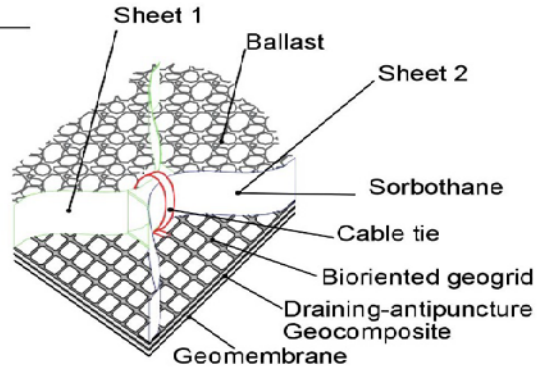
Sorbothane:
Grade: 70
Tensile strength: 173 psi
Compression set: 3%
Elongation at break: 395%
Specific gravity:1.318
Dynamic Modulus at: 10,15,20%
05Hz–180, 204, 238
15Hz–223, 252, 294
30Hz–258, 291, 338
50Hz–289, 325, 377

Bitumen:
Binder type: Cationic bitumen emulsion(200 penetration)
Application rate: 8 to 13.5 litre/m2
Spray width: 3.7m
Spray bar: 20 tp 25,, diameter pipe nozzles
Progress: 1.5 to 2.0 m/min

Bottom Layer Connection Design

Notes:
The sheets are connected by cable tie to produce a honeycomb shape. Additional geosynthetic material can be placed at the bottom of the geocell.

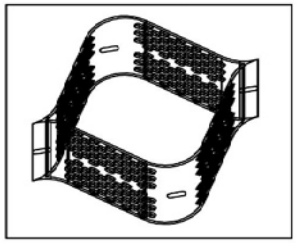
Cable tie should have high tensile strengths.



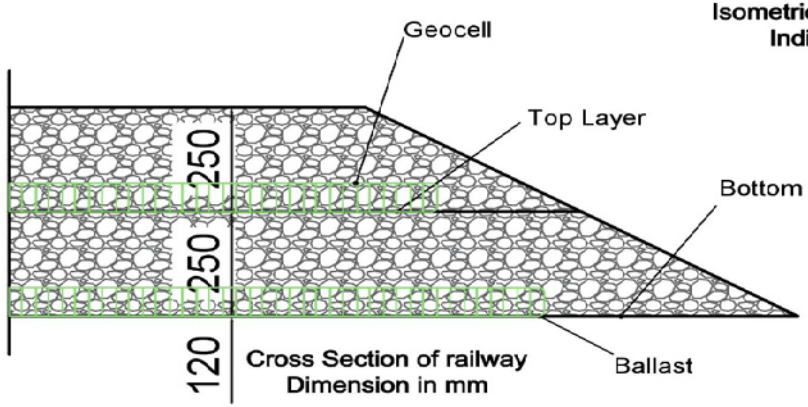
Case Senarios

Different combination are to made from these alternative:

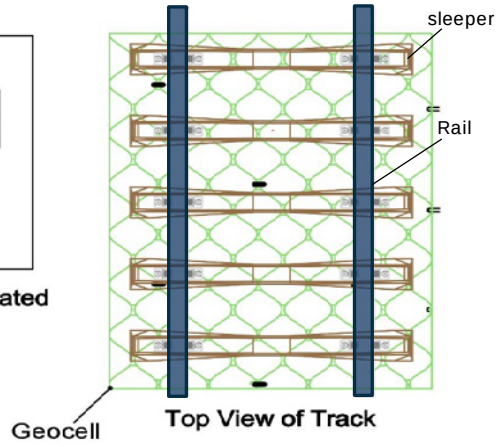
- Geocell at top layer
- Geocell at bottom layer
- Bitumen Sprayed
- No Bitumen Sprayed
- Type of connection used



Isometric view of perforated Individual Geocell



Cross Section of railway
Dimension in mm



Top View of Track

UNMC	NOT FOR CONSTRUCTION
BALLAST REINFORCEMENT DETAILED DESIGN	
DATE JUNE 2016	DRAWN BY C. TOSHAN RAMPAT
SCALE NTS / SHEET 1OF1	CHECKED BY DR. A.ABDULLAHI

Figure 3.10: Sample detailed Design

3.6 CONCLUSION

It is proposed that bitumen reinforcement can prevent degradation if a sufficiently strong adherence is provided, increase rigidity if lateral strain is reduced and diminish vibration. Geocells are expected to alter the stress path and increase the lateral confinement of ballast. It was noted that bitumen improves waterproofness. From the literature, use of bitumen and rubber geocells have been widely used for reinforcing pavement. Bitumen, being a visco-elastic material, has proven to have vibrational damping properties. Furthermore, owing to its highly adhesive nature, can prevent movement of ballast by filling up the pores. Once the geocell confines the ballast and helps to increase shear strength, bending resistance, tensile strength and bearing capacity by allowing greater load distribution and improved frictional characteristics. Greater lateral confinement will produce superior track stiffness that will improve the ride characteristics for passengers. Routine maintenance costs are also expected to decrease due to a vast reduction in sleeper movement and track misalignment. Greater confining pressure on track bends will also allow faster train speeds owing to a decreased risk of lateral (outwards) sleeper travel. A testing methodology on how to check the efficiency of the reinforcement has also been discussed. The numerical modelling and laboratory testing were performed, and the analysis and results are presented in Chapter 4, 5 and 6.

CHAPTER 4: FINITE ELEMENT MODELLING OF RAIL PROFILES

4.1 INTRODUCTION

It should be noted that the reinforcement method described in Chapter 3 is only about increasing the strength of existing foundations and nothing about rails has been discussed. The aim of this chapter is to identify the parameters that cause an increase in dynamic loads in relation to track quality and speed and attempt to decrease the dynamic impacts by optimising track components such as pads. In Chapter 2, it was noticed that pads could contribute to about 20% in settlement reduction. Optimisation of other track components such as sleeper shapes and clips are beyond the scope of this research. As a result, a new method for calculating the stress that the rail-sleeper will exert on the ballast is needed since this is where the highest deterioration of ballast occurs. CONTACT (Vollebregt 2014) software was used to model the interaction between the wheel and the rail, and the results were fed into Ansys transient structural module to calculate the stresses that are exerted by the sleepers on the ballast due to these stresses. Several types of corrugation and their effects have also been tested. The parameters that govern ballast deterioration have been identified, and the methods of analysis have been compared with other analytical or numerical methods since in-situ validation can be troublesome.

4.2 BACKGROUND

If a high-speed train runs on a conventional line that is several decades old, track non-linearity is expected to be present. For high-speed lines, the tolerance in terms of acceptable vertical deflection is usually very low: about

1-2mm (Chandra & Agarwal 2007). When designing railway lines, static wheel loads are factored by a dynamic impact factor (DAF), but sinusoidal effects or irregularities of the rail is not considered in most of DAF calculation. The complete list of formulae that are currently used by railway engineers is attached in Appendix A.2, and it can be seen that there is no direct relationship in between track quality and rail speed. L.Baeza et al. (2011) used the Timoshenko beam theory and considered an infinite cyclic train–track system running. They highlighted that the effect of velocity has a significant effect on the system. Therefore, it is essential to assess if high-speed trains can run on bad quality tracks since the damage has already been done.

After an extensive literature review on railway ballast, railway mechanics, and ballast modelling, it was noticed that current numerical simulation or laboratory tests do not account for high-frequency sinusoidal effect of the dynamic loads caused by corrugation or unevenness of the rails. Modelling of such problem can be complicated because of the complexity of modelling vibration since the characteristic of generated vibrations varies widely due to the differences between train/track features (Connolly et al. 2015). In current numerical analyses, loads are applied at a frequency of approximately 10-15 Hz,assuming a train speed of 100km/h and a wheel spacing of 2.6m. However, such small values of frequency would not generate violent vibrations and dynamic excitation, and further investigation was carried out in this chapter in order to understand the real behaviour at the wheel-rail interface. As trains are moving faster and faster, higher impact loads are generated owing to the irregularities on the rail and non-linear stiffness of the substructure. A

numerical analysis conducted by T.X. Wu (2000) on the non-linear dynamic interaction between a wheel and a rail, revealed that roughness was an important factor since it caused dynamic excitation. According to the experience gathered, classic ballasted tracks on high-speed lines of Deutsche Bahn show irregular settlements and defects of track position as well as destroyed ballast in certain places, particularly in places with irregularity, such as rail defects, welded joints, insulated rail joints, bridges crossing etc. (Lichtberger 2011). Furthermore, the coupled dynamic response of the train and track is in high demand by the industry since wheel-flats or track irregularities are of great practical interest.

4.3 MODEL

In order to analyse dynamical problems, several models have been developed by several researchers and each model is distinct since the track is treated differently in each case (Baeza & Ouyang 2011). Accurate simulations of a railway track require detailed models of each rail component. Most models include the rail profile, rail pads, sleepers and ballast. Wheel and rail are coupled together at a contact point where dynamic excitation is introduced owing to track irregularities. Several models have been combined in order to create a new method of analysing the problem in this research. The methodology by which the problem is solved has been broken down into **3** steps. In step 1, the static load that is generated due to the wheel load is applied on the different types of rail profiles, and the resultant stress is recorded. In step 2, the different contact stresses are added together to form rail profile, and finally, in step 3, all the loads are fed into Ansys transient

structural module, and the output is recorded. The steps have been explained in detail as below.

4.3.1 STEP 1: STATIC 3D CONTACT MODEL

Railway vibration arises from the stresses generated at the contact point at the rail-wheel interface (Connolly et al. 2015). Static CONTACT model provides an accurate stress at the initial point of contact for 1 time step. In other words, the contact point is considered to be subjected to a static load for a very small time.

Note: One time-step will be considered as the time taken for the train to run across its contact area which is the horizontal deformation of the rail and wheel. Figure 4.1 shows the total contact distance, DX1, DX2 and DX3, for one time-step.

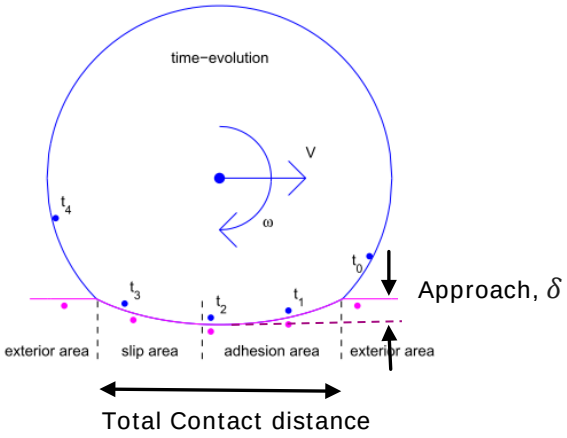


Figure 4.1: Contact distance for One time step (Vollebregt 2014)

The theory of contact focuses on non-adhesive contact where touching bodies can be separated without adhesion forces (Sextro 2007). In rolling contact, a contact force is generated on the rolling object and the supporting structure.

The normally loaded contact can be modelled using Hertz contact theory. However, its main drawback is the restriction to perfectly smooth surfaces. When this assumption is violated, the problem can be said to be non-Hertzian. In the normal direction, one body is pressed onto the other. It tries to push through the other, and this is resisted strongly by the cohesive forces inside the other body. The force by which the bodies are pressed together causes elastic deformation (approach, δ). Consequently, it is said that normal contact behaves like a spring. The stiffness of this spring is variable, dependent not only on the material and geometry but also on the load that is imposed on the contact region. There may be material damping as well, which would give a small dashpot parallel to the spring. Figure 4.2 shows the contact stiffness in the normal and tangential direction. Tangential contact is different in the sense that it allows for large displacements to occur between the two surfaces, with friction being the main physical phenomenon. If a small tangential force is applied to a body, it may bend a little such that some tangential displacement seems to occur. If the applied force is larger, then there may also be some microslip between the surfaces in the contact interface.

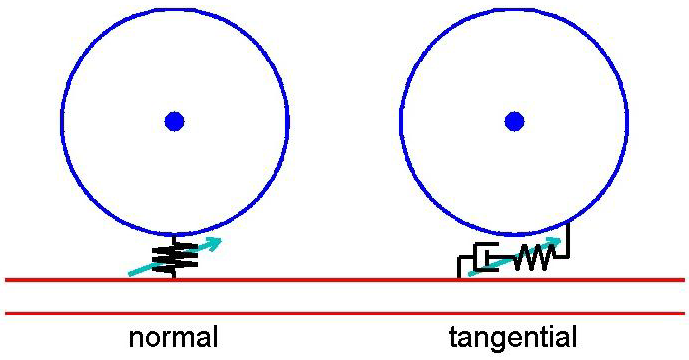


Figure 4.2: Schematizing the contact forces (Vollebregt 2014)

Many researchers argue that models with constant stiffness are unreliable since the possibility of dynamic modulus is not considered (Bowness et al. 2007). Pads, clips, and sleepers have all deterioration processes of their own and are dependent of which forces and bending moments act on them since each component has its own stiffness, and distribution of the stress is non-linear. Therefore, the use of contact mechanics will need to consider individual stiffness at each contact point. CONTACT is a simulation package used for the study of 3D contact (Vollebregt 2014) and to calculate the sub-stresses at the contact point. The CONTACT code that was written and used for this study is attached in Appendix A.3.

According to Vollebregt (2014), each contact area is approximately 12mmx12mm for a rail-wheel contact. This contact area is further discretised into 25 x 25 rectangular elements with a curvature of 3500mm-^{1}. Wheel radius is 460mm. Vertical load and velocity are to be varied in the parametric study. Figure 4.3 shows one discretised contact region that has been developed and used for this research. During the simulation, the wheel is pressed onto the plane of the rail and shifted tangentially. The problem is entered in two phases. The first phase is a frictionless normal problem with a Hertzian geometry. The second and subsequent phases concern the tangential shift problem and are non-Hertzian. Within the contact region, the undeformed distance is shifted to the right over a distance of δq in each iterative step. With $\delta q \approx \delta x \approx \delta y \approx 0.50$ mm, each contact region is shifted by 12mm at the end of the simulation.

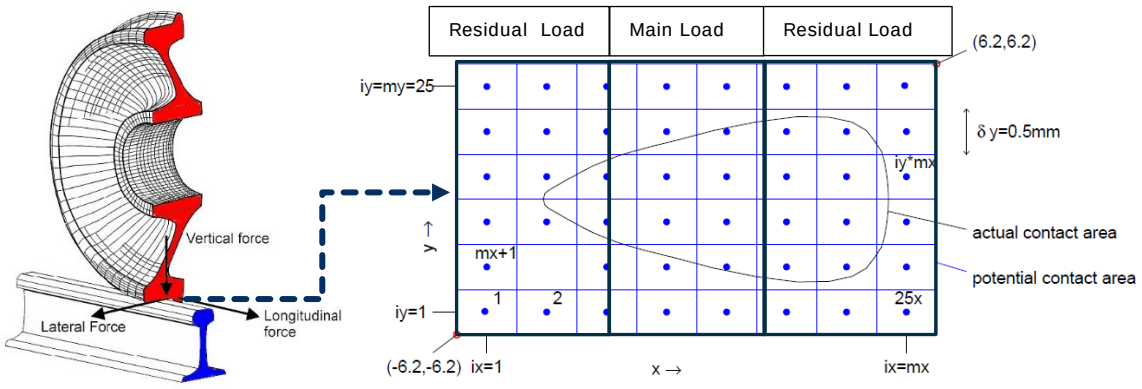


Figure 4.3: One discretised contact region (Vollebregt 2014)

Rough contacts can be very difficult to model since there are irregularities on the roughness as well (spikes on spikes). When a wheel runs on the rails, the unevenness forms an excitation with multiple frequency components which can be regarded as a broad band random process(Koroma et al. 2013). A practical roughness input is therefore needed to simulate the wheel/rail interaction. The roughness profile at the contact regions can be modelled in CONTACT from the surface equations(adopted from Vollebregt (2014)) below which is the addition of a quadratic to the difference of two sine curves in the x-direction.

$$z(x;\, y) = b_1 \sin\big(b_2(x - b_3)\big) - b_4 \sin(b_5(x - b_6)) + x_2/b_7 + y_2/b_8 \qquad \text{Eqn(4)}$$

Where:

b7 and b8 are radii of curvature (mm^{-1}),

b1 and b4 are vertical distances (mm),

b3 and b6 are horizontal positions where the sines are zero (mm),

b2 and b5 are frequencies (rad/mm).

4.3.2 STEP 2: CREATING RAIL PROFILE

After the stresses are computed for a range of different types of contact, the track profile is made using a combination of the contact areas, and the track is moved relative to a stationary train to model a moving train while the wheels are kept stationary. The technique was also adopted by Otero et al.(2012) and proved to give reliable results since the parameters such as stiffness are discrete(Dynamic stiffness). This assumption brings convenience for the calculation and is reasonable since the speed of the train is much lower than the wave speed in the rail (Thompson et al. 2003).

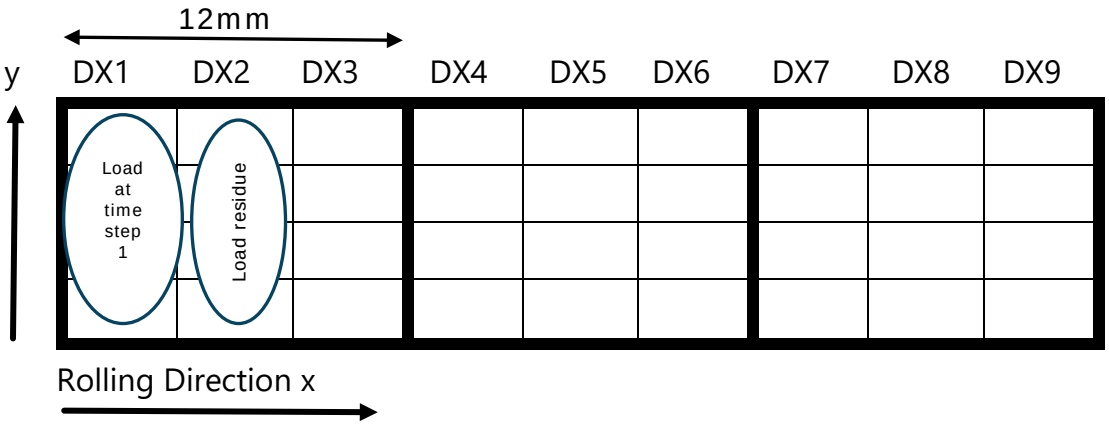


Figure 4.4: Plan view of contact areas added together to form profile at t=1

In Figure 4.4, at time step, t=1, the stress that was calculated using CONTACT is applied on DX1 and another stress (residual stress) is applied on DX2.

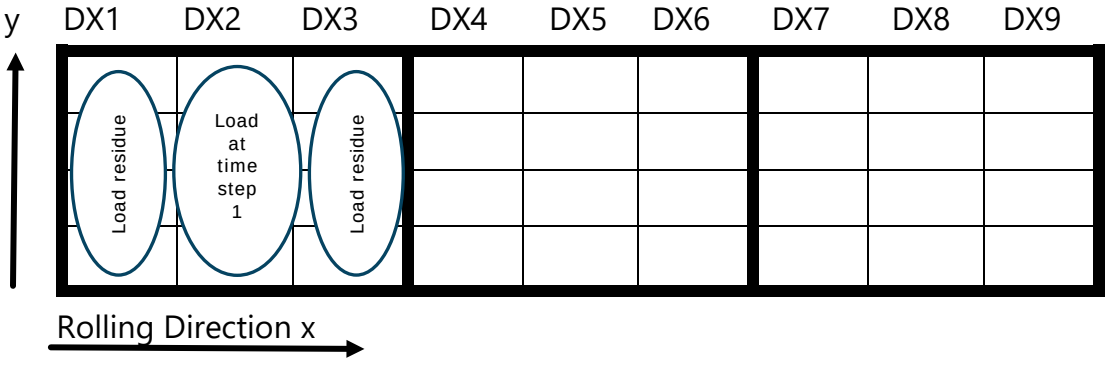


Figure 4.5: Plan view of contact areas added together to form profile at t=2

In Figure 4.5, the main load is applied on DX2 and residuals on DX1 and DX3.

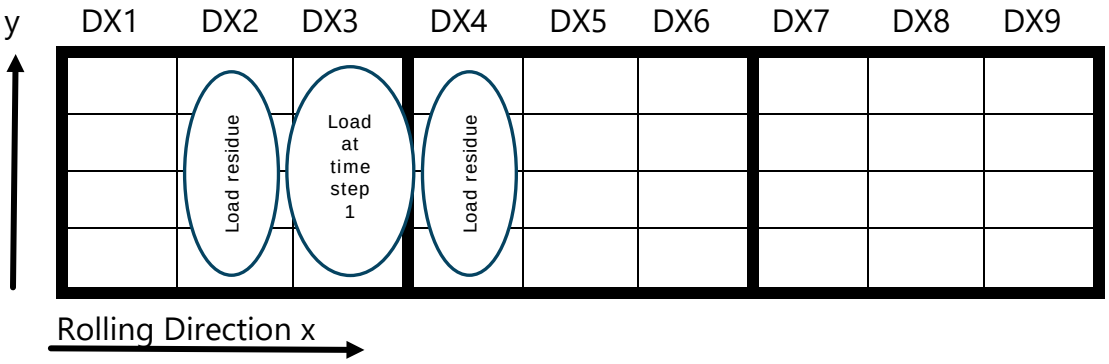


Figure 4.6: Plan view of contact areas added together to form profile at t=3

In Figure 4.6, the main load is applied on DX3 and residuals on DX2 and DX4. DX4-DX6 indicates another contact region. A different type of contact surface can be used here. Using this method, a range of different types of rail profiles can be created. E.g Smooth-Rough-Smooth, Smooth-Rough-Rough. In section, 4.5.1, different types of contact surfaces are tested.

The loads and residue of the loads are superposed so that the resultant force that acts on the sleeper can be obtained. It is essential that the calculation is conducted in time-domain since the principle of superposition does not hold in the frequency domain. Time-stepping techniques rely on uses time-mesh independent events (Saussine et al. 2006). The loads are then applied with respect to the velocity of the train since the value of the time step is dependent on the value of the velocity. Sleeper rotation, movement and deformation are not considered at this stage.

For a 10kN train moving at V m/s, over a distance of 20 mm, with DQ 0.5mm, the following contact stress need to be applied as shown in Table 4.1. For simplicity, all the Y values have been combined into 1 row. Furthermore, due

to the limitation of Ansys in creating such small meshes, each contact area has been divided into 3 sections instead of 25. The full set of data that was obtained from CONTACT yield results in the form of an array of size 25x25. The value was averaged and fed into Ansys in a 3x1 array, and the input can be found in Appendix A.6.

Table 4.1: Load applied at contact regions DXn over 7 time-steps

Timestep, t	DX1	DX2	DX3	DX4	DX5
0	0	0	0	0	0
1	Load DX1	0	0	0	0
2	Load DX2 Residue 2	Load DX2	0	0	0
3	0	Load DX1 Residue 1	Load DX3	0	0
4	0	Load DX3 Residue 2	Load DX2 Residue 1	Load DX4	0
5	0	0	Load DX3 Residue 2	Load DX3 Residue 1	Load DX5
6	0	0	0	Load DX5 Residue 2	Load DX4 Residue 1
7	0	0	0	0	Load DX6 Residue 2

Figure 4.7 shows the variation of the load with respect with the time that was drawn by combining the result from CONTACT. This confirms that, even though the rail and wheel are smooth, the small deformation that occurs due to tangential and normal forces are enough to produce dynamic forces. The residue of the previous load at a specific time is superposed on the force applied at that time. Furthermore, even in such a small area, the stress varies considerably. One full result for 1 contact area is given in Appendix A.4. ANSYS also calculates the lateral and torsional forces on the rail, but these are beyond the scope of this research.

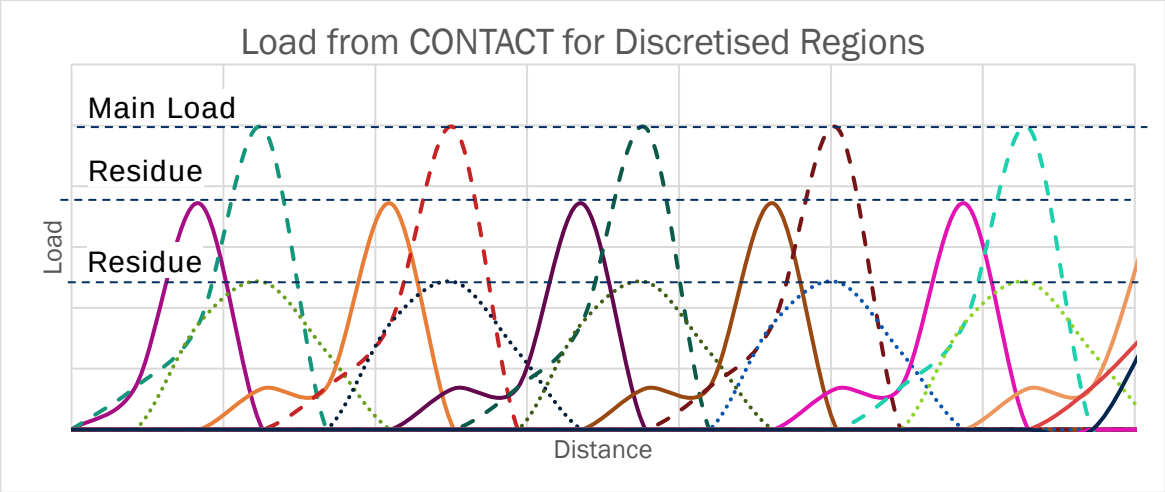


Figure 4.7: Load time Graph for Input

The resultant of superimposing the different loads and their residue can be seen in Figure 4.8.

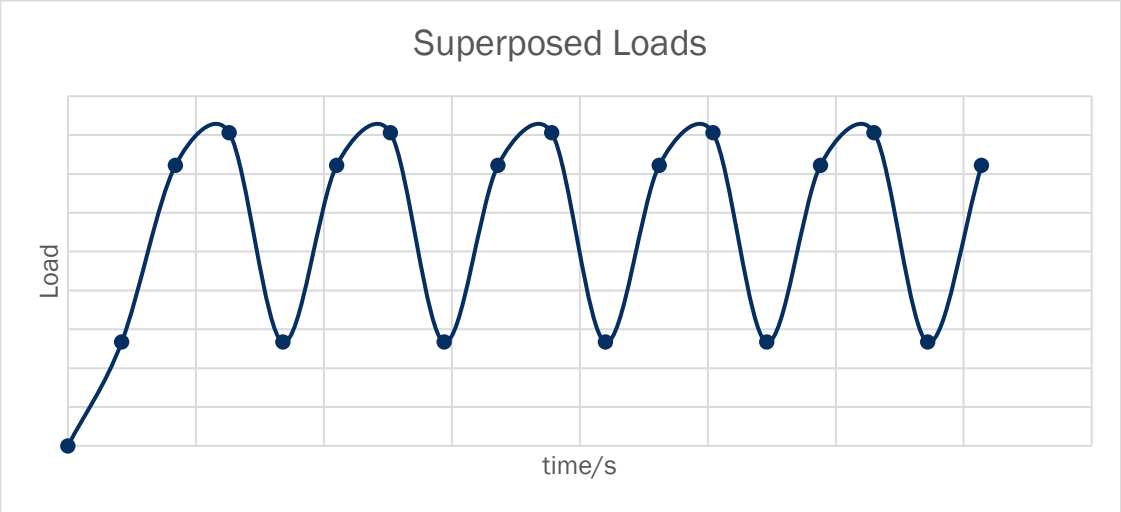


Figure 4.8: Resultant force from superposed graph in time-domain

It can be seen that using this simple method of discretisation of contact area into sections and then moving the load, a static load can be converted into a dynamic one. The frequency of the load will depend on the contact area and the velocity.

4.3.3 STEP 3: CALCULATING REACTION FORCES

Stresses are computed at the bottom of the sleeper, after being fed into the transient finite element analysis. The wheel exerts a transient load while the rail is modelled as a beam where the supports correspond to sleepers. In between the rail and each sleeper, a stiffness and a damper are used to model the rail pad. The method has proven to be more accurate than a multi-layered linear elastic analysis (lots of springs over springs)(Kargarnovin et al. 2005). Figure 4.9 shows how the problem is modelled in Ansys, Transient Structural 2016 module.

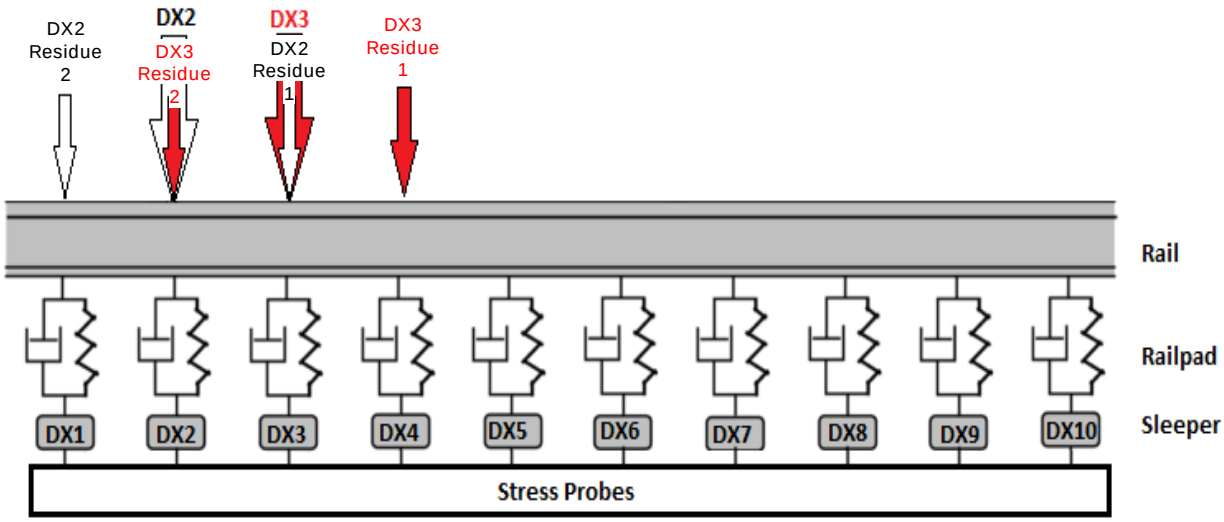


Figure 4.9: Transient loading

The transient model offers the same possibilities as a cyclic model (Baeza & Ouyang 2011). It should be noted this procedure is different from the modelling procedure used in elastic foundation of distributed springs called Winkler theory. In Winkler theory, the beam is supported by a range of springs where each spring is point reacting. Hence discarding any shear forces between

individual springs. In transient structural modules, shear forces are taken into account, thus making the simulation more accurate.

The reaction force is then calculated automatically using Ansys. The ballasted track considered in this work is a high performance track in which, concrete sleepers which are 0.6 m apart and rails are UIC60 rail having a moment of inertia of 30.55 $x10^{-6}$ m^4 (Oyarzabal et al. 2011). The vertical pad has an elastic modulus of 1100MPa for most of the cases except where the stiffness is varied (Oyarzabal et al. 2011). The wheel is 460mm in diameter and is made up of structural steel. Materials have not been modified and are available in the ANSYS 16.0 default library. Details about the parameters that were used during the simulation can be found in Table 4.2 and Table 4.3. The geometry that was used for both the explicit dynamics and transient static simulation is shown in Figure 4.11. Table 4.5 shows all the cases scenarios that were simulated.

Table 4.2: Properties of materials used in CONTACT and ANSYS

Component	**Material**	**Young modulus / MPa**	**Poisson's ratio**	**Density / kg / m^3**
Rail	Steel	210 x 10^3	0.35	7850
Sleepers	Concrete	30 x 10^3	0.25	2400
Pads	Rubber	Varies	Varies	1100

Once all the loads have been obtained from CONTACT analysis, the rail is drawn in Autodesk Inventor 2016 and is discretised into squares of dimension 0.5 mm. The finite element software, ANSYS Workbench (Module: Transient Static

Structural), is used to calculate the stress at the bottom of the rail section. Stress Probes have been attached to both sleepers. The wheel moves from sleeper 1 to sleeper 2. Figure 4.12 shows the geometry that has been imported in Ansys 16.0 transient structural module.

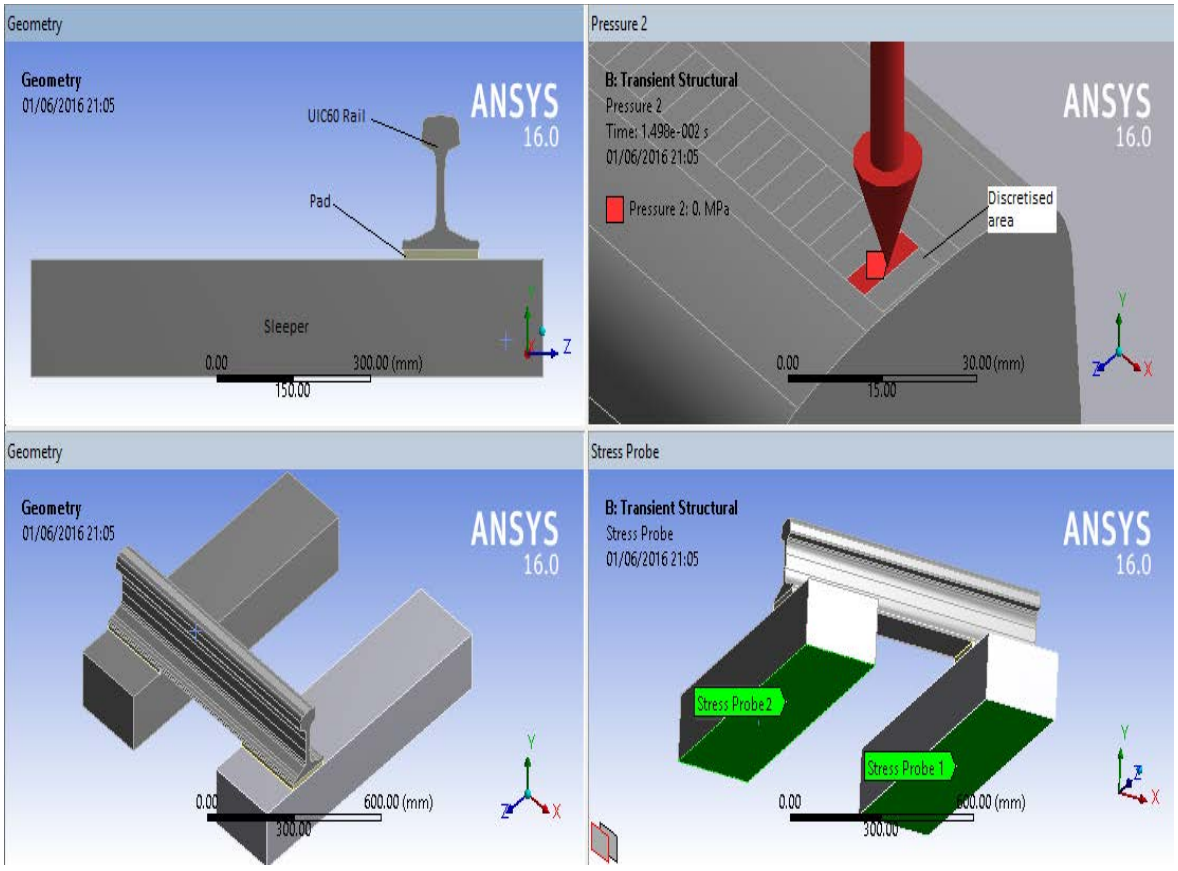


Figure 4.10: Ansys 16.0 transient structural module

The parameters that have been defined to simulate the problems can be found in Table 4.3.

Table 4.3: Parameters used by the programs when solving

CONTACT		ANSYS	
Parameter	**Magnitude**	**Parameter**	**Magnitude**
Modulus of rigidity	82000 N/mm^2	**Number of substep**	214
Poisson's ratio	0.35	**Number of nodes**	223969
Static friction	0.3	**N0. of Elements**	43258
Dynamic friction	0.3	**Contacts**	Bonded
Curvatures	$3500mm^{-1}$	**Solver type**	Newton-Raphson
Creepage	0.000923 rad/mm	**Material for rail**	Structural Steel
Number of elements	25x25	**Material for Pads**	Polyethylene
Coordinates system	1unit=1mm	**Sleeper Material**	Concrete
DQ=DX=DY	0.5		

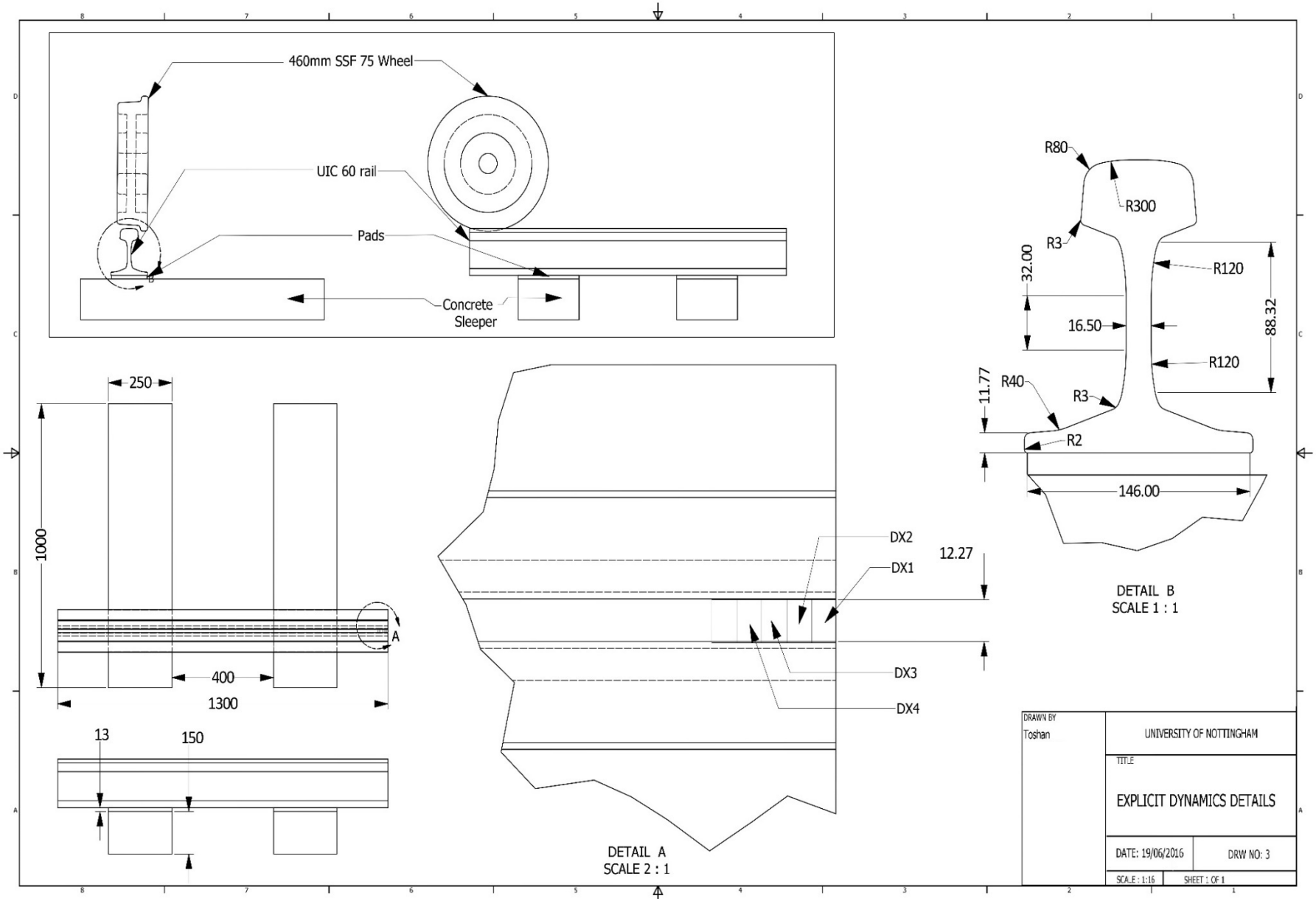


Figure 4.11: Detailed Geometry used for simulation

4.4 PARAMETRIC STUDY

In order to study the parameters that influence the magnitude of the dynamic loads, several cases have been investigated. A designation system has been used that describes s the simulations in different categories. The name of the cases can be read as C for case number, “XX”KN for the wheel Load, “XX”ms for the velocity of the train “XX”MPa for the young modulus of the pad. For Example, in C5 50KN 20 ms 550MPa, Train has wheel load of 50kN and speed is 20m/s while the young modulus of the pads is 550MPa. Table 4.4 shows the parameters that will be compared in each case batch. Table 4.5 contains all the details of the simulation that have been carried out using Ansys workbench 2016.

The main parameters that have been tested are: rail roughness, Dynamic Amplification factors, speed, wheel load, pad stiffness and creepage. It is very difficult to conduct large scale testing on these parameters. Therefore, the Finite element model provides the flexibility of changing parameters that will be very troublesome practically.

Table 4.4: Cases category description

<table>
<tr><th>Case Number</th><th>Parameters compared</th><th>Case Number</th><th>Parameters compared</th></tr>
<tr><td>1</td><td rowspan="3">Wheel load and Velocity</td><td>5</td><td>Pad Stiffness</td></tr>
<tr><td>2</td><td>6</td><td rowspan="2">DAF</td></tr>
<tr><td>3</td><td>7</td></tr>
<tr><td>4</td><td>Rail Profile</td><td>8</td><td>Slippage/creepage</td></tr>
</table>

Table 4.5: Ansys Case Scenarios

Case Name	Contact profile	Wheel Load / N	Velocity ms^{-1}	Pad Young Modulus / MPa	Type of Analysis
C1 50KN 20ms	Smooth	50000	20	1100	Transient Structural
C1 50KN 40ms		50000	40		
C1 50KN 60ms		50000	60		
C1 50KN 80ms		50000	80		
C1 50KN 100ms		50000	100		
C2 150KN 20ms		150000	20		
C2 150KN 40ms		150000	40		
C2 150KN 60ms		150000	60		
C2 150KN 80ms		150000	80		
C2 150KN 100ms		150000	100		
C3 300KN 20ms		300000	20		
C3 300KN 40ms		300000	40		
C3 300KN 60ms		300000	60		
C3 300KN 80ms		300000	80		
C3 300KN 100ms		300000	100		
C4 50KN 20ms	Corrugated	50000	20		
C4 300KN 20ms		300000	20		
C5 50 KN 20ms 110MPa	Smooth	50000	20	110	
C5 50 KN 20ms 500MPa		50000	20	500	
C5 50 KN 80ms 110MPa		50000	80	110	

C5 300 KN 20ms 110MPa		300000	20	110	
C6 100KN		100000	-	1100	
C6 200KN		200000	-	1100	
C6 250KN		250000	-	1100	
C7 50KN 20ms EXP		50000	80	1100	
C7 50KN 80ms EXP		50000	80	1100	
C7 150KN 20ms EXP		150000	20	1100	
C7 150KN 80ms EXP		150000	80	1100	Explicit
C7 300KN 20ms EXP		300000	20	1100	Dynamics
C7 300KN 80ms EXP		300000	80	1100	
C8 50KN 20ms Creep		50000	20	1100	
C8 50KN 80ms Creep		50000	80	1100	

4.5 VALIDATION

4.5.1 CONTACT MODEL

4.5.1.1 Analytical method 1: Frequency-Domain Analysis

In order to validate the results obtained from CONTACT analysis and confirm that there were no errors when using the CONTACT program, analytical methods has been used and the results were compared with CONTACT which uses numerical method for this simulation. For a linear system which is not dependent on time, the problem can be expressed in the frequency-domain. Grassie et al. (1982) proposed the formula below (Eqn5) to find the dynamic force developed at the point of contact when a wheel rolls over a rail having a sinusoidal profile on its running surface that is a corrugated rail. In a simple

case of vertical interaction between the rail and the wheels, the force at the contact region, F which is a function of the frequency, ω, is given by:

$$F(\omega) = -\frac{R(\omega)}{\alpha^W(\omega) + \alpha^C(\omega) + \alpha^R(\omega)} \quad \text{Eqn(5)}$$

Where:
R is the relative displacement between the rail and the wheel,
a^W is the displacement per unit force of the wheel,
a^R is the displacement per unit force of the rail,
a^C is the displacement per unit force of the wheel approximated using Hertz Law.
The formula, which is exact for cylindrical shapes, was further simplified by Thompson (1993) into:

$$F = C_H(x_w - x_r - r)^{3/2} \quad \text{Eqn(6)}$$

Where:
F is the force at the contact region in N,
x_w is the wheel displacement in m,
x_r is the rail displacement in m,
r is the roughness in m,
C_H is the Hertzian constant. (9.37×10^{10} N/m$^{2/3}$)

To verify the reliability of the CONTACT model, Eqn(6) has been used and the output compared. For wheel and rail displacement, the approach, δ, value has been used, and r is the wavelength of the roughness. Where in this case, wavelength is the distance between 2 successive peaks.Analytical method 2: Space-Domain Analysis

Furthermore, Steenbergen & Esveld (2006) pointed out the relationship between the gradient of the rail geometry and the speed of the train. The experiments showed good correlation with their calculation than a method that

relied on vertical tolerances. Eqn(7) shows the approximate formula that is used to calculate the maximum dynamic force, $F_{dyn,max,}$ for at the contact region between the rail and the wheel. This expression for the dynamic contact force can be transformed into the space domain since the dynamic contact force is a function of the first time derivative.

$$F_{dyn,max} = \beta M V^2 \left|\frac{dz}{dx}\right|_{max} \qquad \text{Eqn(7)}$$

Where:

β accounts for dynamic influences which were not modelled, inaccuracies introduced by assumptions on the response and non-linearities; its value can be chosen as a discontinuous function of the line-section speed and should be determined from the validation measurements. A value of 1 will be used for this research,

M is the equivalent track mass in kg,

V is the velocity of the train,

$\frac{dz}{dx}$ is the inclination gradient

4.5.1.2 Comparison of different methods of analysis

Table 4.6: Stresses for different rail profile

Rail profile	Gradient at X=0	Approach/m	Wavelength/m	Stress using analytical method 1 /MPa	Stress using analytical method 2 /MPa	CONTACT Stress /MPa
1	0.794	0.007	0.0062	3176	2116	1710
2	2.381	0.007	0.0062	9524	2116	1890
3	1.043	0.007	0.0031	4172	16938	1730
4	0.0	0.007	0.024	616	-	70
5	0.154	0.007	0.024	616	-	1191

Depending on the profile of the corrugation and the method used for calculation, the stress changes. It will be conservative to carry future calculation of stress using different approaches. Small wavelength corrugation, should be calculated in the frequency-domain, whereas, large vertical tolerances should be calculated in the space-domain. Time-Domain yield values approximately in between those calculated by the other methods. Concerning the validity of the model, it can be seen that the CONTACT yields values which are about 40% lower than the analytical methods. However, the differences between the analytical methods are themselves very large. The reason for which these formulae were devised vary in application, this may explain the difference in the results. Therefore, even though the difference in between the methods is large, it is difficult to say which one is closer to the real value. Analytical method 1 applies for exact cylindrical shapes while analytical methods 2 accounts for inertial effects. Calculations using CONTACT accounts for material

deformation, rolling, friction and creepage. The model is also a non-Hertzian model.

4.5.2 ANSYS MODEL

4.5.2.1 Explicit dynamics test

In-situ validation of the ANSYS model is very difficult. Since inertial effects and damping are ignored in static analyses, an explicit dynamic test is essential in order to validate the model developed. The Boussinesq contact theory, in which the pressure distribution in the contact area is predicted for a discrete number of rectangular elements, is assumed. The contact theory accounts for shear forces in the contact zone and enables detailed surface texture to be included.

In dynamic analysis, nodal forces associated with mass/inertia and damping are included. In nonlinear implicit analysis, the solution of each step requires a series of trial solutions (iterations) to establish equilibrium within a certain tolerance. In explicit analysis, no iteration is required as the nodal accelerations are solved directly. Explicit analysis handles nonlinearities with relative ease as compared to implicit analysis. This would include treatment of contact and material nonlinearities. However, the computational effort needed is significantly more than for a transient structural analysis.

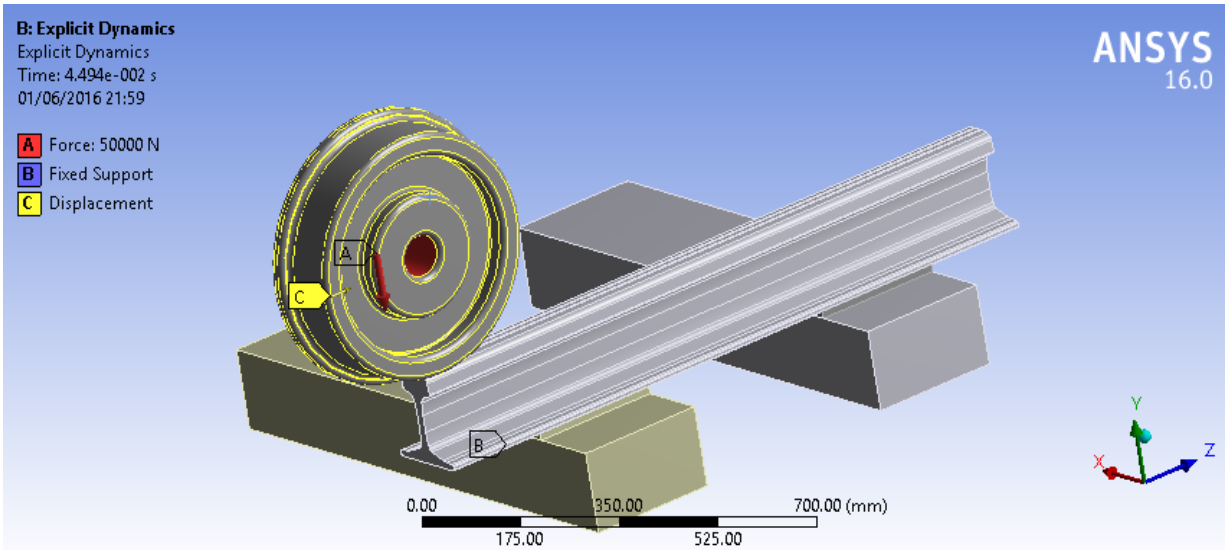


Figure 4.12: Ansys 16.0 Explicit Dynamics

The results were compared in section 4.5. The same parameters that were used in transient structural model were used in this case.

4.5.2.2 1D Simply supported beam

Please note that the stiffness of the pads and elasticity of the materials are ignored in this simple calculation. The two extreme cases that can be obtained when modelling can be shown in case 1 and case 2.

Case 1

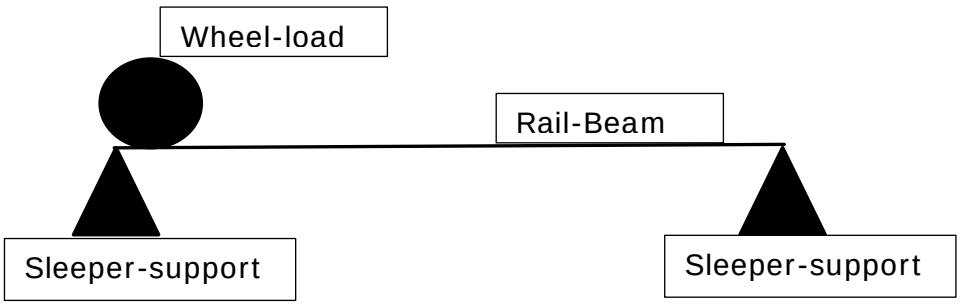


Figure 4.13: Simple supported beam case 1

Case 2

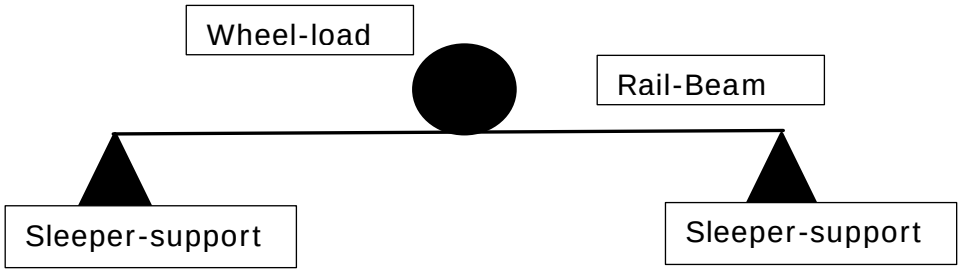


Figure 4.14: Simply supported beam case 2

The area of the sleeper is 1000mmx250mm. Therefore, the stress range that needs to be recorded is shown in Table 4.7.

Table 4.7: Analytical results vs FEM results

Wheel Load/kN	Stresses recorded by Ansys static/ kPa	Simple beam stress/ kPa
50	230-180	200-100
150	730-682	600-300
300	1618-950	1200-600

Results obtained by Ansys can be found in Table 4.12. It can be concluded that the results obtained using Ansys and by modelling the problem by a simply supported beam are close to each other, about 15%. This difference can be explained by the elastic deformation of the pads, rail and sleeper themselves which is not included in the simple beam analysis. From these results, it can be concluded that the Ansys model and the CONTACT model were correctly setup.

4.6 LIMITATION OF MODELS

It is assumed that contact between the wheels and the rail is linear and there is no loss of contact which results is dynamic impact. It is also assumed that the roughness only exists on the rails and not on the wheels. In the model that

was set up in Ansys, the sleepers were fixed, any damping effects that could be provided by the subgrade, in a real case scenario, would therefore not be present. Hence, providing larger reaction forces. The main reason for not including ballast bed is because a controlled environment is needed. The purpose is to get the loads that would then be used for DEM simulations. Furthermore, the material parameters and behaviour of the ballast, geocell and bitumen mixture would not be easy to define. However, such a mixture can be made by defining the materials independently in DEM.

It should also be noted that a section of a rail is modelled, while in other analytical methods such as the beam on elastic foundation, a infinite beam is considered. Therefore, additional deflection of the rails might be observed.

4.7 RESULTS AND DISCUSSION

4.7.1 EFFECT OF CORRUGATION

A rail corrugation is a form of wear that appears on the surface of a rail. Its development amplifies noise and vibration, and therefore reduction of corrugation should decrease dynamic loads and track maintenance. It is important to understand how loads are affected by irregularities since the high stress concentrations can lead to crack initiation and propagation. Since the principal cause of vibration is the fluctuation of the forces in the wheel-rail contact, derived from wheel profile irregularities (Otero et al. 2012), it is important to study the type of profile that causes the most deterioration. The change of profile shape deeply affects the dynamic characteristics of railway vehicles such as stability and comfort of the passengers (Braghin et al. 2006).

Contact forces change magnitude and direction as the wheel travels through irregularities and surface perturbations.

Contact profiles can be drawn using the surface equation (Eqn 4). In this research, only 2 types of rails have been considered, namely: smooth and corrugated. Figure 4.15 and Figure 4.16 show the 3D illustration and 2D illustration of a corrugated contact region respectively while Figure 4.19 and Figure 4.20 shows a smooth contact. It should be noted that each contact area is 4π x 4π mm^2 with crest and though of 1mm. The value of π(Pi) has been used so that it becomes easier to use sines and cosines to model the profile. Values used in the surface equation (Eqn 4) can be found in Table 4.8.

Table 4.8: B-Values for surface equation

B-Values	b1	b2	b3	b4	b5	b6	b7	b8
Smooth	1	1	0	0	0	0	3500	3500
Corrugated	0	0	0	0	0	0	3500	3500

4.7.1.1 Corrugated contact region

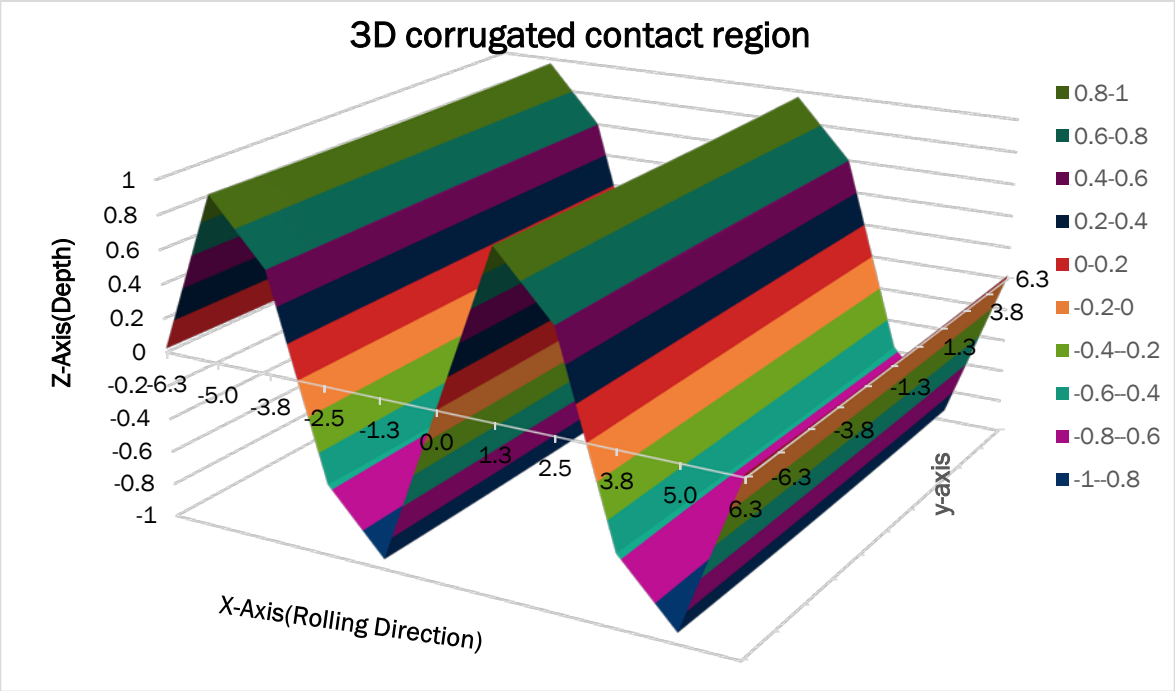


Figure 4.15: 3D corrugated contact Profile

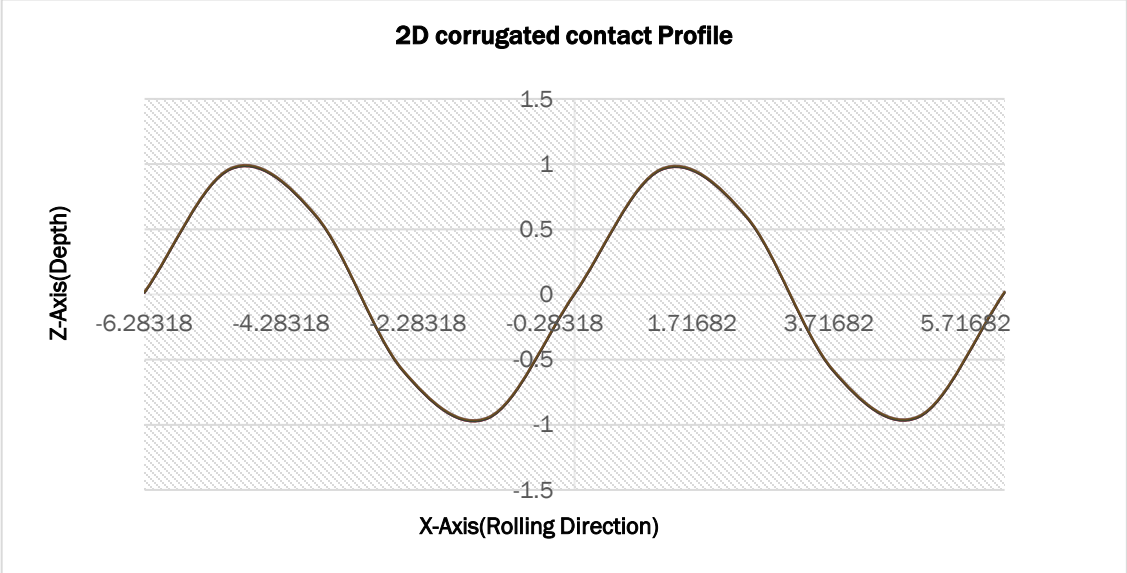


Figure 4.16: 2D corrugated contact Profile

When the simulation is run, the surface tractions are solved first and subsurface stresses are evaluated immediately thereafter. The results are

printed as shown in the 3D graph below and then converted into time step loads for transient structural analysis. The range of stresses at each contact point is plotted, for each time step. A sample of the result is shown in Table 4.9. The colours in the table indicated the intensity of the stress. Red means high while green means low. An output from CONTACT of the result for one contact region is provided in the Appendix A.4. The wheel load applied for the case below was 10kN. Figure 4.17 shows the stress at a contact area when the rail profile is corrugated.

Table 4.9: Results for discretised contact region of corrugated profile

x→	DX= 1			DX= 2			DX= 3					
y↓ | z↘	-6.3	-5.0	-3.8	-2.5	-1.3	0.0	1.3	2.5	3.8	5.0	6.3	Total stress/MPa
-6.3	6.4	10	19	31	36.08	29.06	19.87	14.24	17.21	20.93	16.78	221.915
-5.0	8.7	15	32	58	66.95	46.35	26.38	19.6	38.46	49.07	33.98	396.22
-3.8	11	21	45	85	95.99	60.96	29.94	27.18	64.9	81.4	53.61	578.93
-2.5	14	27	57	106	114.1	67.66	29.33	36.21	87.75	106.4	68.68	716.13
-1.3	17	33	67	118	120.4	65.94	26.19	47.03	106.3	122.6	77.24	802.8
0.0	19	37	74	124	117.9	58.45	24.37	58.5	119.8	129.9	79.28	844.42
1.3	20	38	76	121	107.1	47.67	26.18	67.03	125.2	128.1	75.59	833.29
2.5	19	36	69	107	88.61	36.3	29.4	69	119.4	116.8	67.24	758.86
3.8	16	30	55	83	66.16	27.48	30.58	62.95	101.8	96.57	55.24	625.94
5.0	12	21	37	52	41.39	21.14	27.9	49.48	73.7	68.58	40.52	446.11
6.3	8	13	20	24	20.68	16.28	21.97	32.71	42.24	38.89	25.77	265.314
Max Stress/Pa	20	38	76	124	120.4	67.66	30.58	69	125.2	129.9	79.28	

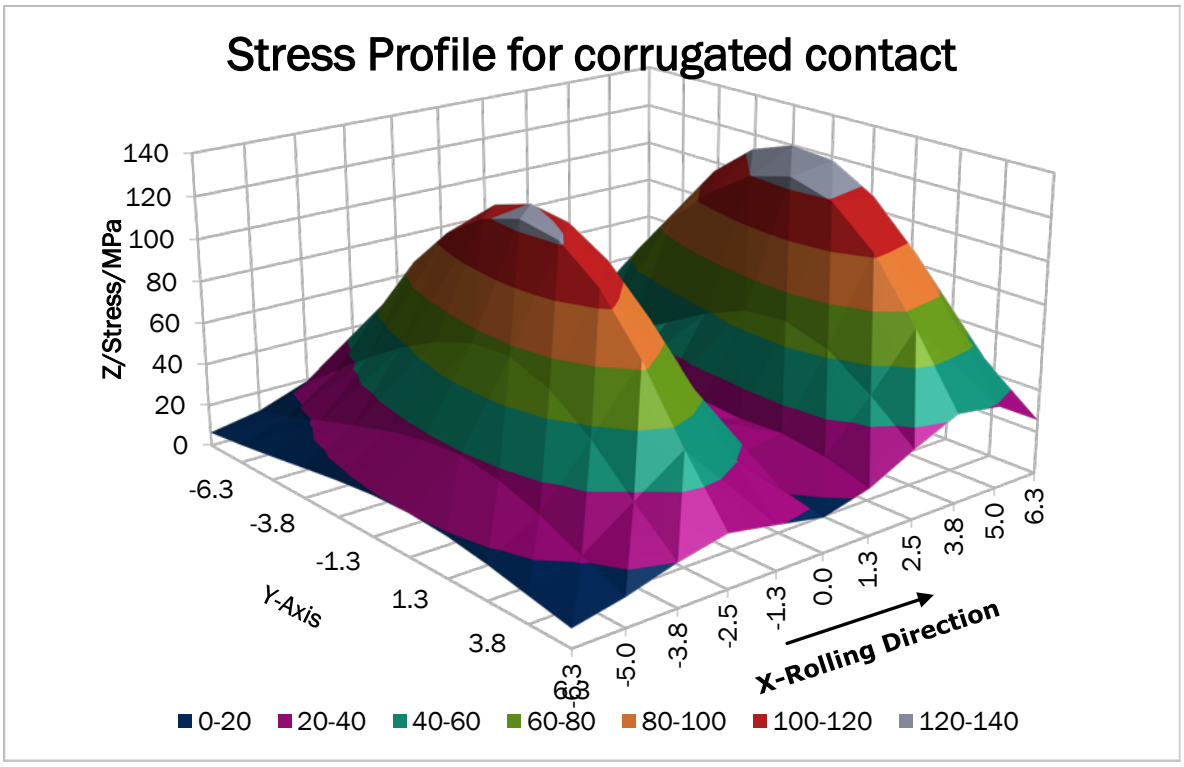


Figure 4.17: Stress profile of a corrugated rail at Contact Area

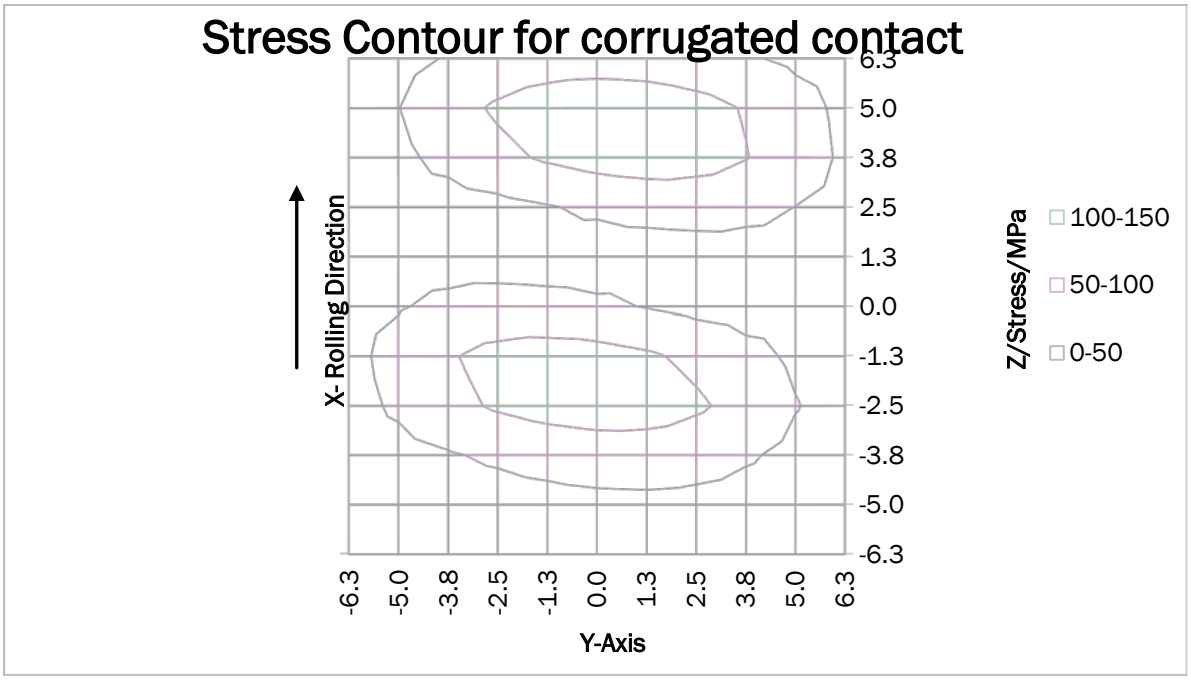


Figure 4.18: Stress Contour of a corrugated rail at Contact Area

4.7.1.2 Smooth rail

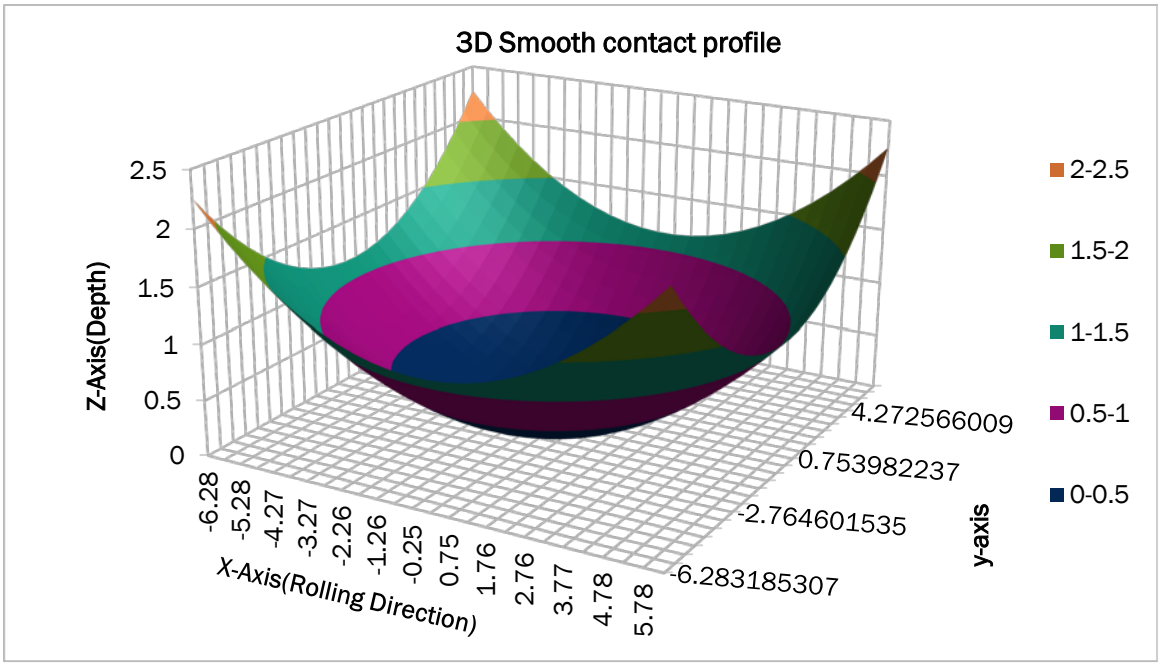


Figure 4.19: 3D Smooth contact profile

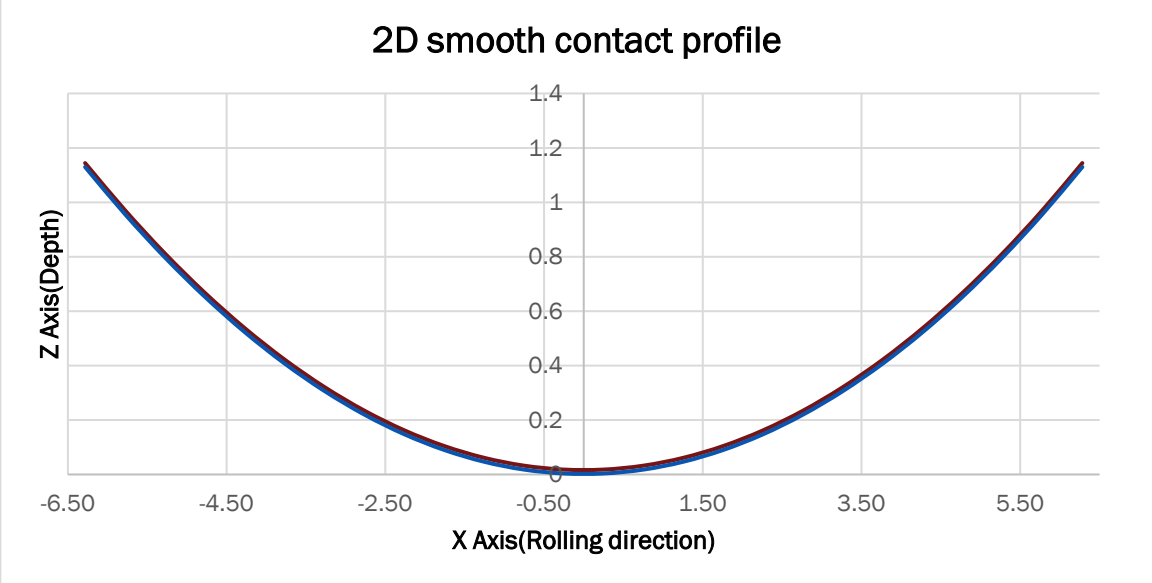


Figure 4.20: 2D Smooth contact profile

Table 4.10: Results for discretised contact region of corrugated profile

x→	DX= 1					DX= 2				DX= 3				
y↓ | z↘	-6.0	-5.0	-4.0	-3.0	-2.0	-1.0	0.0	1.0	2.0	3.0	4.0	5.0	6.0	Total Stress/N/mm²
-6.03	14.5	17.4	20.8	24.5	28.2	31.1	32.2	31.1	28.3	24.5	20.8	17.4	14.5	305.4
-5.03	17.4	21.7	27.4	34.6	42.8	53.1	55.8	52.7	43.5	34.6	27.4	21.7	17.4	449.9
-4.02	20.8	27.4	37.6	55.5	68.0	73.6	74.9	73.7	69.8	53.5	37.5	27.3	20.8	640.3
-3.02	24.5	34.6	53.6	72.5	79.9	83.8	84.9	84.0	80.2	72.7	54.6	34.6	24.5	784.4
-2.01	28.3	43.7	69.1	79.9	86.2	87.1	86.3	87.3	86.6	80.4	68.0	42.9	28.2	874.0
-1.01	31.1	52.6	73.4	83.7	87.0	52.5	43.6	51.2	87.5	84.5	74.4	52.5	31.1	805.0
0	32.2	55.8	74.9	84.9	86.3	43.6	36.3	42.7	87.2	85.7	76.0	54.8	32.0	792.2
1.01	31.1	53.2	74.1	84.2	87.2	51.5	42.7	50.3	88.1	85.0	75.3	51.9	31.0	805.6
2.01	28.2	42.7	69.6	80.8	86.9	87.8	87.1	87.7	87.3	81.5	72.8	43.8	28.3	884.6
3.02	24.5	34.6	56.2	74.2	81.2	84.8	85.7	84.8	81.3	74.4	53.6	34.6	24.5	794.3
4.02	20.8	27.3	37.5	54.2	72.7	75.1	76.0	74.8	69.5	54.8	37.5	27.3	20.8	648.3
5.03	17.4	21.7	27.4	34.5	43.9	51.8	54.7	52.5	43.2	34.5	27.3	21.7	17.4	448.0
6.03	14.5	17.4	20.8	24.5	28.3	31.0	32.0	31.1	28.3	24.5	20.8	17.4	14.5	305.0
Max Stress/N/mm²	28	56	75	85	87	88	87	88	88	86	76	55	32	

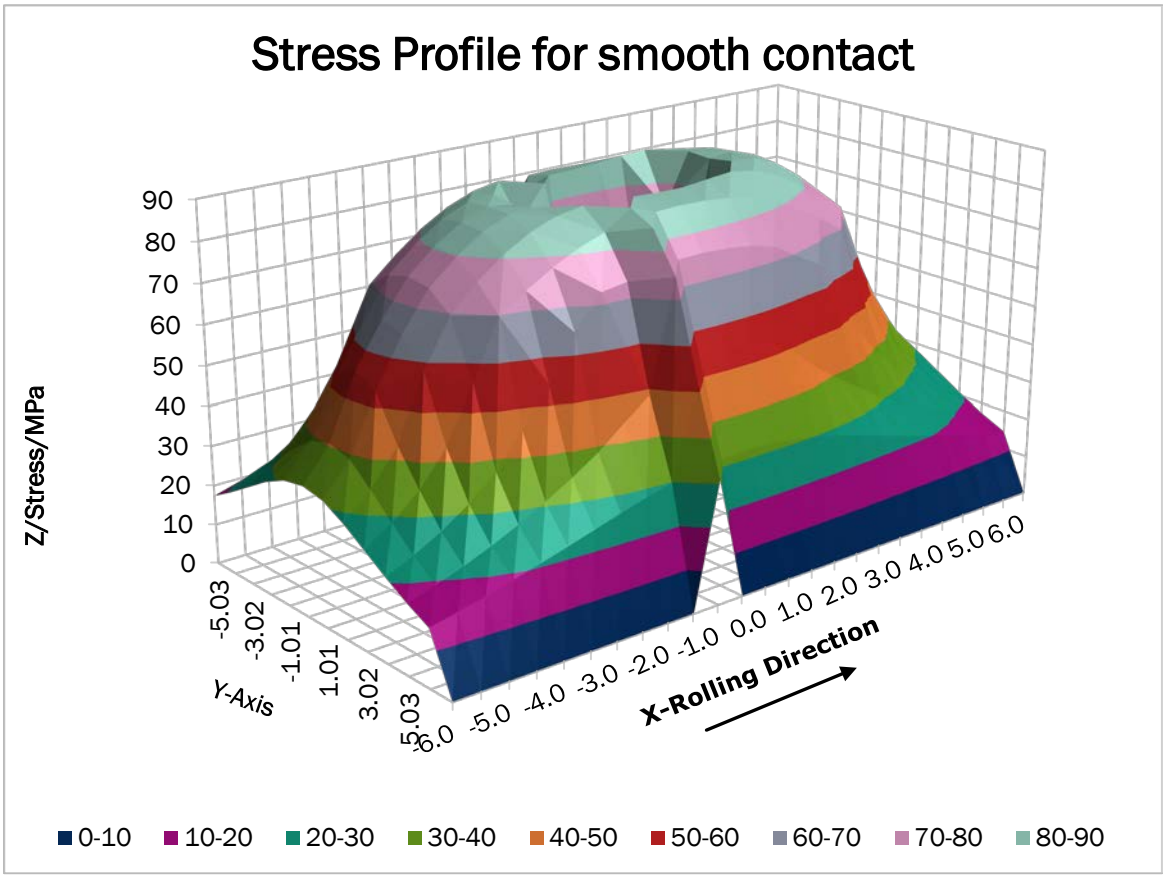


Figure 4.21: Stress profile of a smooth rail at Contact Area

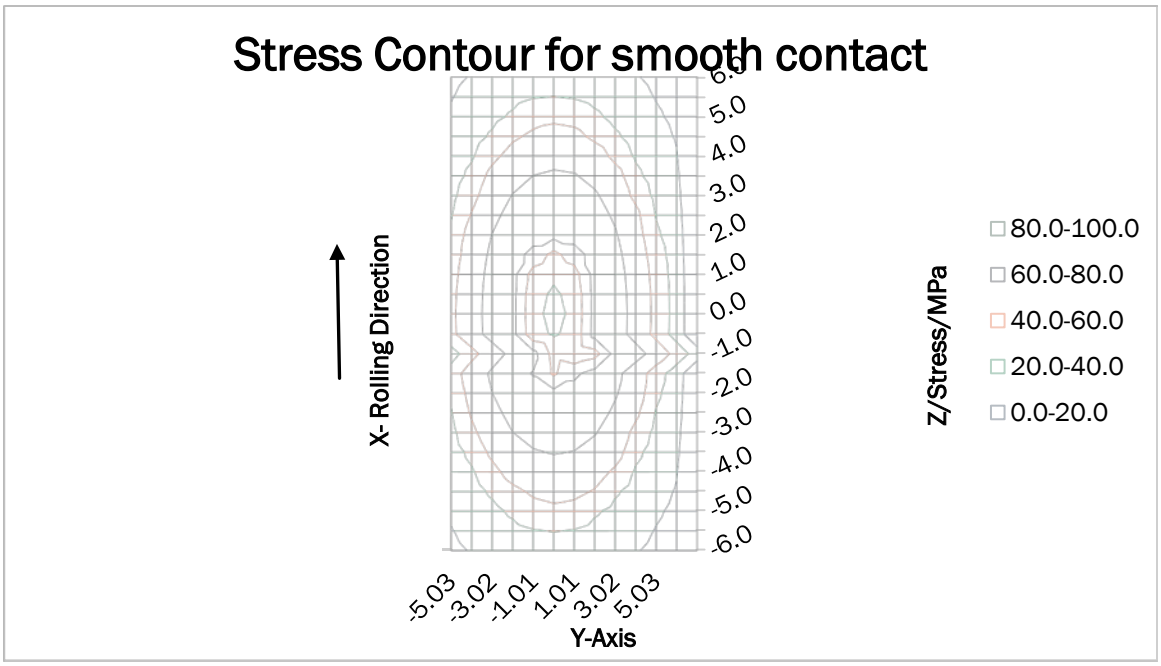


Figure 4.22: Stress contour of a smooth rail at Contact Area

From Figure 4.17 and Figure 4.21, it can be seen that the contact area profile is very influential on the stress distribution. The shapes that were obtained were very different and very much related to the shape of the spikes. For smooth rail, only 1 peak was observed in the stress plot, which was at the contact between the rail and the wheel. However, for the case of the corrugated rail (Figure 4.17), 2 peaks can be seen. This suggests that the dynamic load would be or higher frequency in the case of corrugated rail as 2 different types of stresses are induced in the same area. Furthermore, the maximum load of the smooth contact was only 90 N/mm^2 while for the case of corrugated rail, the stress was almost twice as large, 140 N/mm^2. From the stress contours, which can be seen in Figure 4.18 and Figure 4.22 which are for the corrugated and smooth rail respectively, it is obvious that this spectacular increase in load was because of the significant decrease in the

contact area. Stress concentration can be seen to be much higher in case of corrugated profiles.

4.7.1.3 Some Corrugation Profiles

Since, the profile of the corrugation and the method used for calculation, has a significant effect on the outcome of the result, several profiles have been modelled in CONTACT, and their stress profiles have shown through Section 4.5.1.3.1 to Section 4.5.1.3.5 where 5 different types of profiles have been modelled. The aim of using different profiles of corrugation is to identify the parameters that cause the stresses to increase. Figure 4.23 shows how the rail profiles have been quantified in order to perform the parametric study and Table 4.11 provides the specification of each rail profile.

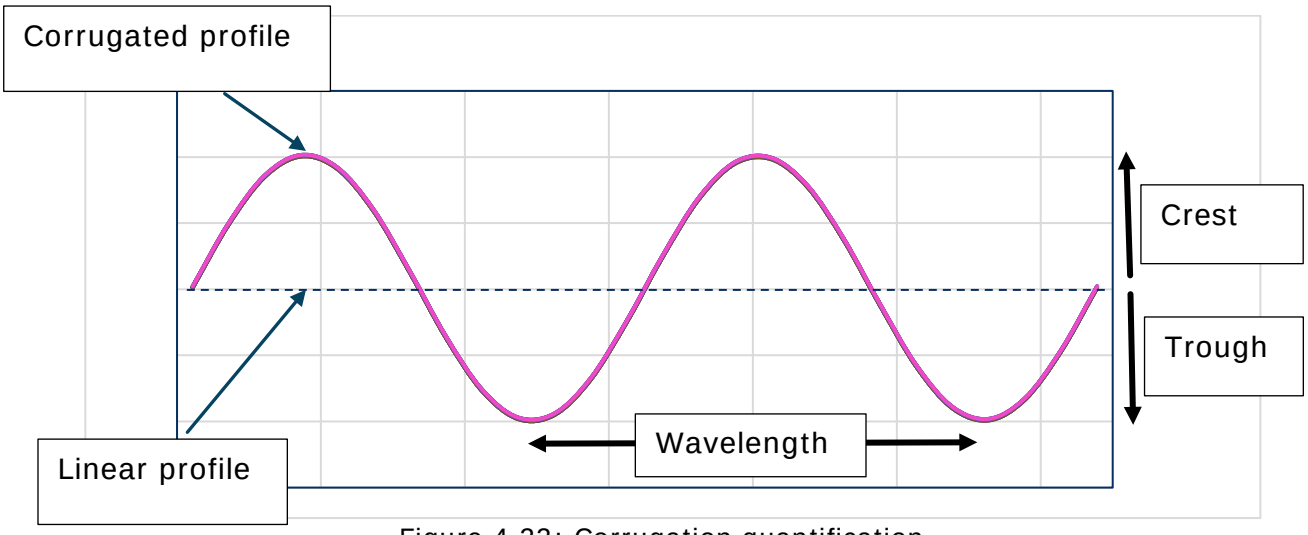


Figure 4.23: Corrugation quantification

Table 4.11: Corrugation description

Profile	Wavelength /mm	Crest /mm	Trough /mm	Description
1	6.28 (2*PI)	1	1	Corrugated with spikes 3mm apart ranging from 0-1mm
2	6.28 (2*PI)	3	3	Corrugated with spikes ranging 3mm apart from 0-3mm
3	1.57 (PI/2)	1	1	Corrugated with spikes 1.5mm apart ranging from 0-1mm
4	12.56 (4*PI)	1	0	Corrugated with spikes 12mm apart ranging from 0-1mm
5	12.56 (4*PI)	0	1	Corrugated with spikes 12mm apart ranging from 0-1mm

4.7.1.3.1 CORRUGATION PROFILE 1

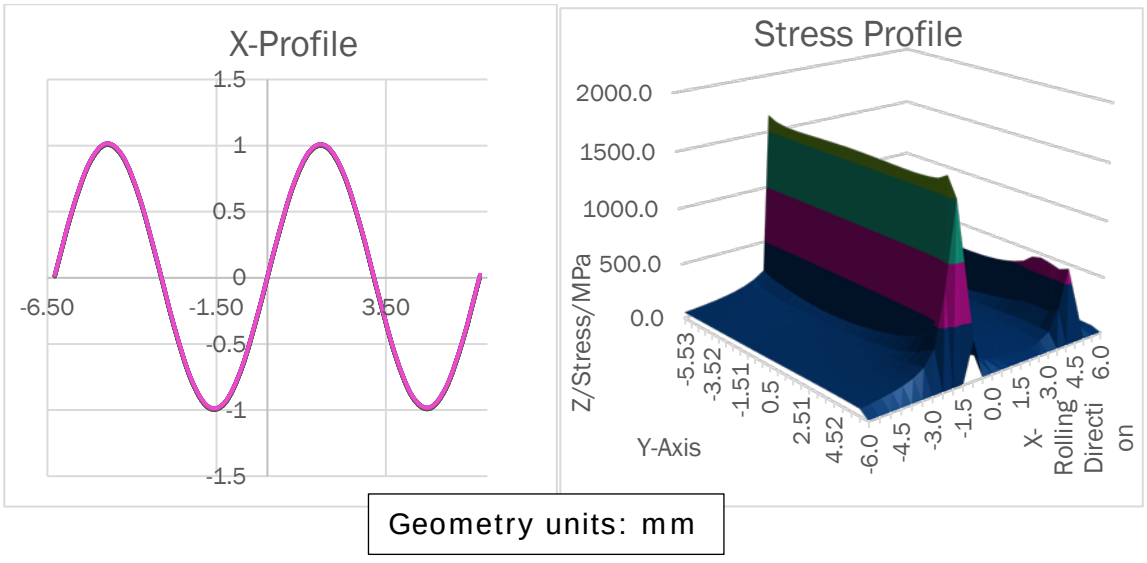


Figure 4.24: Corrugation profile 1

Maximum Stress was found to be 1710 MPa at the point of contact where X=0. A second stress peak was observed at X=4.5. Eqn(6) and CONTACT yield

approximately same results. Calculation in the space-domain yields higher values for each case.

4.7.1.3.2 CORRUGATION PROFILE 2

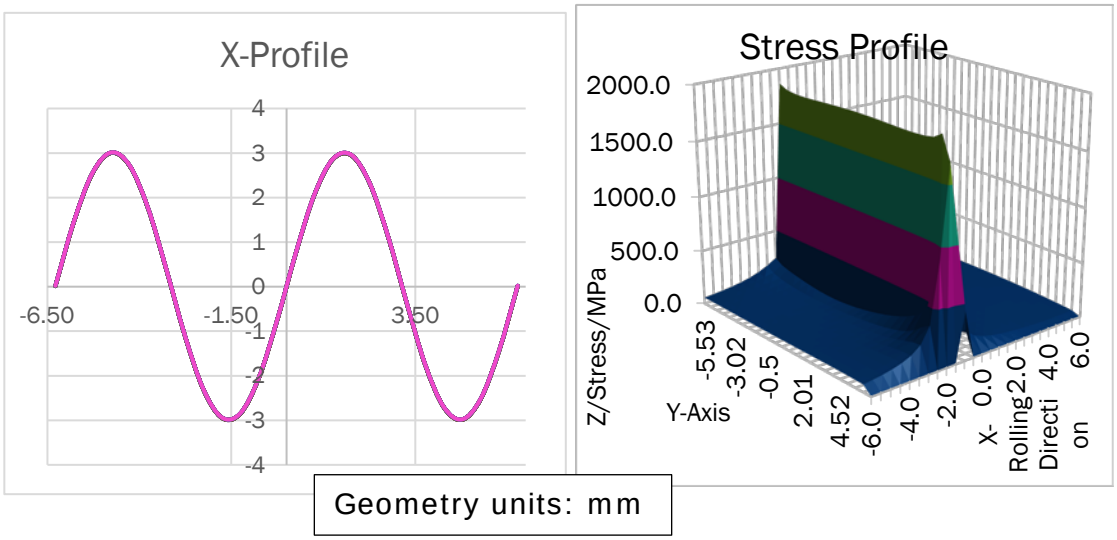


Figure 4.25: Corrugation profile 2

Maximum Stress was found to be 1890 MPa at the point of contact where X=0. This value is slightly higher than in corrugation profile 1, but the 2nd peak that was observed in the 1st case is missing. All the stress was concentrated at only one contact area. This is probably due to the fact that the amplitude of the corrugation is 3mm as compared to 1mm in case 1. The wheel does touch all the contact region. Therefore, the more the greater the corrugation depth, the higher the stress since a lesser area is in contact. Calculation in the space-domain yields impressively high values, which is about 400% higher than that calculated using CONTACT.

4.7.1.3.3 CORRUGATION PROFILE 3

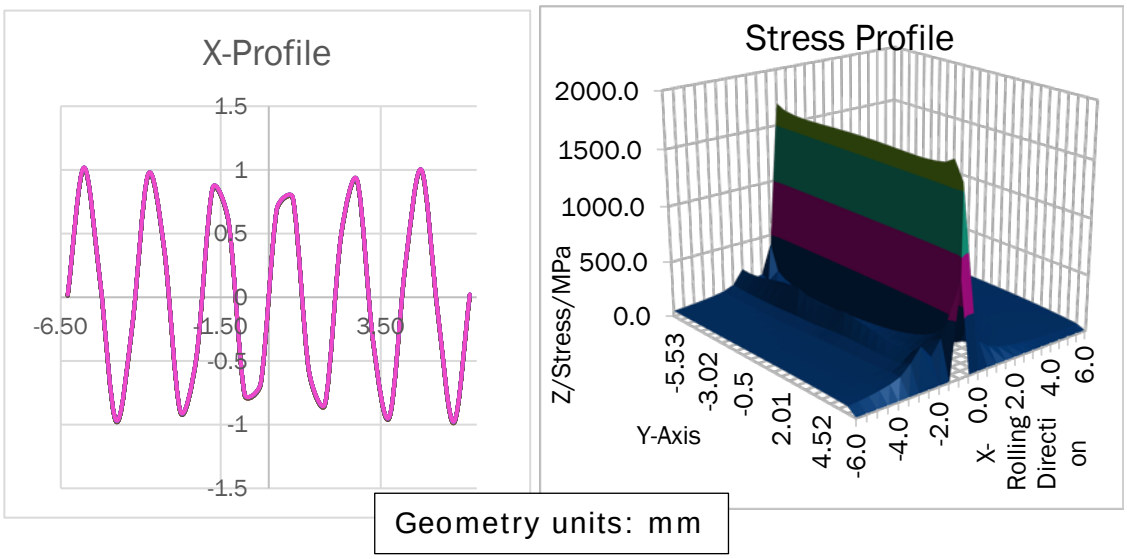


Figure 4.26: Corrugation profile 3

Maximum Stress was found to be 1730 MPa at the point of contact where X=0. This value does not differ by much from the 1st case. Therefore, the amount of corrugation does not affect the load significantly when calculated in the time-domain. The difference when using Time-Domain and Frequency-Domain approach becomes striking when compared with Thompson extended equation. A difference of 879% was observed. From the equation, it can be concluded that the smaller the wavelength of the corrugation, the higher the contact force will be.

4.7.1.3.4 CORRUGATION PROFILE 4

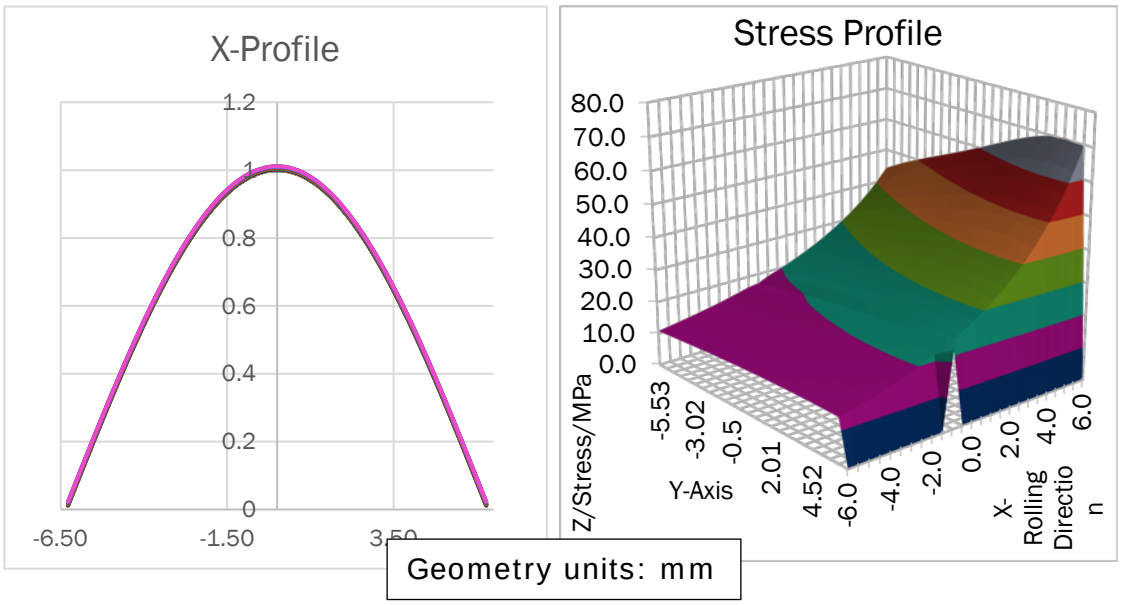


Figure 4.27: Corrugation profile 4

The maximum load was only 70 MPa at x=y=6.0. This value is very small as compared to all the rest. The profile is practically smooth due to the large area.

4.7.1.3.5 CORRUGATION PROFILE 5

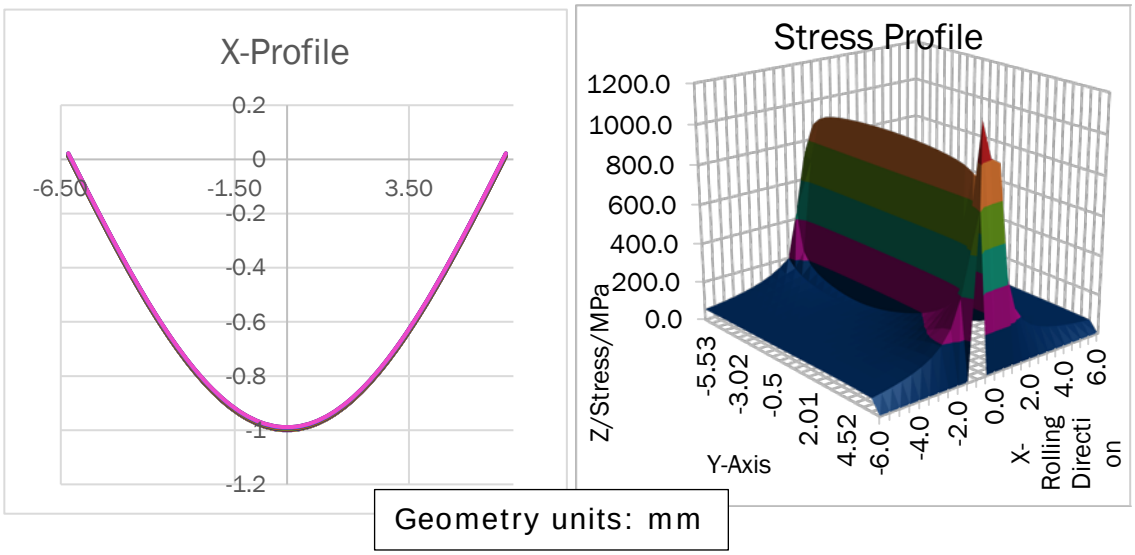


Figure 4.28: Corrugation profile 5

The maximum stress was 1191 MPa which is more than 10 time larger than that in case 4. Form all the cases, it can be concluded that a tough profile generates a higher impact load than a crest, and the values increase if the depth is large. It should be noted that a profile with more peaks will generate more impact loads than a smooth one. Paixao et al. (2015) simulated different stiffness profiles using finite element analysis, and similar stress peaks were observed. The corrugation profiles is therefore similar to a stiffness transition problem; the contact stiffness spring varies with the rail profile. According to Thompson & Wu (2000), the difference between the non-linear and linear interactions is found to be small if the roughness level is not extremely severe and a typical static contact preload exists. The difference increases for low preloads or for high roughness amplitudes. This confirms that the dynamic load is due to the deformation of the rail and the wheel.

4.7.2 Effect on Dynamic Amplification Factor

Table 4.12 shows all the results that have been calculated using Ansys for all the case scenarios described in Table 4.5. The maximum static load was calculated using the maximum stress from case 6. Dynamic amplification factor which is the ratio of the maximum dynamic load that was obtained from the CONTACT and Transient structural analysis to a static finite element analysis (similar to the beam on elastic foundation method) where inertial effects are ignored. The DAF was calculated using the following formula:

$$\mathrm{DAF} = \frac{Max\ Static\ Stress}{Max\ Dynamic\ Stress} \qquad \text{Eqn(8)}$$

Maximum dynamic stress was the stress obtained when the stress obtained from contact were fed into ANSYS Workbench. Frequency is the reciprocal of the time taken to cover 1 contact distance, DX. Talbot formula can be found in Appendix A.2.

Table 4.12: Results from ANSYS

Case Number	Max Static Stress / kPa	Max Dynamic Stress / kPa	DAF	DAF Talbot	Percentage Exceeded	Average frequency / kHz
C1 50KN 20ms	230.9	186.9	0.81	1.82	44.59	1.59
C1 50KN 40ms	230.9	186.9	0.81	2.63	30.77	3.17
C1 50KN 60ms	230.9	186.9	0.81	3.45	23.49	4.76
C1 50KN 80ms	230.9	186.9	0.81	4.26	19.00	6.35
C1 50KN 100ms	230.9	186.9	0.81	5.08	15.95	7.94
C2 150KN 20ms	730.6	684.12	0.94	1.82	51.58	1.59
C2 150KN 40ms	730.6	684.12	0.94	2.63	35.60	3.17
C2 150KN 60ms	730.6	684.12	0.94	3.45	27.18	4.76
C2 150KN 80ms	730.6	684.12	0.94	4.26	21.98	6.35
C2 150KN 100ms	730.6	684.12	0.94	5.08	18.45	7.94
C3 300KN 20ms	1617.9	957	0.59	1.82	32.59	1.59
C3 300KN 40ms	1617.9	957	0.59	2.63	22.49	3.17
C3 300KN 60ms	1617.9	957	0.59	3.45	17.17	4.76
C3 300KN 80ms	1617.9	957	0.59	4.26	13.88	6.35
C3 300KN 100ms	1617.9	957	0.59	5.08	11.65	7.94
C4 50KN 20ms	230.9	1040	4.50	1.82	248.13	1.59
C4 300KN 20ms	1617.9	2761	1.71	1.82	94.01	1.59
C5 50 KN 20ms 110Mpa	346.0	294	0.85	1.82	46.81	1.59

C5 50 KN 20ms 500Mpa	261.0	222	0.81	1.82	44.59	1.59
C5 50 KN 80ms 110Mpa	346.0	294	0.81	2.63	30.77	3.17
C5 300 KN 20ms 110Mpa	2116.0	1567	0.81	3.45	23.49	4.76
C6 100kN	480.75	460	0.81	4.26	19.00	6.35
C6 200kN	1005	713	0.81	5.08	15.95	7.94
C6 250kN	1293.6	850	0.94	1.82	51.58	1.59
C7 50KN 20ms EXP	230.9	263	1.14	4.26	26.76	1.59
C7 50KN 80ms EXP	230.9	495	2.14	4.26	50.32	6.35
C7 150KN 20ms EXP	730.6	2632	3.60	1.82	198.45	1.59
C7 150KN 80ms EXP	730.6	3480	4.76	4.26	111.78	6.35
C7 300KN 20ms EXP	1617.9	4561	2.82	1.82	155.31	1.59
C7 300KN 80ms EXP	1617.9	5060	3.13	4.26	73.44	6.35
C8 150KN 20ms Creep	730.6	2686	3.68	1.82	202.54	1.59
C8 150KN 80ms Creep	730.6	2897	3.97	4.26	93.06	6.35

From the finite element analysis, it was observed that the maximum load does not change with an increase in speed. Speed has no effect on the DAF. In practice, speed is considered because of the rapid change of loads due to the contact. This yields high-frequency vibrations. When compared to the static analysis, the stress imposed on the ballast by the sleeper gradually decreases. However, the maximum values were higher than when contact was not considered. Yoon et al. (2013) conducted field measurements under train

speeds of 100 km/hr to 300 km/hr on Yeonjae Bridge, South Korea. The impact factor was observed to decrease with heavier trains that have larger static deflection. A similar trend was observed in this research. DAF decreases with increasing load.

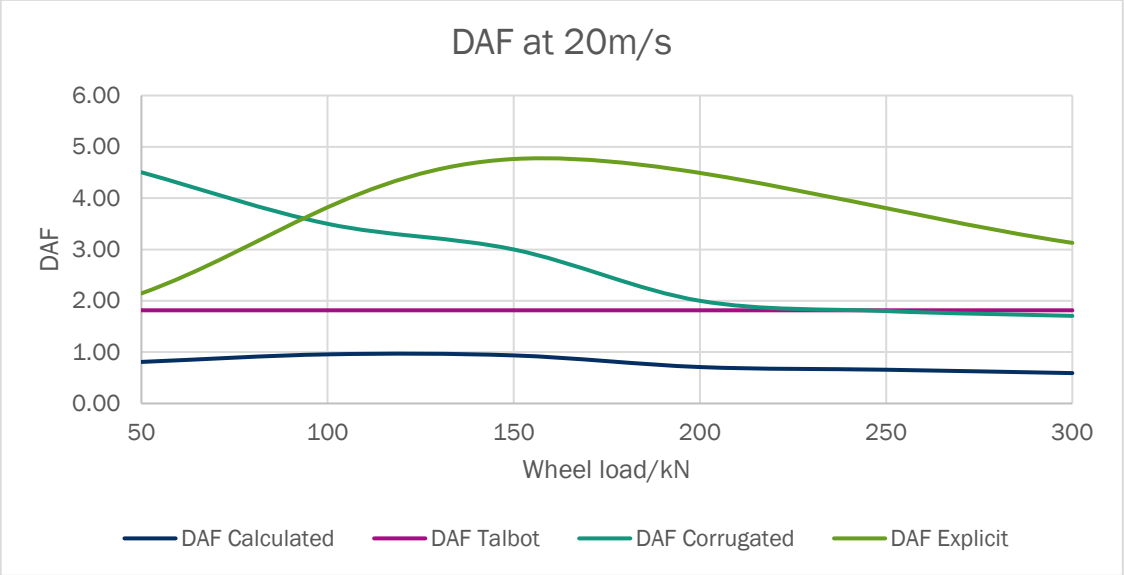


Figure 4.29: Variation of DAF at 20m/s

From Figure 4.29, it is clear that even at low speed, the DAF can be very high. Talbot formula states that speed is a factor that needs to be considered, However the results show that speed has no effect on the DAF. It is the rail profile that needs attention. A simple corrugated area was modelled, in CONTACT (case: C4). The profile is illustrated in Figure 4.16. The DAF in this case was very high, exceeding the allowable DAF by 400%. The numerical simulation conducted using the Explicit Dynamics module yield different results. The DAF were much higher in the case of the explicit dynamics module. When case C7 were compared among each other, it was noticed that then this module was used, speed has a significant effect. For the case of C7 300KN 20ms EXP

and C7 300KN 80ms EXP, there was a slight difference in the dynamic load that was calculated (4561 kPa vs 5060kPa) compared to a mere 957 MPa in the C3. Therefore, a smoother track should decrease the DAF and can be used for high-speed applications and if numerical methods that considered the effect of inertia, yield much higher results.

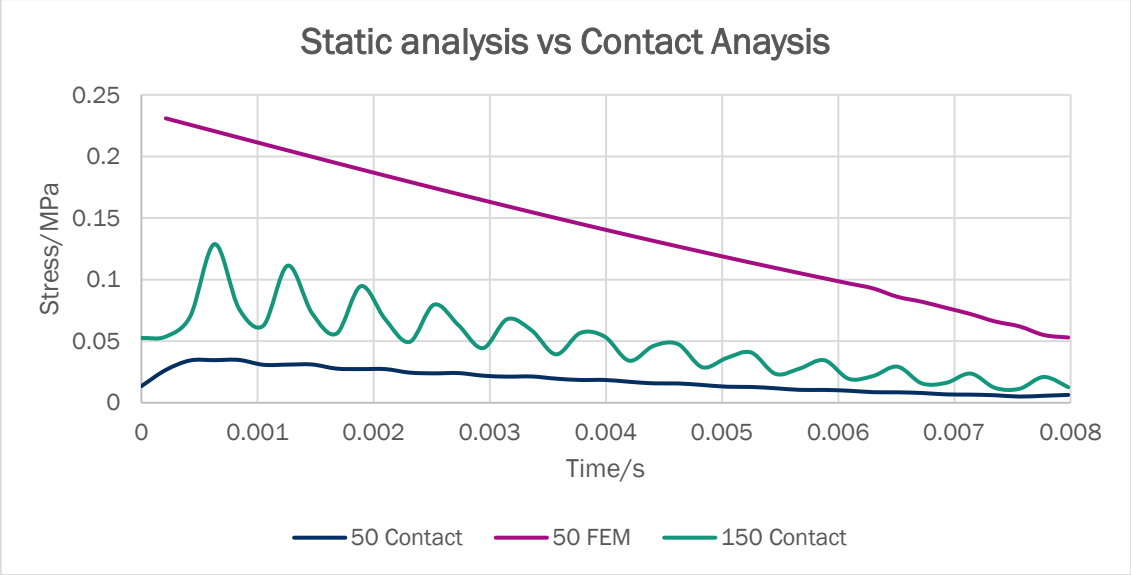


Figure 4.30: Static analysis vs Contact Analysis

At a closer look, for only 40 time-steps, it is clear that when contact geometry is considered, the load was fluctuating by a much greater amount when wheel load was larger. Contact stresses should be considered when designing since this dynamic load can be detrimental even at low speed. While the static finite element results show a linear trend, CONTACT analysis results show that is also the frequency of the load that increases with increase in load. A heavier wheel load would cause much more vibration even on a smooth track because of the elastic deformation at the contact region, which will be larger. Despite ignoring the large inertial effects such as vehicle-track interaction, it can be

concluded that vertical excitation can occur owing only to quasi-static forces. These results further confirm Colaço et al. (2015) findings where he stated that the most influential variable that influences the vibration levels is the unsprung mass of the train.

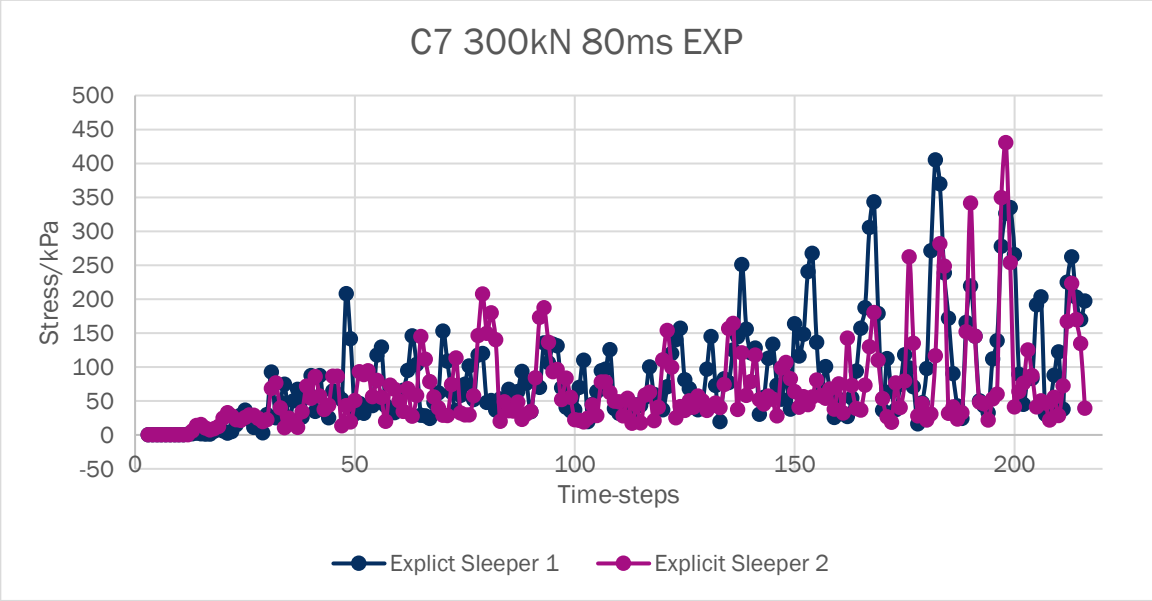


Figure 4.31: Explicit dynamics results for C5 300kN 80ms EXP

The results are presented in terms of time steps, and there is a total of 214 steps. Figure 4.31 shows that when the inertial effect is considered, the stresses looks very similar to those in case 1-3. It can be concluded that the methodology using CONTACT and ANSYS is accurate. The frequency is therefore dependent on speed.

4.7.3 Effect of Speed and Load

Even though the track is flat and does not have any corrugation, it can be deduced that the load varies with respect to time. Over the same number of time steps, 214 in this case, the shape and the maximum stress of 186.9 kPa for both sleepers does not change. However, over the same frequency, the

higher speed train stresses fluctuate much more. A stress of 979 kPa was recorded for the 300kN trains but load has no effect on the frequency of the train. Speed of train only affects the intensity of the frequency of the load but not the amplitude. Therefore, it is important to consider the effects of both load and frequency separately. Figure 4.32shows the wheel load variation with respect to time. Sleeper 1-80m/s, and Sleeper 2-80m/s are the results of stress probe 1 and 2 respectively for the case where the velocity was 80m/s. (See Figure 4.10 to see where probes are attached). The line chart named FEM 50kN in Figure 4.32 is case 6, where a static analysis was performed. No contact analysis was done and a load of 50kN was applied directly to the rail in ANSYS 2016. For comparison, according to Figure 2.5, the stress exerted from a 100kN wheel is in the order of 300kPa, which is similar to the results obtained from ANSYS.

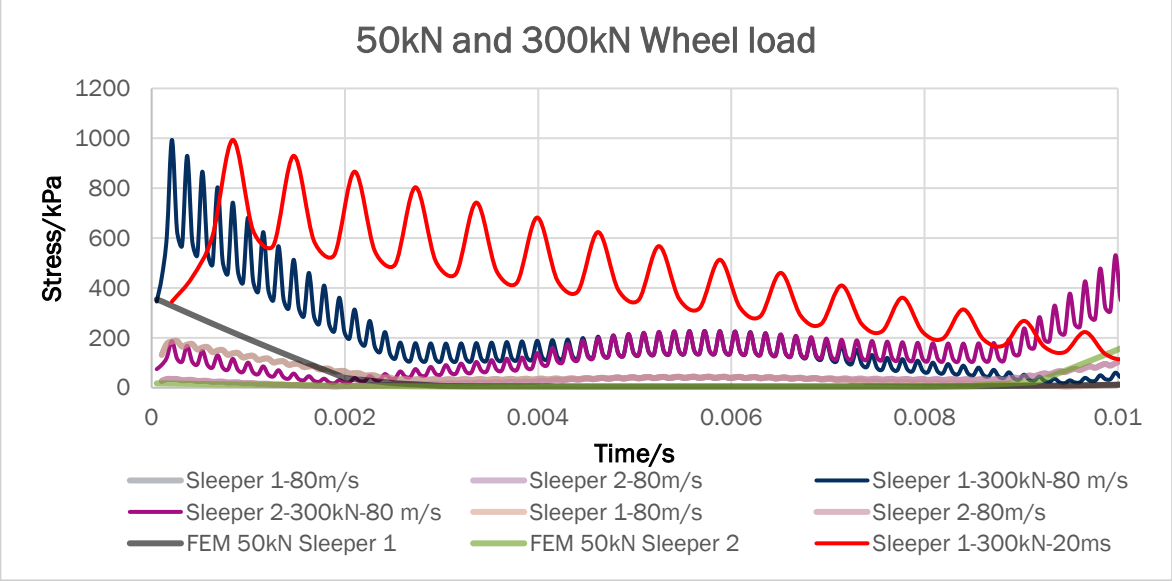


Figure 4.32: The stress fluctuation in the wheel-rail contact at different speed and wheel load.

The graph has been compared with field measurements conducted by Liu & Xiao (2010) on a 30m/s 50kN wheel load freight train and a 60m/s 30kN wheel load passenger train. Stress was measures at the subgrade level, and the shape of the graph is similar to that in Figure 4.32. Hence confirming the statement that speed does not affect the magnitude of the dynamic load. Regarding the decaying sinusoidal shape of the curve, Baeza & Ouyang (2011) ,who proposed a numerical based on modal substructuring and cyclic boundary conditioned, obtained similar results for a train speed of 144km/h. Zhai et al. (2004) measured the acceleration of the ballast of a Chinese main type freight car passing a velocity of 60km/h. Comparison of time histories of the ballast acceleration obtained from their research with Figure 4.31 and Figure 4.32 indicates that the vibration level in the ballast is directly related to the stress on the sleeper. Therefore, appropriate damping brought to either the structure above or below the sleepers can stabilise the whole system.

4.7.4 Effect of Pad Stiffness

Ferreira & López-Pita (2015) performed a numerical parametric study on the high-speed train on ballasted tracks and stated that stability of the track could be increased by increasing the elasticity of the super structure or by increasing the bearing capacity of the substructure. According to Sol-Sánchez et al. (2015), who placed a range of elastic materials in the substructure to reduce vibration, the most significant reduction in acceleration was accomplished by placing under-sleeper pads. Therefore, a parametric study has been performed by altering the elasticity of the pads and check if it is possible to decrease the DAF at this level. Furthermore, damping properties is closely related to the

natural frequency of a system. According to Esveld (2001), mitigating measure, to reduce noise and vibration, that can be taken at the source are include the reduction of natural frequency and provision of low spring constants. The increase of the fundamental natural frequency is usually achieved by increasing stiffness, although in some cases it is also attained by reducing the effective mass of the system. The young's modulus is related to the intrinsic mechanical properties of the material (independently of its geometry) while stiffness is commonly associated to the properties of a structure. Stiffness classically corresponds to a ratio between force and length change while young's modulus is calculated with stress (Force/Area) and strain (Elongation/initial length). It is much easier to modify the young modulus of a material in Ansys. Therefore, the young modulus of the pads was changed to assess the effects of stiffness in reducing the dynamic loads. Case 5 results were shown in the graph below.

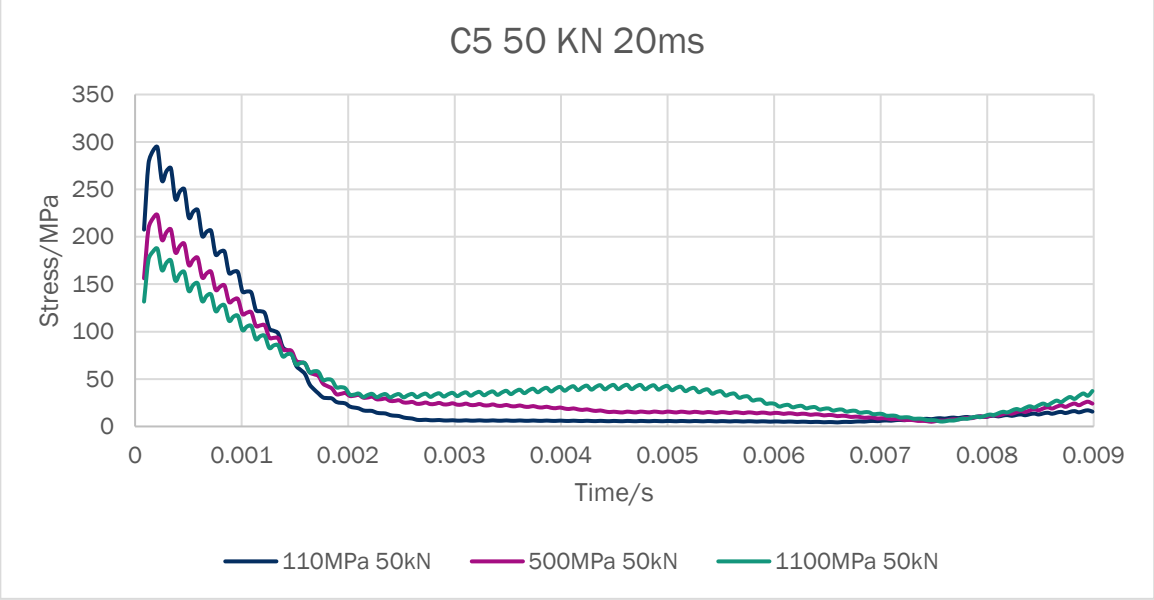


Figure 4.33: Effect of Pad Stiffness

The frequency of the loads remained unchanged, but the stress imposed on the sleeper varied considerably. A softer pad, 110MPa, attenuated the load the least when the load was directly over the sleeper. But when the load is imposed between the sleepers, the harder pad attenuated the load the least. This relationship was found to be the same for heavier loads. Since frequency remained unchanged, it was useless to perform the test using different speeds. Due to the relationship between load, speed and stiffness, it is very difficult to find an appropriate stiffness for the pad. Furthermore, the fact that irregularities affect stress at the contact area makes the problem more difficult. However, among those tested, it was found that harder pads were better since the amount of vibration is reduced.

4.7.5 EFFECT OF CREEPAGE

First attempts to simulate wear and microslips models were oversimplified in order to achieve a reasonable computational time (Braghin et al. 2006). The models did not account for global contact forces and creepage. The effect of micro-slips on dynamic loads on ballast has not been thoroughly studied. Creepage or overall slip can be generated when the wheel rotational speed, is greater or less than the free-rolling speed. Since this can only be calculated when rolling friction is considered, the explicit dynamics modules were enhanced to check the effect of creepage. Assuming a creepage of 0.00092 (Vollebregt 2014), which is common in railways, the following values that are shown in Table 4.13 needed to be inputted.

Table 4.13: Explicit Dynamics setting for Case 8

End-Time	0.045s	0.01125s
Velocity	20 m/s	80 m/s
Angular velocity	43.5 rad/s	174.1 rad/s

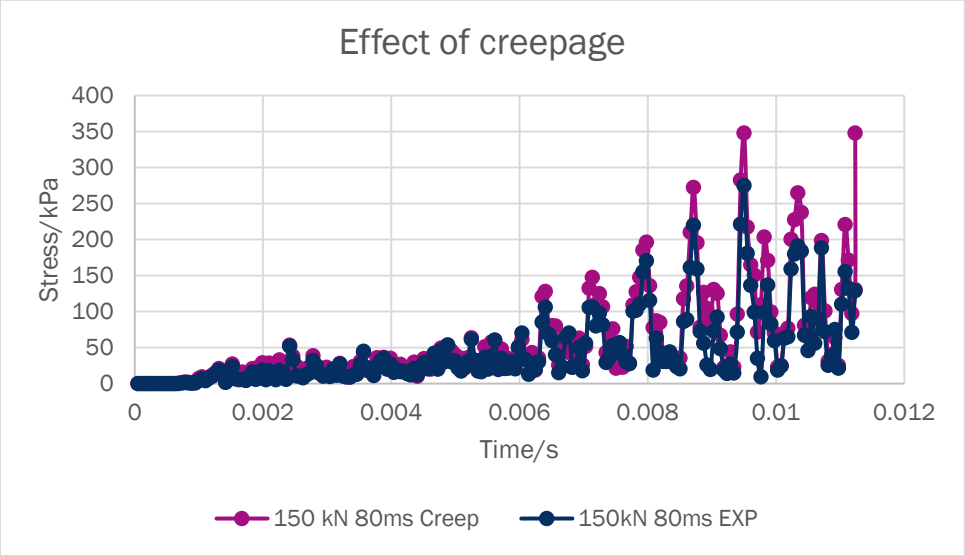


Figure 4.34: Effect of creepage

From Figure 4.34 it can be concluded that creepage does not affect the frequency or the maximum dynamic loads significantly. 150kN 80ms Creep and 150kN 80ms EXP are similar to each other.

4.8 CONCLUSION

CONTACT and ANSYS software were used to model the effect of corrugation on different types of roughness profiles. The models were validation using closed form solutions and the difference between the analytical and numerical methods were quite large. Depending on the profile of the corrugation and the method used for calculation, the stress that was obtained from calculation varies. It will be conservative to carry future calculation of stress using different approaches. Small wavelength corrugation, should be calculated in

the frequency-domain, whereas, large vertical tolerances should be calculated in the space-domain. Time-Domain yield values approximately in between those calculated by the other methods. Therefore, it was concluded that the stress distribution due to track irregularity causes uneven distribution of the stress which causes fluctuations in the reaction forces at the supports (sleepers) and hence, dynamic load.

Optimisation of the rail pads was attempted, and it was concluded that the frequency of vibrations does not decrease with the insertion of softer or harder pads. The ballast can reduce the vibration since the pads did not have significant effect for a range of different cases. DAF was used as a comparing factor to assess the effects of speed and wheel load. Stresses were on average twice as large for a moving train on corrugated rails as that on smooth rails. The difference in load per time step was found to be increasing with the increase in load. Therefore, it is not speed that causes vibration but the wheel load at the contact area since there would be more elastic deformation between the wheel and the rail. The stresses at the point contact area would thus vary considerably. In terms of superstructure optimisation, it is can be concluded that it is impossible to reduce vibration and dynamic loads unless there is no elastic deformation between the wheel and the rail. This can only be provided by very stiff wheel and rails on perfectly smooth surfaces.

This chapter has helped to classify the parameters that would be affected when a high-speed train would run on a conventional line at the micro-level. Since the parametric study revealed that it was not practical and useful to reduce

the dynamic loading at the source, further research was conducted in chapter 5, where the elasticity and bearing capacity of the ballast was changed in an attempt to reduce the dynamic load. Furthermore, the frequency of application of the load is too high to be practically tested, therefore in Chapter 5, Discrete Element method is used to simulate ballast under very high frequency of loading, i.e., Cyclic loading generated from material deformation rather than passage of wheels.

CHAPTER 5: DISCRETE ELEMENT MODELLING OF REINFORCED BALLAST

5.1 INTRODUCTION

One of the common criticisms of the analysis of granular matter is the appropriateness of using elastic continuum models. Railway ballast behaves non-linearly under wheel load and finite element analysis of the ballast using the Drucker-Prager model to simulate repeated loading and monotonic loading is far from acceptable since the results are very different from reality (Lim 2004). Ballast cannot be modelled as a continuum material using continuum mechanics. Therefore, an alternative method needs to be considered if ballast is to be modelled accurately. In this Chapter, the Discrete Element Analysis has been used to model ballast together with its reinforcement. The effective of incorporating the reinforcement has been assessed.

From the previous chapter, it was noticed that the frequency of loading, at which ballast is subjected to, is huge. The aim of this chapter is to model the sub structure of a railway track and to apply high frequency loads on the ballast. Validation of the model is a challenge since it is physically impossible to model such high frequency; therefore, the validation process was performed at low values of loading frequencies. Furthermore, reinforcement methods were also incorporated, and a numerical parametric study was performed. Yade-DEM code was used for the simulation. The code is attached in Appendix A.7.

5.2 MODELLING BALLAST

According to Railtrack Line Specification (R T/CE/S/006 Issue 3, 2000), ballast has to consist of “uniformly graded crushed hard stones, durable, angular and

equidimensional in shape, and free from dust, chemical contamination and cohesive particles". Furthermore, there is a wide range of ballast materials because of the lack of universal agreement on the specifications for ballast. The complete specification can be found in Appendix A.1. All these properties and behaviours are difficult to model, and only some of the parameters were considered. Modelling railway track geometry deterioration is a complex task for researchers because of several other factors, such as dynamic train loads, substructure, material properties and environmental conditions (Thakur et al. 2010; Sadeghi 1997; Thomas et al. 2015; Guler 2013). Numerical modelling of geocells has also been a big challenge due to their complex honeycomb structure. Generally, it is possible to model geometric discontinuities using the Discrete Element Method (DEM) (Stahl & Konietzky 2011; Indraratna et al. 2012; Ching & Kwan 2006; Geng 2010; Yang 2013; Cai 2015) since the later to take into account the grains rearrangements and particle distribution(Chen et al. 2015). The ballast and the geocomposite have to be modelled in order to simulate the different real case scenarios from different permutation of the parameters listed in Table 5.1 below.

Engineering properties of granular materials are defined by their stress-strain relationship when compressed, and by their strength behaviour which depends on the integrity of the individual particle (Lade et al. 1997). A clump is a single entity of overlapping spheres where the overlapping contacts are subtracted and ignored in the calculation (Lu & McDowell 2007). A crushable particle can be modelled as an agglomeration of balls bonded together. The smaller particles are held by strong cohesive forces. When these forces are overcome,

the smaller particle detaches from the clump, thus modelling the breaking for the ballast. Thus, DEM can be used to investigate the heterogeneous stresses in ballast in a way that cannot be achieved using continuum approaches. Other factors that affect the amount of particle breakage are: stress level (proximity to failure), stress path and particle shape (larger particles break more easily due to the fact that they contain more flaws and have a higher probability of interacting with other particles (Lade et al. 1997)). Commercial software has been used for this application, and recent application of PFC^{3D} to model soil particle fracture has demonstrated that it has the ability to reproduce the average strength and variation in strength of real soil particles, consistent with Weibull statistics (C. Chen et al. 2012). Simulating a structure composed of granular and binder materials using DEM is therefore rational (Chang 2009; J. Chen et al. 2012). Furthermore, a clump provides interlocking among particles owing to its geometry. Thus it is more realistic to model ballast by packing balls of different sizes together rather than singles spheres. The selection of spheres to form clumps is completely random, and the size of the agglomerated ball will range from 40mm-60mm (Code attached in Appendix A.6). Angularity, sphericity and surface roughness are thus modelled. Another reason for using clumps is that the mass is not uniformly distributed within the clump, and therefore the moment of inertia will be affected by calculations.

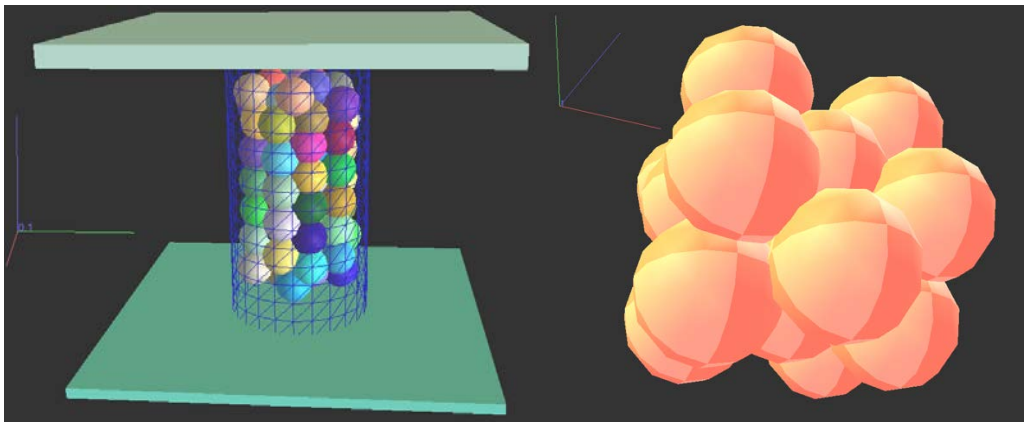


Figure 5.1: Model of a single geocell and agglomerated spheres

The final setup, a mixture, is made up of bitumen binder, air void and ballast confined in a cell. The thickness of bitumen across the actual structure varies considerably, generally within the ranges of 15 µm and 40 µm. The average size of railway ballast is 50mm, based on the particle size distribution of a ballasted track (Appendix A.1) and air void is around 4%-10% in an asphalt mixture. The importance of interlayer bonding has been highlighted from the results of testing and modelling, but with the data at hand, the required values for the interlayer bond in practice are difficult to define.

5.3 DISCRETE ELEMENT MODELLING

The DEM is based on the idea that the time step chosen may be so small that during a single time step disturbances cannot propagate from any sphere further than its immediate neighbours. Then, at all times, the resultant forces on any sphere are determined exclusively by its interaction with the spheres with which it is in contact. It is the key feature of DEM which makes it possible to follow a non-linear interaction of a large number of particles without excessive memory requirements or the need for an iterative procedure. It uses

an explicit numerical scheme in which the interaction of the particles is monitored by contact to contact states of equilibrium. The equilibrium contact forces and displacements of a stressed assembly of spheres are found through a series of calculations tracing the movements of the individual particles. These movements are the result of the propagation through the medium of disturbances originating at the boundaries (a dynamic process), and the motion of the particles is modelled at each time-step. Please note that the smaller the time step, the more computational power is required (Kozicki & Donzé 2009).

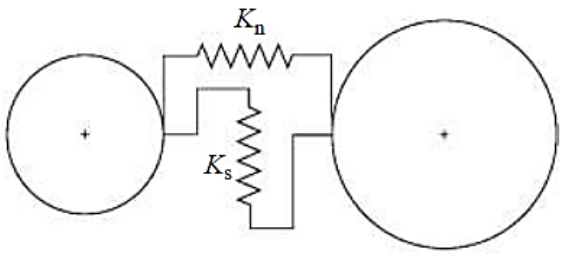


Figure 5.2: Elastic interaction. Normal and shear springs (Donze et al. 1999)

The physics behind the DEM starts from Newton's second law which gives the acceleration of a particle resulting from the forces acting on it. The force-displacement law is used to find contact forces from displacements. In the general case of an assembly of many spheres, the force-displacement law is applied at each contact of any sphere, and the vectorial sum of these contact forces is determined to yield the resultant force acting on that sphere. When this has been accomplished for every sphere, new accelerations are calculated from Newton's second laws (Kozicki & Donzé 2009).

5.3.1 DEM SIMULATION

In the simulations, periodic boundary conditions are assumed in the X and Y direction which are perpendicular to the force applied. Periodic boundary conditions are similar to symmetric conditions used in continuum mechanics. Ballast which leaves the simulation region are replaced in the opposite direction. Since most degradation occurs under the sleeper and large scale models require significant computational power, only small region was modelled in this study. Furthermore, an experimental box test (dimensions 700×300×450mm) conducted by Lim & McDowell (2005) provided coherent results under a sinusoidal load pulse 3kN – 40kN (max axle load of 20-25 tonnes), 1,000,000 cycles @3khz when compared to a full scale test conducted by himself at the Nottingham Railway Facility (S F Brown et al. 2007). Figure 5.3 shows the simulation area that was modelled by Lim and McDowell (2005) and that was numerically modelled in this study.

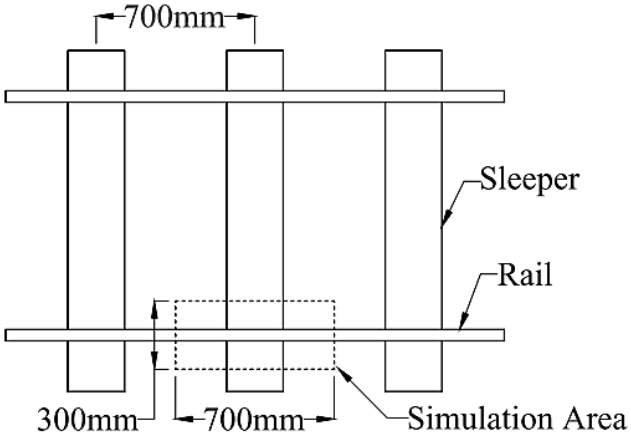


Figure 5.3: Simulation Area (McDowell et al. 2014)

Figure 5.4 shows the model of the simulation area and the model of one geocell. Figure 5.4 is for illustration only. The real simulation was performed using

agglomerated spheres of 10mm diameter. The display feature was disabled in the real simulation due to the huge computational power needed for it.

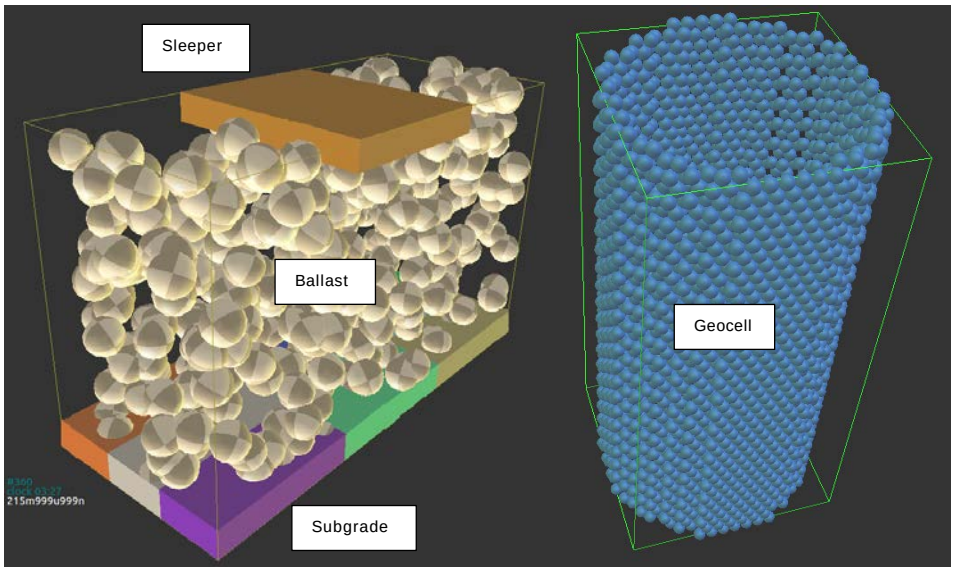


Figure 5.4: DEM Model of Simulation area showing large spheres and one geocell in Yade-DEM

5.3.2 FORCE

From the results of Chapter 4, it can be concluded that the load that acts on the ballast is decaying sinusoidally when one wheel passes over the sleeper. Since a DEM simulation is basically in the form of a loop where the acceleration is updated after each iteration, the iteration number, O.iter, was used to develop Eqn(9). For each iteration, the force is updated. The output of this equation is shown in Figure 5.5 and Figure 5.6. The following equation has been designed for the generation of the dynamic load:

$$F(t) = Sin(O.iter/\pi)\left(\frac{F_{max}}{2}\right) + \frac{F_{max}}{2} \qquad \text{Eqn(9)}$$

Where:

F_{max} is the maximum dynamic force sleeper imposes on ballast for this sleeper area.

O. iter is the iteration number with is dependent on (t)

Note: 1 iteration represents 1 timestep. 215 Iterations = 1 Cycle of 1 wheel, which is the time taken for the wheel to travel from one sleeper to the next sleeper. The distance between the sleepers is the same as that used in Chapter 4.

Figure 5.5 and Figure 5.6 show the load generated from a 50kN wheel load running at 20 m/s (C1 50kN 20ms), for 10 iterations and for 215 iterations (1 wheel cycle). The maximum stress generated from this case was 180kPa which is equivalent to a F_{max} = 13.5kN since the size of the sleeper that is being simulated is 250mm x 300mm. F_{max} acting on the ballast by the sleeper for a wheel load of 300kN was 72.75kN. The speed of 20m/s gives a frequency of 1.6 kHz since the contact area simulated in chapter 4 is 12mm. The frequency is the reciprocal of the time taken for the passage of the wheel over the contact area, over a given speed. It should be noted that the frequency obtained from the finite element analysis is significantly higher than those currently used for ballast testing. The average frequency that is currently being used for cyclic-testing(Lackenby et al. 2007; Leshchinsky 2012) in ballast for high-speed(260km/h) application ranges from 20-40Hz only. This value is minimal compared to that obtained in Chapter 4.

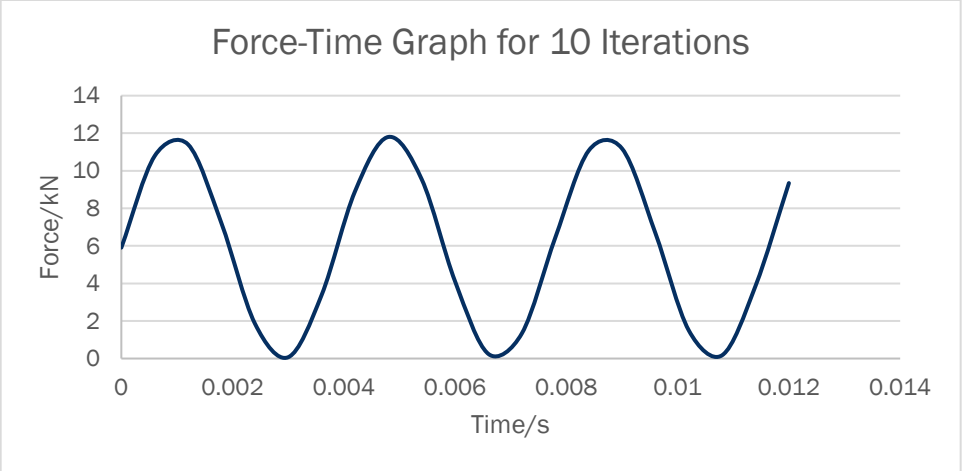


Figure 5.5: Force-Time graph for 10 iterations

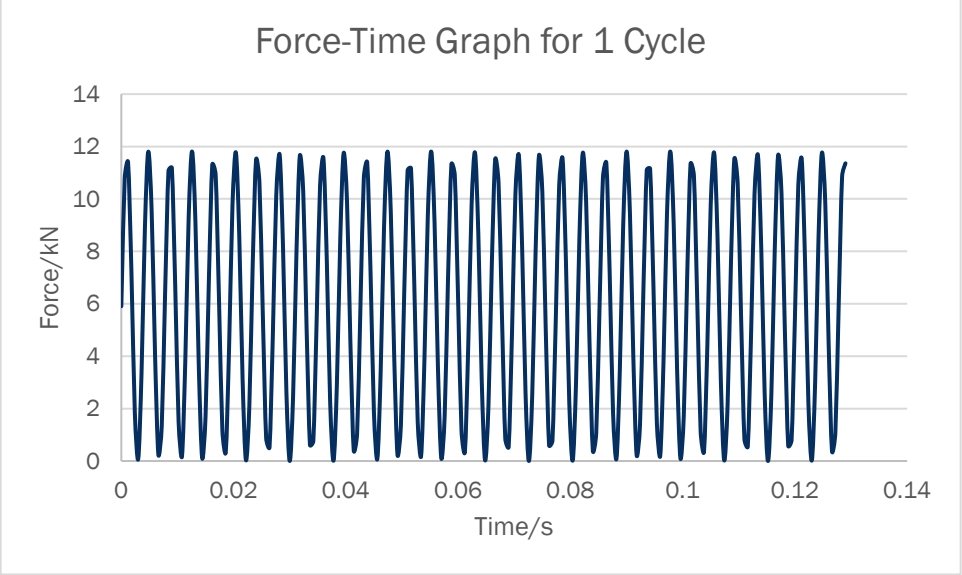


Figure 5.6: Force-Time graph for 1 Wheel Cycle

5.3.3 PARAMETRIC STUDY

The parameters to be varied to achieve desired properties so that the most important material geometry and properties that govern track deterioration, and measurable using DEM, are optimally designed, are listed in Table 5.1. Different cases have been modelled in Table 5.2. Four different cases were addressed. The unreinforced(None) case did not include any material apart

from subgrade, ballast and sleeper. The reinforced cases, on the other hand, included additional material, such as geocell, which was made from spheres of 0.8mm held by strong frictional forces. For the case of bitumen, additional spheres, having the properties listed below, were incorporated in the simulation region. The geometry of the geocells, including the depth of placement, number of geocells, diameter of geocell, where varied in order to obtain a better understanding of the mechanism. Bitumenwas modelled as visco-elastic spheres and was given the same properties as asphalt.

Table 5.1: DEM parameters (Thakur et al. 2010; Elias 2013; Kozicki & Donzé 2009)

Materials	**Size / mm**	**Bond type between spheres**	**Young modulus / MPa**	**Poisson ratio**	**Density kg / m^3**	**Normal Cohesion / Pa**	**Sheer Cohesion / Pa**
Ballast	10mm clumped in 50mm	Cohesion and Friction	250	0.25	1500	2.16e8	8.64e8
Sleeper	10 mm thick box	Friction	17,000	0.3	2400	Friction angle =0.25	
Geocell	0.8mm	Friction	3	0.2	1500		
Bitumen	10mm clumped in 50mm	Viscoelastic	5,000	0.25	1500	5.16e8	10.64e8
Subgrade	10mm thick box	Friction	100	0.3	2400	Friction angle=0.25	

In order to monitor the settlement after each iteration, a probe was attached directly under the sleeper and the relative position of the sleeper itself was monitored. The code for the DEM simulation can be found in Appendix A.7.

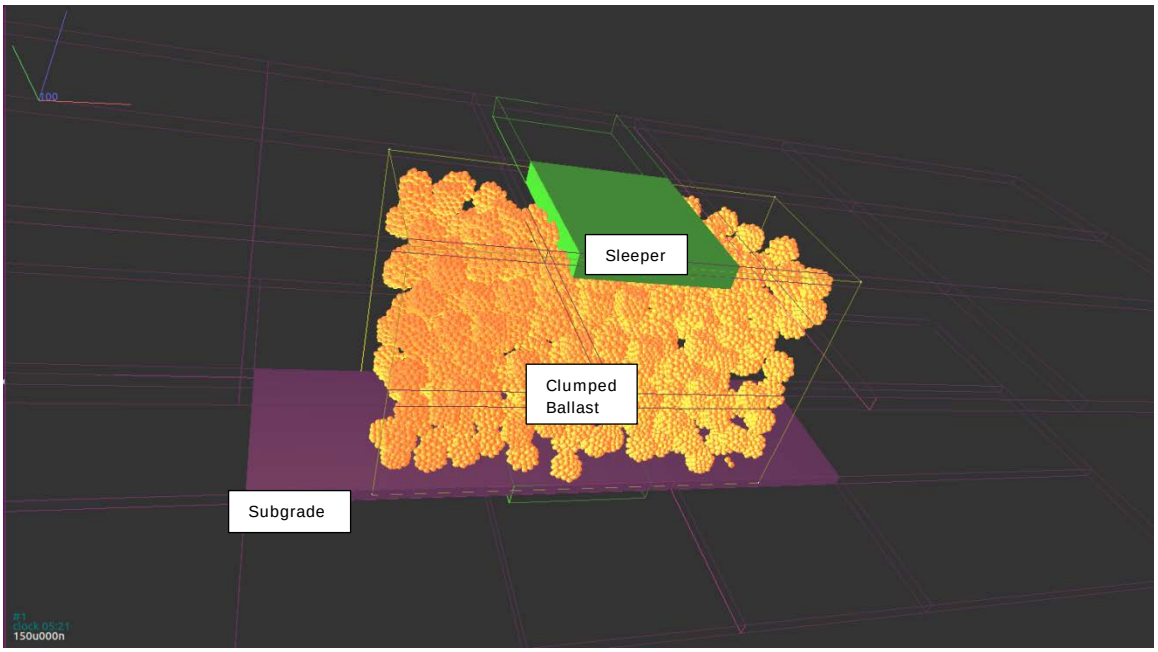


Figure 5.7: DEM Simulation in Yade-DEM

Figure 5.7 shows the model that has been used for the simulations. The displacement of the sleeper is shown after 25 iterations in Table 5.4

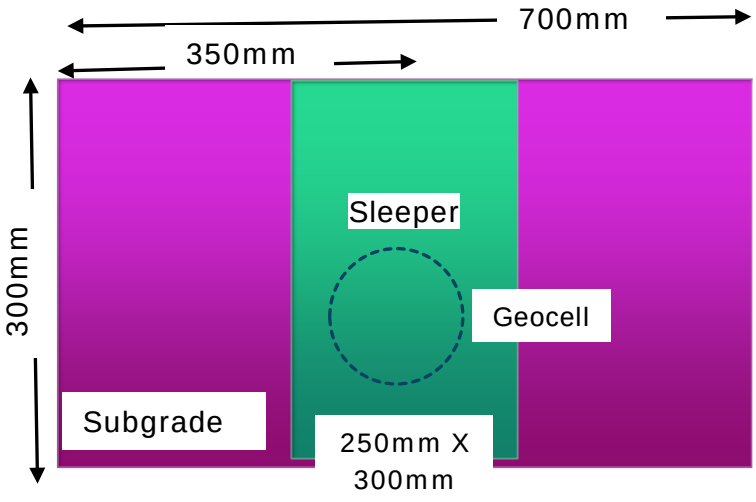


Figure 5.8:Plan view of simulation geometry

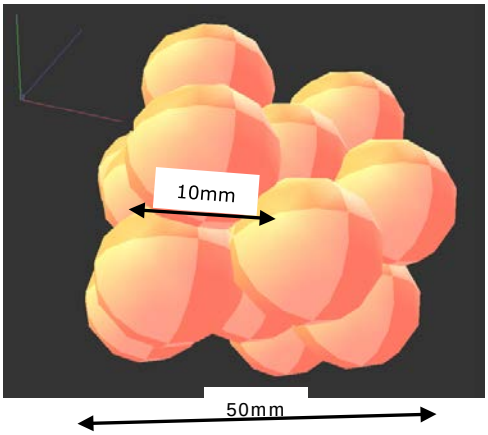


Figure 5.9:10mm particles clumped to 50mm

Three different types of scenarios have been tested. Table 5.2 details the types of test that have been conducted and Table 5.3 details each case.

Table 5.2: Case Scenarios for DEM

Case	Parameters tested
S1-S16	Different reinforcement schemes with varying load and frequency of loading. Reinforcement includes: None: No reinforcement installed which is the control in this test, Geocell: Contains only geocell, Bitumen: Contains only bitumen, Geocell and Bitumen: Contains both geocell and bitumen
S17-S24	Reinforcement only includes geocell with different geometries including: diameter(ø), depth of installation(@Depth), number of geocell(Geocell x number of geocell), length of geocell(xxmm)
S25-S32	None and Geocell and Bitumen has been tested for 1000 wheel cycles, i.e the passage of 1000 wheels at different wheel load and loading frequency. Due to extreme computation effort needed, only 215000 iterations were possible.

Table 5.3: Case Scenarios for DEM

Case	Wheel Load / kN	Maximum Stress / kPa	Frequency / kHz	Velocity / m / s	Reinforcement
S1	50	180	1.7	20	None
S2	50	180	1.7	20	Geocell
S3	50	180	1.7	20	Bitumen
S4	50	180	1.7	20	Geocell and Bitumen
S5	50	180	6.7	80	None
S6	50	180	6.7	80	Geocell

S7	50	180	6.7	80	Bitumen
S8	50	180	6.7	80	Geocell and Bitumen
S9	300	970	1.7	20	None
S10	300	970	1.7	20	Geocell
S11	300	970	1.7	20	Bitumen
S12	300	970	1.7	20	Geocell and Bitumen
S13	300	970	6.7	80	None
S14	300	970	6.7	80	Geocell
S15	300	970	6.7	80	Bitumen
S16	300	970	6.7	80	Geocell and Bitumen
S17	50	180	1.7	20	Geocellx2
S18	50	180	1.7	20	Geocellx4
S19	50	180	1.7	20	Geocell 150mm
S20	50	180	1.7	20	Geocell 200mm
S21	50	180	1.7	20	Geocell@50mm
S22	50	180	1.7	20	Geocell@100mm
S23	50	180	1.7	20	Ø30mm Geocell
S24	50	180	1.7	20	Ø150mm Geocell
S25	50	180	1.7 for 1000 Wheel Cycle	20	None
S26	50	180	1.7 for 1000 Wheel Cycle	20	Geocell and Bitumen
S27	300	180	1.7 for 1000 Wheel Cycle	20	None
S28	300	180	1.7 for 1000 Wheel Cycle	20	Geocell and Bitumen
S29	50	180	6.7 for 1000 Wheel Cycle	20	None
S30	50	180	6.7 for 1000 Wheel Cycle	20	Geocell and Bitumen
S31	300	180	6.7 for 1000 Wheel Cycle	20	None
S32	300	180	6.7 for 1000 Wheel Cycle	20	Geocell and Bitumen

5.4 VALIDATION OF MODEL

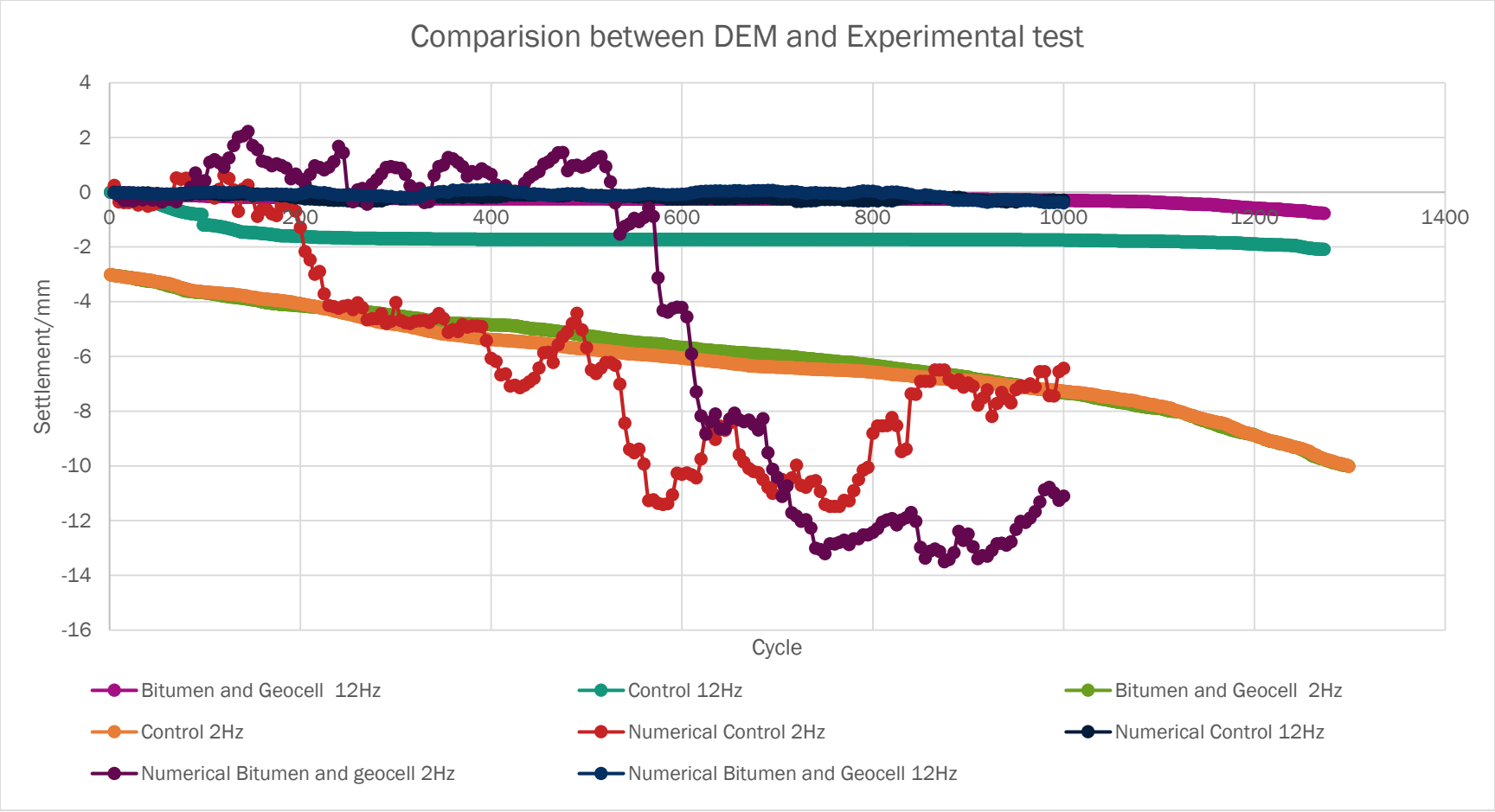


Figure 5.10: Comparison between DEM and Experiment

Figure 5.10 shows the numerical simulation and the results of the experiments conducted in Chapter 6-Test 4. Individual graphs for comparison are given in Appendix A.7.2. The total number of cycles for the DEM was 1000 while for the experiments data was collected until 1250 cycles. The comparison has been made up to 1000 cycles. From the graph, it can be seen that that results from the experiment show a consistent decline while for the DEM the graphs are very choppy. From Table 5.4, it can be seen that the percentage difference between the simulation and experiment is very low for the unreinforced case at 2Hz(Control 2hz), but is very high the 12hz one. The numerical model seems to overestimate values of the settlement when subjected to low-frequency loading and underestimates the results when subjected to higher frequencies. Even though the percentage difference seems to be very high, when compared the absolute values, the difference is very small. For such a complex problem, the absolute difference between the experiments and simulation is in fractions of millimetres. Hence, the numerical model will be used to carry out the parametric study.

Table 5.4: DEM results compared with experimental results

	Numerical /mm	Experiment /mm	% Difference	Absolute difference / mm
Bitumen and Geocell 12Hz	-0.38661	-0.770	49.79091	-0.38339
Control 12Hz	-0.36397	-2.087	82.56013	-1.72303
Bitumen and Geocell 2Hz	-13.5056	-10.00	-35.056	3.5056
Control 2Hz	-11.4849	-10.02	-14.6198	1.4649

5.5 LIMITATION OF MODEL

The shapes used for the simulation are clumped particles. Therefore, breakage of the particles can only occur at these joints. Furthermore, the shapes that are used are not exactly representative of real ballast shapes, hence affecting the particles interlocking behaviour. Furthermore, Geocells were also made by clumping particles together. These provide additional surface area for friction. Owing to the periodic boundary condition, ballast gets replaced when the later gets outside the simulation zone, hence the effects of settlement that are caused by the movement of ballast shoulder is minimised. This condition also raises the fact the uniform track stiffness is considered. Effects such as centre binding are not considered.

5.6 RESULTS AND DISCUSSION

Cycles	50kN 20m/s				300kN 20m/s		80m/s		50kN 20m/s (Geocell geometry)							
	None	Geocell	Bitumen	Both	Both	None	None-50kN	None-300kN	Geocellx2	Geocellx3	150mm	200mm	@50mm	@100mm	Ø30mm	Ø150mm
0	0.00	0.00	0.00	0.00	0.00	0.00	0.00	0.00	0.00	0.00	0.00	0.00	0.00	0.00	0.00	0.00
25	-0.12	0.34	-0.05	0.04	-0.14	-0.21	0.14	-0.01	-0.97	-0.39	0.83	-0.66	-0.42	-1.18	0.77	-0.57
50	-0.36	0.47	-0.09	0.03	-0.26	0.42	0.13	0.00	-0.09	-1.50	-0.05	-1.58	-0.11	-1.60	1.36	1.72
75	-3.48	0.24	0.02	0.31	-0.36	2.30	0.09	0.06	-0.82	-1.82	-0.50	-1.87	0.15	-1.84	0.79	1.28
	-2.56	0.30	0.04	0.67	0.01	2.25	0.15	0.05	-1.22	-2.50	-1.05	-0.67	-1.70	-0.92	0.71	-0.93
125	-1.59	1.18	0.43	0.99	-0.49	2.61	0.15	0.01	-1.33	-2.25	-3.07	-0.77	-4.18	-0.13	-1.14	0.03
150	-2.10	-0.21	0.46	0.19	-0.50	-0.33	0.17	0.04	-0.87	-3.68	-3.46	1.04	-5.38	-0.16	-1.34	-0.76
175	-0.86	-1.31	0.40	-0.08	-0.58	-1.43	0.18	0.04	-1.12	-7.59	-4.52	0.37	-3.50	0.97	-1.34	-0.23
200	-0.91	-2.27	0.00	-0.44	-0.67	-1.03	0.17	-0.01	-1.37	-7.50	-3.80	-0.80	-3.89	0.03	-1.15	-1.00
250	0.63	0.74	0.00	-0.93	-0.91	-1.41	0.01	0.00	-0.72	-0.94	-3.31	-0.71	-2.17	-1.88	-2.29	-1.30
Max +ve	1.41	1.18	0.64	0.99	0.01	2.84	0.19	0.08	0.00	0.25	0.91	2.51	0.36	1.79	1.50	1.72
Max-ve	3.48	2.35	0.22	0.97	1.02	1.91	0.00	0.03	1.47	7.74	4.77	1.98	5.38	2.40	2.59	1.79
Max	3.48	2.35	0.64	0.99	1.02	2.84	0.19	0.08	1.47	7.74	4.77	2.51	5.38	2.40	2.59	1.79

Table 5.5: DEM results for 215 Cycles showing settlement in mm

5.6.1 EFFECT OF REINFORCEMENT

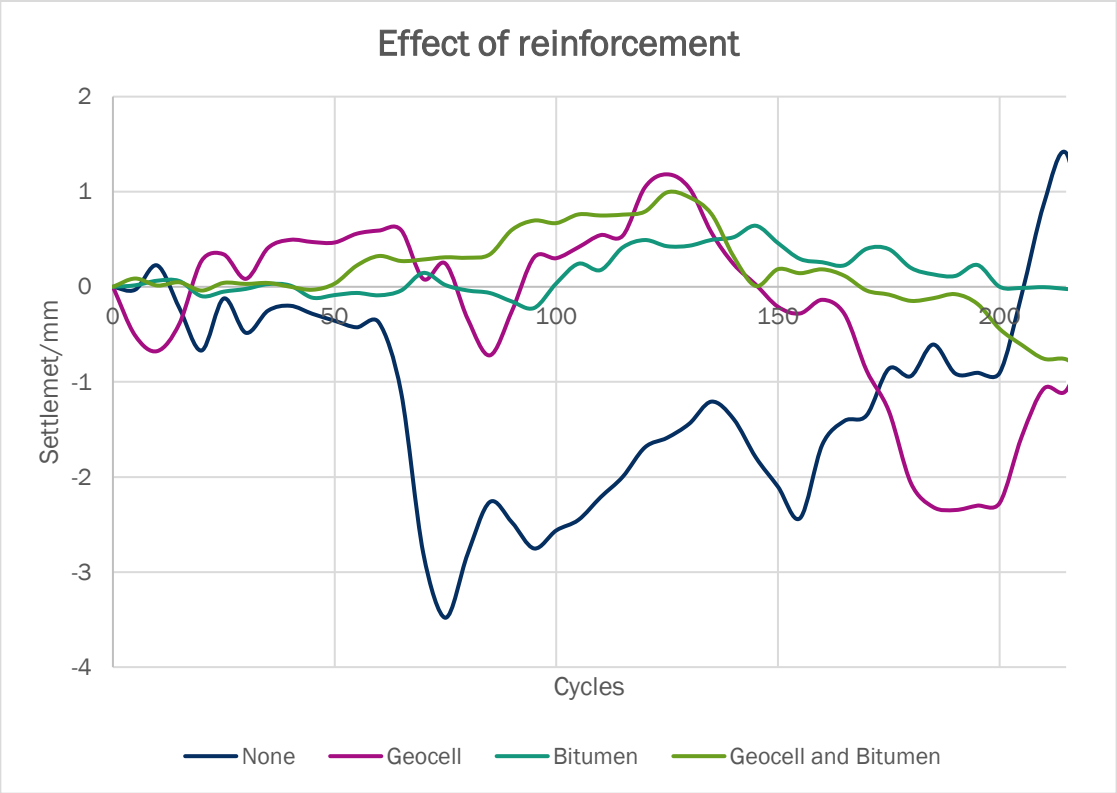


Figure 5.11: Effect of Reinforcement

Figure 5.11 shows the position of the sleeper from 0-215 cyclic loads which are equivalent to 0.129 seconds which is the time taken for 1 wheel to pass 1 contact area if the train is running at 20m/s. Since resilience of the ballast is considered in this study, it is not surprising to find negative settlements, which corresponds to the recovery of the ballast when the load reduces. It is clear that the unreinforced ballast settled by a much greater amount compared to the reinforced ballast. Geocell diminished the maximum settlement from 3.48 mm to 2.35mm, but ballast movement was still very high. Bitumen both reduced the settlement by a much greater amount and the restrained movement of the ballast. Incorporating both geocell and bitumen reduced settlement to 0.99mm but this value is lesser than that of bitumen alone.

Therefore, it is suggested that further investigation is required for determining the geometry of the geocell in section 5.5.2.

5.6.2 EFFECT OF LOAD AND SPEED ON REINFORCEMENT

5.6.2.1 Load

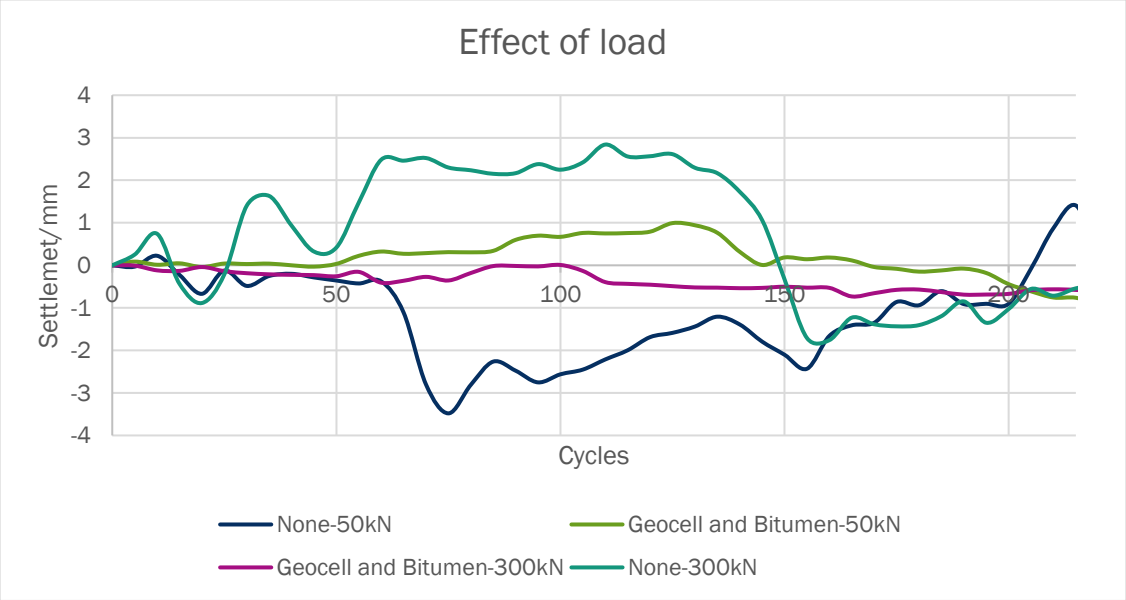


Figure 5.12: Effect of load on reinforcement

For such a small period of time, the effect of the load was not significant. However, settlement was reduced in both the 50kN and 300kN wheel load cases. Long-term effects of the loads have been investigated; it is concluded that after 1000(section 5.4.4) wheel cycles, a larger settlement is observed for the heavier wheel load. Speed also did not have any significant effect on the settlement for the same number of cyclic loads. However, for smaller time steps, the same amount of movement can be observed, but this movement happens in a much smaller time. Therefore, higher frequency vibration is observed. The magnitude of the settlement of faster vehicles was less than that of slower ones as shown in Figure 5.12. This is due to the fact that the

imposed load is not transferred to all the particles. This effect would only be observable in a DEM analysis since individual particles interactions are considered. Analytical methods that resemble DEM are still unknown therefore it is difficult to confirm the validity of these results even though the model was validated in Section 5.4.

5.6.2.2 Speed

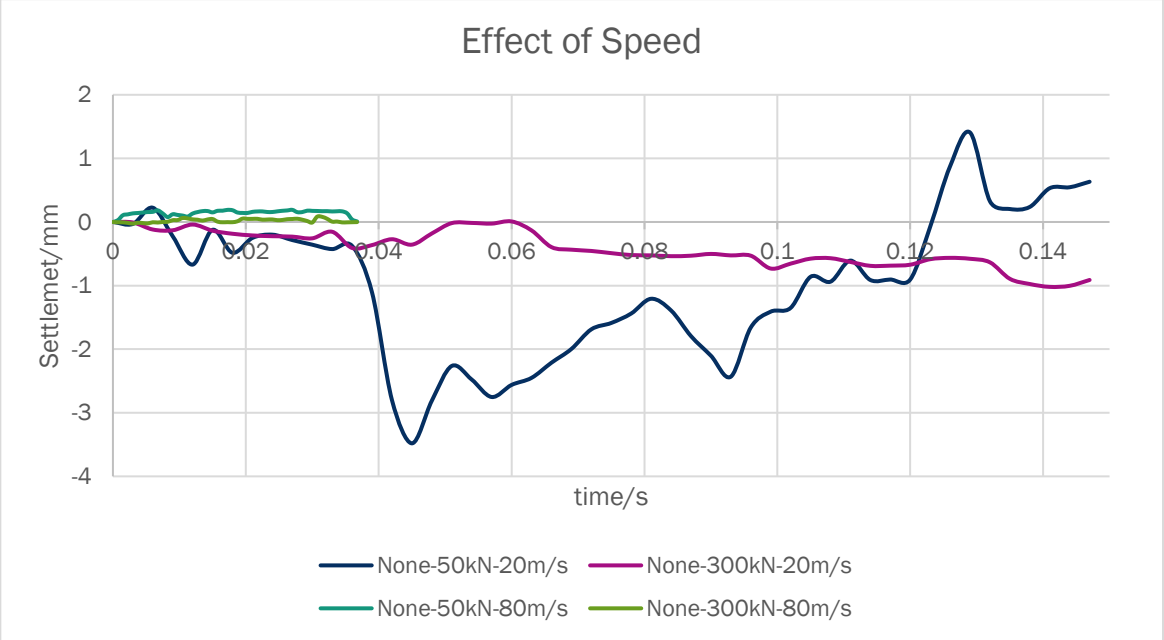


Figure 5.13: Effect of Speed

Figure 5.12 shows the amount of settlement that the sleeper has undergone over a very short period of time. The speeds that were tested were 20m/s and 80m/s. The distance was covered in both cases. The frequency of the loading was most significant. In the case of an unreinforced track, for a wheel load of 50kN and 300 kN at 20m/s the maximum settlement after 215 cycles of load was 1.41mm and 2.84mm which proves that wheel load causes settlement. However, for fast trains, 80m/s, the settlement was 0.00mm and 0.03mm for

a 50kN and 300kN wheel load respectively. This implies that is the frequency of loading is kept very high, the acceleration between the ballast does not propagate fully, and less settlement is observed. Therefore, high-speed trains running on the conventional ballasted track should not be an issue if reinforcement against vibration and deformation has been provided on a smooth track with rigid rails.

5.6.3 EFFECT OF GEOCELL GEOMETRY

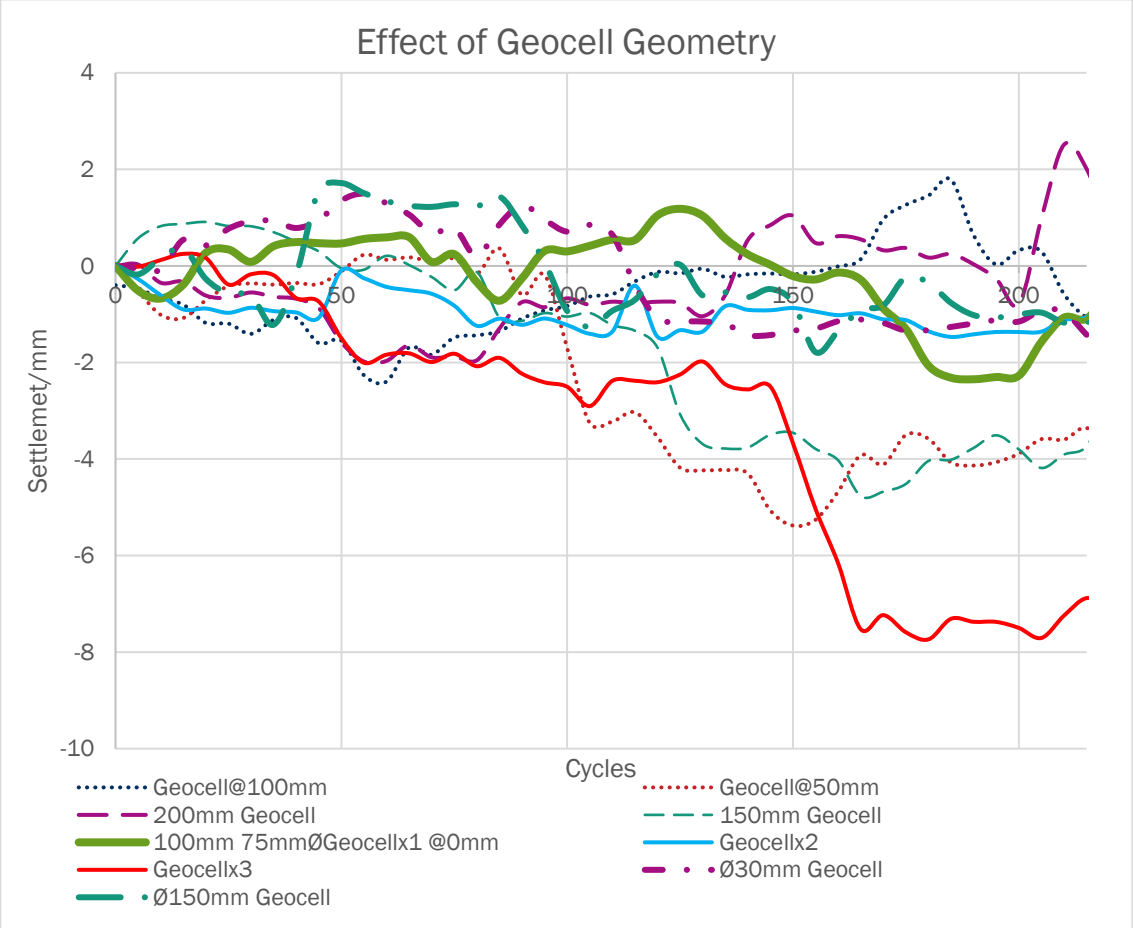


Figure 5.14: Effect of Geocell Geometry

Placing a large number of geocell had the adverse effect; it contributed to increasing settlement. However, from the results and Figure 5.14, it was

concluded that ballast movement and settlement were reduced by a number of individual cells. Less movement would be expected if a large amount of geocell were placed as close as possible and directly below the sleeper. Cell diameter should be as small as possible and the length of cells should be large. In the analysis, the friction between ballast and geocell wall was not significant. To improve interlocking of ballast, some embossed pattern should be provided to the wall of the geocell.

5.6.4 LONG-TERM EFFECTS

Table 5.6 shows the settlement and the percentage decrease in settlement after reinforcement have been incorporated for 1000 passage of wheels.

Table 5.6: Results after 1000 wheel cycles

Case	Force / kN	Frequency / kHz	Reinforcement	Maximum Settlement / mm	Percentage decrease / %
S25	50	1.7 for 1000 wheel Cycle	None	236.50	87.90
S26	50	1.7 for 1000 wheel Cycle	Geocell and Bitumen	28.62	
S27	300	1.7 for 1000 wheel Cycle	None	65.57	84.05
S28	300	1.7 for 1000 wheel Cycle	Geocell and Bitumen	10.46	
S29	50	6.7 for 1000 wheel Cycle	None	-0.01	200.96
S30	50	6.7 for 1000 wheel Cycle	Geocell and Bitumen	0.076	
S31	300	6.7 for 1000 wheel Cycle	None	0.08	22.27
S32	300	6.7 for 1000 wheel Cycle	Geocell and Bitumen	0.10	

It can be seen from Table 5.5 that incorporating both reinforcements had some beneficial effect. For small wheel loads running at high speed, the settlement was observed to be the least. A percentage decrease of 200% was observed.

When the frequency was low, no significant difference was observed in terms on wheel load. An improvement of only 80% was observed. With high-frequency and high wheel load, the reinforcement was only 20% effective in reducing the settlement. Overall, the settlement was decreased for all the cases when reinforcement was incorporated.

5.7 CONCLUSION

Ballast has been modelled by agglomerating spheres of 5mm radius together to form ballast of 50mm in diameter. It was concluded that large wheel loads combined with high speed might not necessarily cause more ballast movement. Even if under static load, ballast breakage is expected from the heavier load. The DEM analysis has proven that reinforcement provided to the ballast can prevent movement of the ballast and reduce settlement. Less movement would be expected if a large amount of geocell were to be placed as close as possible to the sleeper. Cell diameter should be as small as possible, and length of cells should be large. Bitumen has both restrained ballast movement and reduced settlement, but when combined with one geocell, it is less effective. Overall, the settlement was decreased for all the cases when both bitumen and geocell reinforcement was incorporated. It was also noticed that frequency of loading was a very important parameter in decreasing the settlement. When the frequency of loading is kept very high, the acceleration between the ballast does not propagate fully since the load is removed very quickly and less settlement is observed. The effect can only be observed in a DEM simulation since individual particle interaction is considered. Since the reinforcement has

proven to have beneficial effects in reducing the settlement, experimental testing is performed in the next Chapter.

CHAPTER 6: EXPERIMENTAL TESTING

6.1 INTRODUCTION

An engineer can only be confident about using a numerical method once it has been experimentally validated. Since it is difficult to conduct railway ballast testing in-situ, it is important to simulate the conditions experienced in the real track environment and study their behaviour. To achieve the aim of the research, which is to increase the stability of a ballasted track under high-frequency loading, appropriate tests need to be devised in order to check the influence of the parameters that govern the dynamic properties of the track when the reinforcements are implemented. From the finite element analysis(Chapter 4), it was concluded that the high frequency causes the dynamic amplification factor to increase drastically. Furthermore, owing to the presence of irregularities on the tracks, the stresses at the contact area gets amplified, which would require more lateral and vertical resistance to stabilise the track. This chapter consists of 4 tests namely: Vibrating table test, ERUDITE, compressive test and box-test. The aims of the tests are to assess the variation in the compressive strength of ballast arising from different combinations of reinforcement and to test the damping effectiveness of the geocell and bitumen in reducing movement of ballast and ground-borne vibration. The results of the DEM analysis have proven that geocell enhanced the settlement. However, from literature, it was observed that geocell was beneficial in reducing the vibration and this effect cannot be observed in the DEM analysis that was performed. Therefore, geocell has not been ruled out when conducting the experimental testing.

6.2 TEST 1: VIBRATING TABLE TEST

6.2.1 PREPARATION OF SAMPLE

Tests 1 and 2 aim to find the parameters of the different reinforcing schemes that influence the wave propagation and vibration. Damping is a measure of the rate at which energy is reduced as it disperses and passes through a material. The total damping ratio is composed of geometrical and material damping and has a non-linear relationship with frequency. This frequency dependence makes damping modelling more complex for time domain modelling in comparison to frequency domain modelling. In a railway track, damping is mainly provided by ballast and a combination of rail pads, under-sleeper pads and ballast mats. A total of 4 samples were prepared for this test. Further details about the specification of the samples are provided in Table 6.1.



Figure 6.1: Sample details(a)

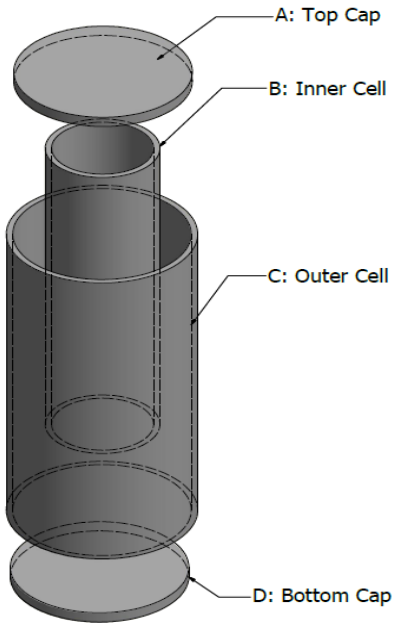


Figure 6.2: Sample details(b)

The outer wall of the sample is made up of rubber, and the sample has a diameter of 150mm, a height of 300mm and a thickness of 6mm. This

thickness ensures that the granular materials do not pierce through the wall when subjected to high compressive stresses. The material used for the inner wall(sample 2 and 4) is 5mm thick of Sorbothane D70 which absorbs up to 95.5% of impact energy, then reforms to its original shape (Sorbothane Inc. 2015). The sheet has an extremely high damping ratio and behaves like a liquid under high impact forces. It was not possible to use Sorbothane to form the whole sample because it is not rigid. The inner cell has a diameter of 90mm, and the sample was assembled using bolts and nuts. Low rigidity plastic was used for the bottom and top of the sample so that the compression strength of the sample is not affected. Sorbothane flexibility also provides the advantage of not decreasing the interlocking between the particles by readily changing shape allowing the particles to re-orientate.

The ballast distribution is as same as for Chapter 5 and was placed into the cell in 3 different layers while placing the sample on a vibrating table for 15 seconds after each layer. This measure ensures that the sample is compacted adequately to an initial density of about 1500kg/m^3(e_o=0.72-0.76). The same ballast was used for all the test. The ballast was obtained from a quarry operated by *Kajang Rocks Groups*™ in Selangor, Malaysia.



Figure 6.3: Scaled Ballast

Bitumen 70 was diluted with kerosene to reduce the viscosity. Bitumen was not heated because of the risk of damaging the sorbothane material. The samples were completely filled with bitumen and allowed to cure overnight. It should be noted that when Polish Railways, sprayed bitumen to a depth of only 50-70mm on a tack, no improvements were observed, and track settlement was not reduced(ORE 1983). To calculate the required amount of bitumen needed, Marais method was used(Marais 1981). 850 ml of bitumen is required for a full scale treatment. For this sample size, the only 400ml of bitumen will be used because of the height of 300mm. Table 6.1 provides information about the individual samples used for Test 1,2 and 3. Photographs of the samples are shown Figure 6.4 through Figure 6.9.



Figure 6.4: Samples for Test 1,2 and 3

Table 6.1: Samples and configurations

Sample	Photograph	Description
1	 Figure 6.5: Sample 1	Contents include ballast only. This sample will be used as a control for comparison purposes.
2	 Figure 6.6: Sample 2	Sorbothane sheet is placed inside the cell.

3	 Figure 6.7: Sample 3	Sample contains bitumen which was placed layer by layer(3 times), and the sample was allowed to cure for 24hours.
4	 Figure 6.8: Sample 4	Sample 4 is a combination of sample 2 and 3 and includes both Sorbothane and bitumen

6.2.2 TESTING

Vibration is a key factor causing deterioration of ballast (Lichtberger 2011), and the parameters that control wave propagation are: density, poisson's ratio, Young's modulus and damping ratio(Connolly et al. 2015). In chapter 4, the young modulus of the pads was changed, but the results were not very attractive. Therefore, the damping ratio of the track needs to be improved. In the field, Chebli et al. (2008) measured the dynamic responses of high-speed trains on ballasted tracks using accelerometers. The accelerometers were placed at different locations, and the highest acceleration peak was measured directly below the sleeper. So far, methods for analysing and testing vibration of the granular ballast have not be made (Zhai et al. 2004). Vibrating table test and Resonant Column tests can be used to calculate the damping ratio (Hushmand 1983) approximately. The seismic response of structure depends

on the dynamic properties of the materials and the characteristic of the motion. However, there are various factors that can disturb the estimation process. The simplest method is to measure the response of samples to an external disturbance where response include displacement, velocity or acceleration.

A simple test using a small shaking table was performed to determine the dynamic properties of the specimen. The table is driven harmonically with the specified frequency (12-50Hz in this case). Zhai et al. Like most models, the test is based on the assumption that, the vibratory movement is the same at the base of the samples and vibratory motion is vertical(Otero et al. 2012). The frequency of the harmonic wave can be controlled step by step and accelerations at the top are captured. The problem can be regarded as a single-degree-of-freedom system. Horizontal movements in the X and Y direction are recorded by the accelerometer that is fixed on the top. The accelerometers are connected to an Arduino, which converts acceleration to an electric signal which is recorded on a computer. The experiment was done 3 times with an interval of approximately 10 seconds for each sample. To increase the accuracy of the experiments 2 accelerometers were used.

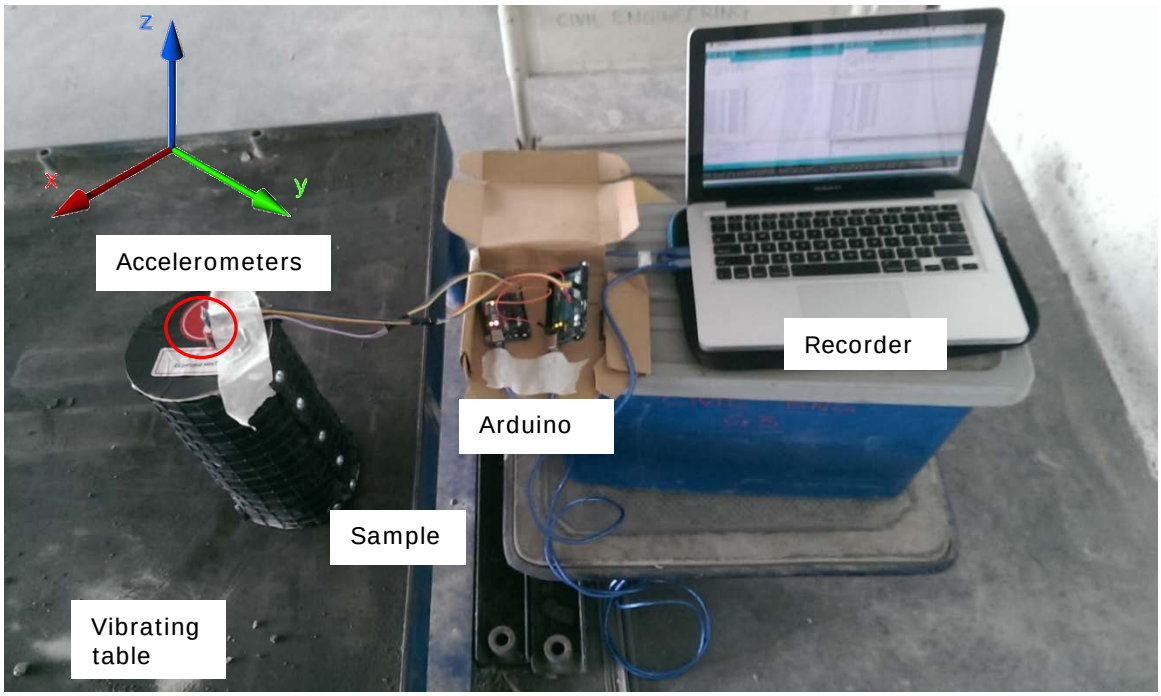


Figure 6.9: Shaking table test setup(a)

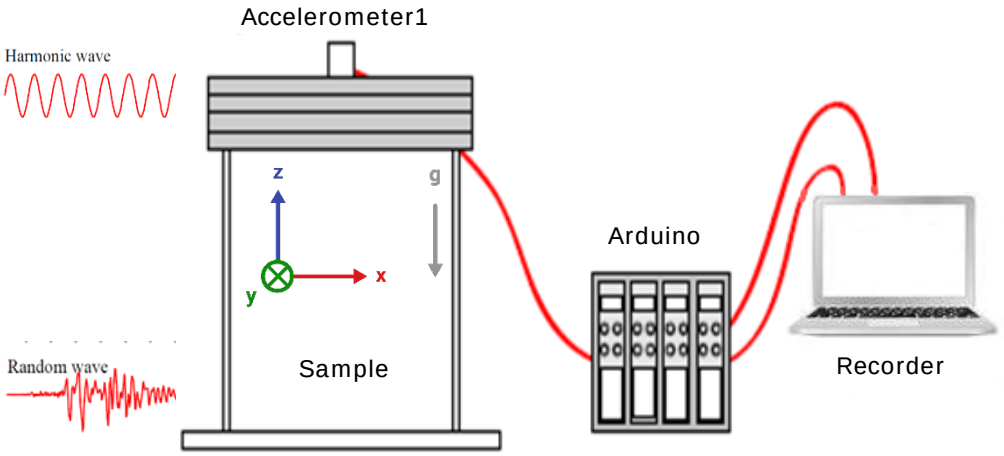


Figure 6.10: Shaking table test setup(b) (Tobergte & Curtis 2013)

Note: Accelerometers should be calibrated to determine their sensitivity, which is necessary to convert measured values to acceleration. The faster movement the accelerometer undergoes, the less damping effect the sample has. The shaking table generates a random wave at the bottom, and the movement is translated to the top where it is registered by the accelerometer.

6.2.3 RESULTS AND DISCUSSION

6.2.3.1 Acceleration and frequency

The accelerations in all the 3 directions were obtained, and the shapes of the graphs that were plotted were similar. Therefore, only the calculations for the X-direction were considered since only the model is considered to have a single degree of freedom. Displacement was recorded at an interval of 10 milliseconds. The graph below shows the results captured by accelerometer 1 and 2 in the X, Y and Z directions for all the 3 trials. A1 is accelerometer 1 and A2 is accelerometer 2. The power output of accelerometer 2 is approximately half that of accelerometer 1. The use of a second accelerometer was to ensure that the results were consistent. Figure 6.11 shows the raw output of the accelerometer. The calibration process indicated that approximately 6 units recorded in by the accelerometer is equivalent to $1 m/s^2$ of acceleration. Results for all the samples can be found in Appendix A.8.

Legend:

A1-X is the displacement registered by accelerometer 1 in the X direction,

A1-Y is the displacement registered by accelerometer 1 in the Y direction,

A1-Z is the displacement registered by accelerometer 1 in the Z direction,

A2-X is the displacement registered by accelerometer 2 in the X direction,

A2-Y is the displacement registered by accelerometer 2 in the Y direction,

A2-Z is the displacement registered by accelerometer 2 in the Z direction.

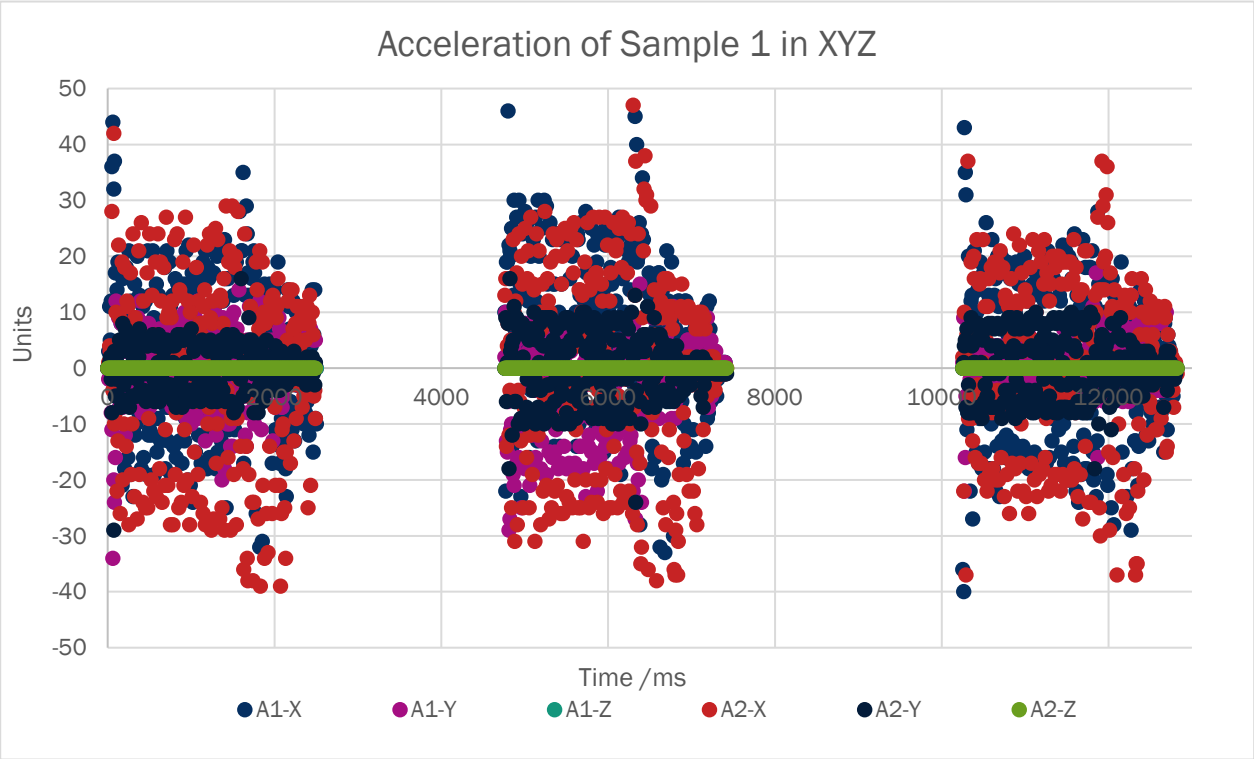


Figure 6.11: Acceleration of sample 1 in XYZ direction

As it can be seen in Figure 6.11, the vertical acceleration, which is the Z-axis, was 0 for all the 3 tests. This implies that the samples were correctly glued and the system can be regarded to move only horizontally. All the 3 trials almost yield the same results since the shapes are almost the same. The graph below shows a close up of the results of accelerometer 1 in the first trial of sample 1.

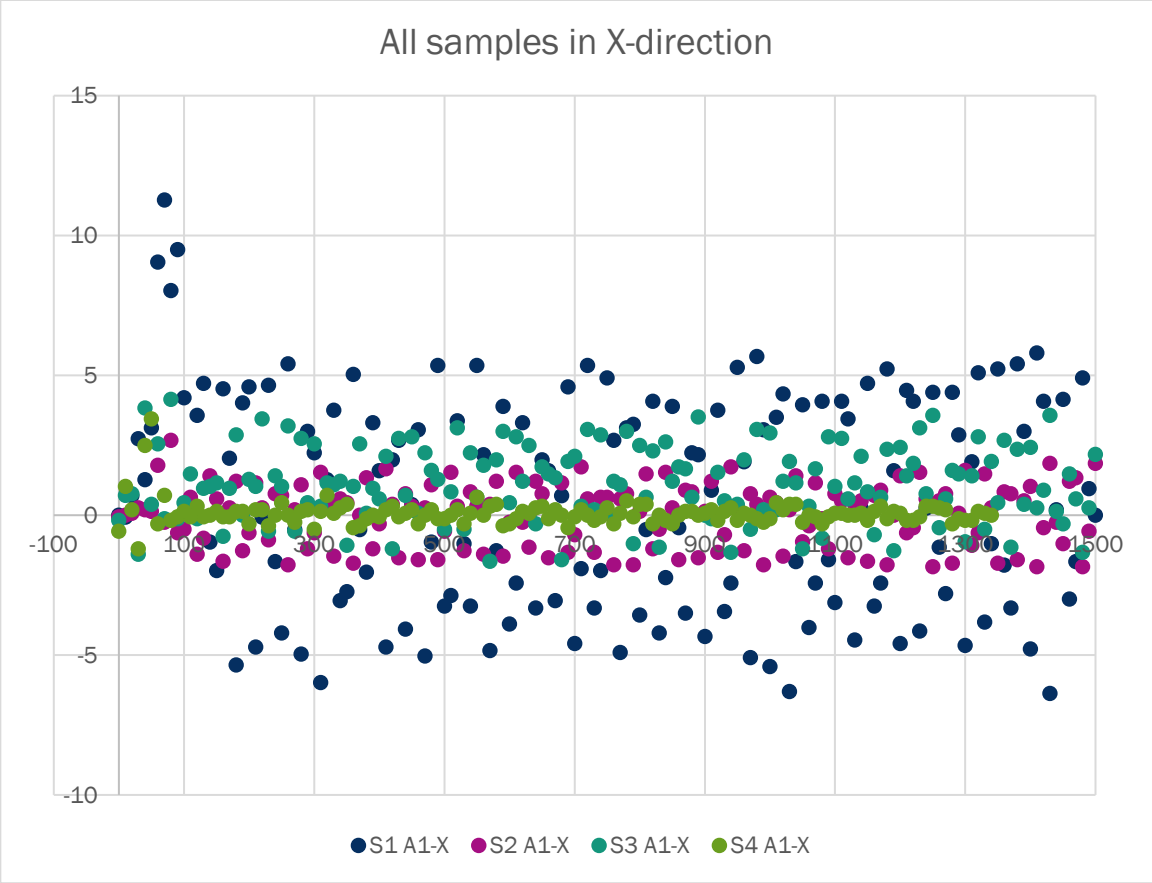


Figure 6.12: Displacement of all samples in X-direction

Legend:

S1 stands for sample 1, S2 stands for sample 2, S3 stands for sample 3,

S4 stands for sample 4.

Figure 6.12 shows all the acceleration for all the samples, and it is clear that all the samples do not have the same response to the random wave. Since it is very different to draw conclusion from Figure 6.14, only a section of the graph was analysed to determine the frequency and wave form.

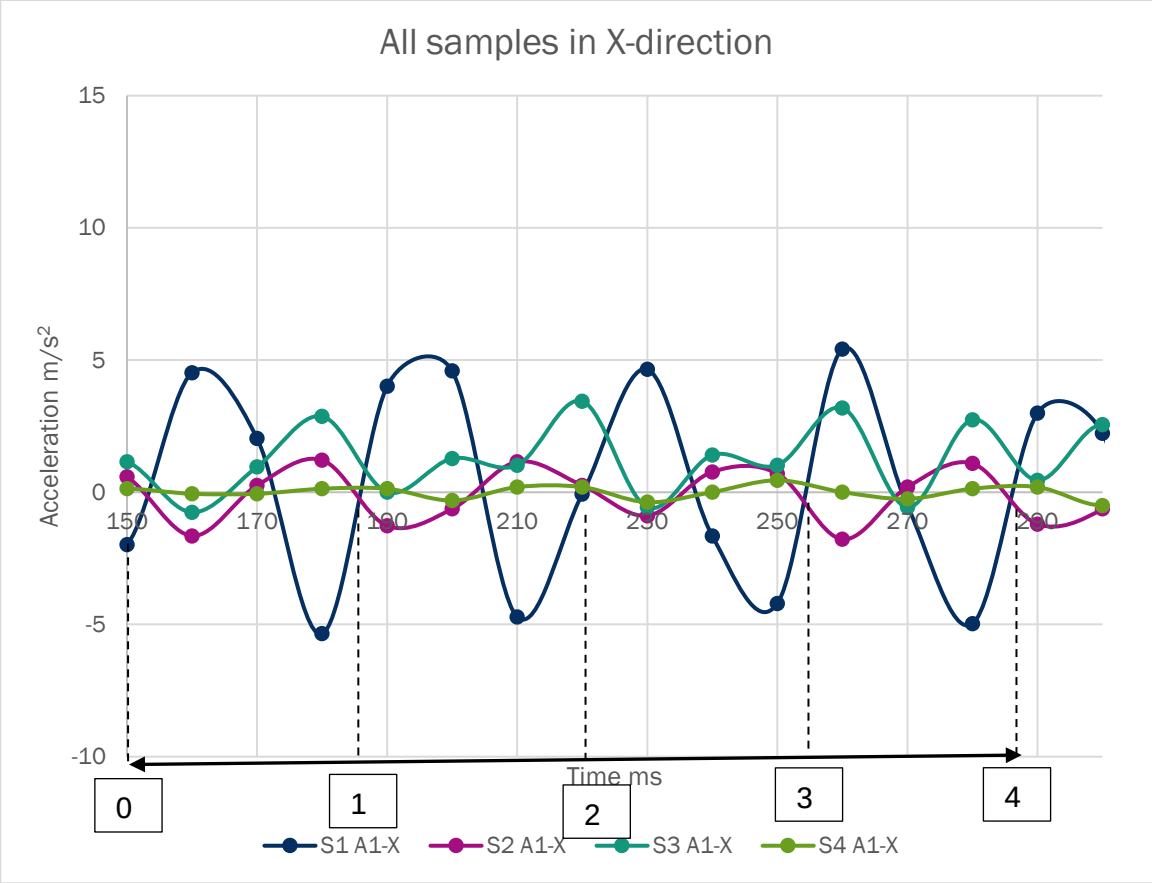


Figure 6.13: Acceleration of all samples in X-direction

An exact frequency of the harmonic wave and peak-to-peak amplitudes can be read from the graph. The chart was isolated from 150-300ms where there is not much noise. From the figure, the frequency of oscillation of the respective samples can be calculated. For all the cases, the frequency is 28Hz and was calculated when averaging the frequencies of the 4 cycles. It is clear that the maximum acceleration is significantly different. The maximum acceleration of each sample has been summarized in Table 6.2.

Table 6.2: Maximum acceleration of all samples

Sample	Max +ve Acceleration / m/s^2	Max –ve Acceleration m/s^2	Average	Frequency /Hz	% Difference
1-Control	13.0	-10.19	0.477033	28	0
2-Sorbothane	5.42	-2.47	0.113125	28	58.4
3-Bitumen	4.14	-1.96	0.29655	28	68.2
4-Bitumen-Sorbothane	3.95	-2.41	0.030184	28	69.7

The results were compared with sample 1 which is considered to be the control in this experiment. From Table 6.2, it is clear that sample 4, which was filled with both bitumen and Sorbothane had the best performance. The maximum acceleration recorded was only 3.9 m/s^2 while the acceleration recorded on sample 1 was 13m/s^2. Furthermore, sample 4 also had the best average compared among all. Sample 3 which was only composed of bitumen was the second best performer with an acceleration of 4.1m/s^2. However, the average value was more than that of sample 2. From Figure 6.14 it can be seen that the waveform is very noisy for sample 3. It should be noted that mass plays a significant role in damping and sample 4 was much lighter compared to the other samples. Mass of the samples can be found in Table 6.4. Overall, all the reinforcement methods helped to decrease the vibration in the samples. The frequency was the same for all the cases.

6.2.3.2 Damping Ratio

Two generic techniques used for solving these vibration control problems are to modify the stiffness, or the fundamental natural frequency of the specified components/subsystems, and their damping (Rivin 2007). An increase in the fundamental natural frequency is usually achieved by increasing stiffness or by

reducing the effective mass of the system.The damping ratio h is roughly determined from the peak value of the curve using the following equation (Tobergte & Curtis 2013):

$$h = \frac{1}{2\rho_{max}} \qquad \text{Eqn(10)}$$

Where, ρ_{max} is the ratio of the amplitude at the top and at the bottom of the sample(a_T/a_B). The recorded acceleration at the bottom was very small when the accelerometer was fixed on the table. The maximum amplitude of the acceleration is 0.3m/s^2 since the maximum output was about 2 units. The raw results (uncalibrated) that are the direct output of the accelerometers are shown in section A.8. Table 6.3 shows the maximum amplitude of the samples once the results have been calibrated.

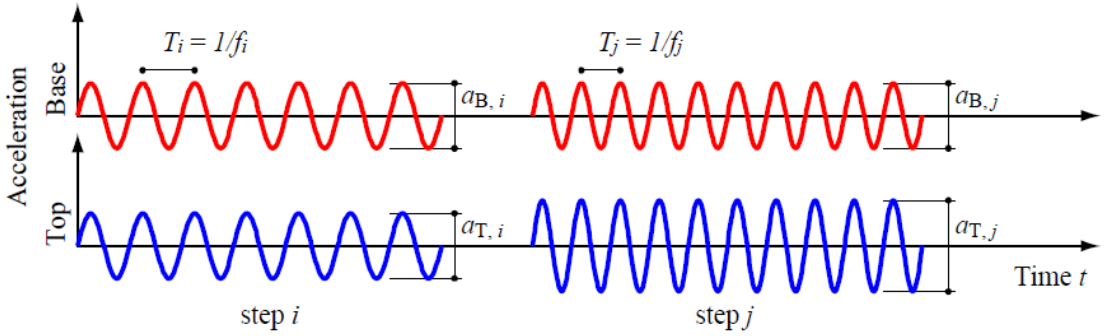


Figure 6.14: a_T and a_B description(Tobergte & Curtis 2013)

Table 6.3: Damping ratio of all samples

Sample	a_T	a_B	ρ_{max}	Damping ratio	% increase
1	13.0	0.3	39.0	0.0128	0
2	5.42	0.3	18.6	0.0268	109
3	4.14	0.3	13.8	0.0362	182
4	3.95	0.3	13.0	0.0384	200

The values of the damping ratio coincide with the acceleration that was recorded. Sample 1, which is the control has the worst performance. A

damping ratio of 0.0128 was calculated. The average increase in damping ratio was 109% when bitumen was added. Sample 4, has the best performance. The damping ratio is about 0.038. The damping ratio increased by 200%, in this experiment. According to Adams & Askenazi (1999), the typical range of metals and concrete structures lie between 0.01-0.05. See Table A.14 in appendix A.8. As it was already concluded in the section above, all the reinforcement methods helped to decrease the vibration in the samples. However, the damping that was provided was impressive. Auto shock absorbers or even rubber have damping ratio of 0.03 and 0.05 respectively, which is very close to the results that was obtained in the experiment.

6.2.4 CONCLUSION OF TEST 1

In terms of the aim of the project, it can be concluded that all the reinforcement methods that were implemented on ballasted helped to stabilise the ballast. The inclusion of bitumen will hugely increase the damping capabilities and reduce settlement of the trackbed. This test was only used to assess the suitability of the materials(bitumen and sorbothane) and their compatibility.

6.3 TEST 2: ERUDITE

Resonant Column Test is commonly used to determine the shear elastic modulus and damping properties of soils. In this method, a cylindrical soil specimen is confined between ends. The test starts by vibrating the cylindrical soil specimen at the top end while the sample is restrained at the bottom. The frequency of vibration is gradually increased until reaching the first-mode fundamental frequency of the sample. In this section, a similar test will be

used. ERUDITE, electronic resonant frequency system which is most commonly used to determine the Poisson's ratio (υ), the modulus of elasticity (E) and the modulus of rigidity (G) of materials is very much the same as the PUNDIT except it uses vibrations instead of wave pulse velocities. Hence, this equipment is used for Quality control of manufactured concrete and to monitor concrete that is damaged by weather exposure. When the maximum specimen vibration amplitude is reached, this corresponds to the resonant frequency. Hence, the Longitudinal, Transverse and Torsional Resonant Frequencies of specimens could be determined. One of the disadvantages of the ERUDITE equipment is that it has low movability and this makes it not very suitable for in-situ testing. The test is performed by positioning an acoustic vibrator at one side of the specimen and mounting an accelerometer on the other. Then the generator drives the acoustic vibrator at a given frequency, while the accelerometer records the vibration of the specimen. The frequency generated is constantly varied until the maximum amplitude of the specimen is reached. At this point, the specimen is driven at its resonant frequency (f_n). After the test is performed, the results can be used to estimate the inverse of Damping Coefficient, Q.

The higher the ability of the sample to prevent dissipation of waves, the higher the ERUDITE resonant frequency is. This is due to the fact that the vibration takes more time to move through the sample. The same samples which were used in test 1 were used again. Since the sample is not a pure material, it can be difficult to judge the suitability of this test. To reduce errors, each sample was tested 5 times, and after each attempt, the sample was placed on a

vibrating table to re-orientate the materials inside the samples. A highly stable variable frequency sinewave oscillator is emitted until the resonant frequency of the sample is reached. The following settings have been used for the test. From Chapter 4 results, a maximum frequency of 8kHz was set. Setting for the equipment is shown in Table 6.4.

Table 6.4: ERUDITE Setting

Starting frequency	1.00 Hz
Ending frequency	8 kHz
Voltage output	0.01V
Steps	5Hz

The equipment was powered on 10 minutes prior to the start of the test for thermal stability. Grease was then applied to the ends of the vibrator and sensor contact rods. The results have been tabulated in Table 6.5.

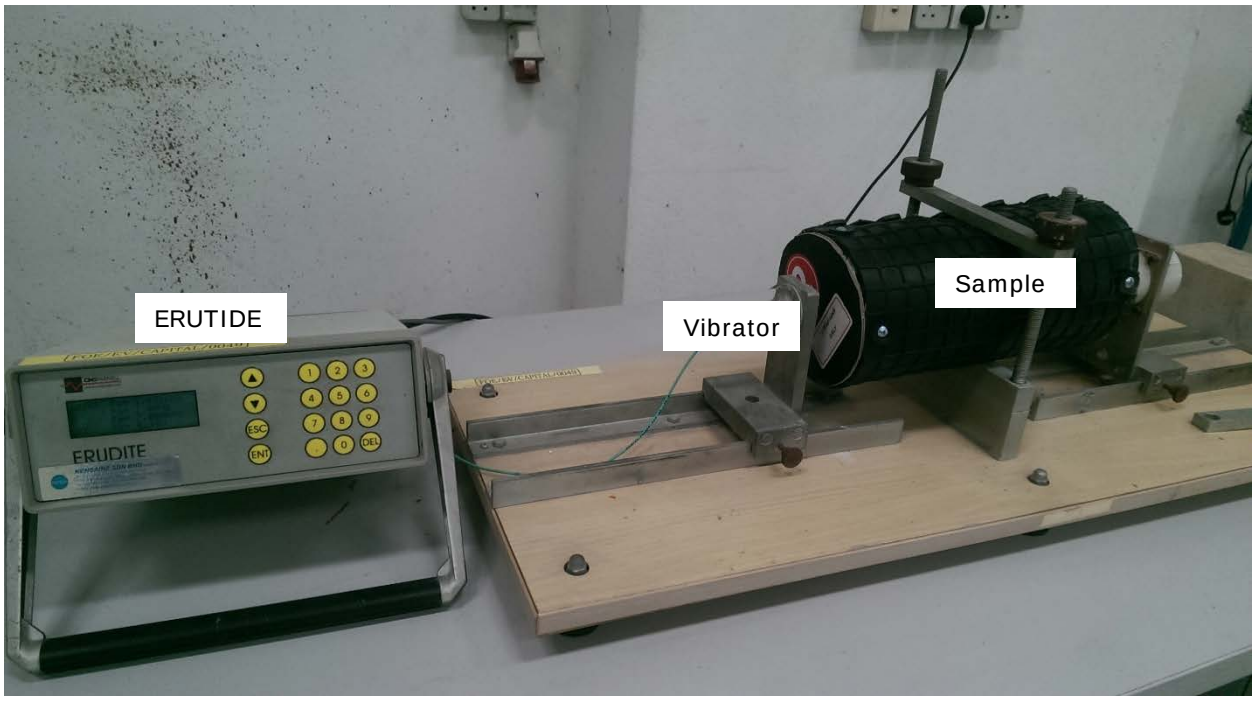


Figure 6.15: ERUDITE equipment

6.3.1 RESULTS AND DISCUSSION

The outputs of the tests are: F_r, F_1, F_2 and Q. Where F_r resonant frequency and Q is the damping constant of the sample calculated from two 3dB frequencies: frequencies on either side of the resonant frequency where the amplitude of vibration drops to 0.707 of the maximum amplitude. f^1, f_2 = frequencies at either side of f_r at which the amplitude drops to 0.707 fr (the 3 dB frequencies).

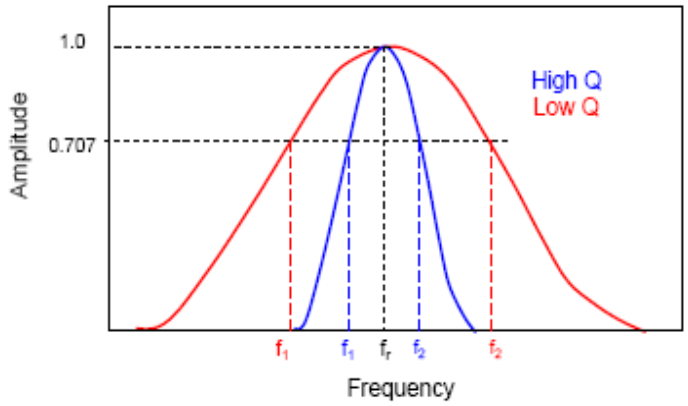


Figure 6.16: Relationship between F_r, F_1, F_2 and Q

When the specimen is driven at f_r the vibration amplitude is at maximum. The damping constant is often a better guide to the "quality" of the material than the dynamic modulus.

Table 6.5: ERUDITE Results

Sample	SSD Mass/ kg	Density/ kgm-3	Quantity	Erudite Results			
				Trial 1	Trial 2	Trial 3	Trial 4
1	6.36	1199	Fr /kHz	1.761	0.1011	0.571	1.461
			F1/kHz	0.616	0.076	0.196	1.454
			F2/kHz	3.246	0.246	3.841	1.736
			Q	0.67	0.59	0.16	5.13
2	6.17	1163	Fr /kHz	1.516	3.946	3.986	1.446
			F1/kHz	1.501	3.921	3.27	1.196
			F2/kHz	1.651	4.046	4.33	1.956
			Q	10.11	31.57	3.76	1.9

3	7.47	1409	Fr /kHz	7.696	5.341	4.55	6.561
			F1/kHz	7.546	5.311	4.501	6.521
			F2/kHz	7.856	5.601	4.721	6.731
			Q	24.83	18.42	20.6	31.24
4	6.78	1279	Fr /kHz	0.231	1.461	0.641	0.311
			F1/kHz	0.201	1.421	0.611	0.301
			F2/kHz	0.401	1.631	0.891	0.491
			Q	1.15	6.96	2.29	1.64

6.3.1.1 Damping

From the results in Table 6.5, it is clear that the results are not very consistent which tend to imply that the test was may not be appropriate. This may be because of the samples that were tested was not a pure material and contained a lot of voids. It was Sample 3 that provided the consistent results with an average Q value of about 20-30. The lowest value of Q was used for calculations. The is probably because this sample was filled with bitumen and the number of voids were limited. Sample 4 was also filled with bitumen but might contain more void because of the presence of sorbothane than will act as a barrier and prevent bitumen from adequately adhering and forming a continuum structure. It should be noted that when bitumen is used, the damping coefficient increases, however, due to the significant increase in sample mass, it is not a wise option. Even though the results seem imprecise, calculations were carried forward. Using the formula for damping in a single-degree-of-freedom system(Eqn 10), the damping ratio was calculated.

$$h = \frac{Q}{2\sqrt{mk}} \qquad \text{Eqn(10)}$$

h is damping ratio,

Q is damping coefficient,

k is spring constant,

m is the mass of the sample.

Values for the spring constant obtained from Test 3.

Table 6.6: Damping calculation from ERUDITE

Sample	**K/ Nmm^{-1}**	**Lowest Q**	***h***
1	37	0.16	0.005
2	21	1.9	0.083
3	81	18	0.366
4	23	1.15	0.046

Results from the Test 1 and Test 2 seem to be very close to each other for samples 1, 2 and 4. For sample 3 on the other hand, the damping ratio that was obtained from the ERUDITE test was too high. Since mass of the system was not considered in test 1, Sample 3 might hot have moved by much. This may have given the wrong impression that Sample 3 has good damping properties while in reality, it was because of the weight that the sample did not move. Sample 4 also contained bitumen but was significantly lighter(see table 6.5). However, both tests come to the same conclusion that inserting bitumen or sorbothane inside the samples will improve the damping properties. Additional test and additional calibrations might be necessary in order to account for the testing condition and to achieve reliable results.

6.3.1.2 Frequency

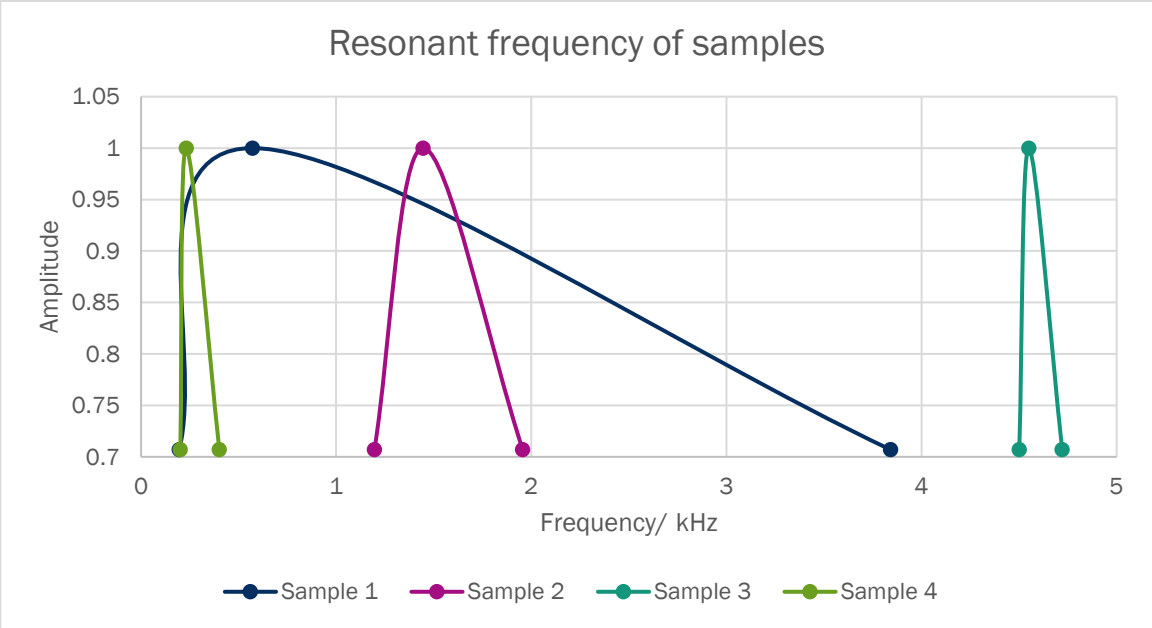


Figure 6.17: Resonant frequency of samples

From Figure 6.17, it can be concluded that the spread of frequency for sample 1 is very large compared to the other samples. Please note that once again, the lowest value was used for plotting the graphs. Sample 3 was the densest among all and the frequency that would cause the sample to have the highest amplitude is much higher. Sample 4 also contained bitumen but has a much lower resonant frequency. From the results of the ERUDITE test, it can be concluded that the test may not be appropriate because of the large variation of the data that was obtained on different trials. For future reference, it is recommended not to conduct ERUDITE test on granular materials even though the test is similar to the resonant column test that is extensively used in geotechnical engineering.

6.3.2 CONCLUSION OF TEST 2

In terms of the aim of the project, test 2 would have allowed to more accurately quantify which type of reinforcement is the best under higher frequency. However, the results obtained from test 2 were very diverse, and it is difficult to judge the suitability of using ERUDITE test on granular materials. Therefore, to be conservative, this test did not yield conclusive results, and another method must be used in the future.

6.4 TEST 3: CYCLIC-COMPRESSIVE TEST

The purpose of the static tests is to identify and shortlist the number of samples since only a limited amount of large box tests can be conducted. It is assumed that the load transmitted from a sleeper to the ballast approximately coincides with the cone distribution and this assumption was validated by numerical results and from experimental field testing (Zhai et al. 2004). Therefore, a compressive test should be appropriate to test the strength of the cell. The sample's diameter is measured and averaged to obtain the cross-sectional area. The sample is placed at the centre of the cyclic compression testing machine. The machine was set to have a cyclic loading of 0-1kPa, and the loading frequency was set to 1.3 Hz owing to the limitation of the machine. It should be noted that the frequency of loading is not being tested but the amount of plastic deformation under cyclic. In other words, the amount of settlement that the samples will undergo under repeated loading. This test aims to assess the stiffness and compressive strength of the samples and the lateral confinement that will be provided when geocells are inserted.

6.4.1 PREPARATION OF SAMPLE 5-10

The test to assess the stiffness and compressive strength was conducted using the 4 samples that were previously used in Test 1 and Test 2, and a further 5 samples were constructed in order to test for the influence of the geometry of the geocell with respect to the settlement and dissipation of lateral load.

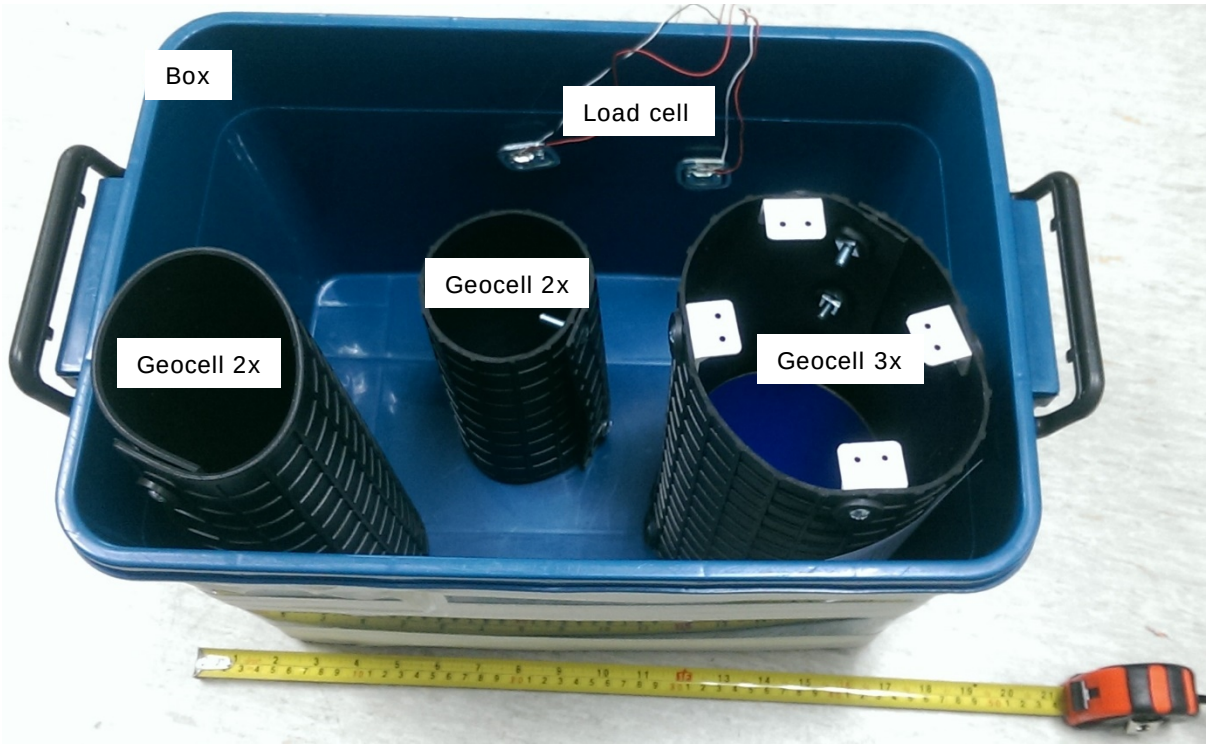


Figure 6.18: Box for cyclic compressive test for samples 5-10

Regarding the other 5 samples, a plastic box of 450mmx300mmx300mm, was filled with ballast, and a load cell was attached on the inner side of the wall. A wooden sleeper of size 100mmx150mmx50mm was used for the load transfer. The load cell was placed between 2 pieces of plastic with very small friction coefficient, one of which is the box wall. The box was reinforced with heavy duty adhesive tapes in order to minimise expansion of the plastic box. During

previous similar experiments carried by Raymond (2002), appropriate reinforcement of wall has proven to increase reliability of results. Leshchinsky et al. (2013) have successfully tested different configuration of geocell layers in similar tests conducted on gravel, 20mm in size. The particle size distribution that was used in the test conducted by the latter contains more than 20% of particles that pass through a 15mm aperture and was did not model the particle distribution of ballast used in railway construction. Furthermore, the model embankment that was used was not scaled, like the gravels. Therefore, different configurations were tested using ballast in a scaled box are shown in Table 6.7. Figure 6.19 illustrates the testing process.

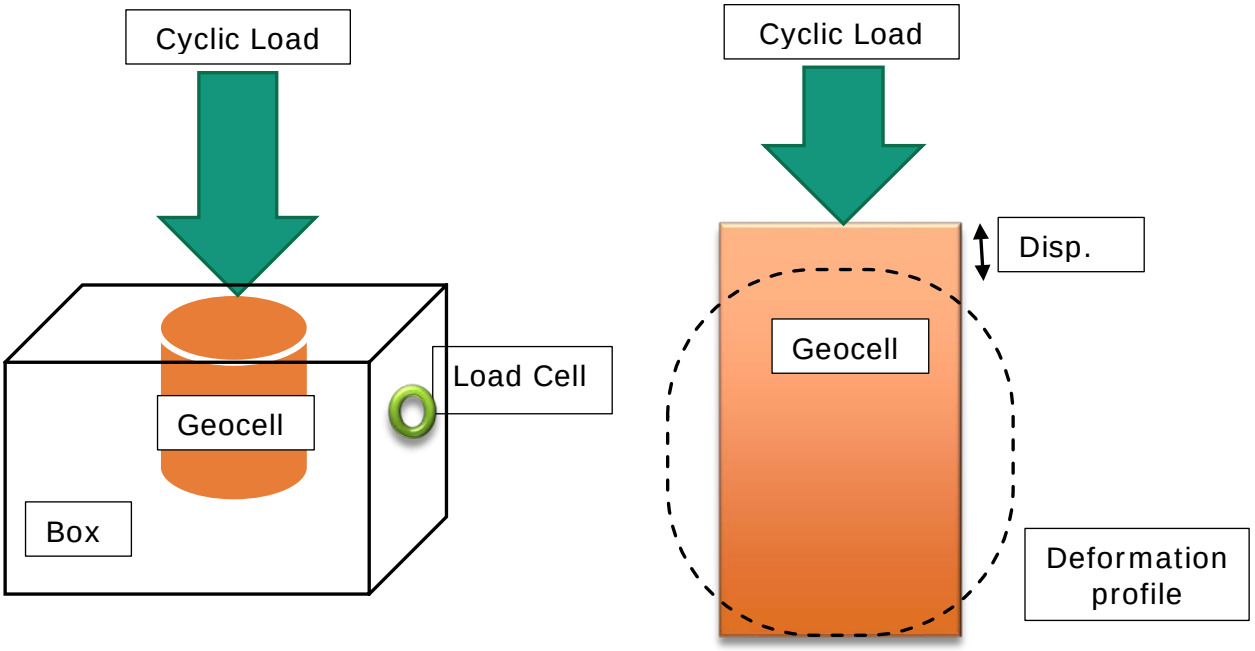
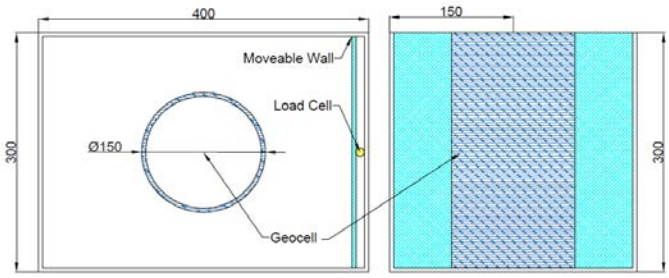
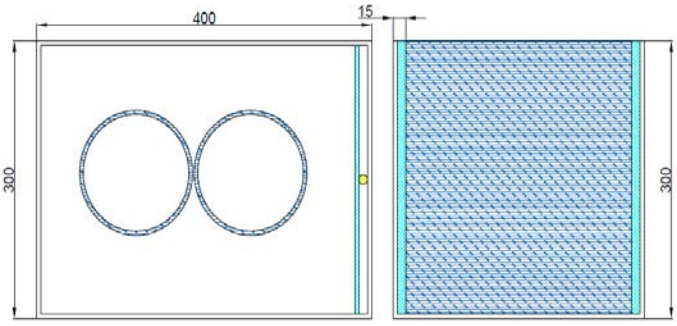
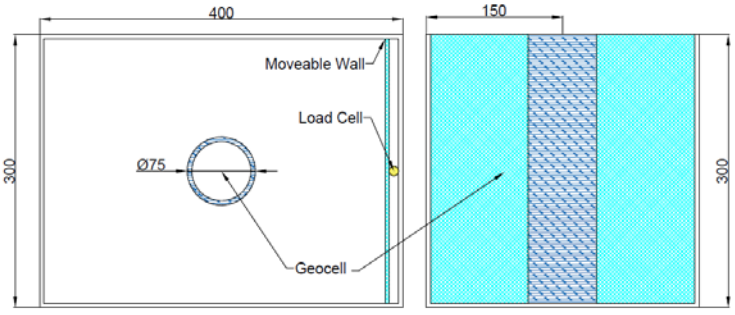
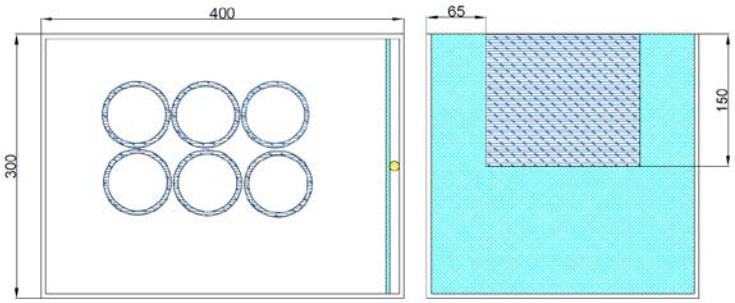
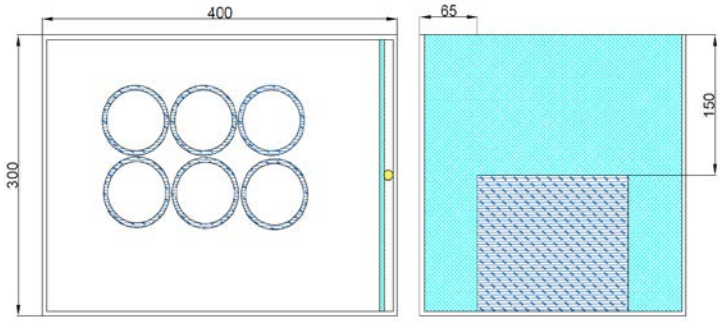


Figure 6.19: Samples under applied load

Table 6.7: Sample Configuration for samples 5-10

Sample	Diagram	Description
5	Control	Box filled with ballast only
6	 Plan View Side View Figure 6.20: Sample 6	Sample 1-4 were placed in the plastic box in the same order
7	 Figure 6.21: Sample 7	Multiple geocell, with diameter 3x ballast size
8	 Figure 6.22: Sample 8	Single geocell with diameter 2x ballast size

9	 Figure 6.23: Sample 9	Multiple geocell with diameter 2x ballast placed on top
10	 Figure 6.24: Sample 10	Multiple geocell with diameter 2x ballast placed at the bottom

6.4.2 TESTING

Several researchers(Aursudkij et al. 2009; Lackenby et al. 2007; Suiker et al. 2005) have used the large scale Triaxial test to conduct tests on ballast. Even though, the confining pressure that the triaxial tests apply is said to mimic the mean geostatic stresses due to particle interaction, it should be noted that ballast is unbound. Lateral force provided by the rubber is negligible since the young modulus of the material was only 0.01GPa.



Figure 6.25: Unbounded sample test for sample 1-4

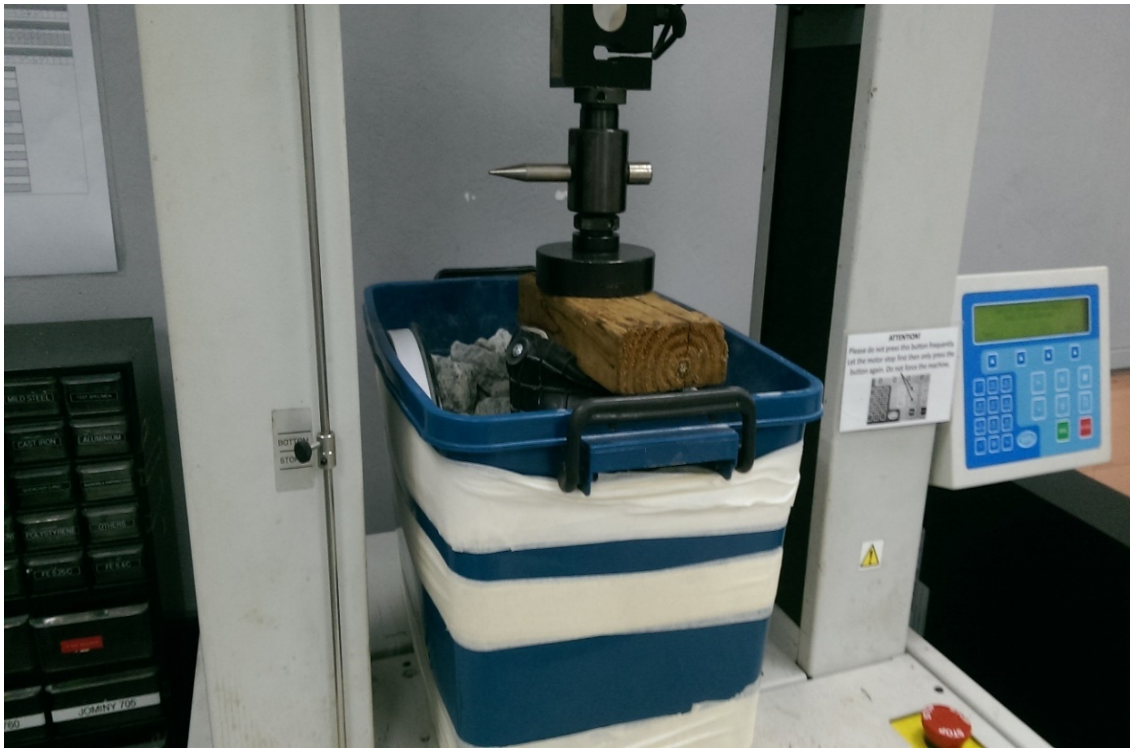


Figure 6.26: Cyclic Box test for sample 5-10

Figure 6.25 and Figure 6.26 show the unbounded samples and small box test respectively. Data was recorded under increasing loads in order to assess the behaviour of the specimen under pure axial load. It is noted that the cylinder needs to be placed at the centre to ensure the load is distributed evenly throughout the cell as the maximum compressive strength can be tested and generated in the computerized form, which gives a stress-strain graph and the ultimate compressive strength.

6.4.3 RESULTS AND DISCUSSION

The deformation under the cyclic load and the corresponding lateral pressure that were recorded for all the samples presented in Table 6.8.

Table 6.8: Compression test results for samples 1-10

Sample	Maximum Displacement after 1st cycle /mm	Maximum Displacement /mm	K / Nmm^{-1}	Maximum Lateral Load/N	Initial Lateral Load/N	% Decrease After 1st cycle
1	25.7	30.8	37	No lateral load to calculate for samples 1-4		
2	41.9	84.3	21			
3	14.1	19.1	81			
4	33.3	52.2	23			
5	9.97	14.3	99	34	92	-63.0
6	18.4	49.2	51	53	42	26.2
7	7.5	7.6	131	57	39	46.2
8	21.2	33.3	45	53	36	47.2
9	16.7	27.7	53	42	29	44.8
10	15.4	25.6	62	42	37	13.5

6.4.3.1 Stiffness

Permanent deformation of granular materials follows a logarithmic pattern under both axial and shear loading (Chen 2013; Chan 1990). It is known that permanent deformation generated in the first cycle could be used to predict plastic strain development. Hence, the 1st cycle was used to calculate the spring constant for all the samples. A nonlinear spring, like Sample 3, has a nonlinear relationship between force and displacement. A graph showing force vs. displacement for a nonlinear spring will be more complicated than a straight line, with a changing slope. However, since the spring constant is a function of force, a linear relationship was assumed for the 1st cycle. Figure 6.27 shows the force-extension of sample 1-4. A simple relationship between force and extension was used to calculate the stiffness: The stiffness of the sample is equal to the force required per unit displacement for the 1st cycle and is shown in Table 6.8. The complete result of the experiment can be found in Appendix A.9. In order to interpret the data more efficiently, the only the initial settlement and final settlement is shown in Figure 6.28.

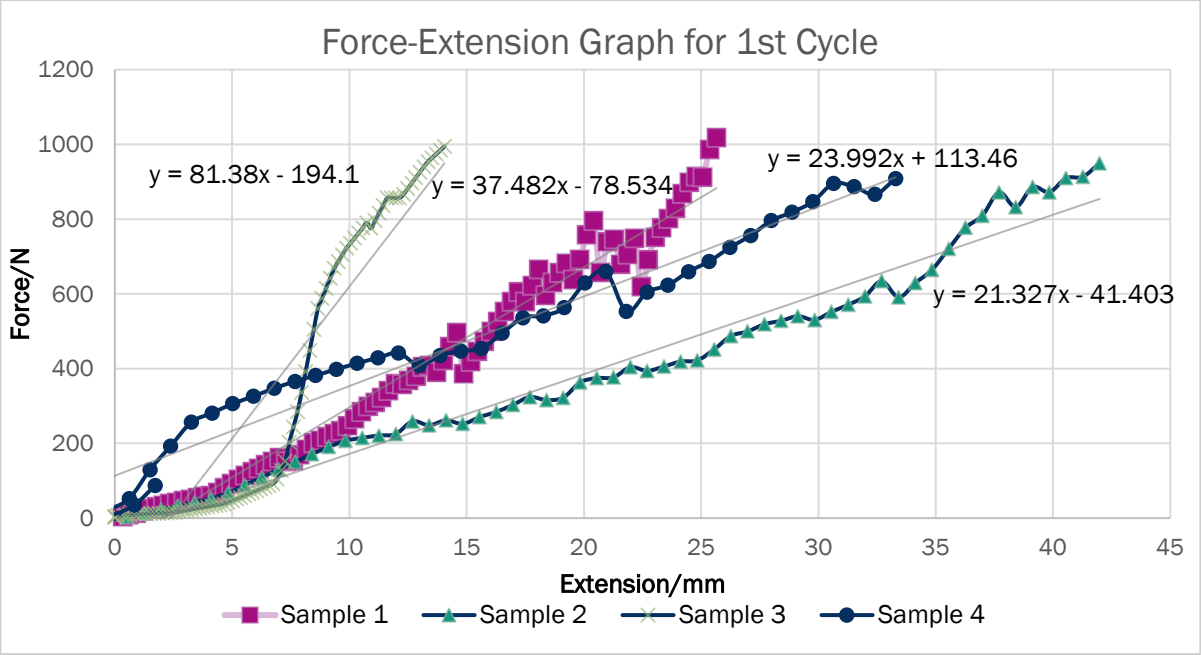


Figure 6.27: Force-extension graph for 1st Cycle for samples 1-4

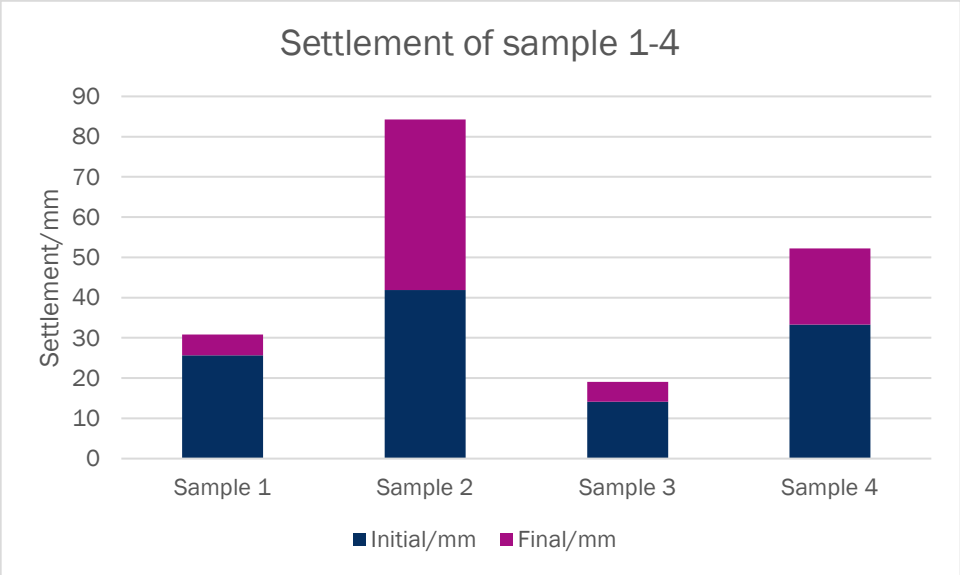


Figure 6.28: Settlement of samples 1-4

For the unbounded samples, these results prove that the reinforcement did have a significant effect on ballast. Unbounded sample 2 and 4, which

contained sorbothane material, had the worst performance in the compressive test. This was due to the reduction in interlocking between ballast that sorbothane material provided.

Bitumen has increased the bearing capacity, and an approximate reduction of 50% in settlement was provided. A stronger adhesive should be provided to resist this static compressive load. Even though sample 4 also contained bitumen, it can be said that the interlocking effect that sorbothane sheet prevented is much more influential to the system than the adhesive effect of bitumen. The stiffness increase that bitumen provided was more than 200% when compared to sample 1 while sample 2 and 4 decreased the stiffness by 50%. However, the main purpose of the geocell was to provide lateral confinement, and this effect is discussed in the next section.

6.4.3.2 Lateral confinement

Figure 6.29 shows the lateral force that was recorded by the load cells which were attached to the wall of the box. See Figure 6.19.

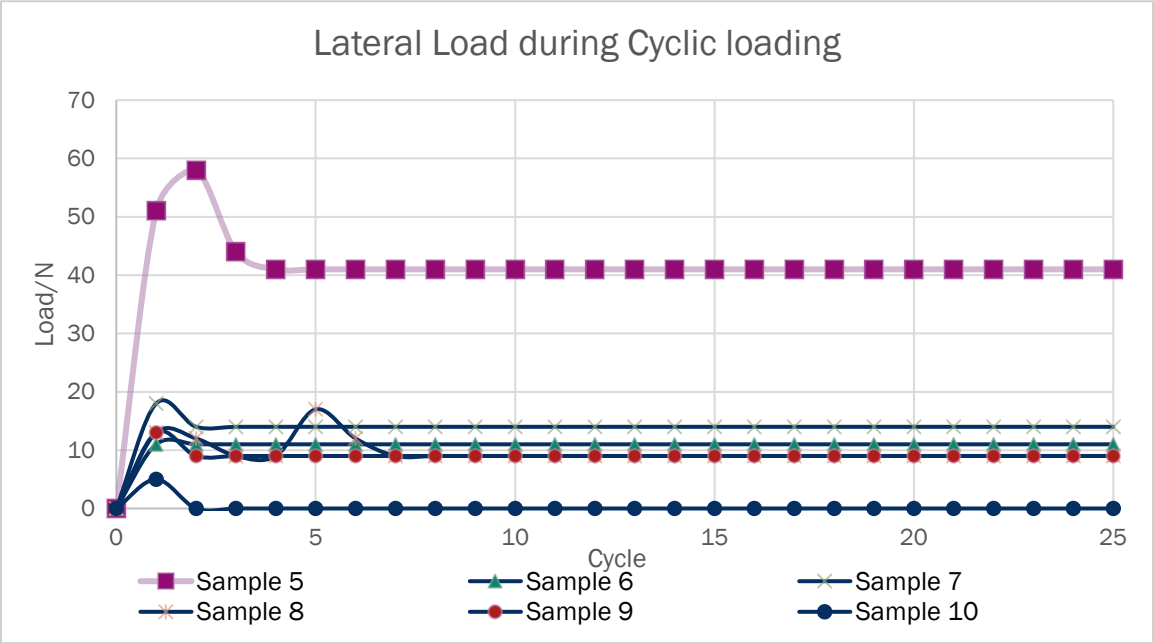


Figure 6.29: Lateral Load during Cyclic loading

According to Chebli et al.(2008) who recorded field data from high speed lines, the lateral force is 20% that of the vertical load. In this low-frequency cyclic test, the lateral load recorded for the control was approximately 5% that of the vertical load. Therefore, the frequency of loading is an important factor that needs to be considered. Sample 5 which is the control in this experiment experiences the highest lateral load of 60N. It is clear that lateral confinement reduced the amount of lateral load that acts on the wall. Sample 10 which consisted of geocell with diameter 2x the ballast diameter placed on top, offered the best performance in reducing the lateral load. In all the cases, the maximum value was observed during the 1st cycle. Lateral load was unchanged

afterwards. Even though a significant amount of decrease in lateral load was observed, the settlement was not greatly reduced.

From Table .6.8, Sample 7 which consisted of 1 geocell having a diameter 3x that of ballast diameter and a length of 300mm, reduced settlement the most. A settlement of 7.5mm was observed compared to 9.97mm when unreinforced. All the other reinforcement schemes increased the settlement by 2-3 times. When comparing samples 6 and 8, it was concluded that the geocell should have an ideal diameter so that no much void is created in order to reduced lateral load on the wall, and should be as long as possible in order to reduce vertical settlement. Settlement and lateral load decreased with the increase in the amount of geocell in all the cases. Performance was better when the geocells were placed near the sleeper (sample 10) than at the bottom (sample 9) in terms of settlement and for long-term lateral load. Lateral load returned to its initial value of 0N after the 1st cycle for sample 10, and a maximum decrease of about 1100% in lateral force was observed when comparing the control with sample 10. The diameter of the geocells affects the amount of ballast that was inside the cell and created a lot of voids, hence, causing large settlement.

6.4.4 CONCLUSION OF TEST 3

It was concluded that inclusion of geocells would indeed decrease the lateral force and prevent settlement by ballast migration. Stiffness was increased hugely when bitumen was placed inside the geocell, but the later reduced interlocking between the particles if an inappropriate diameter of geocell is used. Therefore, the vertical stability of the track can be increased by bitumen

while geocell increases the lateral stability. In the next test, bitumen and geocell will be used at the same time and places under high-frequency loading in order to evaluate its effect when high-speed trains run on the reinforced track.

6.5 TEST 4: LARGE SCALE BOX-TEST

In order to verify the statement, a parametric study which involves the loading reinforced ballast with different frequencies is performed in this test. McDowell et al. (2014) performed a box test (250mm×300mm×150mm) where ballast was cyclically loaded with a sinusoidal load pulse with a minimum load of 3kN and a maximum load of 40kN, at a frequency of 3Hz. The subgrade was modelled with 10 mm of rubber. However, the experiment was not completed successfully because of a failure at the joint of the box. Full-scale tests at the railway test facility(RTF) of the University of Nottingham was also conducted, and the results (resilient modulus and axial strain) were coherent when they were compared with the box test. The pit for the RTF was filled with approximately 900mm of silt and 300mm of ballast. The equipment can produce sinusoidal load control at 3Hz between 4kN and 94kN, the cyclic frequency that simulates ‘high-speed’ train travel, namely 20 Hz with a phase difference between actuators and can last for six million cycles. Three 100kN actuators are fitted under deep beams which span the width of the pit and these are aligned with three sleepers which are placed on the ballast at a lateral spacing of 650mm. Figure 6.30 shows a diagram of the RTF and how the geocell reinforcement could be tested. However, due to unavailability of the equipment, only the critical region, directly underneath the sleeper, of the

track was modelled. Woodward et al. (2012) performed similar cyclic loading tests on reinforced ballast using XITRACK placed in a steel tank of size 1000mmx3mmx1150mm using the GRAFT I facility. Trustworthy results were obtained from this box test since their reinforcement schemes than were implemented in more than 15 locations. From the results obtained from the finite element analysis in Chapter 4, it can be deduced that the frequencies that are being applied in current tests are too small, to simulate the real behaviour of ballast under traffic loading. Nimbalkar (2015) conducted a triaxial test on ballast under high-frequency loading and concluded that the frequency of loading had a significant effect on the permanent deformation and degradation of ballast layer. However, vibrations and structure-borne noise mainly occur at lower frequencies below 50 Hz at higher frequencies these vibrations attenuate increasingly rapidly. To observe this effect, the frequency was set to a maximum of 20 Hz.

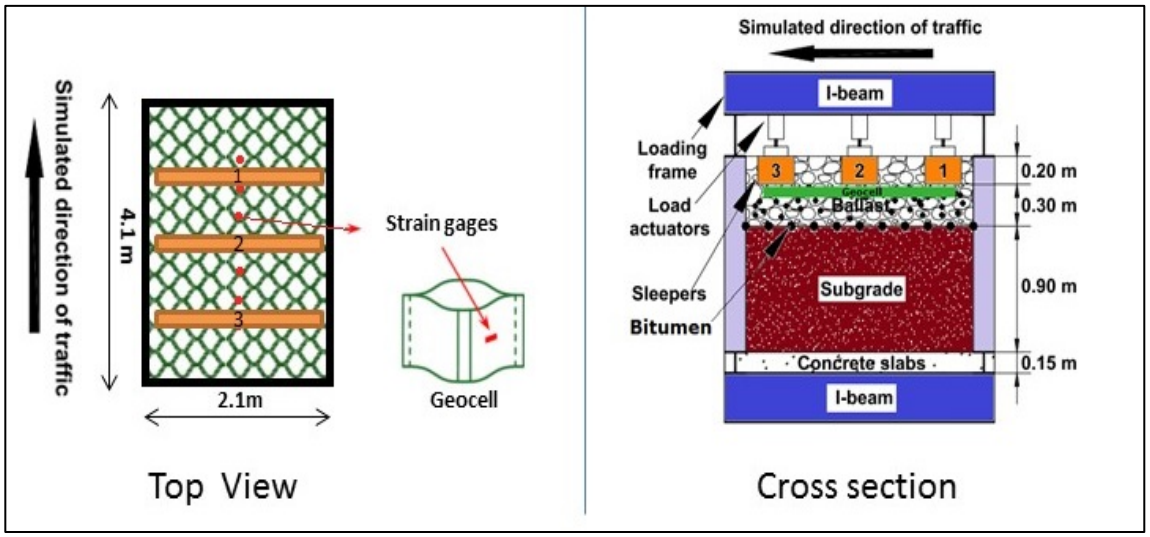


Figure 6.30: Railway Test Facility(S F Brown et al. 2007)

To validate the numerical model and study the long-term behaviour of the reinforcement, an accelerated scaled testing needs to be performed with high-frequency loads. The box test was devised by Norman and Selig (1983) in which the settlement of the sleeper, volumetric and density changes and stiffness of ballast were investigated during cyclic loading. Lim & McDowell (2005) further developed the test to simulate the effects of tamping on the performance of ballast. Both resilient and permanent behaviour of ballast were investigated. Suiker et al. (2005) have conducted static and cyclic Triaxial testing on ballast and found that under cyclic loading, the granular matter compacted much more when compared to the static test. This behaviour results in a significant increase in material stiffness and strength. Similar experiments were carried out by S. F. Brown et al. (2007) to test the efficiency of reinforcing ballast by using geogrid by using a Composite element Test. It was concluded that the relationship between resilient stiffness at low stain and low tensile strength of the geo-grid was non-linear.

A new full-scale laboratory box test is developed to study the performance of both unreinforced and reinforced railway track substructure systems. Since only a limited amount of samples can be tested due to the large amount of labour required, the results from Test 3 are used. Only 3 Boxes will be tested where Box 1 is just filled with ballast and Box 2 has geocell with a diameter of 2x the ballast size and a length of 150mm placed on top. Box 3 had both geocell with the geometry described for Box 2 and had bitumen poured inside. 18L of bitumen was required for the test. Lateral loads cannot be calculated from this test due to the enormous load that the actuator applies. The cell load

that was provided only could support a maximum load of 500N each. Figure 6.31 shows a graphical representation of the Box.

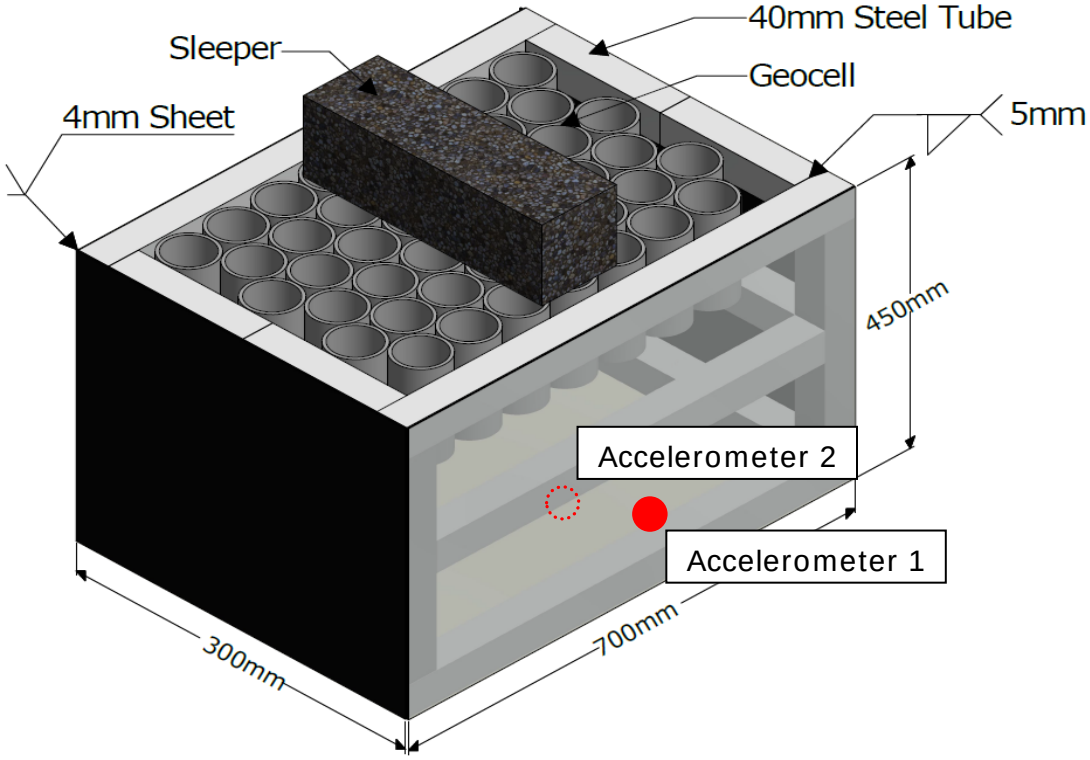


Figure 6.31: Large-Scale box test

A sinusoidal load is applied directly to the ballast by a servo-controlled hydraulic actuator, which will simulate the passage of a moving wheel. The metal frame was filled with ballast in 3 layers, and each one was compacted manually. 10mm of rubber was placed inside the box to act as subgrade. Two accelerometers were placed: one at the bottom of the box and one was placed 150mm from the bottom of the box. The accelerometers are used to access the damping properties of the reinforcement and the efficiency in preventing ground-borne vibrations. The range of frequencies that the samples that have been tested with are listed and detailed in Table 6.9.

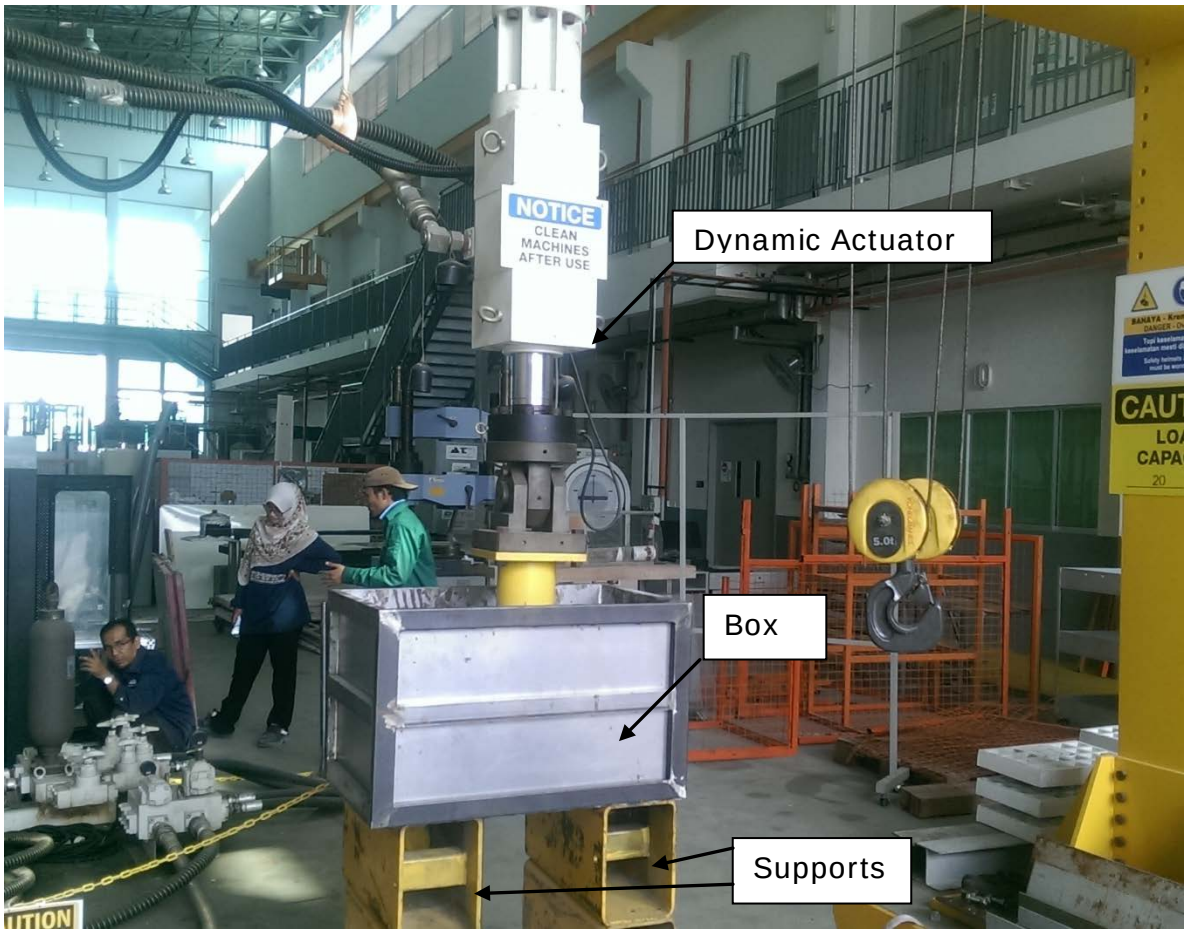


Figure 6.32: Box test setup

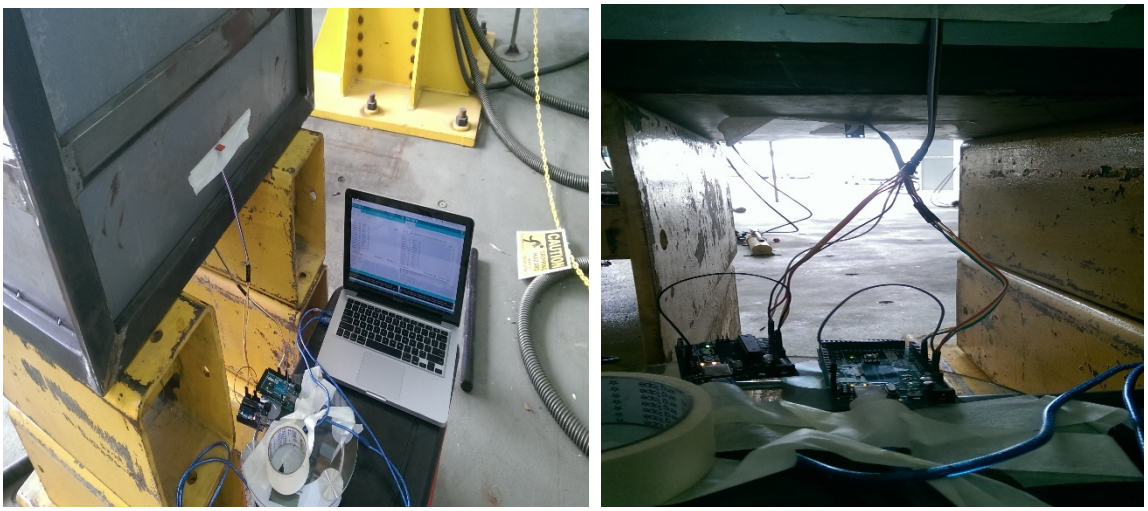


Figure 6.33: Accelerometer location

Table 6.9: Large-scale Box test sample details

Sample	Photograph
Box 1: Control	 Figure 6.34: Box 1
Box 2: Geocell	 Figure 6.35: Box 2

Box 3: Geocell and Bitumen	 Figure 6.36: Box 3

The photographs of the 3 samples can be seen in Figure 6.34, Figure 6.35 and Figure 6.36. The samples were tested through a range of frequencies namely: 2Hz, 6Hz, 12Hz, 15Hz and a maximum of 20Hz.

6.5.1 RESULTS AND DISCUSSION

Table 6.10: Large-scale box test results

Sample	Maximum Settlement /mm	Max. accelerometer output 1/units			Max. accelerometer output 2 /units		
		X	Y	Z	X	Y	Z
Control @2Hz	3.2025	0	2	0	0	2	0
Control @6Hz	0.9487	4	6	13	4	9	7
Control @12Hz	2.0870	3	9	7	11	11	5
Control @15Hz	1.2714	7	9	4	2	7	3
Control @20Hz	0.9039	13	10	5	2	11	3
Geocell @2Hz	13.31	2	0	2	4	11	2
Geocell @6Hz	1.6299	5	5	2	3	1	6
Geocell @12Hz	1.1730	6	3	2	2	8	2

Geocell @15Hz	1.099	7	3	3	2	5	3
Geocell @20Hz	0.9880	14	4	6	2	12	4
Geocell and Bitumen @2Hz	7.1813	2	2	0	4	0	0
Geocell and Bitumen @6Hz	0.9257	4	5	9	2	6	4
Geocell and Bitumen @12Hz	0.7709	7	6	15	4	11	4
Geocell and Bitumen @15Hz	0.6446	4	7	4	2	9	5
Geocell and Bitumen @20Hz	0.6399	4	3	10	1	8	3

Table 6.10 shows the maximum displacement that the actuator has to undergo before reaching a load of 10 kN. The maximum output recorded by both accelerometers in all 3 directions have also been tabulated in Table 6.10. Figure 6.37 shows the axis of the accelerometers. Please note that the values were not converted into acceleration in order to increase the accuracy. Since the results are compared relative to each other, the raw outputs of the accelerometers were used for discussion. All the results of the tests can be found in Appendix A.10.

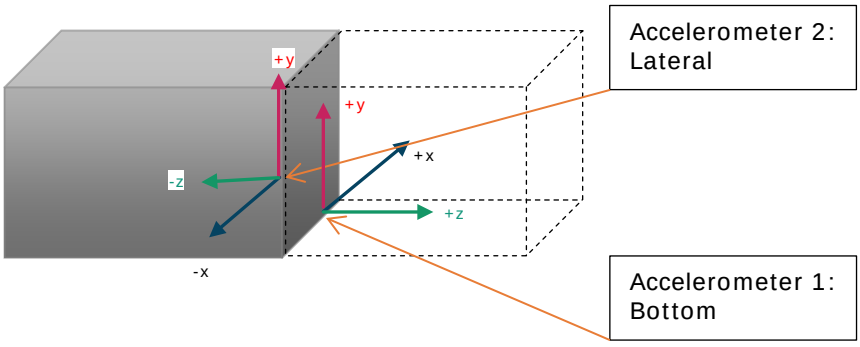


Figure 6.37: Accelerometers axis

6.5.1.1 Settlement

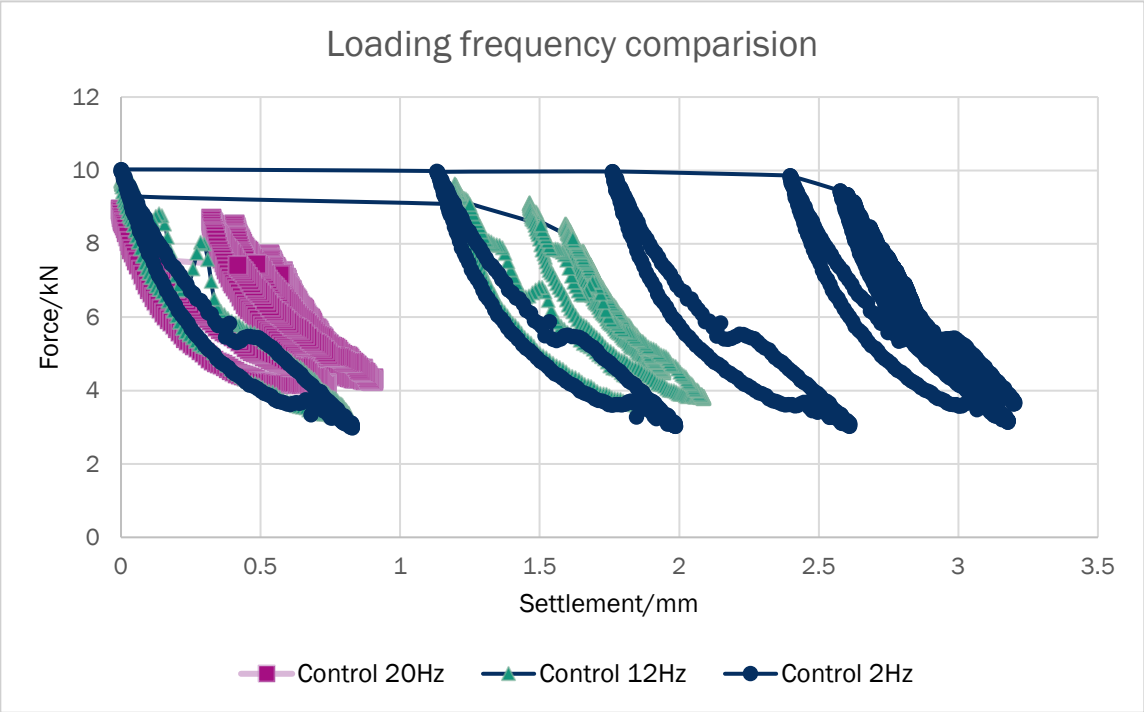


Figure 6.38: Loading frequency comparison

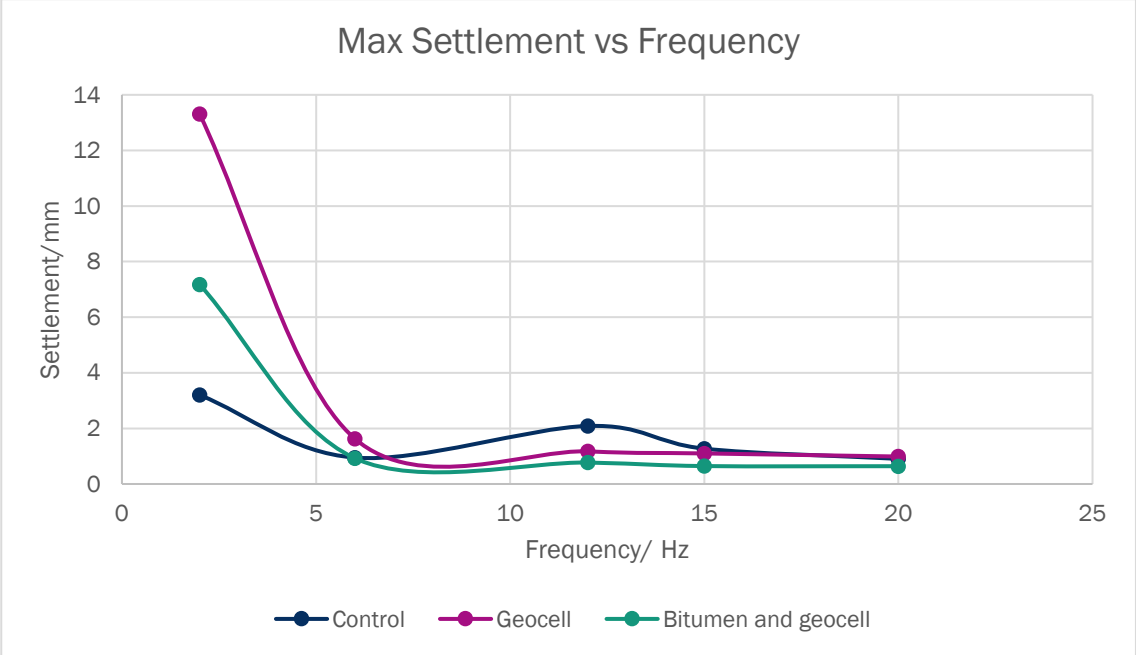


Figure 6.39: Settlement vs frequency

Figure 6.38 shows the settlement that occurred for the unreinforced sample(Box 1) when the load was varied from 3kN to 10kN with different frequencies. In order to make the results clearer, the results were plotted in intervals of 200 cycles up to a total of 1000 cycles. The higher frequency with is 20Hz caused the less settlement. A maximum displacement of 3.2mm, 2.09mm and 0.90mm was observed for box 1 with a loading frequency of 2Hz, 12Hz and 20Hz respectively. Owing to the limitation of the machine, the frequency could be increased to a higher value, even though the values of frequency calculated in Chapter 4, were around 1.6kHz for a vehicle running at 20m/s. The results confirm that the higher the frequency of loading, less settlement is expected. The maximum settlement of the other boxes have been plotted in Figure 6.39, and it is clear that the trend is similar for the reinforcements as well.

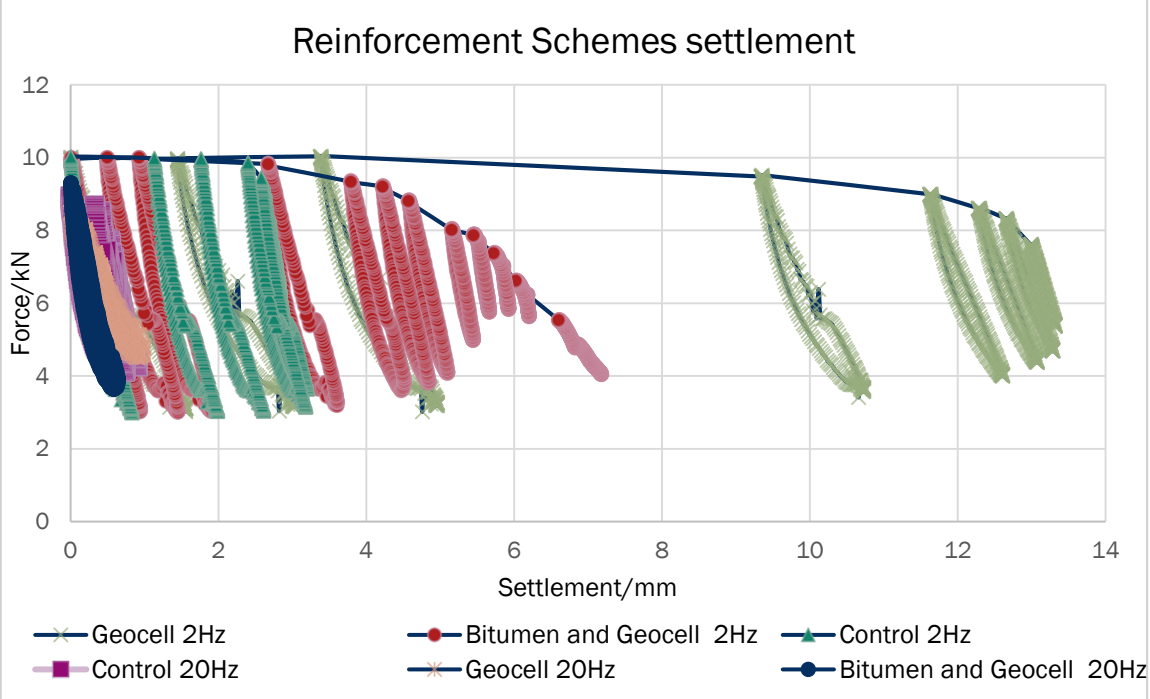


Figure 6.40: Comparison of reinforcement settlement

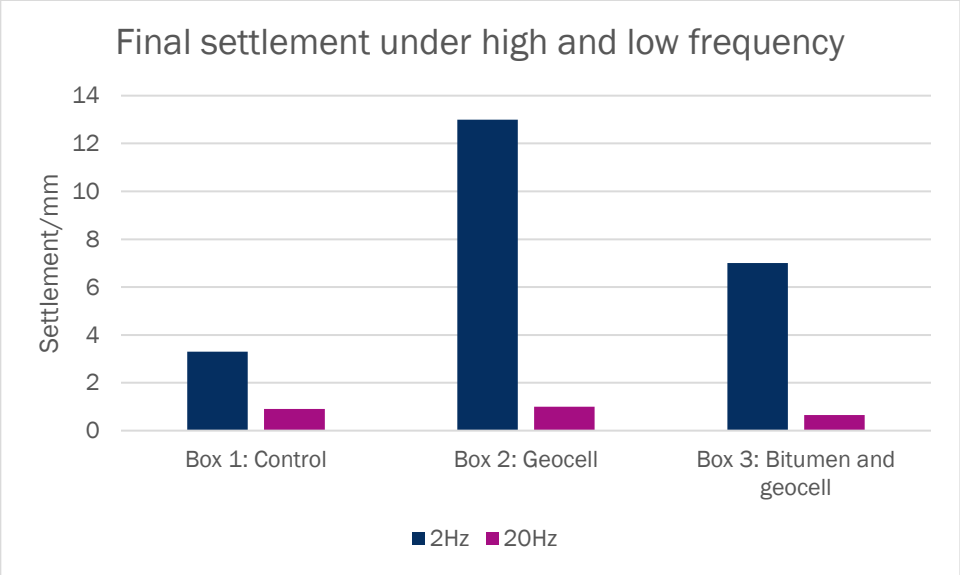


Figure 6.41: Final settlement under high and low frequencies

Figure 6.40 shows the settlement during the 1000 cycles of the samples at high and low frequencies. Initially, the ballast is in a very loose state, manual compaction was attempted, however, the degrees of compaction achieved was not very good. At low frequency, the geocell performed worse followed by the control. Bitumen and geocell performed much better than geocell at both high and low frequencies. Therefore, the bitumen and geocell would is beneficial at reducing the settlement. Use of geocell only is not advisable since the conditions are worse than the control itself, for both high and low frequencies. It can be concluded that the settlement caused due to the decrease of interlocking between ballast because of the geocells cannot be compensated with the increase in lateral confinement. Furthermore, it was noticed that the use of geocell was not very practical since when large amounts of ballast were poured, the geocell bend and got crushed. Ballast had to be placed in each cell manually before compaction. Furthermore, bitumen did not reach the bottom

of the box. Only 150mm of ballast was in contact with bitumen. Figure 6.40 was implied into Figure 6.41 and it can be seen that even though, settlement is still high for box 3 initially, the amount of settlement decreased under higher frequencies. Therefore, it can be concluded that under high frequencies, bitumen and geocell can be beneficial. In the next section, the vibrational damping effects that were provide by the reinforcement will be tested.

6.5.1.2 Vibration

Complete results of all the tests can be found in Appendix A.10.2, and a lot was processing was performed to clean up the graphs. The noise was filtered by ignoring all values between -1 to 1.

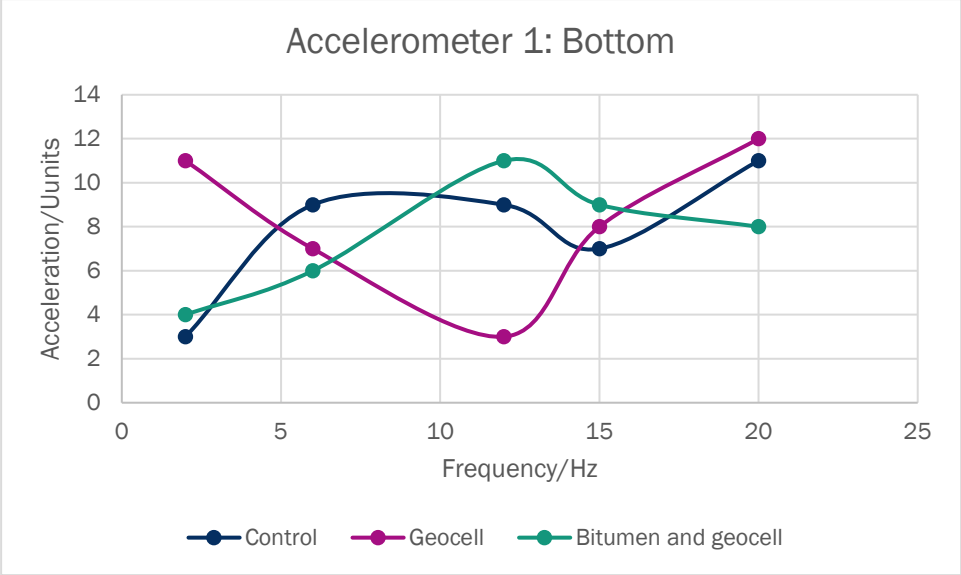


Figure 6.42: Accelerometer 1 results for reinforcement schemes

The maximum accelerations have been plotted against frequency of loading in Figure 6.42. As the frequency increases, the acceleration of the unreinforced sample also increases. When bitumen and geocell were incorporated, the displacement recorded were much more violent and did not increase damping

at all. Geocells, on the other hand, performed better than the other tests, for low frequencies at the bottom, but when the frequency was increased to 20Hz, the recorded acceleration was much higher. This tends to suggest that for low frequencies, geocells can reduce the amount of vibration, however, then the ballast have been fully compacted, the geocell perform worse. If the trend in Figure 6.42 is extrapolated, it can amount of vibration that could have been recorded is expected increase. Since accelerations have been broken down into its X,Y and Z components and have been shown in Figure 6.43 and Figure 6.44.

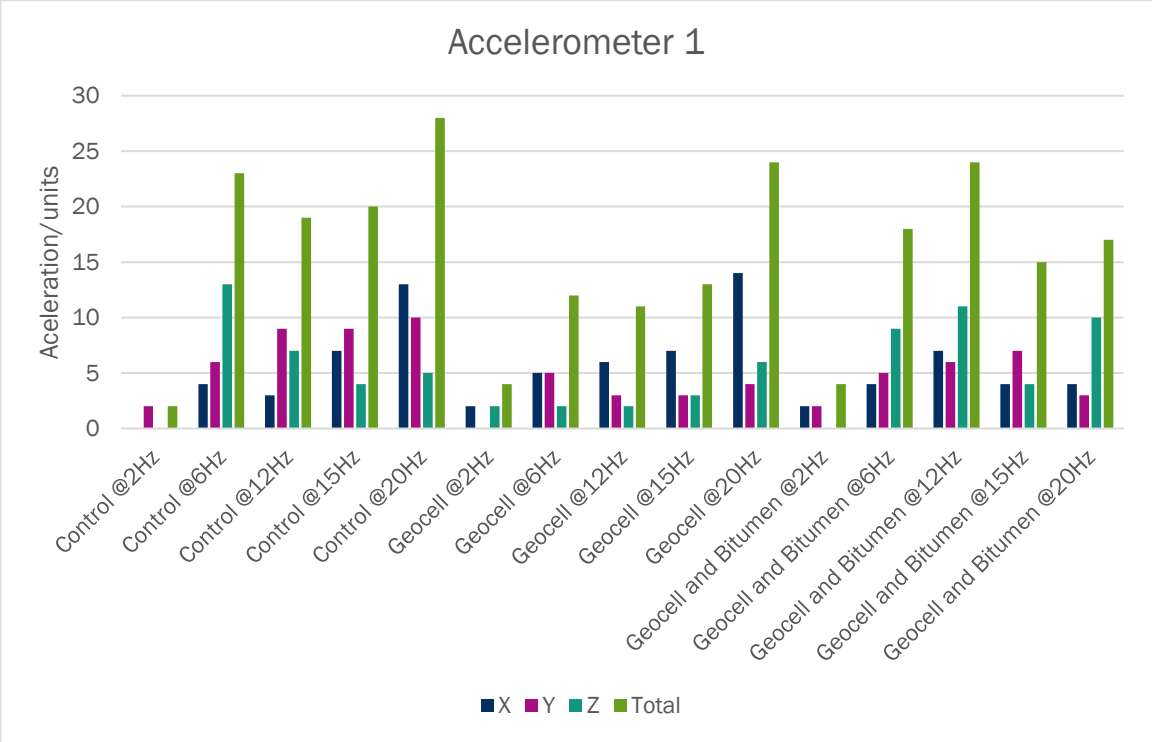


Figure 6.43: Peak accelerometer 1 results

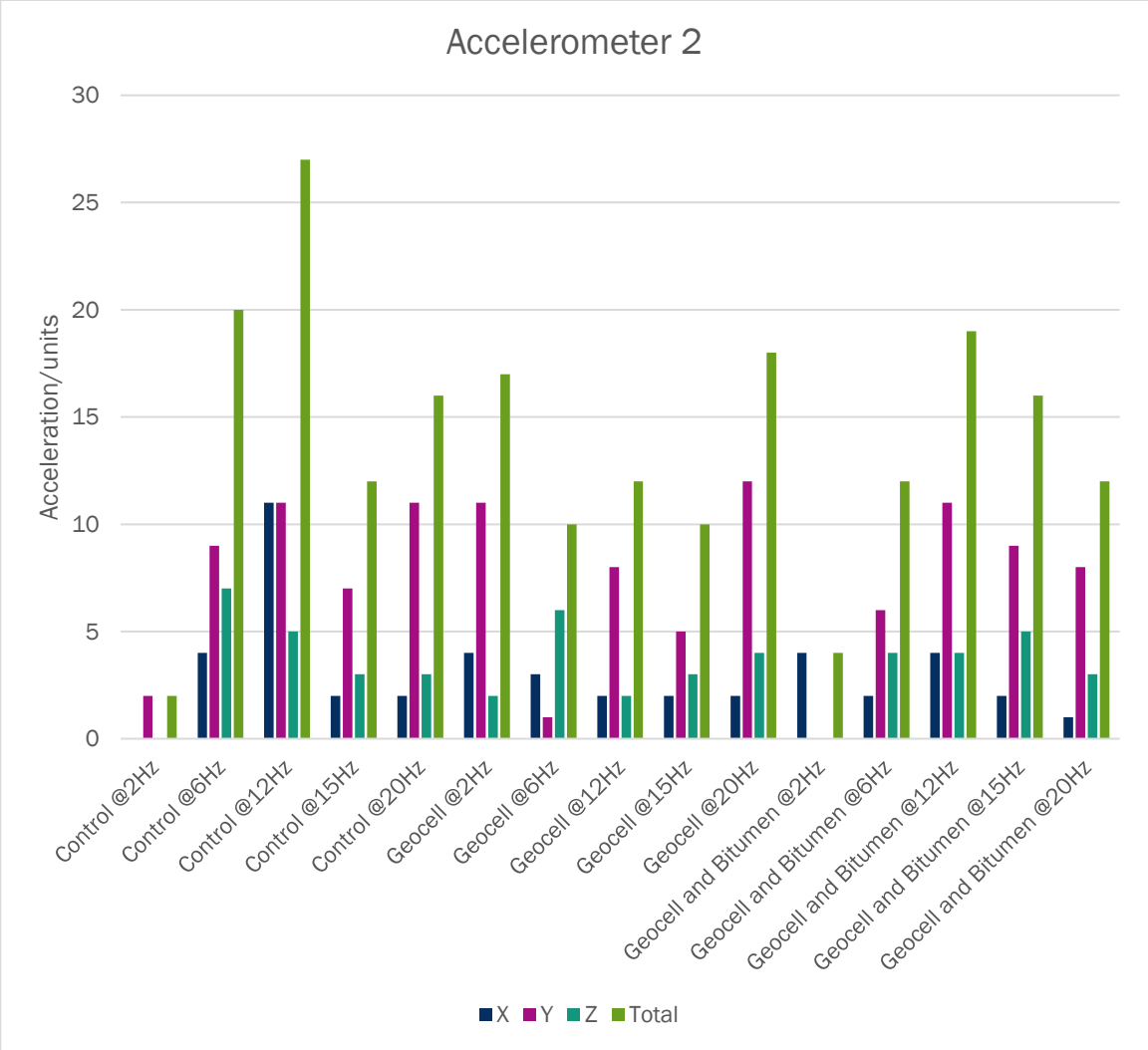


Figure 6.44: Peak accelerometer 2 results

Figures 6.43 and Figure 6.44 show the maximum acceleration of both accelerometers and the peak values in each direction have been summed. Accelerometer 2 which was placed on the side of the box recorded almost the same values for all the tests. It is because there is not much vibration on the sides, and in terms of lateral vibration, the reinforcements do not make a significant difference. For accelerometer 1, on the other hand, there are clear

trends. The following conclusions can be brought when Figure 6.43 is examined closely:

- As the frequency of loading is increased, the total acceleration increases for all the 3 box tests.
- Inclusion of geocells and bitumen decreases vibrations, with geocells having the best effects.
- As frequency increases, the amount of vertical acceleration remained unchanged, but the acceleration in the X and Z directions started to increase. This means that the box started to vibrate laterally. See Figure 6.37 for axis description.
- At initial loadings, the reinforcements have no effect, but once the samples have been compacted, the reinforcements start to decrease the amount of vibration.

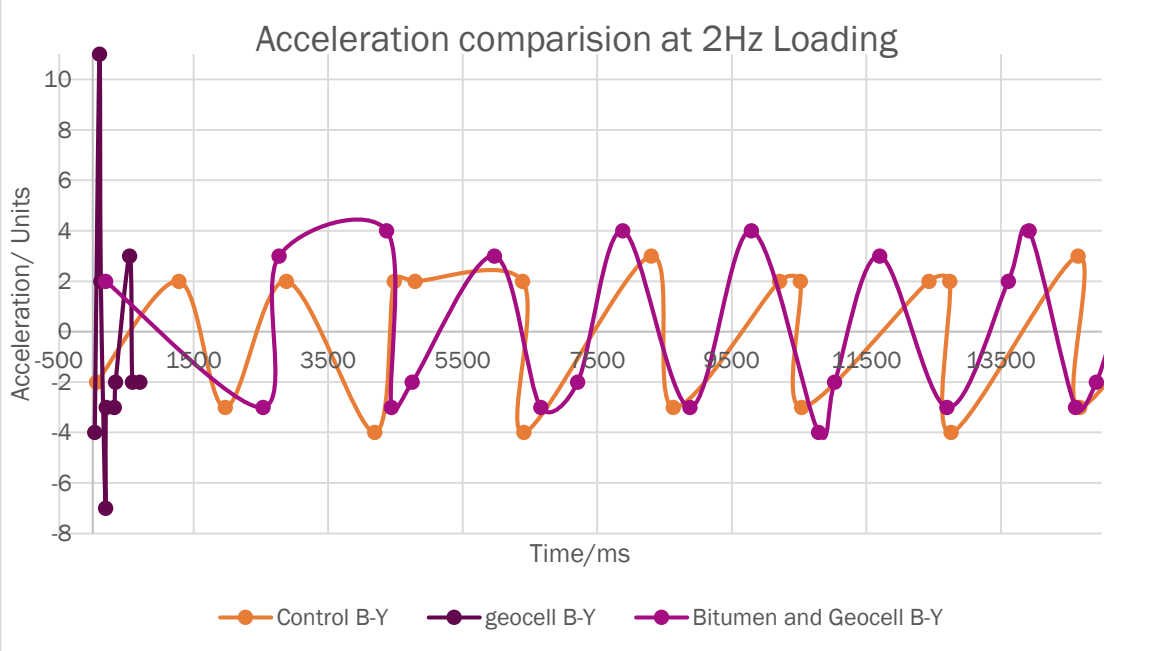


Figure 6.45: Acceleration comparison at 2hz loading

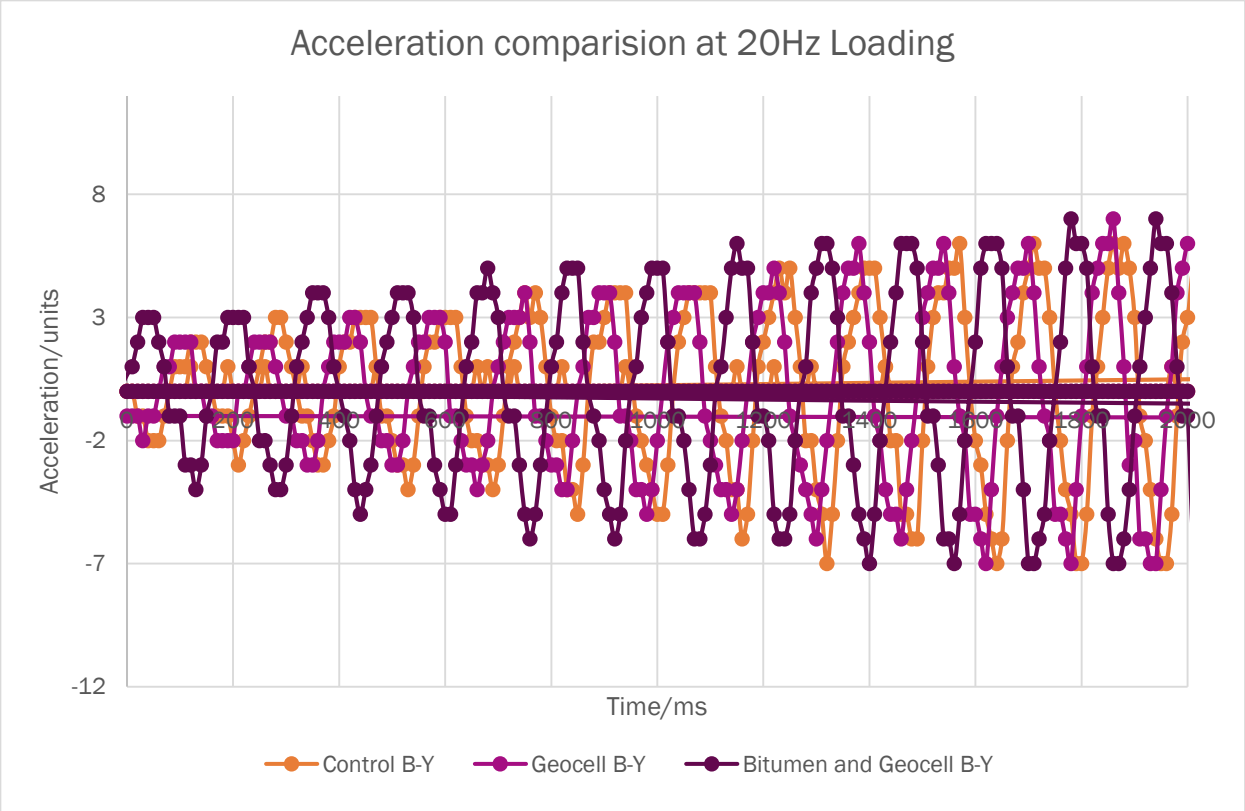


Figure 6.46: Acceleration comparison at 20hz loading

Figure 6.45 shows the initial loading of the boxes at low frequency of 2hz. A huge spike can be seen for the box that was reinforced with geocell. This is because when geocell was used initially, the amount of void was much larger compared and huge settlements were seen. Bitumen and geocell did not provide any difference to the control, and the acceleration was almost the same. The is because bitumen filled the voids that were created by implementation of geocell. However, as it can be seen in Figure 6.46, that when the samples were properly compacted, the amount of acceleration was the same for all the three samples and increase constantly. Therefore, initial benefits that were observed disappear when the samples are sufficiently compacted.

6.5.2 CONCLUSION OF TEST 4

Settlement and acceleration do not go hand in hand. Overall the energy that is applied needs to be dissipated by some means. This is why we get this inverse relationship. When the reinforcement is damping the vibration, the settlement is much larger, and when settlement is low, vibration is very high. If a track is made stiffer so that faster trains are allowed to run on it, vibration is expected to increase significantly even if bitumen was applied. After proper compaction, the damping effects that are provided initially disappear.

6.6 LIMITATION OF THE EXPERIMENTS

In all the experimental tests, lateral movement ballast was constrained while on a railway track, ballast is unbound. Therefore, it should be noted the settlement might be less than expected.

In the ERUDITE, granular material was tested, and this test has not been carried out by previous research. The amount of void present in the samples might yield extremely different result. The effect of incorporating the inner geocell, might not be observed in the test.

In the large box test, bitumen was not premixed because main purpose of the experiment is to increase the stability without intervention. Furthermore, due to lack of equipment, injecting bitumen under high pressure was not possible.

6.7 CONCLUSION

After the development of the reinforcement concept, optimum geocomposite properties have been defined, giving clear guidance on the use, reinforcing mechanism and efficiency of the new geocomposite for reinforcing ballast.

Table 6.11 summarises the results and conclusions of all the experiments. A positive percentage indicated that the treatment was beneficial and negative means that it was not relative to the control of the experiment.

Table 6.11: Summary of experiments

Treatment	Damping	Stiffness	Settlement under frequency		Vibration Decrease High frequency	Lateral stability
			Low	High		
Geocell	+109%	-50%	-293%	-11%	-9%	+1100%
Bitumen	+182%	+200%	-	-		-
Geocell and bitumen	+200%	-50%	-112%	+27%	+27%	-

It was concluded that adding bitumen to the ballast did enhance its structural capabilities of a track since the stiffness of the track would increase significantly. However, when geocells are inserted, the stiffness of the track decreases since the geocells prevent interlocking of the particles and increase the amount of void even though the lateral stability was improved. The vibrating table test concluded that all the reinforcements act as damping materials. However, when the vibration test was conducted in a larger scale, it was noticed that the amount of damping is dependent on the frequency of the application of the load. Vibration does decrease in specific cases, but the overall trend indicates that vibration was not decreased in both the vertical direction and the lateral direction. It should be noted that ERUDITE is not an appropriate test or granular material and should not be used in the future since the results varied significantly.

A stiffer track can be made with the inclusion of bitumen, and the reinforcement should increase the overall stability of the track, however higher vibration is expected. The result of this experiment proves that a ballasted track can be given the properties of a slab track which is normally used for high speed by solidifying the ballast using bitumen. Geocell performs better when subjected to high-frequency loads, and if the huge initial settlement is ignored, geocell can be beneficial as well.

CHAPTER 7: CONCLUSION

7.1.1 FINITE ELEMENT ANALYSIS

After an extensive literature review, it was noted that realistic loads that act on the ballast need further investigation. Analytical methods are almost inexistent. Furthermore, it was important to understand the effects of increasing trains speeds while keeping the quality of the tracks unchanged. In other words, it was important to understand if the mechanics of the problem would change and if current empirical design methods, e.g., calculation of the DAF to convert static load into dynamic loads, would hold. From contact mechanics, the point load was calculated using the computer program CONTACT written by Kalker (1990). The stresses at each contact area would yield a dynamic load since the stress is not the same at each point of the contact. The dynamic loads were fed into the finite element software, ANSYS Workbench 2016. Both the CONTACT model and the ANSYS model were validated using analytical problems. The stresses that the sleeper exert onto the ballast per unit time were thus obtained. The parametric study carried in the finite element analysis revealed that pad stiffness cannot be used to reduce dynamic impacts for all cases. A single value of track stiffness is only appropriate for specific cases and will be detrimental to another. . The load was much more influential as compared to speed. Results revealed that an increase in speed does not necessarily result in a corresponding increase in the deformation and stresses in track components, which necessitates the use of a heavier track structure. The loads, deformations, and stresses in the track components were found to be augmented as a result of the incongruous movement of vehicles on the track which occurs when the track is poorly maintained. Therefore, it is

possible to operate the same vehicles at a higher speed on a given track structure without imposing any additional loads and stresses, provided that the standards of maintenance of the track and the vehicles are sufficiently improved so as to control these inhibiting movements of the vehicle when it runs at higher speeds. Dynamic amplification factors that are currently being used in the industry should include some sort of factor that accounts for track quality. The dynamic load that occurs due to elastic deformation of materials. Since the loading frequency that can be achieved experimentally is limited, Discrete element method was thus used to test the effect of the high frequency dynamic loads on ballast.

7.1.2 DISCRETE ELEMENT ANALYSIS

The Discrete Element method was then used to find the interaction of individual particles for different reinforcement schemes under different frequencies of loading. YADE-DEM was used for modelling and the validation process. It was concluded that the model yields reasonably good results. From the parametric study conducted, it was concluded that the reinforcement indeed prevented ballast movement and reduced settlement. DEM required considerable computational effort and, therefore, only a limited amount of geocell could be modelled. Increasing the cohesive and adhesive properties had a positive impact on the ballast; less ballast movement was observed. This means that there was less ballast breakage and the settlement was much less. Geocell implementation, on the other hand, had the adverse effect. With an increasing number of geocell, more ballast movement and settlement was observed. This may probably be due to the fact that the walls of the geocell do not interlock with the ballast. They rather provide a more natural way for the ballast to move downwards.

It was also observed that when the frequency of loading was high, the settlement was very small. This effect can only be observed in a DEM analysis since individual particle interaction is considered. In high-frequency loadings, the loads are removed before proper propagation of the acceleration of individual particles. Such high frequencies cannot be experimentally tested; therefore, a smaller range was used for experimental testing. DEM also allowed a significant number of different cases to be modelled with relative ease. Over 32 different cases were modelled, and at the end of the analyses, the best combination of geocell size and dimension and bitumen was chosen to be carried forward for experimental testing. Another aim of the chapter was to shortlist the number of tests that would be experimentally tested and to identify which parameters could be improved to enhance the stability of a ballasted track. The test revealed that reinforcement provided to the ballast could prevent movement of the ballast and reduce settlement if both geocell and bitumen is used. Less movement would be expected if a large amount of geocell were to be placed as close as possible to the sleeper. Cell diameter should be as small as possible, and length of cells should be large. Bitumen has both restrained ballast movement and reduced settlement but when combined with one geocell, it is less effective. Lateral confinement and vibration absorption could not be tested in this therefore experimental testing were required to fully verify the results obtained in the chapter.

7.1.3 EXPERIMENTAL TESTING

The insertion of geocell did provide noticeable lateral confinement by reducing the lateral load that was imposed on the walls. Geocells should be as rigid as possible if lateral confinement is needed. Experimental testing

showed that bitumen did not have any observable effect on ballast in decreasing the amount of vibration for both high and low-frequency loadings. The experimental test gave the same results in terms of settlement as the DEM simulation. In terms of damping effects, tests conducted using the vibrating table concluded that adhered ballast by bitumen would increase the damping effects of ballast but promote dynamic impacts since the elasticity of the material would decrease. All the reinforcement schemes improved the damping properties of ballast. A stiffer track can be made with the inclusion of bitumen, and the reinforcement should increase the overall stability of the track, however higher vibration is expected. The results of this experiment prove that a ballasted track can be given the properties of a slab track which is normally used for high speed by solidifying the ballast using bitumen, however, the amount of vibration is expected to increase drastically. Geocell performs better when subjected to high frequency loads, and if the huge initial settlement is ignored, geocell can be beneficial as well. Vibration at the bottom was not reduced by damping, but it was by reducing the amount of settlement. Lateral vibration was not reduced by any reinforcement scheme. From the large-scale test, it was noticed that the use of geocell was not very practical since when large amounts of ballast were poured, the geocell could bend and get crushed. Ballast had to be placed in each cell manually before compaction. Furthermore, bitumen did not reach the bottom of the box. Only 150mm of ballast was in contact with bitumen. Bitumen needs to be injected at high pressure. The practicality of application of the reinforcement scheme needs to be addressed.

7.1.4 OVERALL CONCLUSION

A new geocomposite using a design philosophy analogous to that of reinforced concrete was created, and its behaviour and benefits understood. The concept and bounds of geocomposite, mixing materials to get both properties, was assessed. It is to be noted that dynamic structural innovation can be brought to the conventional train track without introducing a new construction cost (Ferreira & López-Pita 2015). Even though the results of the DEM state that geocell did not improve the ballasted track, there is still a wide range of materials that can be used for geocell. Other factors such as interlocking mechanisms can be provided by the wall of the geocell if modifications are brought to the walls of the geocells. If correctly implemented, the proposed research is expected to increase mobility and lead to cost-effective maintenance that minimizes the occurrence and duration of disruptions since ballast breakage is minimised by bitumen. These benefits directly lead to reliability and safety improvements, longer service life and improved long-term track and ride quality. Cost savings made through this scheme may be redirected to the improvement of other track components such as geocomposite installation. However, based on the results of this research it can be concluded that the proposed scheme can be detrimental to a railway track if not improved or altered.

7.1.5 FUTURE WORKS

- Owing to limited resources on the behaviour of granular materials with adhesives and inadequate existing numerical constitutive models, it is challenging to model the real behaviour and vibrations of the track

components (Shen 2015). Vibration can be modelled numerically to better understand the phenomenon of wave propagation.

- Studies have shown that using rubber granules for conventional tracks reduced deterioration, but when the design was implemented on high-frequency tracks, the vibrations were amplified for unknown reasons (Alfaro Albalat et al. 2011). Large-scale trials using high-frequency loading are evidently needed. Moreover, Bitumen Spray Treatment did not seem to work well at Butte 439-441, United States, railway track for reasons that were not discovered (Ebru Akoglu 2012). The results provided by this research have proven that bitumen improved the structural capabilities of the track. The results of this research and the field trials conducted by Alfaro Albalat et al. (2011) are contradictory. Further investigation is definitely needed in order to model field conditions more accurately in laboratory tests.
- Variation of foundation stiffness, time-dependent soil behaviour, and the presence of water was not considered (Zhang 2012; Abdullah et al. 2009). Soil stiffness and the existence of pore water pressure were ignored. Furthermore, Paixao et al. (2015) pointed out that the settlement profile and magnitude under the sleeper affect the deterioration of the track. Future studies need to couple FEM and DEM and also consider the subgrade. Modelling vibrations induced by railway traffic are complex. Further research must be conducted to study the dynamic interaction and propagation of waves between train, track, reinforcement and ground.

REFERENCES

Ben A. Leshchinsky, 2011. Enhancing Ballast Performance using Geocell Confinement. *ASCE*, pp.4693–4702.

Abdullah, a. et al., 2009. Ground improvement techniques for railway embankments. *Proceedings of the ICE - Ground Improvement*, 162(1), pp.3–14. Available at: http://www.icevirtuallibrary.com/content/article/10.1680/grim.2009.162.1.3.

Adams, V. & Askenazi, A., 1999. *Building better products with finite element analysis*,

Alfaro Albalat, S. et al., 2011. Crumb Rubber Modified Bitumen for sub-ballast layer. *9th World Congress on Railway Research*, pp.1–9.

Anon, 2009. *Comparing environmental impact of conventional and high speed rail*, Available at: http://scholar.google.com/scholar?hl=en&btnG=Search&q=intitle:Comparing+environmental+impact+of+conventional+and+high+speed+rail#0.

Aursudkij, B., McDowell, G.R. & Collop, a. C., 2009. Cyclic loading of railway ballast under triaxial conditions and in a railway test facility. *Granular Matter*, 11, pp.391–401.

Baeza, L. & Ouyang, H., 2011. A railway track dynamics model based on modal substructuring and a cyclic boundary condition. *Journal of Sound and Vibration*, 330(1), pp.75–86. Available at: http://dx.doi.org/10.1016/j.jsv.2010.07.023.

Balfour Beatty, 2015. XiTRACK Polyurethane Ballast Reinforcement - Case studies. *Balfour Beatty Rail Limited*, (235437), pp.1–11.

Berggren, E., 2009. *Railway Track Stiffness-Dynamic Measurements and Evaluation for Efficient Maintenance*. Royal Institute of Technology (KTH).

Bowness, D. et al., 2007. Monitoring the dynamic displacements of railway

track. *Proceedings of ImechE. Part F. Journal of Rail and Rapid Transport*, 221(1), pp.13–22.

Boyce, J.R., Brown, S.F. & Pell, P.S., 1976. *The resilient behaviour of a granular material under repeated loading*.

Boyle, N.F., 1980. *Railway Track Design: A review of Current Practice*, Australian Government Publishing Services.

Braghin, F. et al., 2006. A mathematical model to predict railway wheel profile evolution due to wear. *Wear*, 261(11–12), pp.1253–1264.

Brown, S.F. et al., 2007. The Nottingham railway test facility, UK. *Proceedings of the Institution of Civil Engineers - Transport*, 160(2), pp.59–65. Available at: http://www.icevirtuallibrary.com/doi/abs/10.1680/tran.2007.160.2.59.

Brown, S.F., Kwan, J. & Thom, N.H., 2007. Identifying the key parameters that influence geogrid reinforcement of railway ballast. *Geotextiles and Geomembranes*, 25(6), pp.326–335.

Cai, W., 2015. Discrete Element Modelling of Permanent Pavement Deformation in Granular Materials. *University of Nottingham*, (June).

Carol, D.J. et al., 2011. An Introduction to High Speed Rail - A Multidisciplinary Challenge. *Network*, (73), p.92. Available at: http://www.csa.com/partners/viewrecord.php?requester=gs&collection=ENV&recid=1530439%5Cnhttp://www.pbworld.com/pdfs/publications/pb_network/pbnetwork73.pdf.

Chandra, S. & Agarwal, M.M., 2007. Railway Engineering. *Oxford University Press*, 1(2), p.620. Available at: http://www.arup.com/Publications/The_Arup_Journal.aspx%5Cnhttp://www.omegacentre.bartlett.ucl.ac.uk/ProjectProfiles/CTRL/RelatedLinks/2-2.1 Arup Journal 2004 Railway Engineering.pdf.

Chang, P.J.Z.M.F., 2009. Study on permanent deformation characetistics of asphalt pavement based on Discrete Eolement Method. *ASCE*,

pp.2114–2121.

Chebli, H., Clouteau, D. & Schmitt, L., 2008. Dynamic response of high-speed ballasted railway tracks: 3D periodic model and in situ measurements. *Soil Dynamics and Earthquake Engineering*, 28(2), pp.118–131.

Chen, C., 2013. Discrete element modelling of geogrid-reinforced railway ballast and track transition zones. *University of Nottingham*, (June). Available at: http://etheses.nottingham.ac.uk/3399/1/Final_printed_thesis_upload.pdf.

Chen, C., McDowell, G.R. & Thom, N.H., 2012. Discrete element modelling of cyclic loads of geogrid-reinforced ballast under confined and unconfined conditions. *Geotextiles and Geomembranes*, 35, pp.76–86. Available at: http://linkinghub.elsevier.com/retrieve/pii/S0266114412000672.

Chen, J. et al., 2015. Micromechanical characteristics of aggregate particles in asphalt mixtures. *Construction and Building Materials*, 91, pp.80–85. Available at: http://linkinghub.elsevier.com/retrieve/pii/S0950061815005735.

Chen, J. et al., 2012. Predicting the dynamic behavior of asphalt concrete using three-dimensional discrete element method. *Journal of Wuhan University of Technology-Mater. Sci. Ed.*, 27(2), pp.382–388. Available at: http://link.springer.com/10.1007/s11595-012-0470-y.

Chen, X., 2014. A Sustainability Analysis on the Wuhan-Guangzhou High-Speed Railway in China. *International Journal of Sustainable Transportation*, 9(5), pp.348–363. Available at: http://www.tandfonline.com/doi/abs/10.1080/15568318.2013.797526.

Ching, C. & Kwan, J., 2006. *Geogrid Reinforcement of Railway Ballast*. unversity of nottingham.

Colaço, A., Costa, P.A. & Connolly, D.P., 2015. The influence of train

properties on railway ground vibrations. *Structure and Infrastructure Engineering*, 2479(October), pp.1–18. Available at: http://www.tandfonline.com/doi/full/10.1080/15732479.2015.1025291.

Connolly, D.P. et al., 2015. Benchmarking railway vibrations – Track, vehicle, ground and building effects. *Construction and Building Materials*, 92, pp.64–81. Available at: http://linkinghub.elsevier.com/retrieve/pii/S0950061814007661.

Cook, J., Buckley, J. & Dobie, M., 2015. The Use of Multiaxial Geogrids in Rail Trackbed the Use of Multiaxial Geogrids in Rail Trackbed Stabilisation Stabilisation. , (JUNE 2015).

Cope, D.L., Ellis, J.B. & Institution, P.W., 2001. *British Railway Track: Plain line maintenance*, Permanent Way Institution. Available at: https://books.google.com.my/books?id=txR5MwEACAAJ.

Cossio, M.L.T. et al., 2012a. MODERNIZATION OF TH E BALLASTED RAILWAY TRACK NETWORK IN MALAYSIA. *Uma ética para quantos?*, XXXIII(2), pp.81–87. Available at: http://www.ncbi.nlm.nih.gov/pubmed/15003161.

Cossio, M.L.T. et al., 2012b. Study of Railway Ballast compactness under Tamping Operation. *Uma ética para quantos?*, XXXIII(2), pp.81–87. Available at: http://www.ncbi.nlm.nih.gov/pubmed/15003161.

Costa, P.A. et al., 2015. Critical speed of railway tracks. Detailed and simplified approaches. *Transportation Geotechnics*, 2, pp.30–46. Available at: http://linkinghub.elsevier.com/retrieve/pii/S2214391214000348.

Dahlberg, T., 2004. *Railway track settlements - a literature review*, Available at: http://ohio.ikp.liu.se/Research/RTRSETTL.PDF.

Dash, S.K. & Shivadas, A.S., 2012. Performance Improvement of Railway Ballast Using Geocells. *Indian Geotechnical Journal*, 42(3), pp.186–193.

DiMaggio, J.A. & Cribbs, M.M., 1996. The role of geosynthetics on USA

highways. *Geotextiles and Geomembranes*, 14(5–6), pp.243–251. Available at: http://www.sciencedirect.com/science/article/pii/0266114496000131.

Dyk, B.J. Van et al., 2014. Evaluation of Dynamic and Impact Wheel Load Factors and their Application for Design. *Transportation Research Board 93rd Annual Meeting. January 12-16, Washington, D.C.*, 5(217).

Ebrahimi, A. & Keene, A.K., 2011. Maintenance Planning of Railway Ballast. *AREMA Annual Conference*. Available at: http://www.arema.org/files/library/2011_Conference_Proceedings/Maintenance_Planning_of_Railway_Ballast.pdf.

Elias, J., 2013. Dem Simulation of Railway Ballast Using. *Particles*, pp.1–10.

Eroglu S., Toprak S., Urgan O, MD, Ozge E. Onur, MD, Arzu Denizbasi, MD, Haldun Akoglu, MD, Cigdem Ozpolat, MD, Ebru Akoglu, M., 2012. Substructure investigation and Remediation for high Tonnage Freight Line. *Saudi Med J*, 33, pp.3–8.

Esmaeili, M., Nouri, R. & Yousefian, K., 2015. Experimental comparison of the lateral resistance of tracks with steel slag ballast and limestone ballast materials. *Proceedings of the Institution of Mechanical Engineers, Part F: Journal of Rail and Rapid Transit*, 0(0), pp.1–10. Available at: http://pif.sagepub.com/lookup/doi/10.1177/0954409715623577.

Esmaeili, M., Zakeri, J.A. & Mosayebi, S.A., 2014. Effect of sand-fouled ballast on train-induced vibration. *International Journal of Pavement Engineering*, 15(7), pp.635–644. Available at: http://www.scopus.com/inward/record.url?eid=2-s2.0-84897116267&partnerID=tZOtx3y1.

Esveld, C., 1997. Innovations in Railway Track. *Rail technology advancedments in the Netherlands. International conference*, pp.15–1. Available at: http://www.esveld.com/Download/TUD/Innovations.PDF.

Esveld, C., 2001. *Modern Railway Track*,

Esveld, C. & Steenbergen, M., 2005. Force-based assessment of weld

geometry. *8th International Heavy Haul Conference, Rio de Janeiro, Brazil*, pp.14–16. Available at: http://www.esveld.com/Download/RAILPROF/Papers/Esveld_IHHC8_final.pdf.

Etzkowitz, H. & Zhou, C., 2008. *The Bitumen Industry, A Global Perspective*,

Fair, P. & Anderson, S.W.F., 2003. The geotechnical behaviour for ballast materials of track maintenance railway. *University of Sheffield*, (July 2003).

Fan, R. et al., 2009. Experimental study of the effect of viscoelastic damping materials on noise and vibration reduction within railway vehicles. *Journal of Sound and Vibration*, 319(1–2), pp.58–76. Available at: http://linkinghub.elsevier.com/retrieve/pii/S0022460X0800312X.

Fan, R. et al., 2008. Internal noise reduction in railway carriages, A case study in China. *Transportation Research Part D: Transport …*, 13, pp.213–220. Available at: http://www.sciencedirect.com/science/article/pii/S1361920908000102.

Fang, M., Cerdas, S.F. & Qiu, Y., 2013. Numerical determination for optimal location of sub-track asphalt layer in high-speed rails. *Journal of Modern Transportation*, 21(2), pp.103–110. Available at: http://link.springer.com/10.1007/s40534-013-0012-0.

Feigenbaum, B., 2013. High-Speed Rail in Europe and Asia : Lessons for the United States. *Reasons*, (May).

Ferreira, P.A. & López-Pita, A., 2015. Numerical modelling of high speed train/track system for the reduction of vibration levels and maintenance needs of railway tracks. *Construction and Building Materials*, 79, pp.14–21. Available at: http://www.sciencedirect.com/science/article/pii/S0950061815000124.

Fortin, J.P., 1882. La déformée dynamique de la voie ferrée.

Fröidh, O., 2014. Design speed for new high-speed lines. *Journal of Rail Transport Planning & Management*, 4(3), pp.59–69. Available at: http://linkinghub.elsevier.com/retrieve/pii/S2210970614000420.

Fu, Z. et al., 2012. Review of High-Speed Train Maintenance. , pp.419–422.

Geng, Y., 2010. Discrete Element Modelling of Cavity Expansion in Granular Materials. *The Unversity of Nottingham*, (September), p.242.

Goicolea, J.M. et al., 2002. New Dynamic Analysis Methods for Railway Bridges in Codes IAPF and Eurocode 1. *Railway Bridges*, (June), p.43. Available at: http://w3.mecanica.upm.es/gmc/publicaciones/jgoicolea-english.pdf.

Grassie, S.L. et al., 1982. THE DYNAMIC RESPONSE OF RAILWAY TRACK TO HIGH FREQUENCY VERTICAL EXCITATION. , 24(2).

Guler, H., 2013. Prediction of railway track geometry deterioration using artificial neural networks: a case study for Turkish state railways. *Structure and Infrastructure Engineering*, 10(5), pp.1–13. Available at: http://www.tandfonline.com/doi/abs/10.1080/15732479.2012.757791.

Hall, B.E. & Giles, E.L., 1991. Effectiveness of Sprayed Bitumen as a Formation Maintenance Technique. In *International Heavy Haul Railway Conference*.

Hampel, U. et al., 1975. United States Patent: Consolidating Ballast.

Han, J. & Thakur, J.K., 2012. Use of Geosynthetics to Stabilize Recycled Aggregates in Roadway Construction. *Icsdec 2012*, pp.473–480. Available at: http://www.scopus.com/inward/record.url?eid=2-s2.0-84887388243&partnerID=tZOtx3y1.

Hay, W.W., 1953. Railroad Engineering.

Hegde, A. & Sitharam, T.G., 2015. 3-Dimensional numerical modelling of geocell reinforced sand beds. *Geotextiles and Geomembranes*, 43(2), pp.171–181. Available at: http://www.sciencedirect.com/science/article/pii/S026611441400124

1.

Hegde, A.M. & Sitharam, T.G., 2014. Effect of infill materials on the performance of geocell reinforced soft clay beds. *Geomechanics and Geoengineering*, (July), pp.1–11. Available at: http://www.tandfonline.com/doi/abs/10.1080/17486025.2014.921334.

Hushmand, B., 1983. *Experimental studies of dynamic response of foundations*. California Institute of Technology.

Hussaini, K., 2013. An experimental study on the deformation behaviour of geosynthetically reinforced ballast.

Indraratna, 2010. The Behaviour of Ballasted Track Foundations: Track Drainage and Geosynthetic. , (Gsp 199), pp.2378–2387.

Indraratna, B. et al., 2015. Behavior of Geocell-Reinforced Subballast Subjected to Cyclic Loading in Plane-Strain Condition. *Journal of Geotechnical and Geoenvironmental Engineering*, 141(1), p.4014081.

Indraratna, B. et al., 2012. Behaviour of Fresh and Fouled Railway Ballast Subjected to Direct Shear Testing - A Discrete Element Simulation. *International Journal of Geomechanics*, 14(February), p.121004134817003.

Indraratna, B. et al., 2010. Field Assessment of the Performance of a Ballasted Rail Track with and without Geosynthetics. *Journal of Geotechnical and Geoenvironmental Engineering*, 136(7), pp.907–917.

J. Han, X. Yang, et al., 2007. Behavior of Geocell-Reinforced Sand under a Vertical Load. , (August), pp.1–14.

J.Bathurst, R., 2009. Leaflets on Geosynthetics Applications.

Judge, T., 2002. Ballast breakthroughs.

Judge, T., 2006. Clean ballast is better ballast.

Kargarnovin, M.H. et al., 2005. Ride comfort of high-speed trains travelling over railway bridges. *Vehicle System Dynamics: International Journal*

of Vehicle Mechanics and Mobility, 43(3), pp.173–197. Available at: http://www.informaworld.com/10.1080/00423110512331335111.

Katzenbach, R., Geotechnics as a high-tech discipline of civil engineering; Actual R&D Examples. , pp.3–10.

Keene, A. et al., 2010. Modeling the Effect of Polyurethane Stabilization on Rail Track Response. *Geo-Congress 2013@ sStability and …*, 155, pp.154–161. Available at: http://ascelibrary.org/doi/abs/10.1061/9780784412787.141.

Kennedy, J., 2011. *A full-scale laboratory investigation into railway track substructure performance and ballast reinforcement*. Heriot-Watt University.

Kidd, J. & Stumm, M., 2007. CHINA ' S NEED FOR ULTRA - HIGH SPEED RAILWAYS.

Koroma, S.G., Hussein, M.F.M. & Owen, J.S., 2013. the Effects of Preload and Nonlinearity on the Vibration of Railway Tracks Under Harmonic Load. , (September), pp.9–12.

Kozicki, J. & Donzé, F.V., 2009. YADE-OPEN DEM: an open-source software using a discrete element method to simulate granular material. *Engineering Computations*, 26(7), pp.786–805.

Krylov, V. V, 1996. Vibrational impact of high-speed trains. I. Effect of track dynamics. *J. Acoust. Soc. Am*, 100(5), pp.3121–3134.

Kuo, C.-M. & Huang, C.-H., 2009. Two Approaches of Finite-Element Modeling of Ballasted Railway Track. *Journal of Geotechnical and Geoenvironmental Engineering*, 135(3), pp.455–458.

Lackenby, J. et al., 2007. Effect of confining pressure on ballast degradation and deformation under cyclic triaxial loading. *Géotechnique*, 57(6), pp.527–536.

Lackenby, J., 2006. Triaxial behaviour of ballast and the role of confining pressure under cyclic loading. *University of Wollongong*.

Lade, P. V., Yamamuro, J. a. & Bopp, P. a., 1997. Significance of Particle Crushing in Granular Materials. *Journal of Geotechnical and Geoenvironmental Engineering*, 123(9), pp.889–890.

Lee, S.-H. et al., 2014. Evaluation of asphalt concrete mixtures for railway track. *Construction and Building Materials*, 73, pp.13–18. Available at: http://www.sciencedirect.com/science/article/pii/S0950061814010691.

Leheis, S., 2012. High-speed train planning in France: Lessons from the Mediterranean TGV-line. *Transport Policy*, 21, pp.37–44. Available at: http://linkinghub.elsevier.com/retrieve/pii/S0967070X11001326.

Leshchinsky, B.A., 2012. *Enhancing Ballast Performance using geocell Confinment*. Columbia University. Available at: http://www.ncbi.nlm.nih.gov/pubmed/15003161.

Leshchinsky, B., Ling, H. & Asce, M., 2013. Effects of Geocell Confinement on Strength and Deformation Behavior of Gravel. *Journal of Geotechnical and Geoenvironmental Engineering*, 139(FEBRUARY), pp.340–352.

Leshchinsky, B. & Ling, H.I., 2013. Numerical modeling of behavior of railway ballasted structure with geocell confinement. *Geotextiles and Geomembranes*, 36, pp.33–43. Available at: http://dx.doi.org/10.1016/j.geotexmem.2012.10.006.

Lichtberger, B., 2005. Track Compendium. , pp.1–192.

Lichtberger, B., 2011. *Track Compendium: Track System, Substructure, Maintenance, Economics*, Eurailpress. Available at: https://books.google.com.my/books?id=X8tctwAACAAJ.

Lim, W.L., 2004. *Mechanics of railway ballast behaviour*. The University of Nottingham. Available at: http://etheses.nottingham.ac.uk/60/.

Lim, W.L. & McDowell, G.R., 2005. Discrete element modelling of railway ballast. *University of Nottingham*, 7(1), pp.19–29. Available at: http://link.springer.com/10.1007/s10035-004-0189-3.

Lin, Y.-L. et al., 2009. Engineering behaviors of reinforced gabion retaining wall based on laboratory test. *Springer*, 60(2), pp.444–449.

Liu, J. & Xiao, J., 2010. Experimental Study on the Stability of Railroad Silt Subgrade with Increasing Train Speed. *Journal of Geotechnical and Geoenvironmental Engineering*, 136(6), pp.833–841. Available at: http://dx.doi.org/10.1061/(ASCE)GT.1943-5606.0000282.

Lu, M. & McDowell, G.R., 2008. Discrete element modelling of railway ballast under triaxial conditions. *Geomechanics and Geoengineering*, 3(4), pp.257–270.

Lu, M. & McDowell, G.R., 2007. The importance of modelling ballast particle shape in the discrete element method. *Granular Matter*, 9(1–2), pp.69–80. Available at: http://link.springer.com/10.1007/s10035-006-0021-3.

Madshus, C. & Kaynia, A.M., 2000. High-Speed Railway Lines on Soft Ground: Dynamic Behaviour At Critical Train Speed. *Journal of Sound and Vibration*, 231(3), pp.689–701. Available at: http://linkinghub.elsevier.com/retrieve/pii/S0022460X99926470.

Manda, K.R., 2014. Vertical Load Path Under Static and Dynamic Loads in Concrete Crosstie and.

Marais, C.., 1981. Surface treatements. *Materials and Design Course*, (CSIR).

Marto, A., Oghabi, M. & Eisazadeh, A., 2013. Effect of geocell reinforcement in sand and its effect on the bearing capacity with experimental test; A review. *Electronic Journal of Geotechnical Engineering*, 18 Q, pp.3501–3516.

Mcdowell, G., Micro mechics of railway ballast degradation. *Nottingham Centre for Geomechanics*.

McDowell, G.R., Thom, N.H. & Chen, C., 2014. Investigating geogrid-reinforced ballast: Experimental pull-out tests and discrete element modelling. *Soils and Foundations*, 54(1), pp.1–11. Available at:

http://dx.doi.org/10.1016/j.sandf.2013.12.001.

Meyer, A.E.N., 2010. Verification of the load transfer mechanism of geocell rein forced soil in large scale model tests and different in-situ test fields. *Design*, (GSP 199), pp.1498–1506.

Di Mino, G. et al., 2012. A Dynamic Model of Ballasted Rail Track with Bituminous Sub-Ballast Layer. *Procedia - Social and Behavioral Sciences*, 53, pp.366–378. Available at: http://linkinghub.elsevier.com/retrieve/pii/S1877042812043509.

Minsili, L.S. et al., 2012. Preventive Maintenance of Railway Tracks : Ballast Performance Anticipation in the Cameroon Railway. , 4(5), pp.398–406.

Mishra, Y.Q.E.T.M.A.D. & Hasan, K., 2014. Behavior of Geogrid Reinforced Ballast at Different Levels of Degradation. , (1987), pp.158–167.

Mohamed, M., Fung, H.-N. & Wong, C.-Y., 2015. Convergence innovation in railway technology: how ERL of Malaysia attained its co-evolution structure for systemic development. *Asian Journal of Technology Innovation*, 23(sup1), pp.93–108. Available at: http://www.tandfonline.com/doi/full/10.1080/19761597.2015.1012787.

Mohd. Jakarni, F., 2012. *Adhesion of asphalt mixtures*. University of Nottingham. Available at: http://etheses.nottingham.ac.uk/2646/.

Neupane, M. & Members, C., 2007. Strength and Resistivity Properties of Fouled Ballast.

Nimbalkar, S., 2015. Implications of ballast degradation under cyclic loading.

ORE, 1983. Effect on track quality of various subgrade protective layers. *International Union of Railways*.

Otero, J. et al., 2012. A mathematical model to study railway track dynamics for the prediction of vibration levels generated by rail vehicles. *Proceedings of the Institution of Mechanical Engineers, Part F: Journal of Rail and Rapid Transit*, 226(1), pp.62–71. Available at:

http://pif.sagepub.com/lookup/doi/10.1177/0954409711406837.

Oyarzabal, O. et al., 2011. Modelling rail corrugation with specific-track parameters focusing on ballasted track and slab track. *Vehicle System Dynamics*, 49(11), pp.1733–1748. Available at: http://www.tandfonline.com/doi/abs/10.1080/00423114.2010.536557.

Paixao, a., Fortunato, E. & Calcada, R., 2015. A numerical study on the influence of backfill settlements in the train/track interaction at transition zones to railway bridges. *Proceedings of the Institution of Mechanical Engineers, Part F: Journal of Rail and Rapid Transit*, 0(0), pp.1–13. Available at: http://pif.sagepub.com/lookup/doi/10.1177/0954409715573289.

Penman, B.J. & Priest, D.J., 2009. The Use of Geogrids in Railroad Applications. *Continuing Education*, (October).

Pimentel, P.K.C.A., Bathurst, R.J. & Palmeira, E.M., 2009. Geosynthetics in Railroads. *igs*.

Pokharel, S.K. et al., 2010. Investigation of factors influencing behavior of single geocell-reinforced bases under static loading. *Geotextiles and Geomembranes*, 28(6), pp.570–578. Available at: http://linkinghub.elsevier.com/retrieve/pii/S0266114410000713.

Powrie, W., Presentation: Current RRUK Research into Railway Track and Sub-Base Performance.

Priest, J. a. & Powrie, W., 2009. Determination of dynamic track modulus from measurement of track velocity during train passage. *Journal of Geotechnical and Geoenviromental Engineering*, 135(135), pp.1732–1740. Available at: http://dx.doi.org/10.1061/(ASCE)GT.1943-5606.0000130.

Prud'homme, Resistance of the Track to Lateral Loads Exerted by Rolling Stock. *1967*.

Puzavac, L., Popović, Z. & Lazarević, L., 2012. Influence of Track Stiffness

on Track Behaviour under Vertical Load. *PROMET - Traffic&Transportation*, 24(5), pp.405–412.

Rahman, A., 2013. Permeability, Resistivity and Strength of Fouled Railroad Ballast. *The effects of brief mindfulness intervention on acute pain experience: An examination of individual difference*, 1.

Raoul, J.-C., 1997. How high-speed trains make tracks. *Scientific American*, 277(4), pp.100–105.

Raymond, G.P., 1999. Railway rehabilitation geotextiles. *Geotextiles and Geomembranes*, 17(November 1998), pp.213–230.

Raymond, G.P., 2002. Reinforced ballast behaviour subjected to repeated load. *Geotextiles and Geomembranes*, 20(1), pp.39–61.

Rivin, E.I., 2007. Use of Stiffness / Damping / Natural Frequency Criteria in Vibration Control. *Proceedings of Twelfth World Congress in Mechanism and Machine Science*.

Sadeghi, J., 1997. Investigation of characteristics and modelling of railway track system. , p.262.

Sanders, P.J., 2001. Reinforced Asphalt Overlays. *University of Nottingham*, (October), p.381.

Saussine, G. et al., 2006. Modelling ballast behaviour under dynamic loading. Part 1: A 2D polygonal discrete element method approach. *Computer Methods in Applied Mechanics and Engineering*, 195, pp.2841–2859.

Selig, E.T. & Waters, J.M., 1994. *Track Geotechnology and Substructure Management*, T. Telford. Available at: https://books.google.com.my/books?id=ZHxW4D6XT0MC.

Sextro, W., 2007. *Dynamical Contact Problems with Friction*,

Shen, Y.L.Y.X.X.X. and J., 2015. Model Updating of Ballast Track Settlement and Accumulative Settlement. , pp.1780–1786.

Siew, J.S., Mirza, O. & Kaewunruen, S., 2015. Nonlinear Finite Element

Modelling of Railway Turnout System considering Bearer / Sleeper-Ballast Interaction. , 2015.

Singh, Y. & S, R.S., 2015. Design of Geocell Reinforced Flexible Pavement. , 4(3), pp.1011–1014.

Sitharam, T.G. & Sireesh, S., 2006. Effects of base geogrid on geocell-reinforced foundation beds. *Geomechanics and Geoengineering*, 1(3), pp.207–216. Available at: http://www.tandfonline.com/doi/abs/10.1080/17486020600900596.

Snowdon, J.C., 1958. The choice of resilient materials for anti-vibration mountings. *British Journal of Applied Physics*, 9(12), p.461. Available at: http://stacks.iop.org/0508-3443/9/i=12/a=301.

Sol-Sánchez, M., Moreno-Navarro, F. & Rubio-Gámez, M., 2014. The Use of Deconstructed Tires as Elastic Elements in Railway Tracks. *Materials*, 7(8), pp.5903–5919. Available at: http://www.mdpi.com/1996-1944/7/8/5903/.

Sol-Sánchez, M., Moreno-Navarro, F. & Rubio-Gámez, M.C., 2015. The use of elastic elements in railway tracks: A state of the art review. *Construction and Building Materials*, 75, pp.293–305. Available at: http://www.sciencedirect.com/science/article/pii/S0950061814012392.

Sorbothane Inc., 2015. Sorbothane Standard Products Guide. Available at: http://www.sorbothane.com/Data/Sites/31/pdfs/product-guides/Sorbothane-SPG.pdf.

Stahl, M. & Konietzky, H., 2011. Discrete element simulation of ballast and gravel under special consideration of grain-shape, grain-size and relative density. *Granular Matter*, 13, pp.417–428.

Steenbergen, M.J.M.M., 2013. Physics of railroad degradation: The role of a varying dynamic stiffness and transition radiation processes. *Computers and Structures*, 124, pp.102–111. Available at: http://dx.doi.org/10.1016/j.compstruc.2012.11.009.

Steenbergen, M.J.M.M. & Esveld, C., 2006. Relation between the geometry of rail welds and the dynamic wheel - rail response: numerical simulations for measured welds. *Proceedings of the Institution of Mechanical Engineers, Part F: Journal of Rail and Rapid Transit*, 220(4), pp.409–423. Available at: http://pif.sagepub.com/lookup/doi/10.1243/0954409JRRT87.

Su, B., 2005. Effects of Railroad Track Structural Components and Subgrade on Damping and Dissipation of Train Induced.

Suiker, A.S.J., Selig, E.T. & Frenkel, R., 2005. Static and Cyclic Triaxial Testing of Ballast and Subballast. *Journal of Geotechnical and Geoenvironmental Engineering*, 131(6), pp.771–782.

Sun, Q.D. et al., 2010. Deformation and Degradation Mechanisms of Railway Ballast under High Frequency Cyclic Loading. , pp.1–12.

Tafreshi, S.N.M. & Dawson, a. R., 2010. Behaviour of footings on reinforced sand subjected to repeated loading - Comparing use of 3D and planar geotextile. *Geotextiles and Geomembranes*, 28(5), pp.434–447. Available at: http://dx.doi.org/10.1016/j.geotexmem.2009.12.007.

Teixeira, P.F., López Pita, a. & Ferreira, P. a., 2010. New possibilities to reduce track costs on high-speed lines using a bituminous sub-ballast layer. *International Journal of Pavement Engineering*, 11(4), pp.301–307. Available at: http://www.tandfonline.com/doi/abs/10.1080/10298431003749733.

Thakur, P.K., Vinod, J.S. & Indraratna, B., 2010. Effect of particle breakage on cyclic densification of ballast: A DEM approach. *IOP Conference Series: Materials Science and Engineering*, 10, p.12229.

Thallak, S.G., Saride, S. & Dash, S.K., 2007. Performance of surface footing on geocell-reinforced soft clay beds. *Geotechnical and Geological Engineering*, 25(5), pp.509–524. Available at: http://link.springer.com/10.1007/s10706-007-9125-8.

Thomas, S., Woodward, P. & Laghrouche, O., 2015. Influence of stiffening ballasted track bed overlying a masonry arch bridge using a

polyurethane polymer material. *Construction and Building Materials*, 92, pp.111–117. Available at: http://www.sciencedirect.com/science/article/pii/S0950061814008733.

Thompson, D., Wu, T. & Armstrong, T., 2003. Wheel / Rail Rolling Noise - the Effects of Non- Linearities in the Contact Zone. *Tenth International Congress on Sound and Vibration*, pp.1–20.

Thompson, D.J. & Wu, T.X., 2000. Theoretical Investigations of Wheel / Rail Non-linear Interaction due to Roughness Excitation. *Sound And Vibration*, (852), p.44.

Tobergte, D.R. & Curtis, S., 2013. No Title No Title. *Journal of Chemical Information and Modeling*, 53(9), pp.1689–1699.

Vickerman, R., 1997. High-speed rail in Europe: experience and issues for future development. *The Annals of Regional Science*, 31(1), pp.21–38. Available at: http://dx.doi.org/10.1007/s001680050037%5Cnhttp://link.springer.com/10.1007/s001680050037.

Vollebregt, E.A.H., 2014. User guide for CONTACT, Rolling and sliding contact with friction.

Wang, J. & Zeng, X., 2004. Numerical Simulations of Vibration Attenuation of High-Speed Train Foundations With Varied Trackbed Underlayment Materials. *Journal of Vibration and Control*, 10(8), pp.1123–1136.

Wei, Y., 2014. Preface : Current research progress on mechanics of high speed rail. , 30, pp.846–848.

Wesseloo, J., Visser, a. T. & Rust, E., 2009. The stress-strain behaviour of multiple cell geocell packs. *Geotextiles and Geomembranes*, 27(1), pp.31–38. Available at: http://linkinghub.elsevier.com/retrieve/pii/S0266114408000460.

Wong, W.G. et al., 2002. High-speed rail operations on an existing network: An assessment model for China. *Transportation Planning and*

Technology, 25, pp.239–254. Available at: http://dx.doi.org/10.1080/0308106022000019008.

Woodward, P., Kennedy, J. & Medero, G., 2009. Three dimensional track reinforcement using polymer geocomposites. *Proceedings of the American …*, 44(0). Available at: http://www.arema.org/files/library/2009_Conference_Proceedings/Three-Dimensional_Track_Reinforcement_Using_Polymer_Geocomposites.pdf.

Woodward, P.K. et al., 2011. Application of in situ polyurethane geocomposite beams to improve the passive shoulder resistance of railway track. *Proceedings of the Institution of Mechanical Engineers, Part F: Journal of Rail and Rapid Transit*, 226, pp.294–304. Available at: http://pif.sagepub.com/lookup/doi/10.1177/0954409711423460.

Woodward, P.K. et al., 2012. Application of polyurethane geocomposites to help maintain track geometry for high-speed ballasted railway tracks. *Journal of Zhejiang University SCIENCE A*, 13(11), pp.836–849. Available at: http://www.springerlink.com/index/10.1631/jzus.A12ISGT3.

Yang, D., 2013. Microscopic Study of Granular Material Behaviours under General Stress Paths. *University of Nottingham*, (November).

Yang, L. a, Powrie, W. & Priest, J. a, 2009. Dynamic Stress Analysis of a Ballasted Railway Track Bed during Train Passage. *Journal of Geotechnical and Geoenvironmental Engineering*, 135(5), pp.680–689.

Yoon, H. et al., 2013. Computation of Impact Factor of High-Speed Railway Bridge by KTX Train Riding Test. *Scientific Research*, 5(9), pp.751–755. Available at: http://www.scirp.org/journal/PaperDownload.aspx?DOI=10.4236/eng.2013.59090.

Zhai, W.M., Wang, K.Y. & Lin, J.H., 2004. Modelling and experiment of railway ballast vibrations. *Journal of Sound and Vibration*, 270(4–5),

pp.673–683.

Zhang, L.L.G.G.L.Y.X.H.B. and F., 2012. Innovative Materials and Design for Sustainable Transportation Infrastructure. , (Ingerslev 2012), pp.286–297.

Zhang, M.X., Javadi, a. a. & Min, X., 2006. Triaxial tests of sand reinforced with 3D inclusions. *Geotextiles and Geomembranes*, 24, pp.201–209.

Zicha, J.H., 1989. High-Speed Rail Track Design. *Journal of Transportation Engineering*, 115(1), pp.68–83.

APPENDICES

A.1: BALLAST SPECIFICATION

Table A.1: Ballast specification

Typical Ballast Characteristics	
KEY CHARACTERISTICS	**BS EN STANDARDS/ SPECIFICATIONS**
DURABILITY	
Los Angeles Abrasion	BS EN 1097-2: 1998 / LAA index ≤ 20
Deval Abrasion (wet and dry)	BS EN 1097-1: 1996/ M_{DE} index ≤ 7
Crushing value	BS 812-111: 1990/ ACV ≤22%
SHAPE CHARACTERISTICS	
Flakiness/ Elongation/ Angularity or Particle Length (shape index)	BS EN 933-2/3: 1997/ Flakiness index ≤ 35 and Elongation index ≤ 50. Particle Length ≤ 4
GRADATION	
Size distribution	BS EN 933-2: 1996/ Size to be between 31.5mm to 50mm.
UNIT WEIGHT	
Particle density/ Water adsorption	BS EN 1097-6: 2000/ Specifications of categories in BS EN still not considered appropriate for rail track use
Bulk density and voids	BS EN 1097-3: 1998/ Not available
ENVIRONMENTAL	
Freeze-thaw breakdown	BS EN 1367-1: 2000/ Refer to BS EN 13450: 2002, Annex F
Sulfate soundness	BS EN 1367-2:1998/ Refer to BS EN 13550: 2002, Annex G
COMPOSITION	
Chemical analysis	BS EN 1744-1: 1998/ Not available

A.2: DAF FORMULE

Table A.2: DAF formulae adopted from Steenbergen (2013)

Dynamic Factor	Expression for ϕ	Vehicle Parameters Included						Track Parameters Included					
		Train Speed	Wheel Diameter	Static Wheel Load	Unsprung Mass	Vehicle Center of Gravity	Locomotive Maintenance Condition	Track Modulus	Track Stiffness at Rail Joint	Track Joint Dip Angle	Cant Deficiency in Curves	Curve Radius	Track Maintenance Condition
Talbot	$1+\frac{33V}{100D}$	•	•										
Indian Railways	$1+\frac{V}{3\sqrt{U}}$	•						•					
Eisenmann	$1+\delta\eta t$	•											•
ORE/ Birmann	$1+\alpha+\beta+\gamma$	•				•	•				•	•	•
German Railways	$1+\frac{11.655V^2}{10^5}-\frac{6.252V^3}{10^7}$	•											
British Railways	$1+14.136(\alpha_1+\alpha_2)V\sqrt{\frac{D_j P_u}{g}}$	•		•	•				•	•			
South African Railways	$1+0.312\frac{V}{D}$	•	•										
Clarke	$1+\frac{15V}{D\sqrt{U}}$	•	•					•					
WMATA	$(1+0.0001V^2)^{\frac{2}{3}}$	•											
Sadeghi	$1.098+0.00129V+2.59(10^{-6})V^2$	•											
AREMA C30	For $20<V<120$: $0.6+0.005V$	•											

A.3: CONTACT CODE

```
%Case 1: Transient rolling starting from zero tangential traction.  Frictonless Normal problem
3 MODULE
201102                                                  P-B-T-N-F-S  PVTIME, BOUND, TANG, NORM, FORCE, STRESS
022020
001241

%No. of Iterations
1000        100     30      1       1E-07               MAXGS , MAXIN , MAXNR , MAXOUT, EPS

%Forces and Creepage
                                                        FUN,  FUX,  FUY,
300000.0    0.000   0.000   0.000923                    CPHI

0.3         0.3                                         FSAT,FKIN

%Material Parameters
0.28        0.28    82000.  82000.                     SIGMA 1,2,  GG 1,2

%For the undeformed distance calculation, when not using
%a Hertzian option.
1                                                       IPOTCN
%Discretization options
```

75 25 -6.28 -6.28 0.50 0.50 MX,MY,XL,YL,DX,DY

%elements 25 and timestep

3 1 IBASE, IPLAN

% Profile: the profile is quadratic plus the difference of two sines in x-direction.

0.00 0.00 0.00 0.00 0.00 0.00 3500.00 3500.00 B(I), I=1, 8

%Subsurface Calculation points:

25 25 1 NX, NY, NZ

%points x:

-6.03 -5.53 -5.03 -4.52 -4.02 -3.52 -3.02 -2.51 -2.01 -1.51

-1.01 -0.50 0.00 0.50 1.01 1.51 2.01 2.51 3.02 3.52

4.02 4.52 5.03 5.53 6.03

%points y:

-6.03 -5.53 -5.03 -4.52 -4.02 -3.52 -3.02 -2.51 -2.01 -1.51

-1.01 -0.50 0.00 0.50 1.01 1.51 2.01 2.51 3.02 3.52

4.02 4.52 5.03 5.53 6.03

%points z:

0.0

F

%Distance travelled 1 DX

```
3 MODULE
001101                                                                  P-B-T-N-F-S   PVTIME, BOUND, TANG, NORM, FORCE, STRESS
100020
001241
100             100     30      1           1E-07                       MAXGS , MAXIN , MAXNR , MAXOUT, EPS
300000.00       0.00    0.000   0.000923                                FUN,  FUX,  FUY,
                                                                        CPHI
3               1                                                       IBASE, IPLAN
0.00            0.00    0.50    0.00        0.00    0.00    3500.00 3500.00  B(I), I=1, 8
%Distance travelled     25      DX
3 MODULE
001101                                                                  P-B-T-N-F-S   PVTIME, BOUND, TANG, NORM, FORCE, STRESS
100020
001241
100             100     30      1           1E-07                       MAXGS , MAXIN , MAXNR , MAXOUT, EPS
10000           0       0.000   0.000923                                FUN,  FUX,  FUY,
                                                                        CPHI
3               1                                                       IBASE, IPLAN
0.00            0.00    11.56   0.00        0.00    0.00    3500.00 3500.00  B(I), I=1, 8
0 MODULE
```

A.4: CONTACT RESULT FOR C1 50KN 20MS

Case 1

NORM

Norm: size of Contact, Exterior : 750 1125

Norm: final element division: C, E= 700 1175 ItCG= 30

TANG: SHIFT TRANSIENT

Tang: size of Adhes, Slip area : 700 0

Tang: final element division: A, S= 335 365 ItCG= 40

PBTNFS. PVTIME 2, BOUND 0, TANG 1, NORM 1, FORCE 0, STRESS 2

LDCMZE. FRCLAW 0, DISCNS 2, INFLCF 2, MATER 0, RZNORM 2, RZTANG 0

GIAOWR. GAUSEI 0, IESTIM 0, MATFIL 1, OUTPUT 2, FLOW 4, RETURN 1

NORMAL PROBLEM WITH PRESCRIBED NORMAL FORCE

SHIFT TRANSIENT

CREEPAGE PRESCRIBED

JOHNSON"S METHOD IS USED FOR THE FRICTIONAL STRESS

TOTAL FORCES, TORSIONAL MOMENT, ELASTIC ENERGY, FRICTIONAL POWER

FN	FX	FY	MZ	ELAST.EN.	FRIC.POWER
5.000E+04	-13.39	-212.1	-5.637E+04	849.1	-9.601

FN/G	FX/FSTAT/FN	FY/FSTAT/FN	APPROACH
0.6098	-8.927E-04	-1.414E-02	4.047E-02

CONTACT STATISTICS

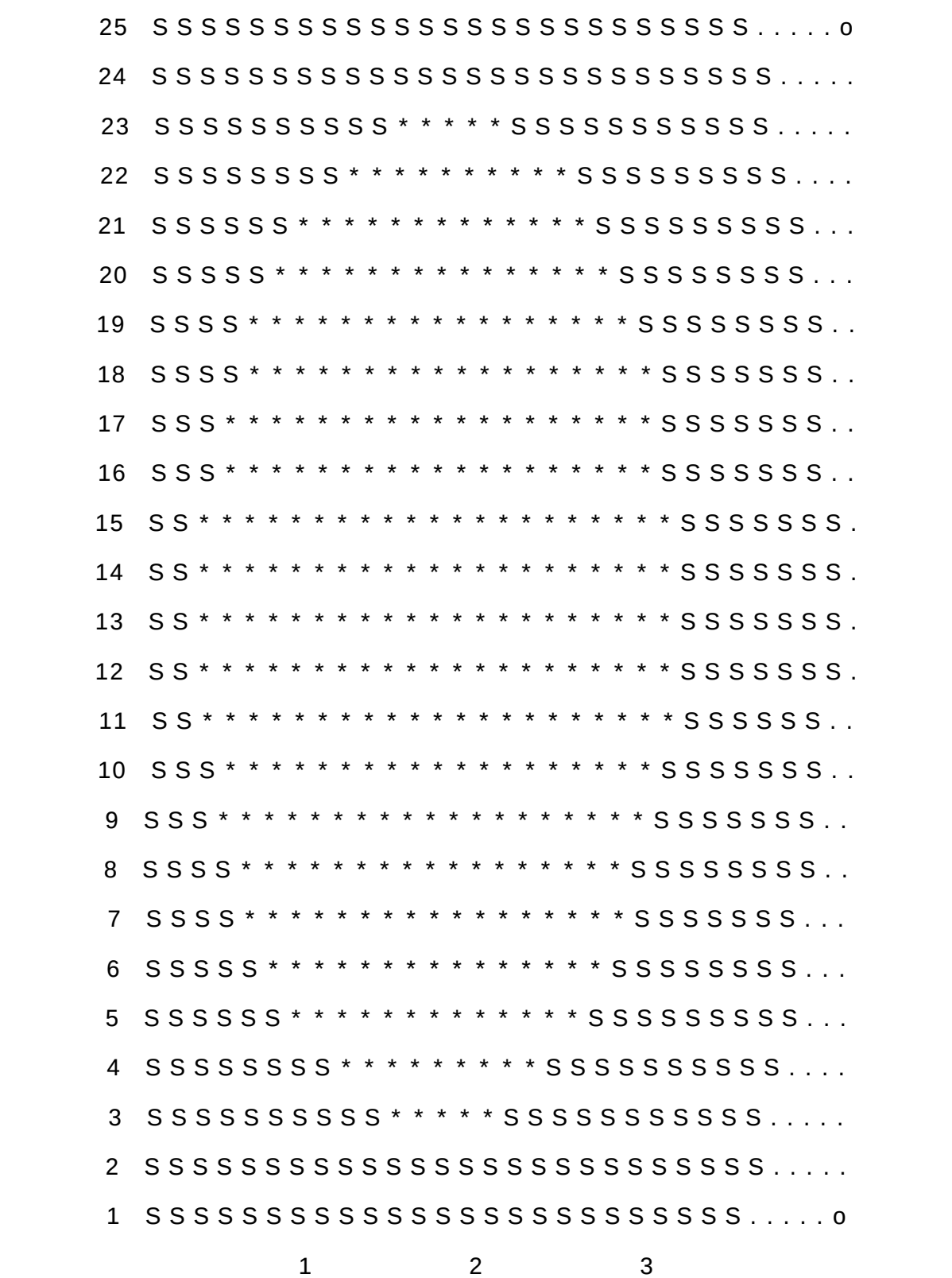
N: NUMBER OF ELEMENTS IN REGION,

POT: POTENTIAL CONTACT AREA

CON: CONTACT, ADH: ADHESION, I: NUMBER OF ITERATIONS IN

NPOT	NCON	NADH	NSLIP	INORM	ITANG
1875	700	335	365	1	1

FORM OF THE CONTACT, ADHESION AND SLIP-AREA`S:



X --> Chi= 0.00 degrees

The CONTACT program ended successfully.

A.5: SUBSURFACE STRESS FOR DX1

Table A.3: Subsurface stress for DX1 for C1 50kN 20ms

z↘	x→																								
y↓	-6.0	-5.5	-5.0	-4.5	-4.0	-3.5	-3.0	-2.5	-2.0	-1.5	-1.0	-0.5	0.0	0.5	1.0	1.5	2.0	2.5	3.0	3.5	4.0	4.5	5.0	5.5	6.0
-6.03	14.6	16.0	17.5	19.2	21.0	22.8	24.8	26.7	28.6	30.2	31.5	32.3	32.6	32.3	31.5	30.2	28.6	26.8	24.8	22.9	21.0	19.2	17.6	16.0	14.7
-5.53	16.0	17.7	19.5	21.7	24.0	26.5	29.2	32.0	34.7	37.4	39.6	40.8	41.1	40.6	39.4	37.5	34.9	32.0	29.2	26.5	24.0	21.7	19.6	17.7	16.0
-5.03	17.5	19.5	21.9	24.6	27.6	31.1	35.1	39.3	43.4	49.6	53.9	56.1	56.7	55.8	53.5	49.7	44.2	39.1	35.0	31.2	27.7	24.6	21.9	19.6	17.5
-4.52	19.2	21.7	24.6	28.1	32.3	37.3	43.5	52.3	59.1	63.8	65.3	66.5	67.5	67.2	64.9	60.1	55.7	51.0	43.9	37.4	32.3	28.2	24.6	21.7	19.2
-4.02	20.9	24.0	27.6	32.3	38.0	45.8	56.3	63.6	69.3	72.9	75.1	76.1	76.5	76.2	75.2	73.4	71.1	62.5	54.4	46.0	38.0	32.3	27.7	24.0	21.0
-3.52	22.8	26.5	31.1	37.3	46.1	56.7	67.1	72.6	76.5	79.3	81.2	82.4	82.7	82.4	81.3	79.4	76.7	73.4	66.7	56.1	45.7	37.2	31.1	26.5	22.9
-3.02	24.7	29.1	34.9	43.9	54.4	66.2	73.9	78.2	81.9	84.6	86.5	87.6	87.9	87.6	86.6	84.9	82.2	78.6	74.1	67.7	55.5	43.5	35.1	29.2	24.8
-2.51	26.7	31.9	39.1	50.8	62.3	73.3	78.3	82.7	86.4	89.0	90.7	91.7	91.9	91.7	90.8	89.2	86.6	83.1	78.6	72.9	63.6	52.1	39.3	32.0	26.7
-2.01	28.5	34.8	44.2	55.6	70.4	76.4	81.8	86.3	89.8	92.3	94.0	94.8	94.9	94.7	94.1	92.6	90.1	86.7	82.3	76.9	69.2	57.4	43.5	34.7	28.6
-1.51	30.1	37.4	49.5	59.7	73.1	79.1	84.5	88.8	92.2	94.7	96.3	96.9	96.9	96.9	96.5	95.0	92.7	89.4	85.2	79.8	73.8	63.3	49.6	37.4	30.2
-1.01	31.4	39.3	53.3	64.4	74.8	81.0	86.3	90.5	93.7	96.1	97.6	98.2	97.7	98.2	97.9	96.6	94.3	91.1	87.1	81.9	75.8	65.1	53.3	39.4	31.5
-0.5	32.1	40.5	55.6	66.9	76.0	82.2	87.4	91.4	94.4	96.5	97.5	97.5	99.1	98.6	98.2	97.1	95.0	92.1	88.2	83.1	77.0	67.9	55.2	40.5	32.2
0	32.4	41.0	56.5	67.4	76.4	82.6	87.7	91.7	94.6	96.3	96.2	92.4	93.1	96.3	97.2	96.9	95.2	92.4	88.6	83.6	77.5	70.1	55.6	40.8	32.4
0.5	32.2	40.7	56.0	66.7	76.2	82.4	87.5	91.5	94.5	96.4	97.2	95.6	91.3	96.0	97.5	96.9	95.0	92.2	88.4	83.4	77.5	70.5	54.7	40.3	32.1
1.01	31.4	39.4	53.8	66.0	75.4	81.5	86.7	90.8	94.0	96.2	97.3	97.1	95.9	97.2	97.6	96.5	94.4	91.4	87.5	82.5	76.7	68.2	52.6	39.1	31.3
1.51	30.1	37.3	49.6	65.6	73.7	79.8	85.1	89.3	92.6	94.9	96.2	96.5	96.3	96.6	96.4	95.2	93.0	89.9	85.9	80.7	75.1	62.9	49.3	37.3	30.1
2.01	28.4	34.5	43.2	59.2	70.7	77.3	82.6	87.0	90.3	92.7	94.1	94.8	94.9	94.8	94.3	92.9	90.6	87.4	83.3	78.2	74.0	55.4	44.4	34.8	28.5
2.51	26.6	31.8	39.2	52.7	66.3	74.1	79.3	83.7	87.1	89.5	91.1	91.9	92.2	92.0	91.2	89.7	87.3	84.0	79.9	75.2	65.8	50.2	39.3	32.0	26.7
3.02	24.7	29.0	34.9	43.2	56.9	71.0	75.5	79.6	83.0	85.5	87.2	88.1	88.4	88.1	87.2	85.6	83.1	79.6	75.6	71.1	54.4	43.7	35.0	29.1	24.7
3.52	22.7	26.4	31.0	37.1	45.3	57.4	70.1	75.2	77.9	80.4	82.2	83.2	83.5	83.1	82.1	80.3	77.8	74.4	71.4	56.5	45.5	37.2	31.1	26.5	22.8
4.02	20.9	23.9	27.5	32.1	37.8	45.7	54.9	65.7	73.8	74.8	76.4	77.3	77.4	77.0	76.1	74.4	70.6	66.8	55.6	45.4	37.9	32.2	27.6	23.9	20.9
4.52	19.1	21.6	24.5	28.0	32.1	37.2	43.7	50.0	55.4	62.5	67.7	70.1	70.0	68.1	65.7	64.4	57.8	52.1	43.1	37.0	32.1	28.0	24.5	21.6	19.2
5.03	17.4	19.5	21.8	24.5	27.5	31.0	34.8	39.0	44.3	49.2	52.4	54.5	55.4	55.0	53.1	49.4	43.7	39.2	34.9	31.0	27.5	24.5	21.8	19.5	17.5
5.53	15.9	17.6	19.5	21.6	23.9	26.4	29.0	31.9	34.7	37.2	39.0	40.1	40.6	40.4	39.3	37.3	34.7	31.9	29.1	26.4	23.9	21.6	19.5	17.6	16.0
6.03	14.6	15.9	17.4	19.1	20.9	22.7	24.7	26.6	28.4	30.0	31.2	32.0	32.3	32.1	31.4	30.1	28.5	26.6	24.7	22.8	20.9	19.1	17.5	16.0	14.6

A.6: ANSYS INPUT DATA

Table A.4: 50 kN processed loads from CONTACT for Ansys Input

Steps	Loads: 50kN Smooth							
1	273.9	0	0	0	0	0	0	0
2	284.2	284.2	0	0	0	0	0	0
3	255.7	255.7	255.7	0	0	0	0	0
4	0	273.9	273.9	273.9	0	0	0	0
5	0	0	284.2	284.2	284.2	0	0	0
6	0	0	0	255.7	255.7	255.7	0	0
7	0	0	0	0	273.9	273.9	273.9	0
8	0	0	0	0	0	284.2	284.2	284.2
9	0	0	0	0	0	0	255.7	255.7
10	0	0	0	0	0	0	0	273.9

Table A.5: 100 kN processed loads from CONTACT for Ansys Input

Steps	Loads: 100kN Smooth							
1	732.3	0	0	0	0	0	0	0
2	433.8	433.8	0	0	0	0	0	0
3	469.8	469.8	469.8	0	0	0	0	0
4	0	732.3	732.3	732.3	0	0	0	0
5	0	0	433.8	433.8	433.8	0	0	0
6	0	0	0	469.8	469.8	469.8	0	0
7	0	0	0	0	732.3	732.3	732.3	0
8	0	0	0	0	0	433.8	433.8	433.8
9	0	0	0	0	0	0	469.8	469.8
10	0	0	0	0	0	0	0	732.3

Table A.6: 150 kN processed loads from CONTACT for Ansys Input

Steps	Loads: 150kN Smooth							
1	1067	0	0	0	0	0	0	0
2	559.6	559.6	0	0	0	0	0	0
3	522.2	522.2	522.2	0	0	0	0	0
4	0	1067	1067	1067	0	0	0	0
5	0	0	559.6	559.6	559.6	0	0	0
6	0	0	0	522.2	522.2	522.2	0	0
7	0	0	0	0	1067	1067	1067	0
8	0	0	0	0	0	559.6	559.6	559.6
9	0	0	0	0	0	0	522.2	522.2
10	0	0	0	0	0	0	0	1067

Table A.7: 200 kN processed loads from CONTACT for Ansys Input

Steps	Loads: 200kN Smooth							
1	1192	0	0	0	0	0	0	0
2	693.2	693.2	0	0	0	0	0	0
3	637.9	637.9	637.9	0	0	0	0	0
4	0	1192	1192	1192	0	0	0	0
5	0	0	693.2	693.2	693.2	0	0	0
6	0	0	0	637.9	637.9	637.9	0	0
7	0	0	0	0	1192	1192	1192	0
8	0	0	0	0	0	693.2	693.2	693.2
9	0	0	0	0	0	0	637.9	637.9
10	0	0	0	0	0	0	0	1192

Table A.8: 250 kN processed loads from CONTACT for Ansys Input

Steps	Loads: 250kN Smooth							
1	1331	0	0	0	0	0	0	0
2	826	826	0	0	0	0	0	0
3	762.6	762.6	762.6	0	0	0	0	0
4	0	1331	1331	1331	0	0	0	0
5	0	0	826	826	826	0	0	0
6	0	0	0	762.6	762.6	762.6	0	0
7	0	0	0	0	1331	1331	1331	0
8	0	0	0	0	0	826	826	826
9	0	0	0	0	0	0	762.6	762.6
10	0	0	0	0	0	0	0	1331

Table A.9: 300 kN processed loads from CONTACT for Ansys Input

Steps	Loads: 300kN Smooth							
1	1476	0	0	0	0	0	0	0
2	956.1	956.1	0	0	0	0	0	0
3	884.9	884.9	884.9	0	0	0	0	0
4	0	1476	1476	1476	0	0	0	0
5	0	0	956.1	956.1	956.1	0	0	0
6	0	0	0	884.9	884.9	884.9	0	0
7	0	0	0	0	1476	1476	1476	0
8	0	0	0	0	0	956.1	956.1	956.1
9	0	0	0	0	0	0	884.9	884.9
10	0	0	0	0	0	0	0	1476

Table A.10: 50 kN processed loads from CONTACT for Ansys Input

Steps	Loads: 50kN Corrugated							
1	330.5	0	0	0	0	0	0	0
2	1710	1710	0	0	0	0	0	0
3	631.4	631.4	631.4	0	0	0	0	0
4	0	330.5	330.5	330.5	0	0	0	0
5	0	0	1710	1710	1710	0	0	0
6	0	0	0	631.4	631.4	631.4	0	0
7	0	0	0	0	330.5	330.5	330.5	0
8	0	0	0	0	0	1710	1710	1710
9	0	0	0	0	0	0	631.4	631.4
10	0	0	0	0	0	0	0	330.5

Table A.11: 100 kN processed loads from CONTACT for Ansys Input

Steps	Loads: 100kN Corrugated							
1	505.3	0	0	0	0	0	0	0
2	2516	2516	0	0	0	0	0	0
3	3641	3641	1125	0	0	0	0	0
4	0	505.3	505.3	505.3	0	0	0	0
5	0	0	2516	2516	2516	0	0	0
6	0	0	0	3641	3641	1125	0	0
7	0	0	0	0	505.3	505.3	505.3	0
8	0	0	0	0	0	2516	2516	2516
9	0	0	0	0	0	0	3641	3641
10	0	0	0	0	0	0	0	505.3

Table A.12: 150 kN processed loads from CONTACT for Ansys Input

Steps	Loads: 150kN Corrugated							
1	665.6	0	0	0	0	0	0	0
2	3313	3313	0	0	0	0	0	0
3	4806	4806	1493	0	0	0	0	0
4	0	665.6	665.6	665.6	0	0	0	0
5	0	0	3313	3313	3313	0	0	0
6	0	0	0	4806	4806	1493	0	0
7	0	0	0	0	665.6	665.6	665.6	0
8	0	0	0	0	0	3313	3313	3313
9	0	0	0	0	0	0	4806	4806
10	0	0	0	0	0	0	0	665.6

Table A.13: 200 kN processed loads from CONTACT for Ansys Input

Steps	Loads: 200kN Corrugated							
1	804.3	0	0	0	0	0	0	0
2	4011	4011	0	0	0	0	0	0
3	5828	5828	1817	0	0	0	0	0
4	0	804.3	804.3	804.3	0	0	0	0
5	0	0	4011	4011	4011	0	0	0
6	0	0	0	5828	5828	1817	0	0
7	0	0	0	0	804.3	804.3	804.3	0
8	0	0	0	0	0	4011	4011	4011
9	0	0	0	0	0	0	5828	5828
10	0	0	0	0	0	0	0	804.3

Table A.14: 250 kN processed loads from CONTACT for Ansys Input

Steps	Loads: 250kN Corrugated							
1	932.8	0	0	0	0	0	0	0
2	4653	4653	0	0	0	0	0	0
3	6790	6790	2137	0	0	0	0	0
4	0	932.8	932.8	932.8	0	0	0	0
5	0	0	4653	4653	4653	0	0	0
6	0	0	0	6790	6790	2137	0	0
7	0	0	0	0	932.8	932.8	932.8	0
8	0	0	0	0	0	4653	4653	4653
9	0	0	0	0	0	0	6790	6790
10	0	0	0	0	0	0	0	932.8

Table A.15: 300 kN processed loads from CONTACT for Ansys Input

Steps	Loads: 300kN Corrugated							
1	1048	0	0	0	0	0	0	0
2	5230	5230	0	0	0	0	0	0
3	2422	2422	2422	0	0	0	0	0
4	0	1048	1048	1048	0	0	0	0
5	0	0	5230	5230	5230	0	0	0
6	0	0	0	2422	2422	2422	0	0
7	0	0	0	0	1048	1048	1048	0
8	0	0	0	0	0	5230	5230	5230
9	0	0	0	0	0	0	2422	2422
10	0	0	0	0	0	0	0	1048

A.7: CASE 4 DEM

A.7.1 CODE FOR CASE 4

```
#Clear the memory
O.reset()

#Import require modules
from yade import utils, plot

from yade import pack ,qt

from yade.params.table import *

#Read data from for batch simulation from file
readParamsFromTable(unknownOk=True,dt=0.0006,force=0.006375,noTableOk
=True)

#print values of force and frequency that has been assigned to the problem
print 'dt' ,'force'

# Set up run

run_name="DEM_Simulation"

data_root_dir="."


# Materials

##Sleeper material parameters
plate_material=FrictMat(
        young=200e9
        ,poisson=0.3
        ,density=8000.
        ,frictionAngle=radians(30)
        ,label='plate_mat')
O.materials.append(plate_material)


##Ballast material parameters

sample_material=CohFrictMat(
        young=4e9
        ,poisson=0.25
```

```
        ,density=2600
        ,frictionAngle=radians(30)
        ,normalCohesion=1e8*1.2
        ,shearCohesion=.4e8*1.2
        ,momentRotationLaw=True
        ,label='sample_mat')
O.materials.append(sample_material)


##Bitumen material parameters
id_Mat3=O.materials.append(FrictMat
(young=3e8,poisson=0.2,density=1500,frictionAngle=0.25))
Geocell=O.materials[id_Mat3]
bitumen_material=O.materials.append(ViscElMat
(kn=1e9,cn=300e4,ks=1.4e4,cs=200e4,frictionAngle=0.36,label='bitumen_mat'
))


#Geometry
##Granular material dimension
sample_diameter=5e-2
sample_radius=sample_diameter/2.0
# Sub-particle dimension
particle_diameter=3e-2
particle_radius=particle_diameter/2.
rotvel=0


##Set up periodic boundary conditions
O.periodic=True
xExt=14*sample_diameter
yExt=4.5*sample_diameter*2 #to block the periodicity in y direction
zExt=0.3
xLim=xExt
```

```
yLim=yExt
zLim=zExt
O.cell.hSize=Matrix3(
        xExt, 0, 0,
        0, yExt, 0,
        0, 0, zExt)
###where:
length=xExt
height=yExt
width=zExt
thickness=0.1*height

##Sleeper Geometry
topBoxes = []
for ix in (0,1,2):
        for iz in (0,1,2):
                topBoxes.append(box(
        center=(xExt/6.*(1+2*ix),0.,zExt/6.*(1+2*iz))
                ,extents=(xExt/6.,thickness/2.0,zExt/6.)
                ,wire=False
                ,material='plate_mat'
                ))
top_id,top_ids = O.bodies.appendClumped(topBoxes)
### Apply BC to allow sleeper to move only down
O.bodies[top_id].state.blockedDOFs='xzXYZ'
###Force changes on each iteration following sine function
plate_downforce=abs(math.sin(O.iter)*-force-force)
O.forces.addF(top_id,(0,plate_downforce,0),permanent=True)
```

```
##Subgrade
bottomBoxes = []
for ix in (0,1,2):
        for iz in (0,1,2):
        bottomBoxes.append(box(
        center=(xExt/6.*(1+2*ix),yLim - thickness/2.0,zExt/6.*(1+2*iz))
        ,extents=(xExt/6.,thickness/2.0,zExt/6.)
        ,wire=False
        ,material='plate_mat'
        ))
### Apply BC to fix subgrade
bottom_id,bottom_ids = O.bodies.appendClumped(bottomBoxes)
O.bodies[bottom_id].state.blockedDOFs='xyzXYZ'

###Meter to measure settlement this individual particle
s1=utils.sphere([0.350,0.435,0.0050],0.010,fixed=False,dynamic=True)
O.bodies.append(s1)

#Ballast creation
## Ballast Packing dimension
min_corner= (0,yLim,0)
max_corner= (xLim, yExt-yLim, zLim)
sp=pack.SpherePack()
sp.makeCloud( min_corner,max_corner, rMean=sample_radius, periodic=False)
##Create cloud
print "Generated ",len(sp)," aggregates"
for s in sp:
        sphere=pack.inSphere((s[0][0],s[0][1],s[0][2]),s[1])
        sp1=pack.randomDensePack(
                sphere
```

```
        ,spheresInCell=2000
        ,radius=particle_radius
        ,memoizeDb='/tmp/triaxPackCache.sqlite'
        ,returnSpherePack=True
        )
sp1.toSimulation(material='sample_mat',color=(0.9,0.8,0.6))
print 'Generated ',len(sp1),' particles'
Gl1_Sphere(stripes=True)

## Bitumen Packing
min_corner= (0,yLim,0)
max_corner= (xLim, yExt-yLim, zLim)
sp2=pack.SpherePack()
sp2.makeCloud( min_corner,max_corner, rMean=5e-2, periodic=False)
sp2.toSimulation(material='bitumen_mat',color=(12,12,1))

##Geocell
###Geocell arrangement:
#9###4###3
#8###1###2
#7###6###5

###Creates hollow cylinders in specified coordinates
pred=pack.inCylinder((0.350,0.400,0.150),(0.350,.200,.150),.078)-
pack.inCylinder
((.350,.400,.150),(.350,.200,.150),.070)
pred2=pack.inCylinder((0.425,0.400,0.150),(0.425,.250,.150),.0375)-
pack.inCylinder
((.425,.400,.150),(.425,.250,.150),.037)
pred3=pack.inCylinder((0.425,0.400,0.225),(0.425,.250,.225),.0375)-
pack.inCylinder
((.425,.400,0.225),(.425,.250,.225),.037)
```

```
pred4=pack.inCylinder((0.350,0.400,0.225),(0.350,.250,.225),.0375)-
pack.inCylinder

((.350,.400,.150),(.350,.250,.150),.037)

pred5=pack.inCylinder((0.425,0.400,0.075),(0.425,.250,.075),.0375)-
pack.inCylinder

((.425,.400,.075),(.425,.250,.075),.037)

pred6=pack.inCylinder((0.300,0.400,0.075),(0.300,.250,.075),.0375)-
pack.inCylinder

((.300,.400,.075),(.300,.250,.075),.037)

pred7=pack.inCylinder((0.225,0.400,0.075),(0.225,.250,.075),.0375)-
pack.inCylinder

((.225,.400,.075),(.225,.250,.075),.037)

pred8=pack.inCylinder((0.225,0.400,0.150),(0.225,0.250,0.150),.0375)-
pack.inCylinder

((.225,.400,.150),(.225,.250,.150),.037)

pred9=pack.inCylinder((0.225,0.400,0.225),(0.225,0.250,0.225),0.375)-
pack.inCylinder

((.225,.400,.225),(.225,.250,.225),.037)


pred01=O.bodies.appendClumped(pack.regularHexa

(pred,radius=0.002,gap=0.,material=Geocell))

pred02=O.bodies.appendClumped(pack.regularHexa

(pred2,radius=0.0002,gap=0.,material=Geocell))

pred03=O.bodies.appendClumped(pack.regularHexa

(pred3,radius=0.0002,gap=0.,material=Geocell))

pred04=O.bodies.appendClumped(pack.regularHexa

(pred4,radius=0.0002,gap=0.,material=Geocell))

pred05=O.bodies.appendClumped(pack.regularHexa

(pred5,radius=0.0002,gap=0.,material=Geocell))

pred06=O.bodies.appendClumped(pack.regularHexa

(pred6,radius=0.0002,gap=0.,material=Geocell))

pred07=O.bodies.appendClumped(pack.regularHexa
```

```
(pred7,radius=0.0002,gap=0.,material=Geocell))
pred08=O.bodies.appendClumped(pack.regularHexa
(pred8,radius=0.0002,gap=0.,material=Geocell))
pred09=O.bodies.appendClumped(pack.regularHexa
(pred9,radius=0.0002,gap=0.,material=Geocell))
id_clump1 = pred01[0]
id_clump2 = pred02[0]
id_clump3 = pred03[0]
id_clump4 = pred04[0]
id_clump5 = pred05[0]
id_clump6 = pred06[0]
id_clump7 = pred07[0]
id_clump8 = pred08[0]
id_clump9 = pred09[0]

O.bodies.addToClump([id_clump2],id_clump1)
O.bodies.addToClump([id_clump3],id_clump1)
O.bodies.addToClump([id_clump4],id_clump1)
O.bodies.addToClump([id_clump5],id_clump1)
O.bodies.addToClump([id_clump6],id_clump1)
O.bodies.addToClump([id_clump7],id_clump1)
O.bodies.addToClump([id_clump8],id_clump1)
O.bodies.addToClump([id_clump9],id_clump1)

# Loop the simulation
O.dt=1*dt
O.engines=[
        ForceResetter(),
        InsertionSortCollider([
                Bo1_Sphere_Aabb()
```

```
                ,Bo1_Box_Aabb()
                ], allowBiggerThanPeriod=True
                ),
InteractionLoop(
        [Ig2_Sphere_Sphere_ScGeom6D()
        ,Ig2_Box_Sphere_ScGeom6D()
        ],
        [Ip2_FrictMat_FrictMat_FrictPhys()
                ,Ip2_CohFrictMat_CohFrictMat_CohFrictPhys(setCohesionNow=True
                ,label="cohesiveIp")
                ],
                [Law2_ScGeom_FrictPhys_CundallStrack()
                ,Law2_ScGeom6D_CohFrictPhys_CohesionMoment()
                ]
        ),
        NewtonIntegrator(damping=0.8,gravity=(0.,9.81,0.)),
]
#Save and plot data
VTKRecorder(fileName='3d-vtk-',recorders=['all'],iterPeriod=100),
SnapshotEngine(iterPeriod=1000,fileBase='3d-',viewNo=0,label='snapshot')
PyRunner(command='finish()',iterPeriod=21500)
O.engines=O.engines+[PyRunner(iterPeriod=5,command='addPlotData
()',label='plotDataCollector')]
def addPlotData():
        yade.plot.addData(t=O.iter,Sleeper_z=O.bodies[0].state.pos
        [1],Ballast_z=O.bodies[2].state.pos[1],plate_downforce=abs(math.sin(O.i
        ter)*-force+force*(-1)))
##Number of runs
O.run(250,True)
##Save data to file
plot.plots={'t':('Sleeper_z',),'t ':('Ballast_z'),' t':('plate_downforce')}
```

```
plot.plot(subPlots=False)

plot.saveDataTxt('results.txt.bz2')

O.step()

##Call graphic display
qt.View()

O.saveTmp()

##Makes video from snapshots
def finish():
        makeVideo(snapshot.snapshots,'3d.mpeg',fps=10,bps=10000)
        O.pause()
        rr=yade.qt.Renderer()
        rr.shape=False
        rr.intrPhys=True
```

A.7.2 DEM COMPARED WITH EXPERIMENT

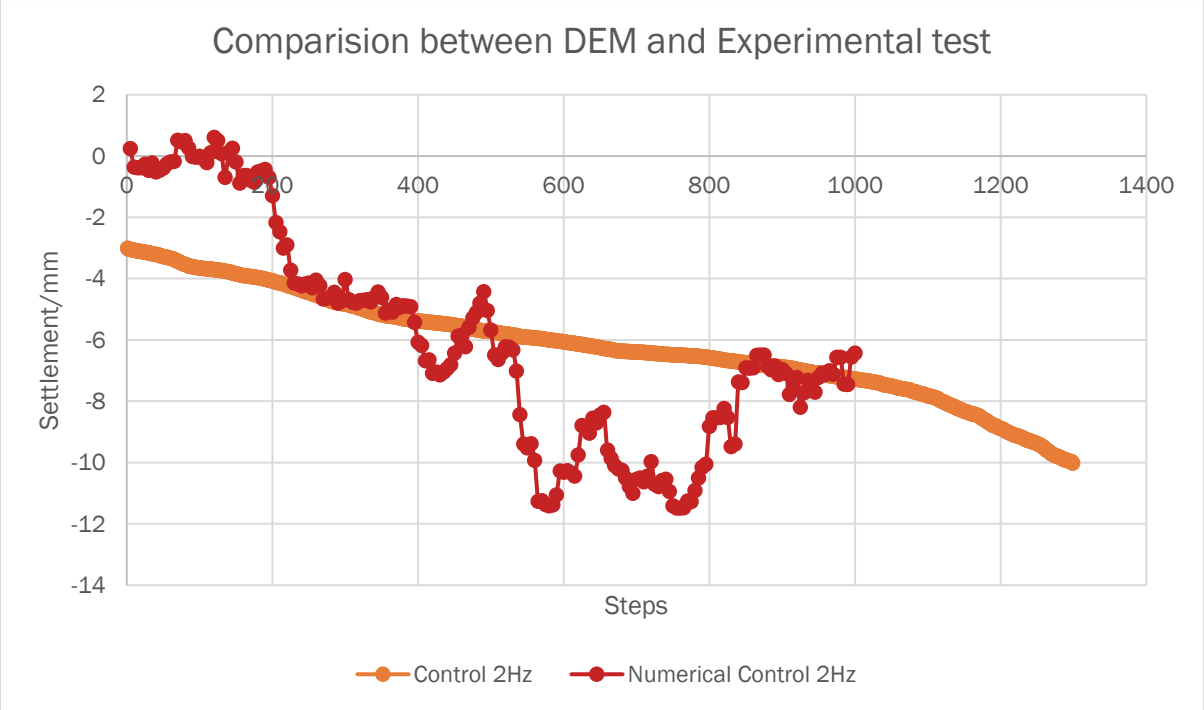


Figure A.1: Comparison between DEM and Experiment for 2Hz loading for Control

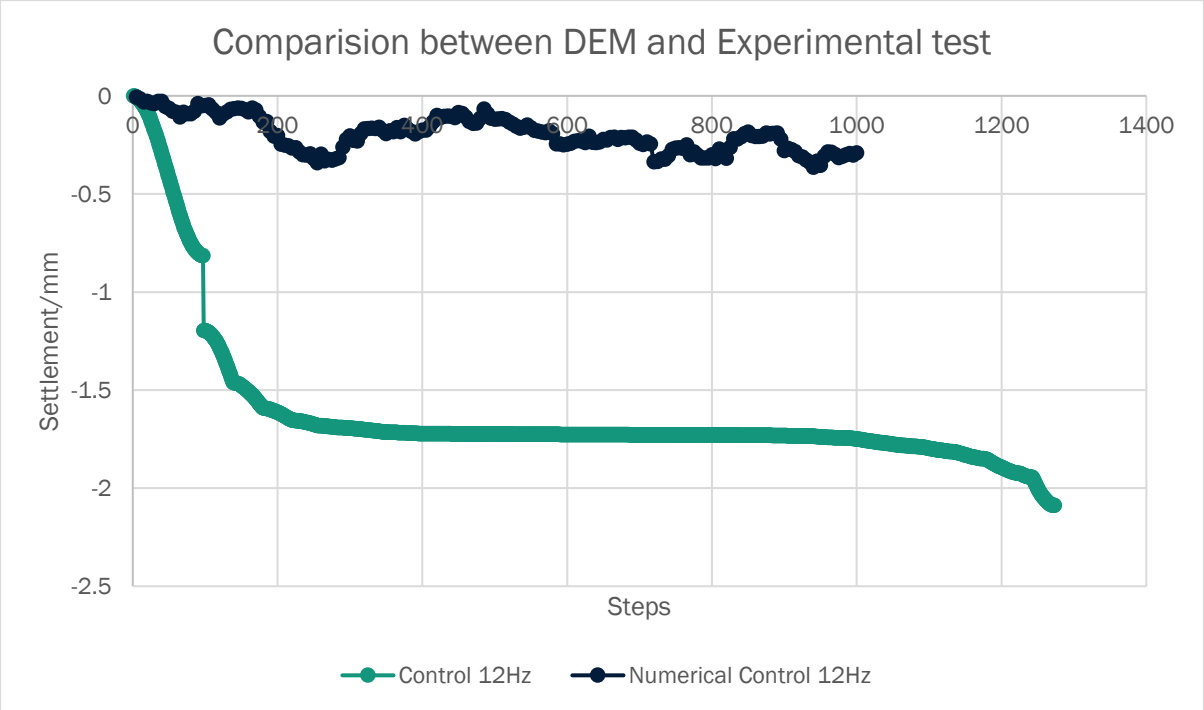


Figure A.2: Comparison between DEM and Experiment for 12Hz loading for control

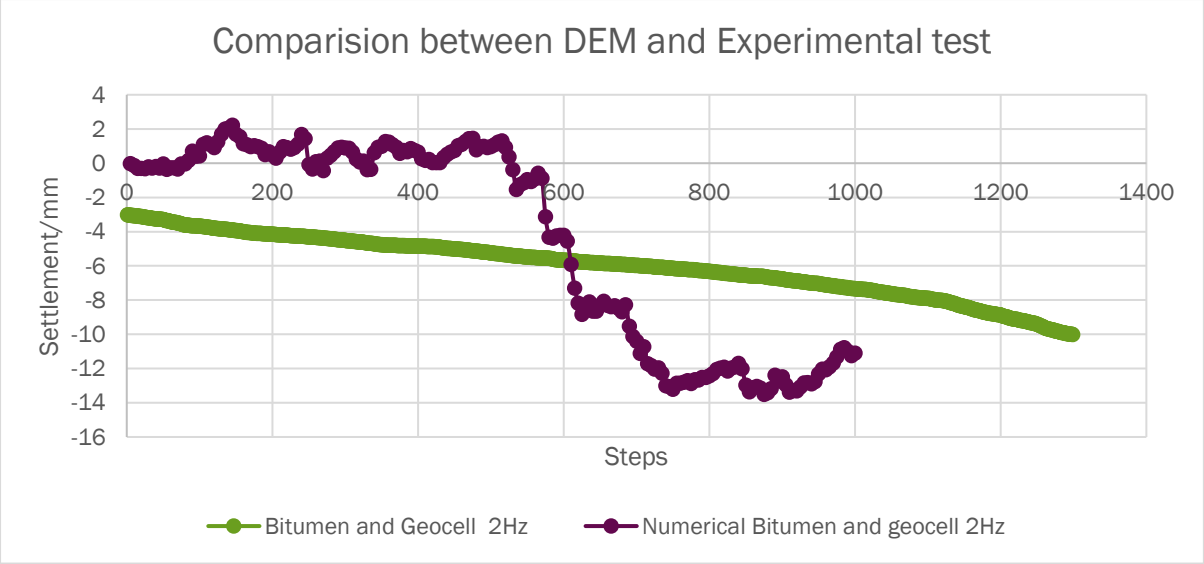


Figure A.3: Comparison between DEM and Experiment for 2Hz loading for Reinforced

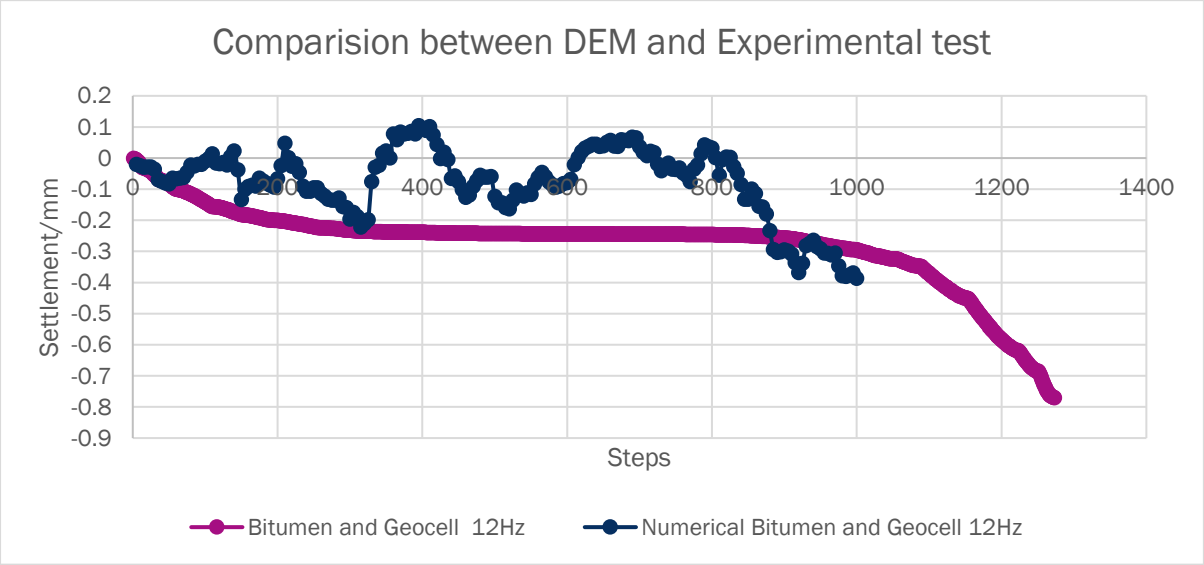


Figure A.4: Comparison between DEM and Experiment for 2Hz loading for reinforced

A.8: VIBRATING TABLE RESULTS

Calibration:

6units=1m/s^2

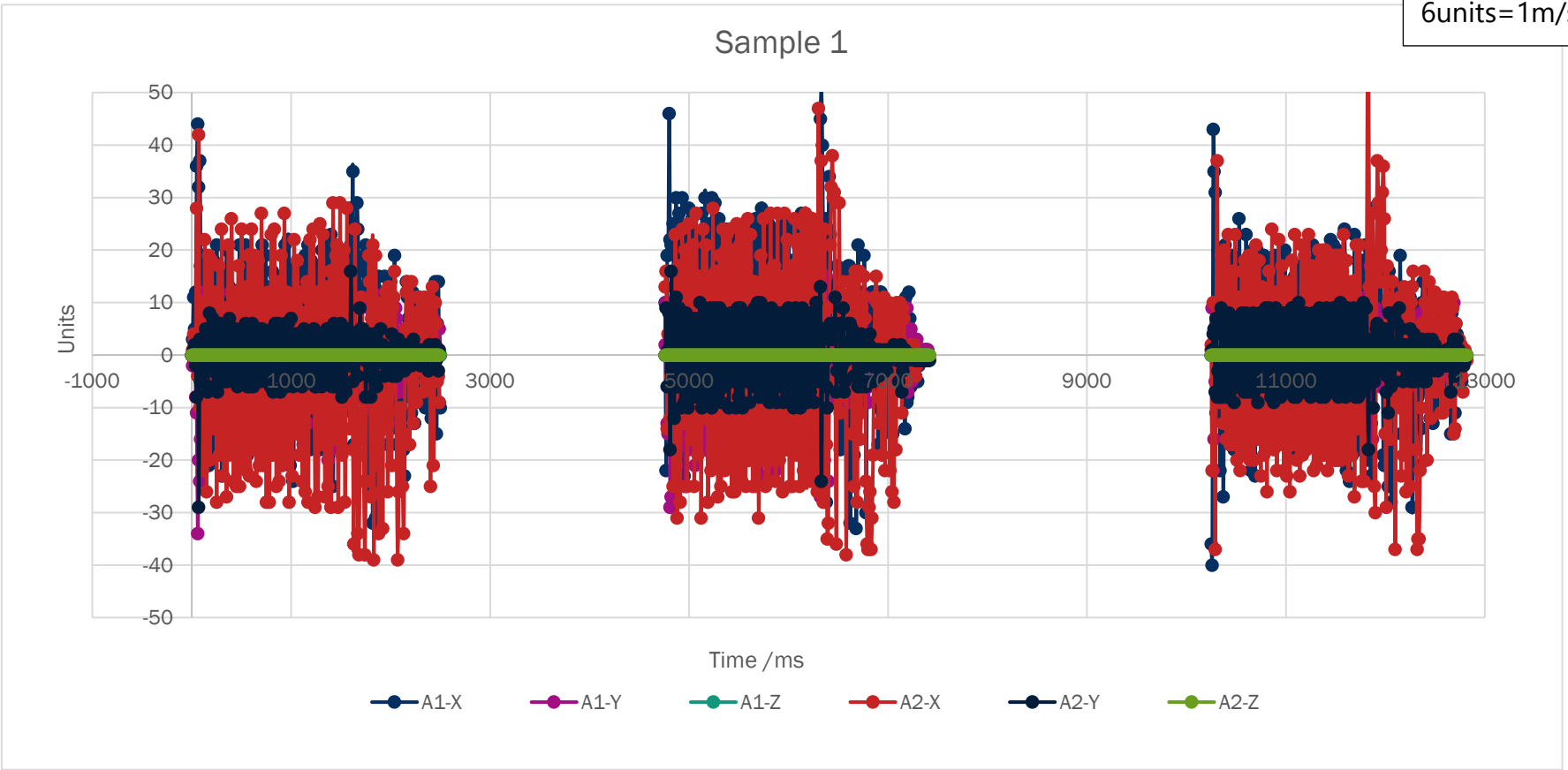


Figure A.5: Vibrating table Results for sample 1

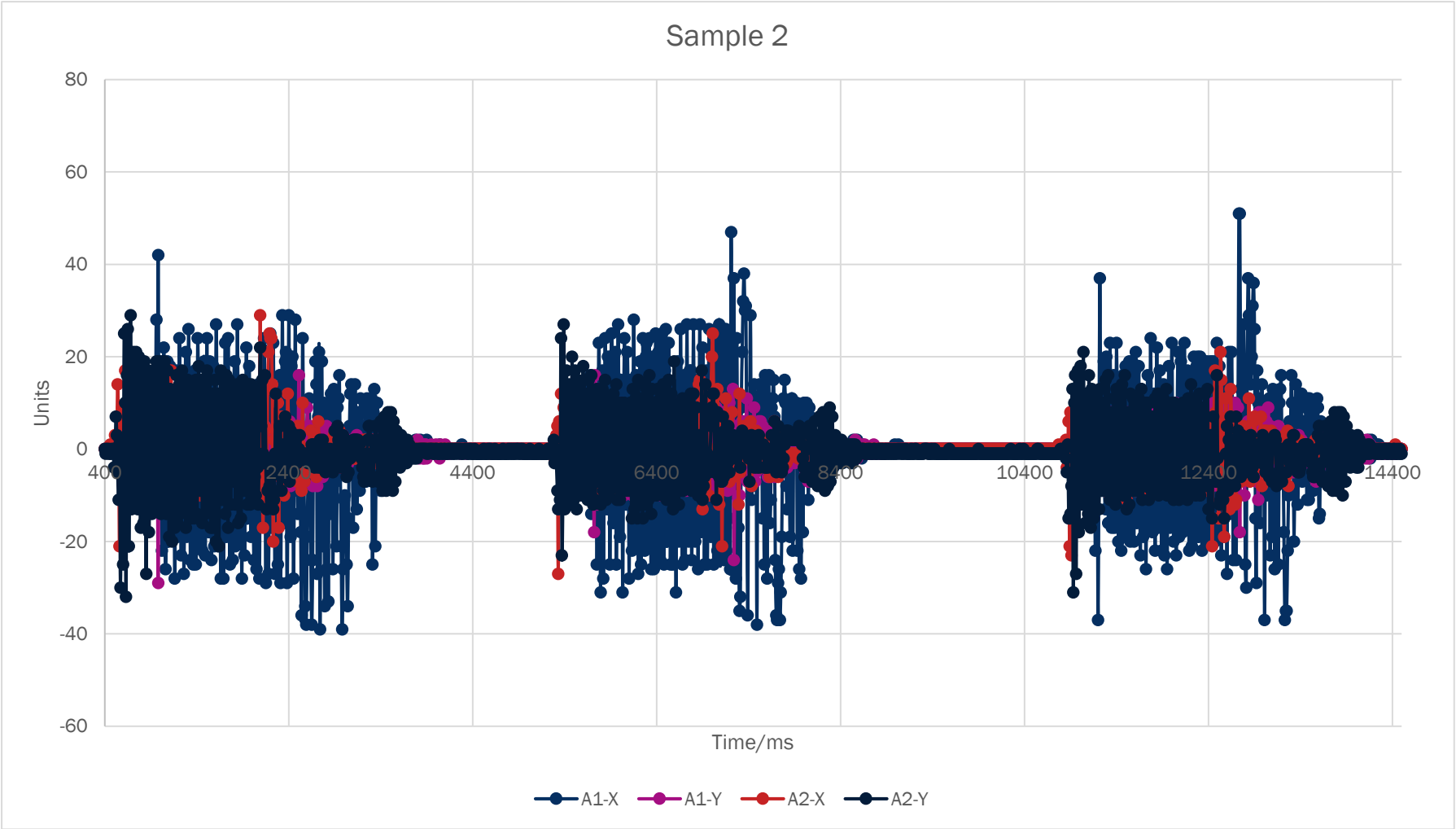


Figure A.6: Vibrating table Results for sample 2

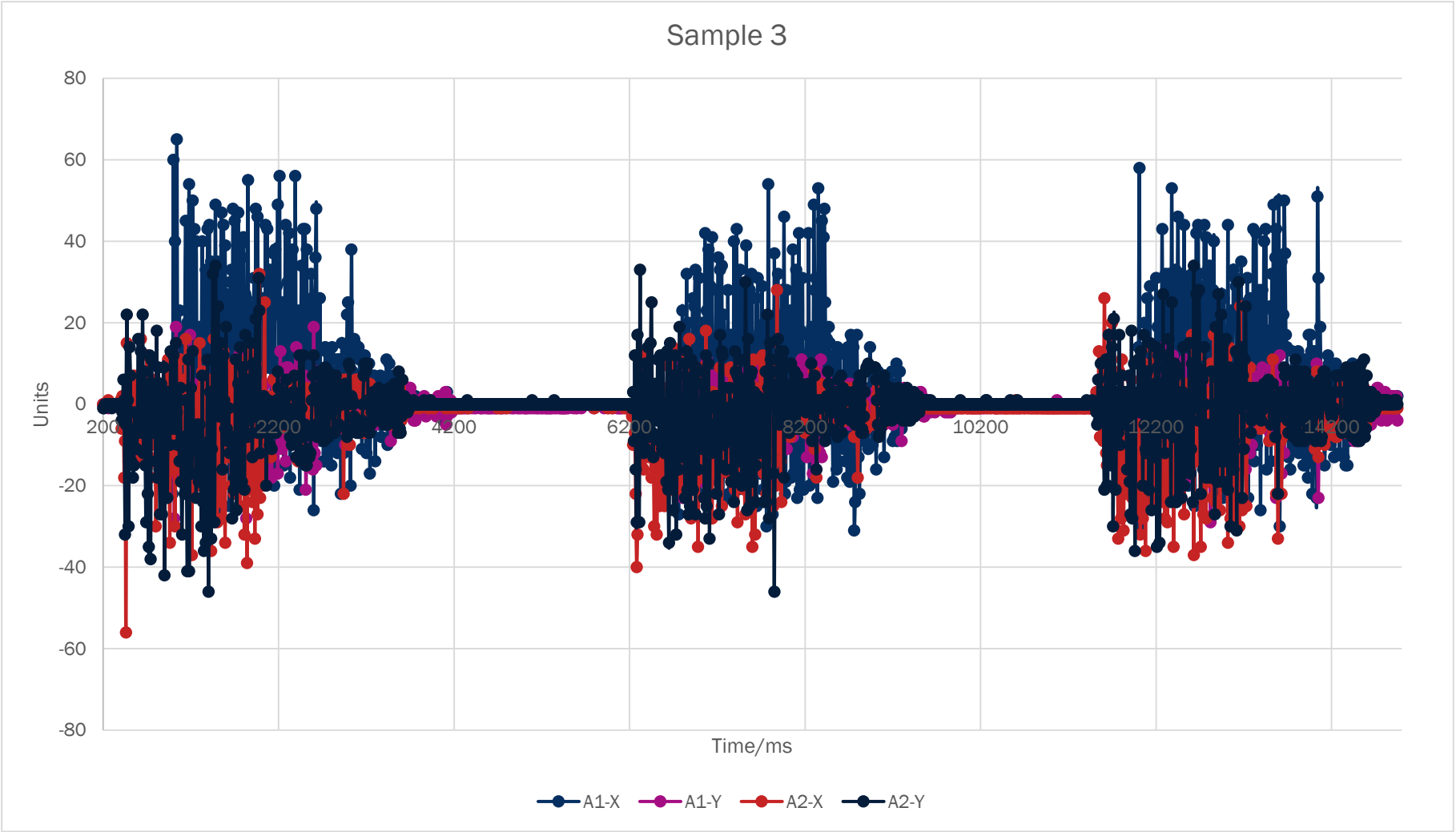


Figure A.7: Vibrating table Results for sample 3

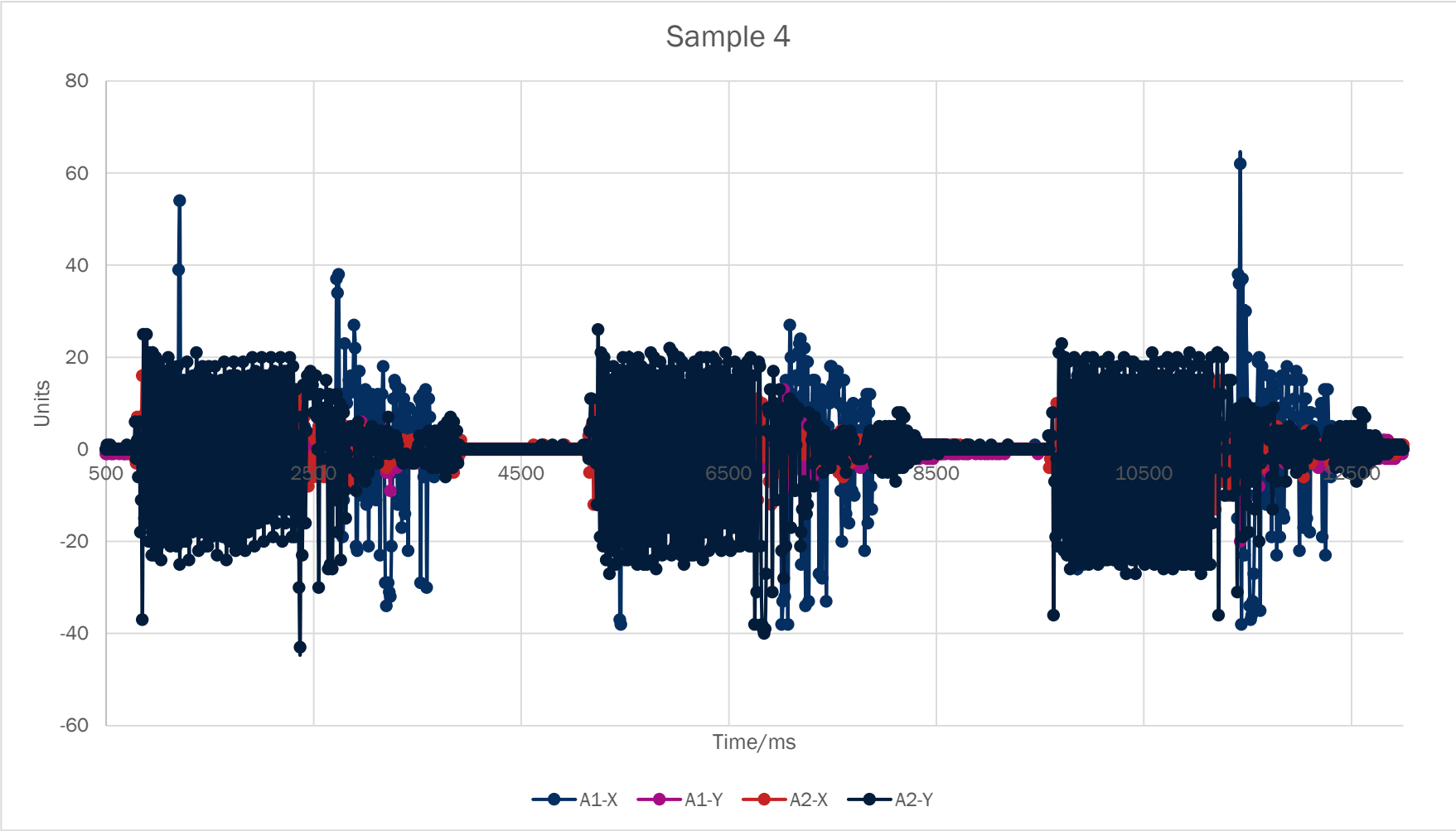


Figure A.8: Vibrating table Results for sample 4

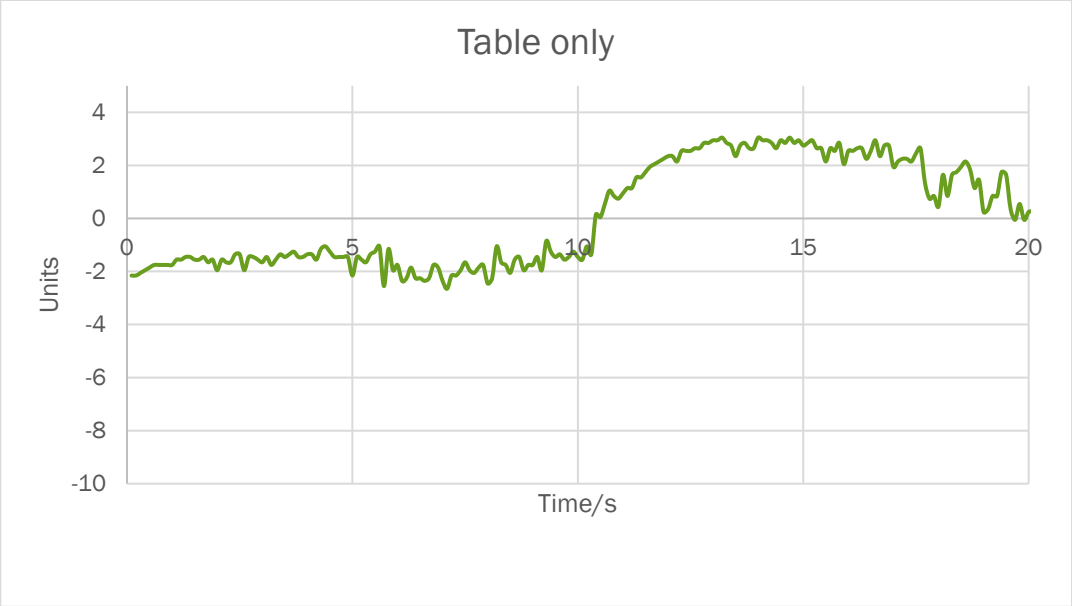


Figure A.9: Vibrating table Results for table only

Table A.14: Damping ratio of all samples (Adams & Askenazi 1999)

Table 3. Representative Damping Ratios	
System	Viscous Damping Ratio ξ
Metals (in elastic range)	<0.01
Continuous Metal Structures	0.02 to 0.04
Metal Structure with Joints	0.03 to 0.07
Aluminum / Steel Transmission Lines	≈0.0004
Small Diameter Piping Systems	0.01 to 0.02
Large Diameter Piping Systems	0.02 to 0.03
Auto Shock Absorbers	≈0.30
Rubber	≈0.05
Large Buildings during Earthquakes	0.01 to 0.05
Prestressed Concrete Structures	0.02 to 0.05
Reinforced Concrete Structures	0.04 to 0.07

A.9: CYCLIC-COMPRESSIVE TEST RESULTS

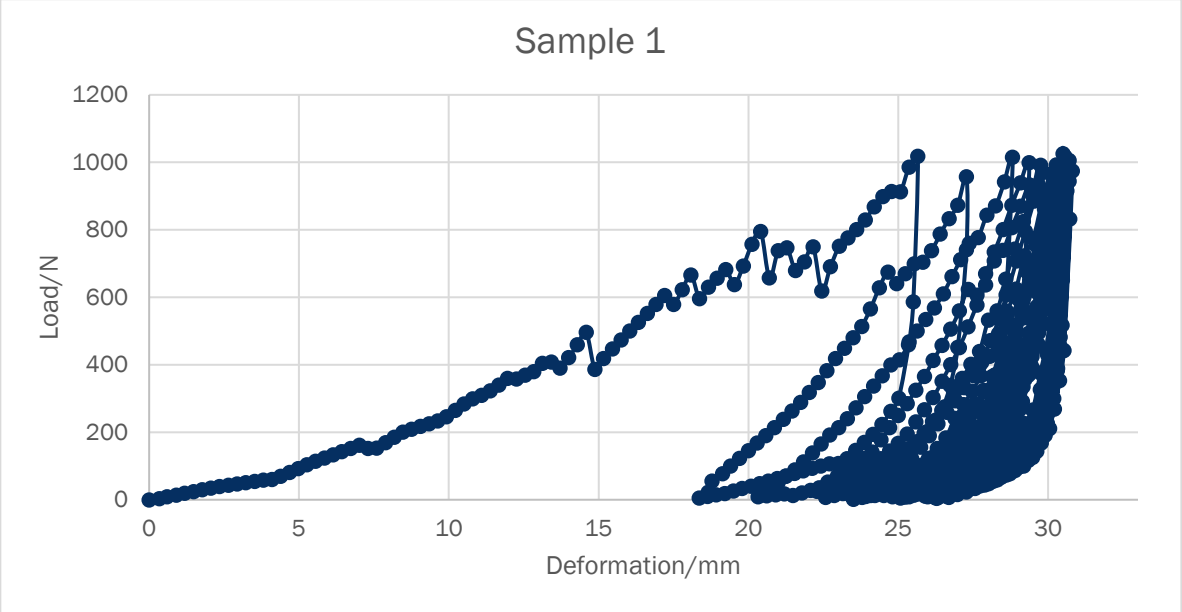


Figure A.10: Cyclic compressive test results for sample 1

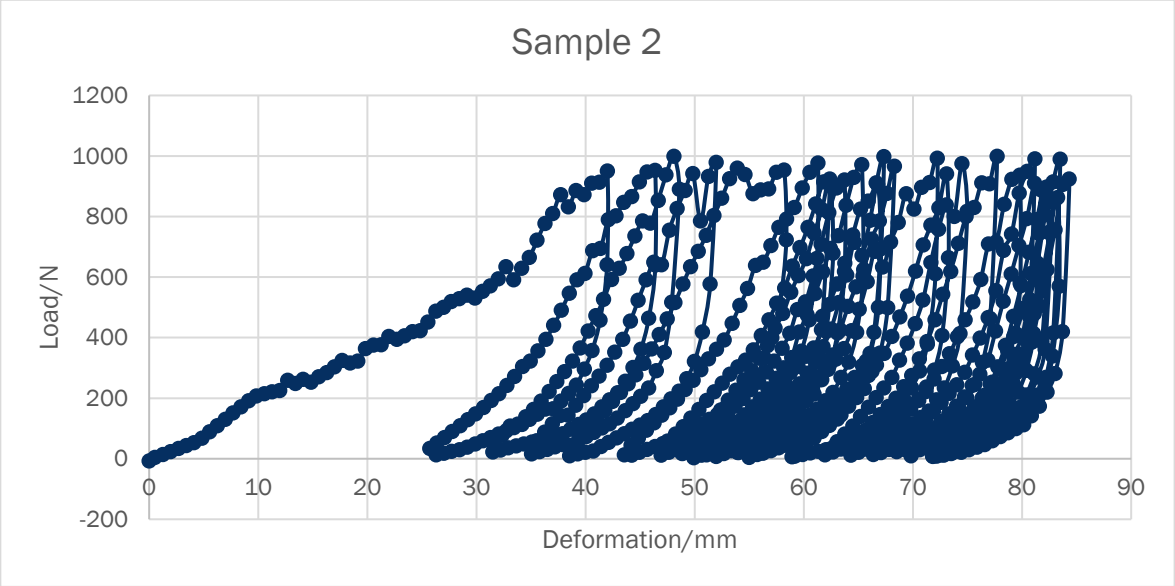


Figure A.11: Cyclic compressive test results for sample 2

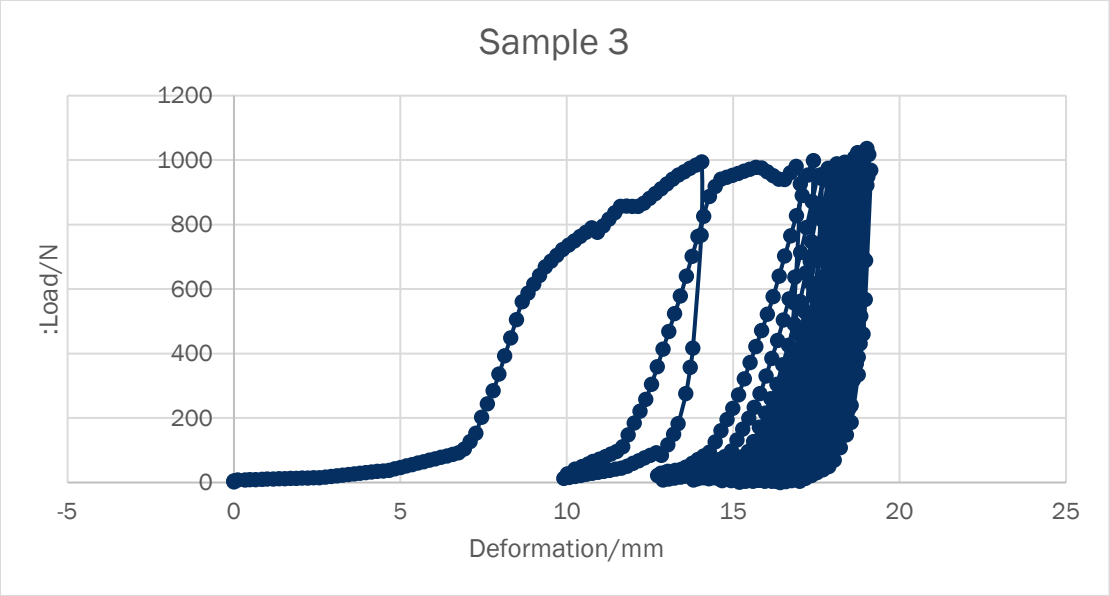


Figure A.13: Cyclic compressive test results for sample 3

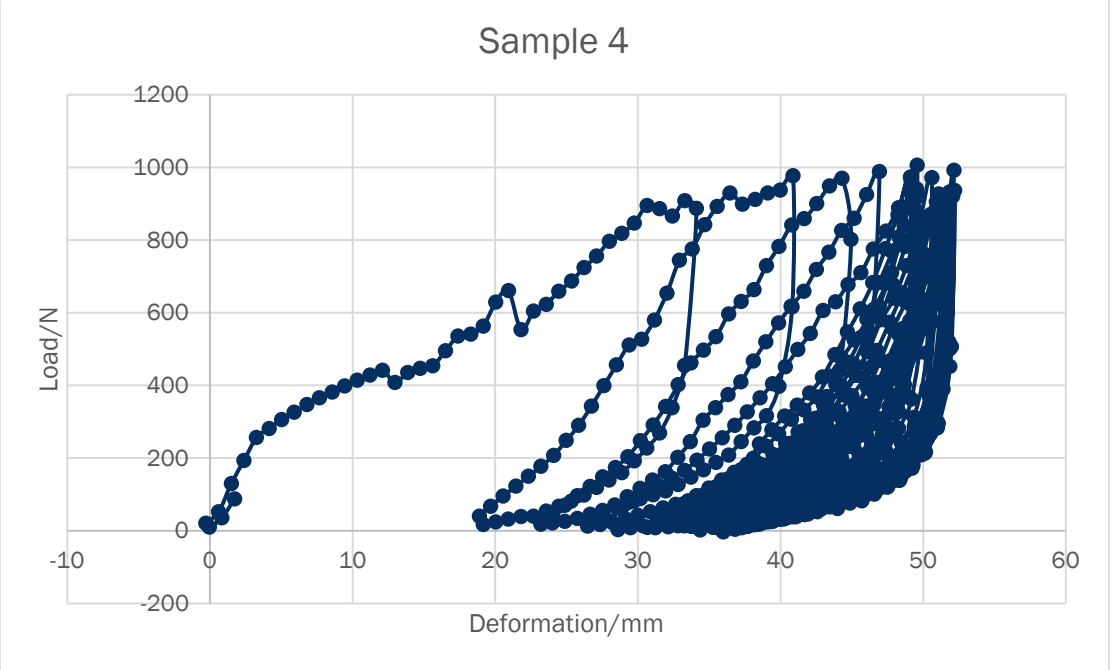


Figure A.12: Cyclic compressive test results for sample 4

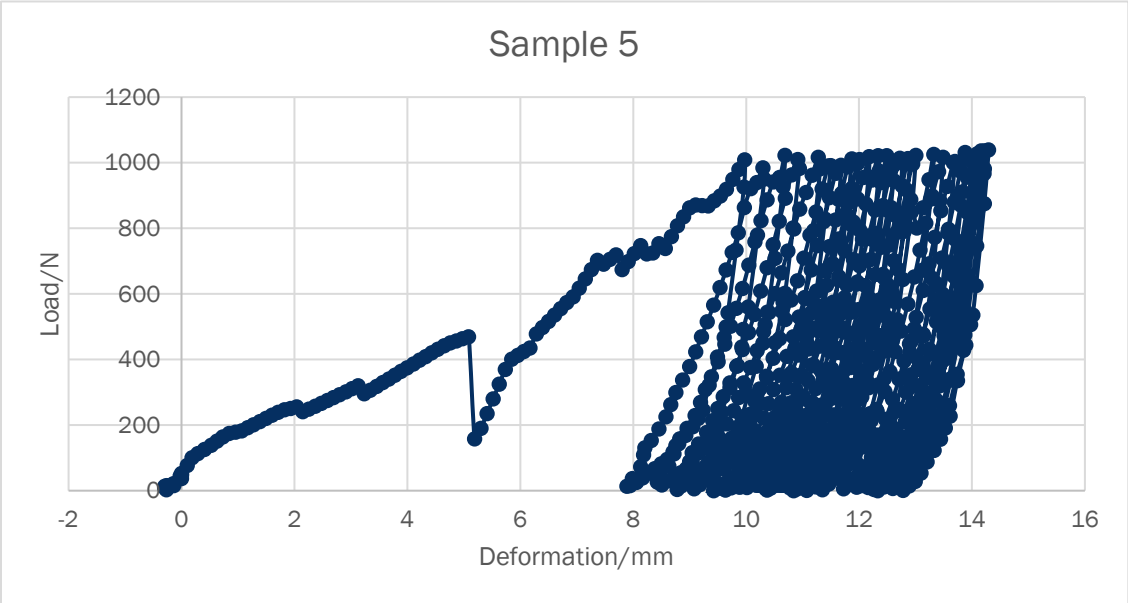


Figure A.15: Cyclic compressive test results for sample 5

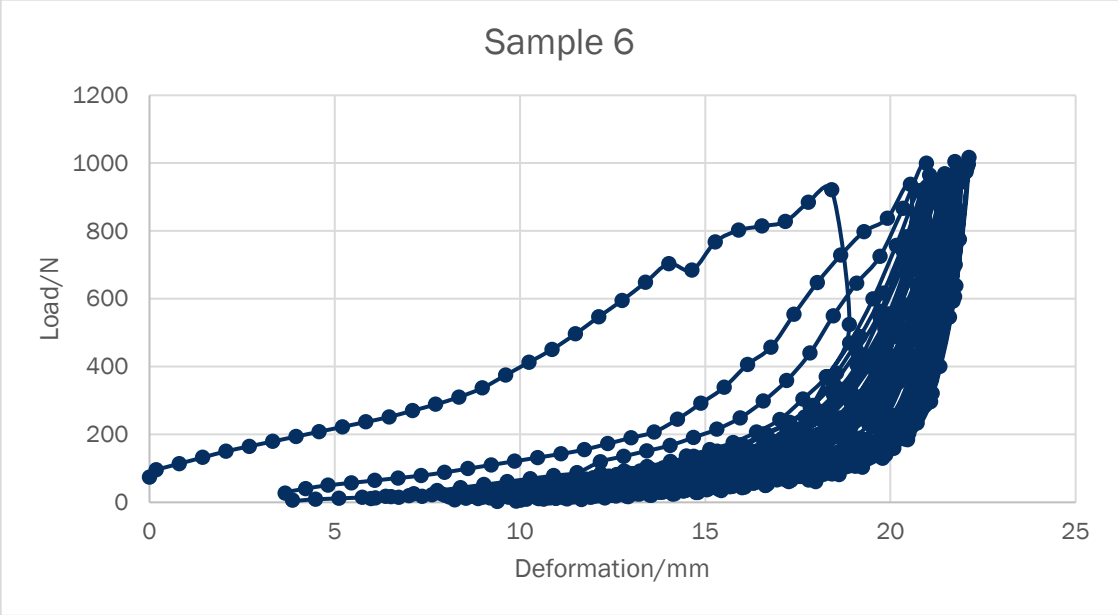


Figure A.14: Cyclic compressive test results for sample 6

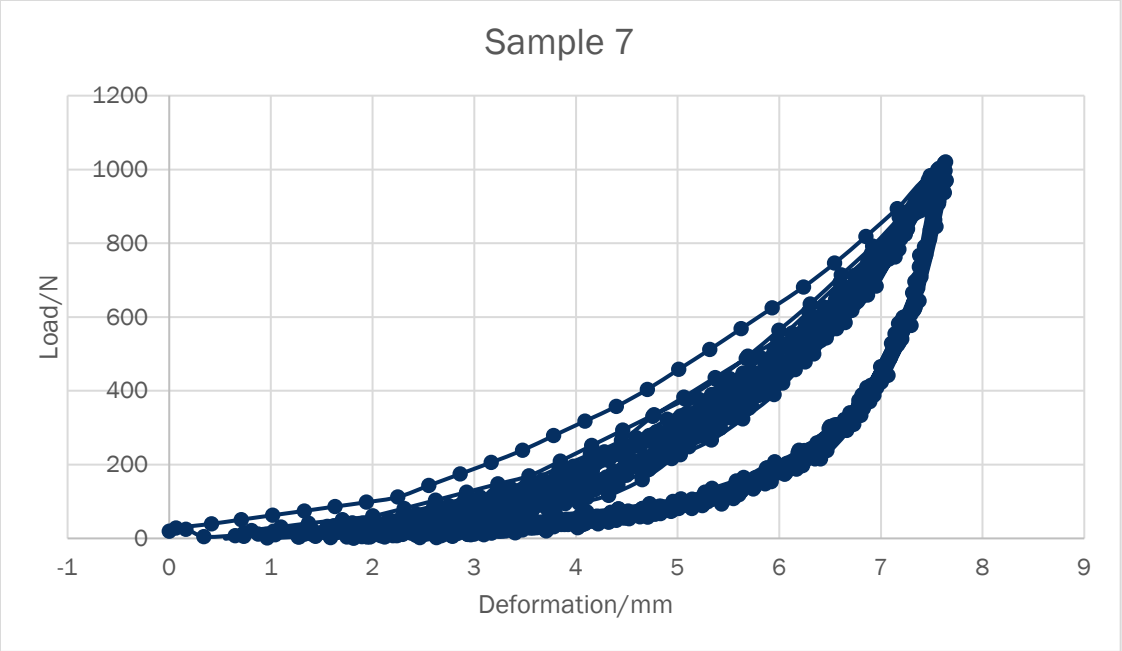


Figure A.16: Cyclic compressive test results for sample 7

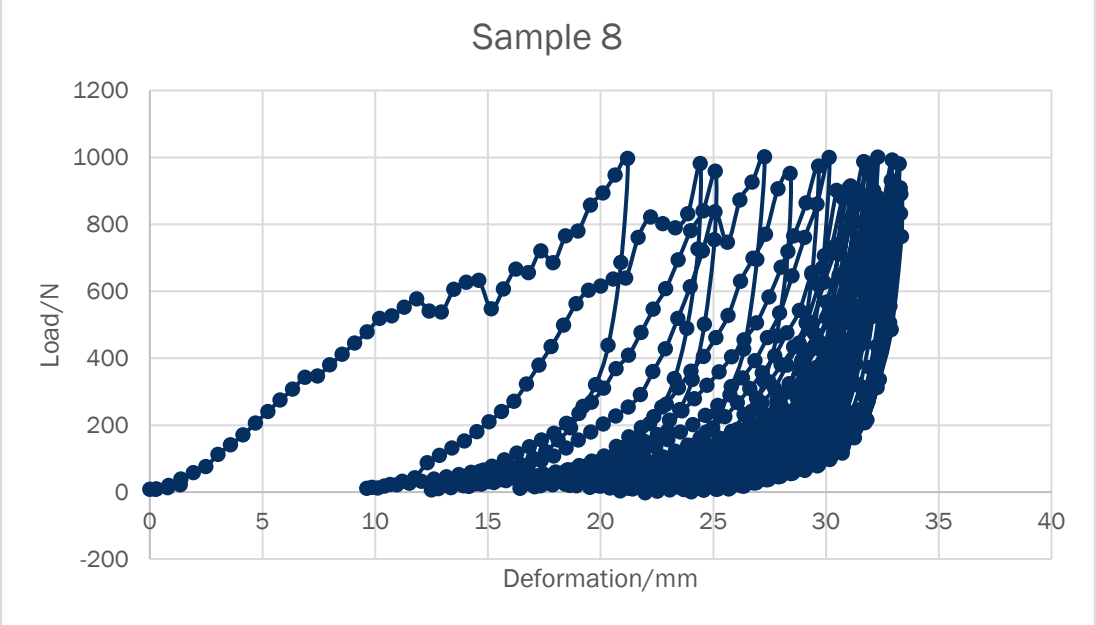


Figure A.17:Cyclic compressive test results for sample 8

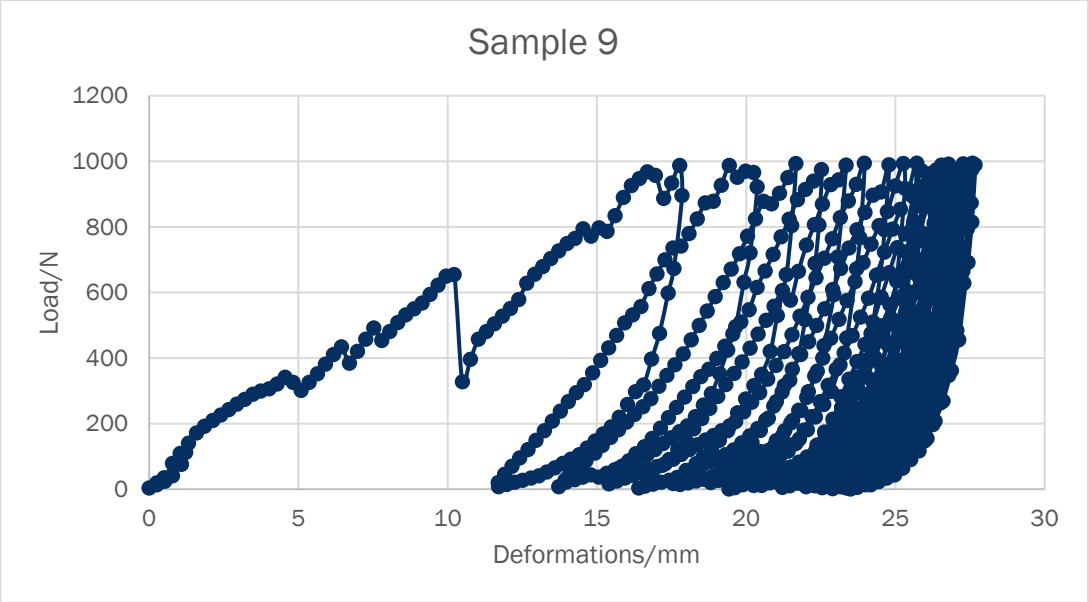


Figure A.19: Cyclic compressive test results for sample 9

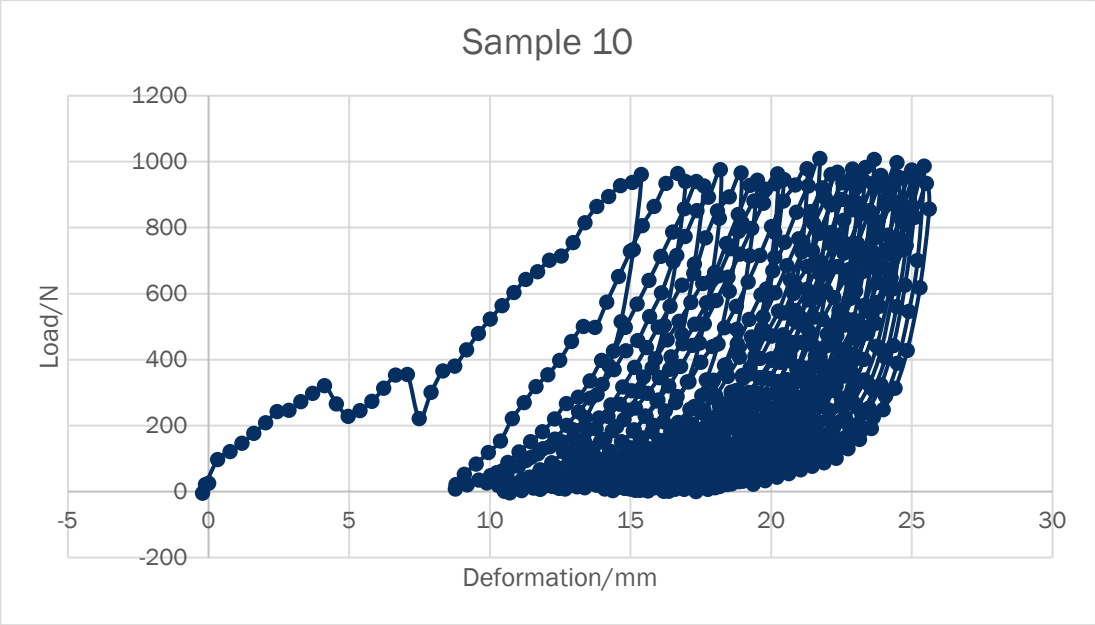


Figure A.18: Cyclic compressive test results for sample 10

A.10 LARGE SCALE BOX TEST RESULTS

A.10.1 Box Cyclic-compression results

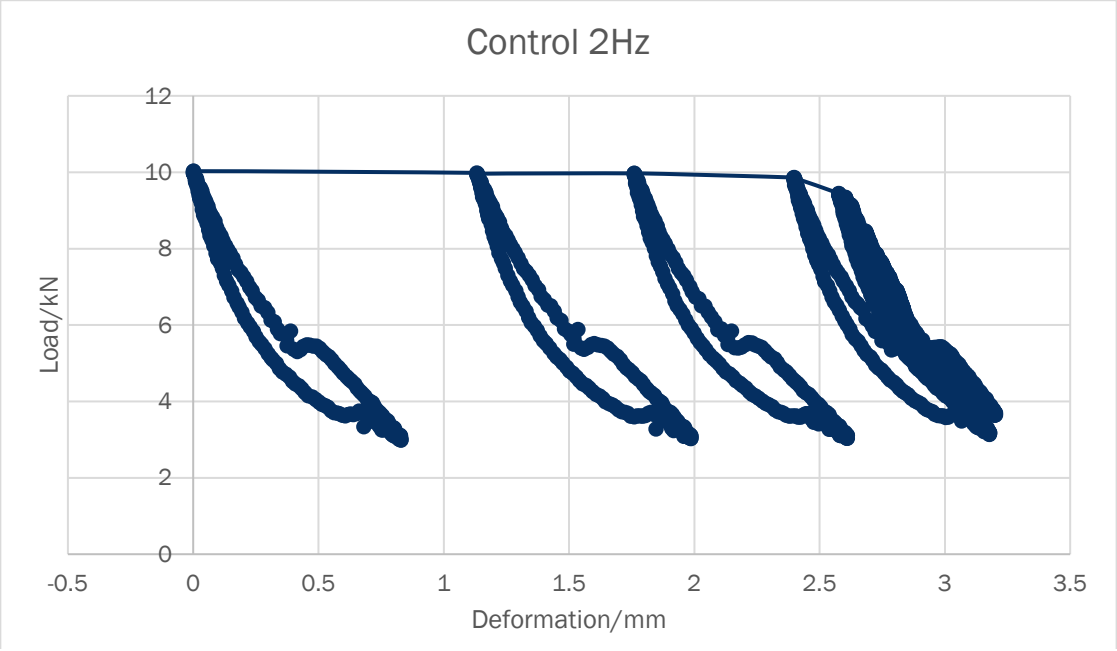


Figure A.20: Box test results for control at 2Hz

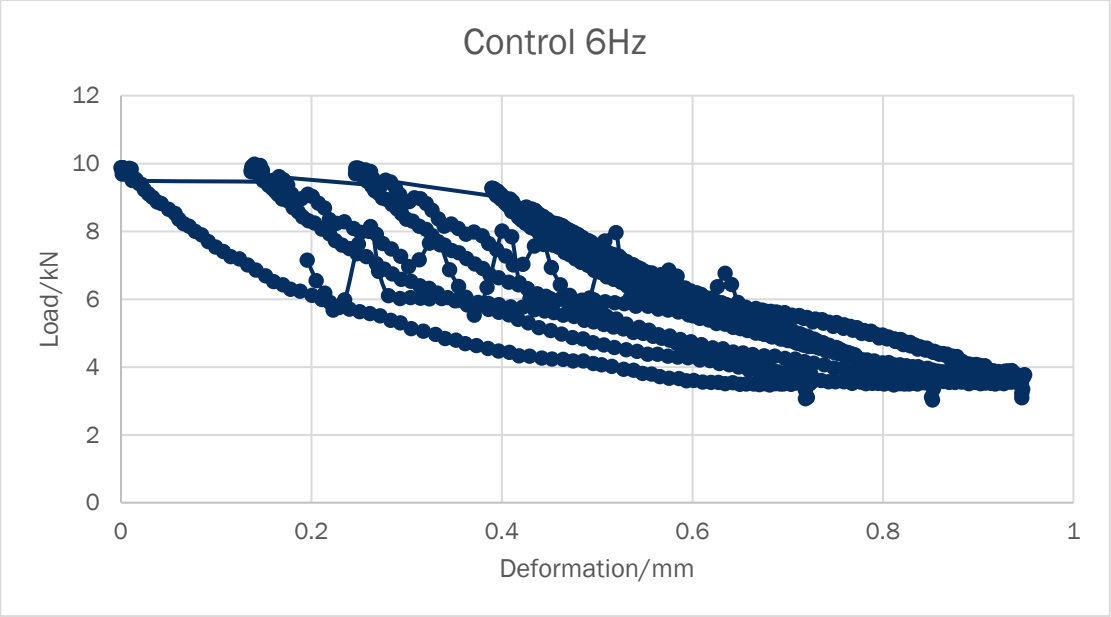


Figure A.21: Box test results for control at 6Hz

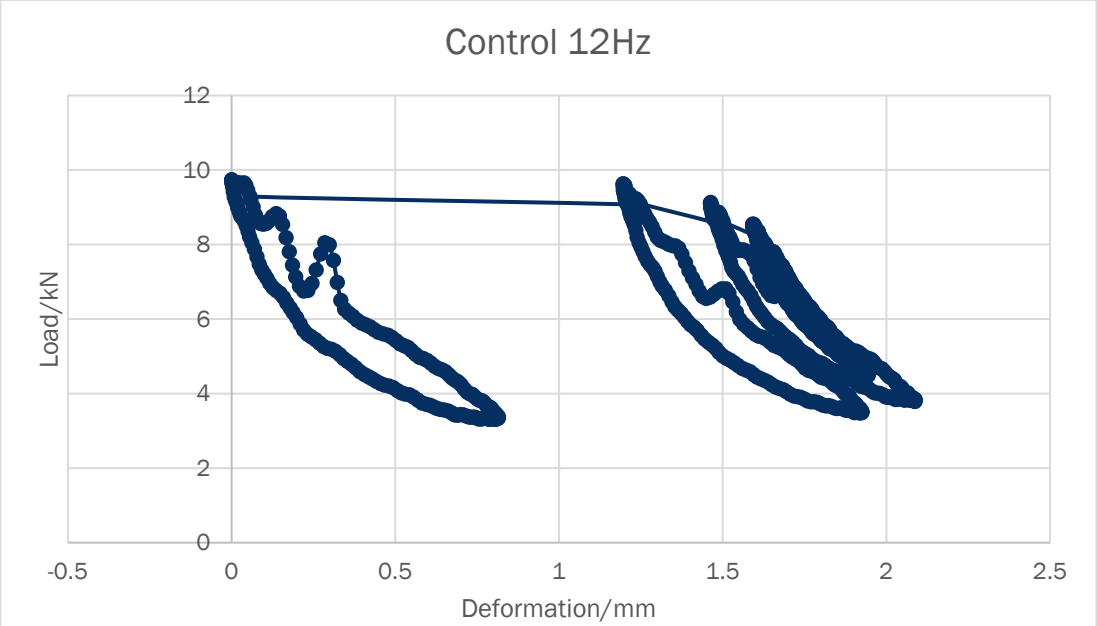


Figure A.22: Box test results for control at 12Hz

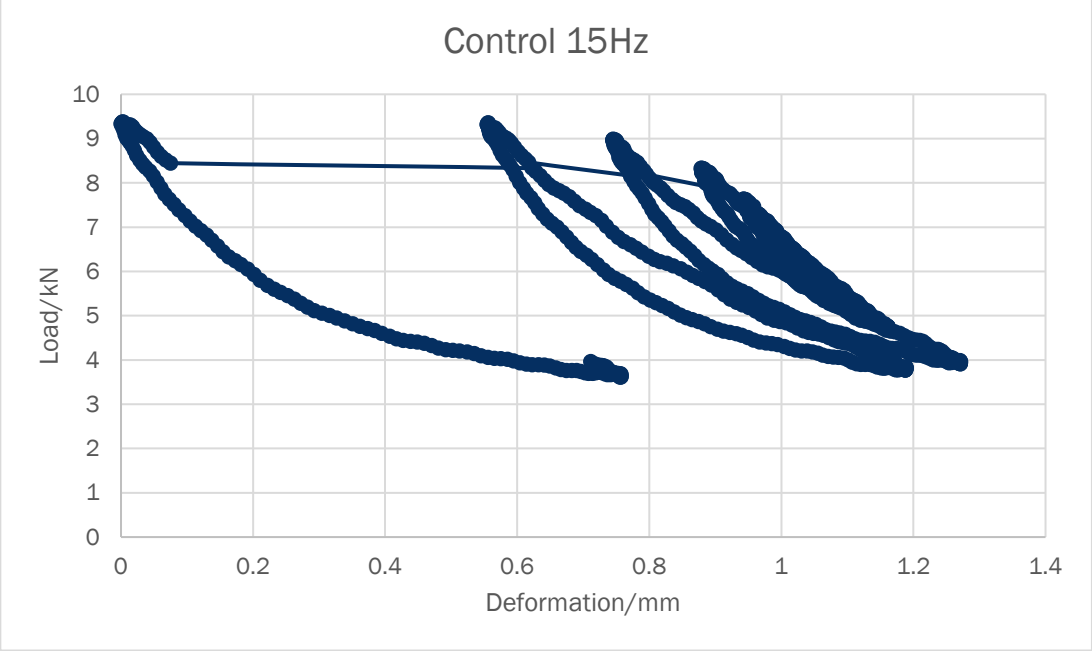


Figure A.23: Box test results for control at 15Hz

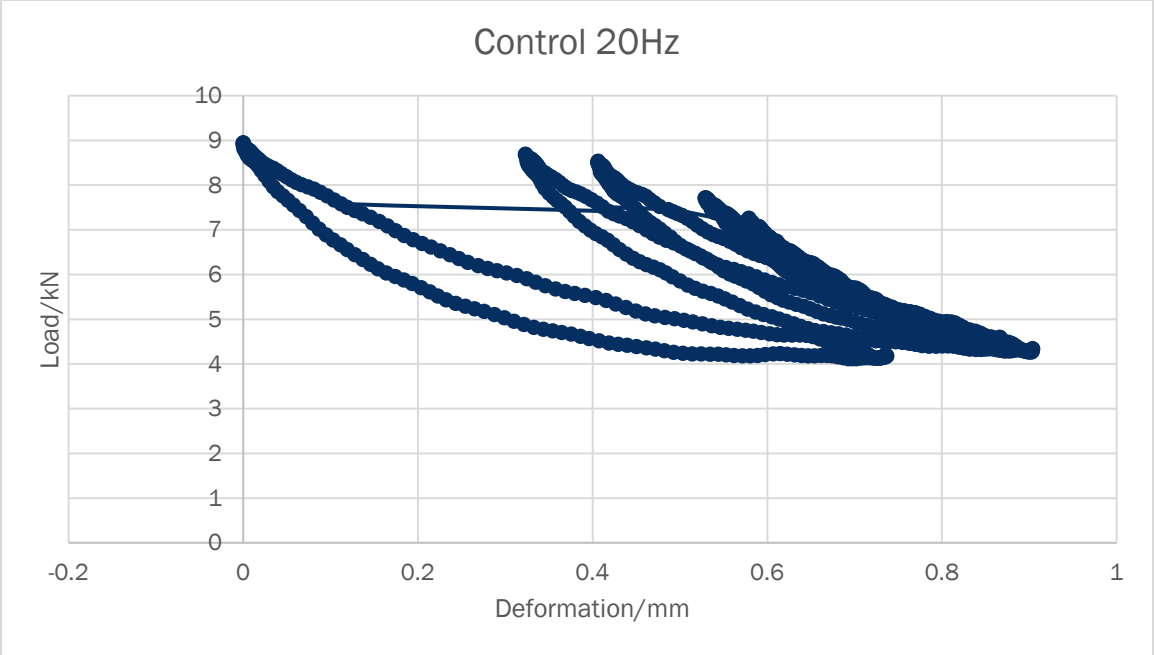


Figure A.24: Box test results for control at 20Hz

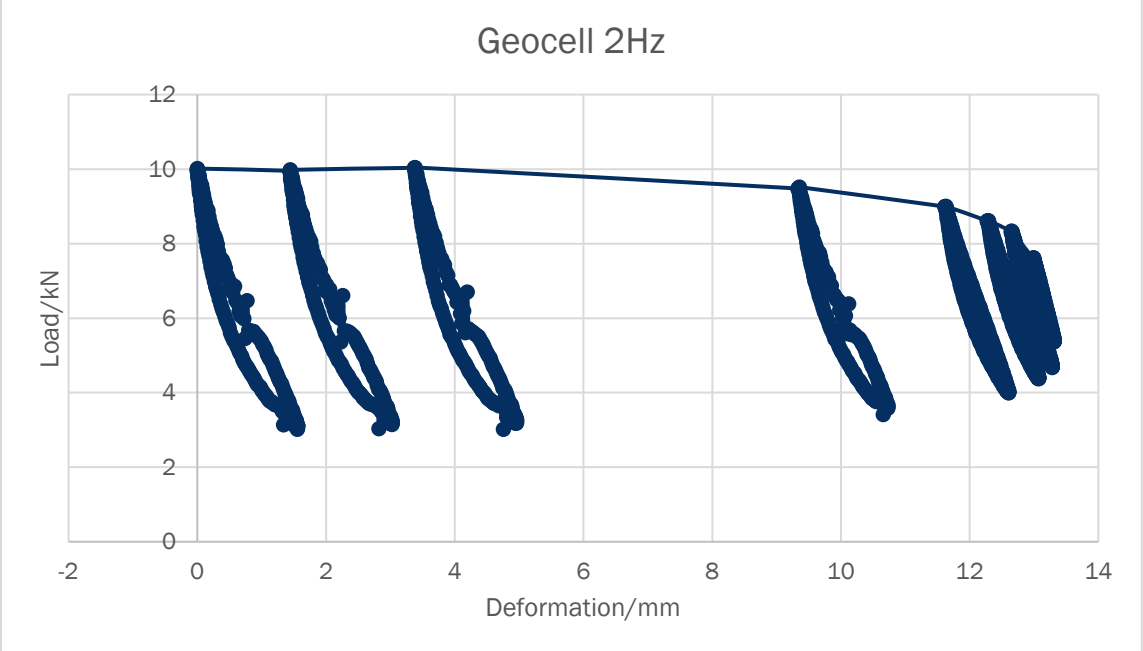


Figure A.25: Box test results for sample reinforced with geocell at 2Hz

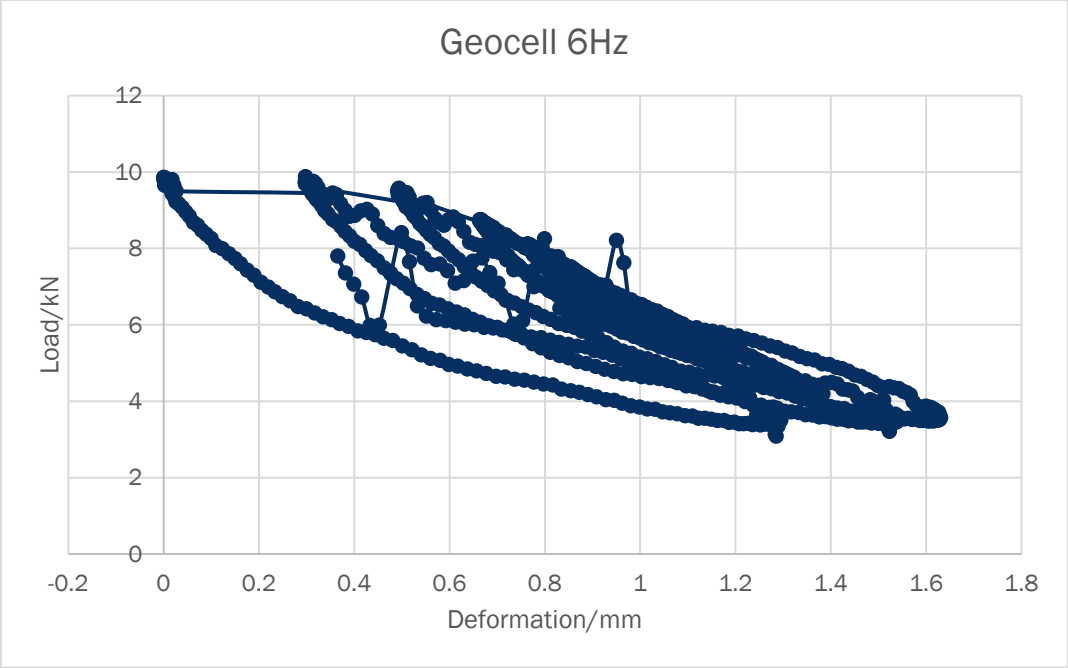


Figure A.26: Box test results for sample reinforced with geocell at 6Hz

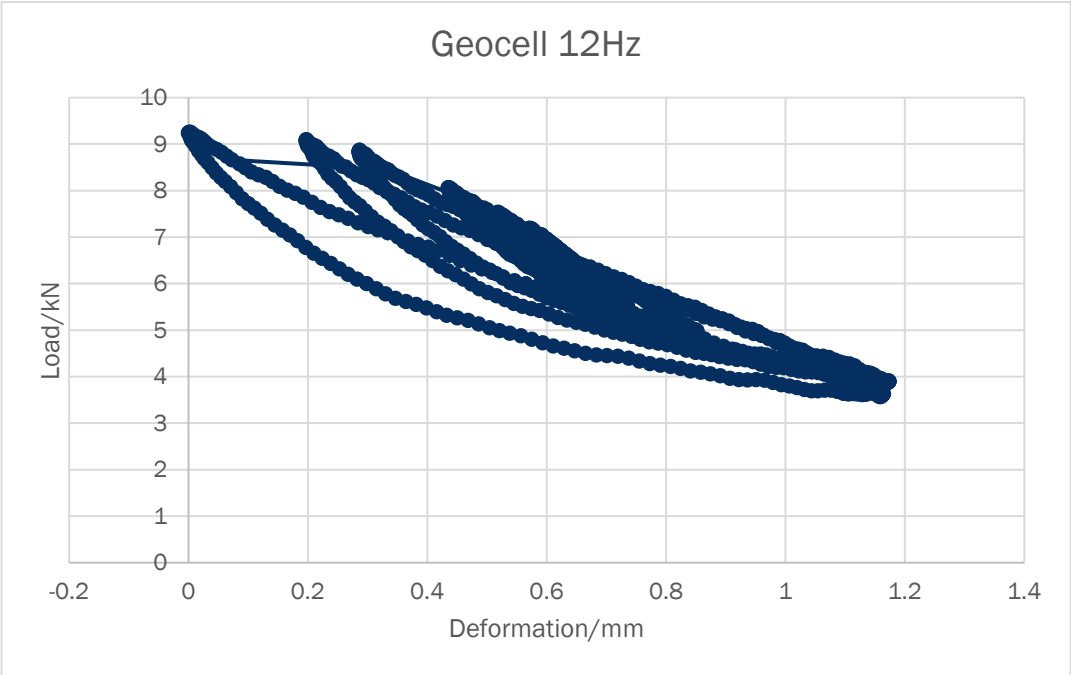


Figure A.27: Box test results for sample reinforced with geocell at 12Hz

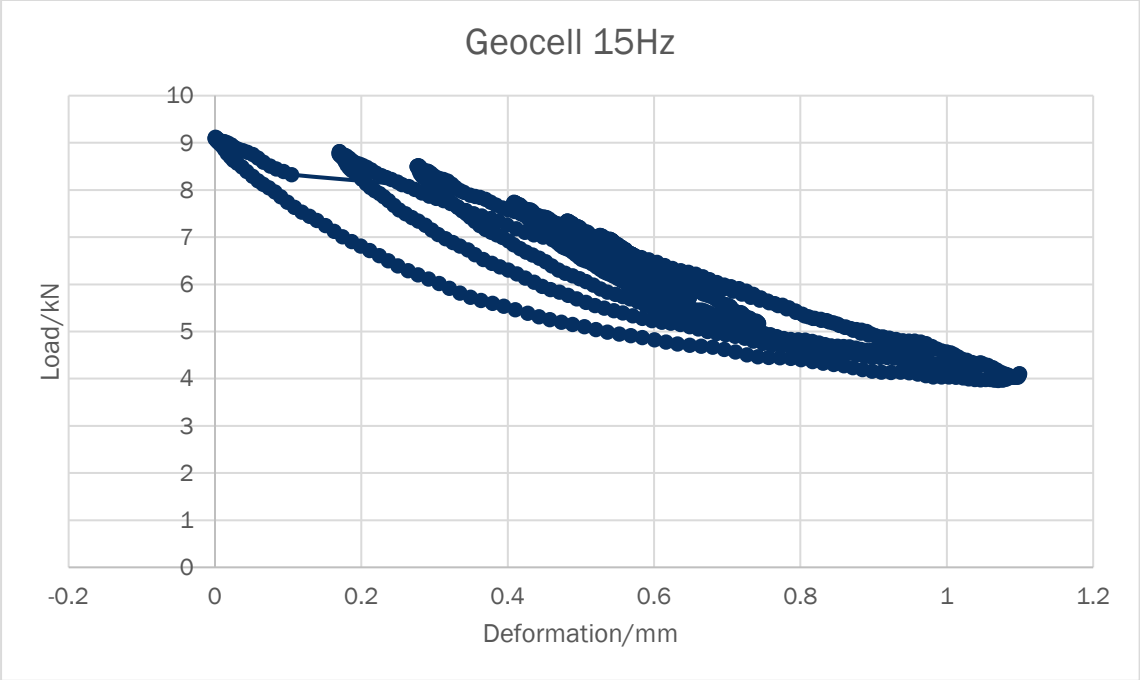


Figure A.28: Box test results for sample reinforced with geocell at 15Hz

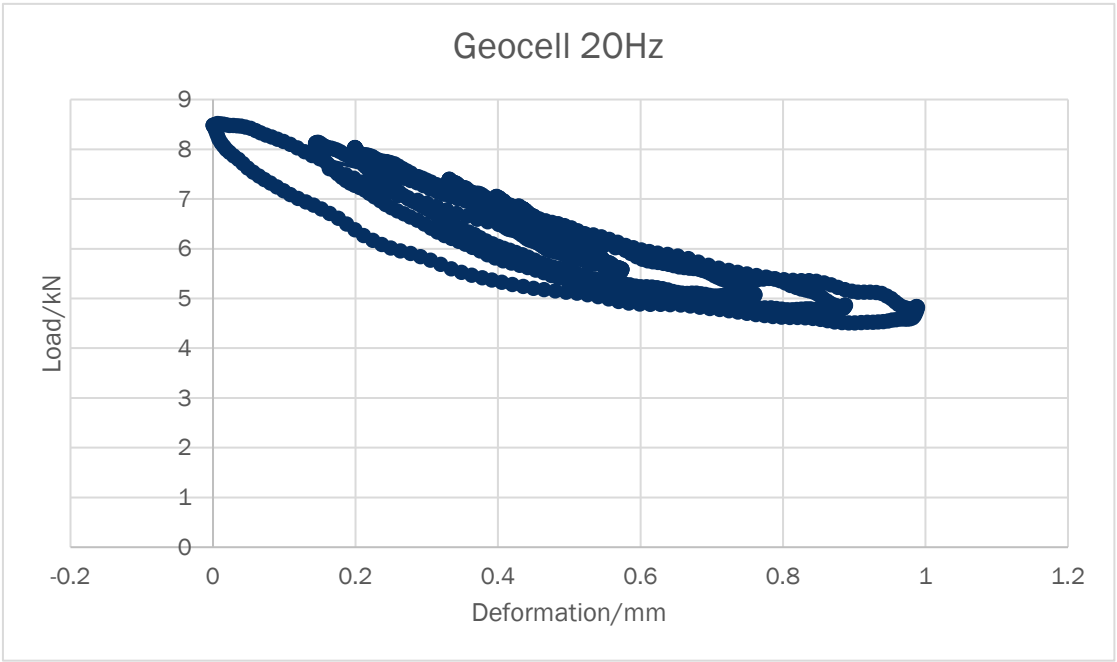


Figure A.29: Box test results for sample reinforced with geocell at 20Hz

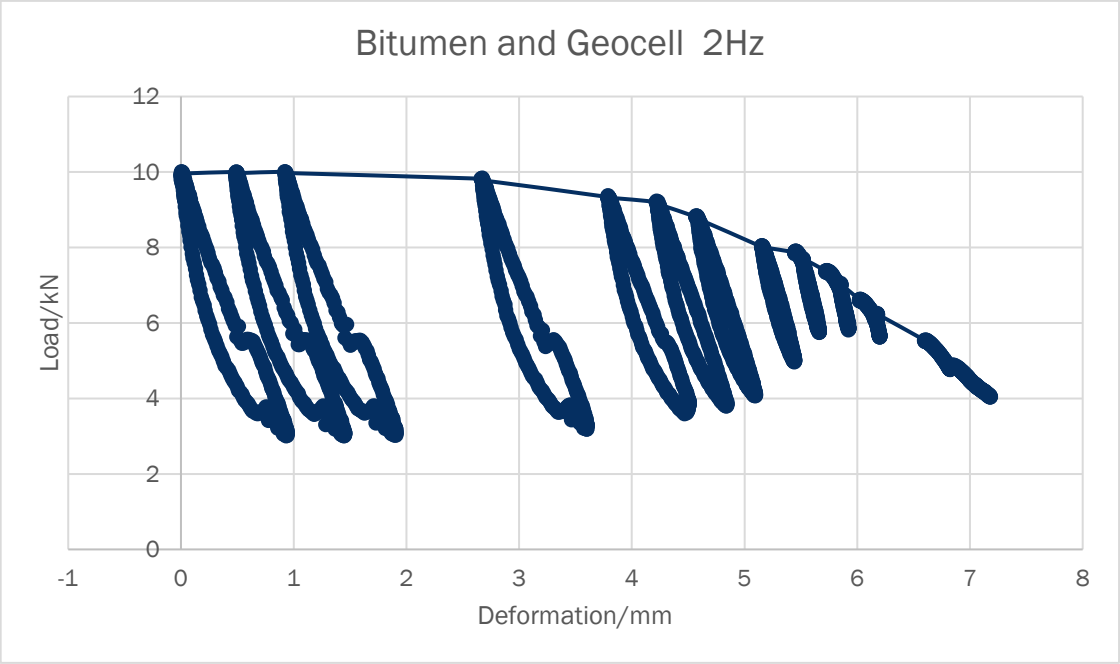


Figure A.30: Box test results for sample reinforced with geocell and bitumen at 2Hz

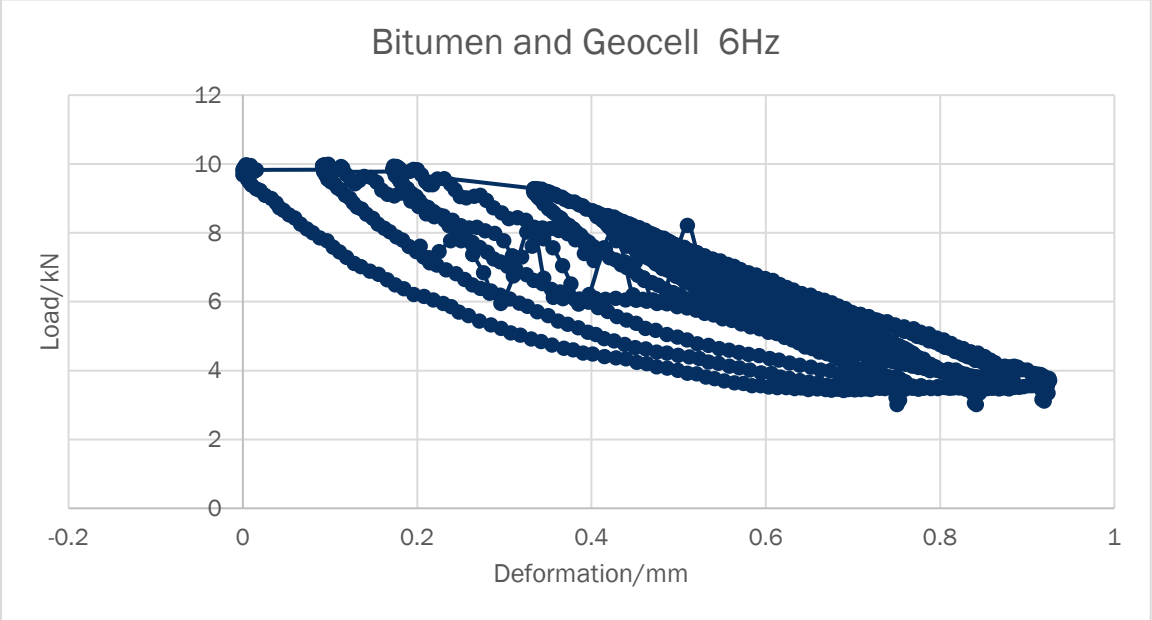


Figure A.31: Box test results for sample reinforced with geocell and bitumen at 6Hz

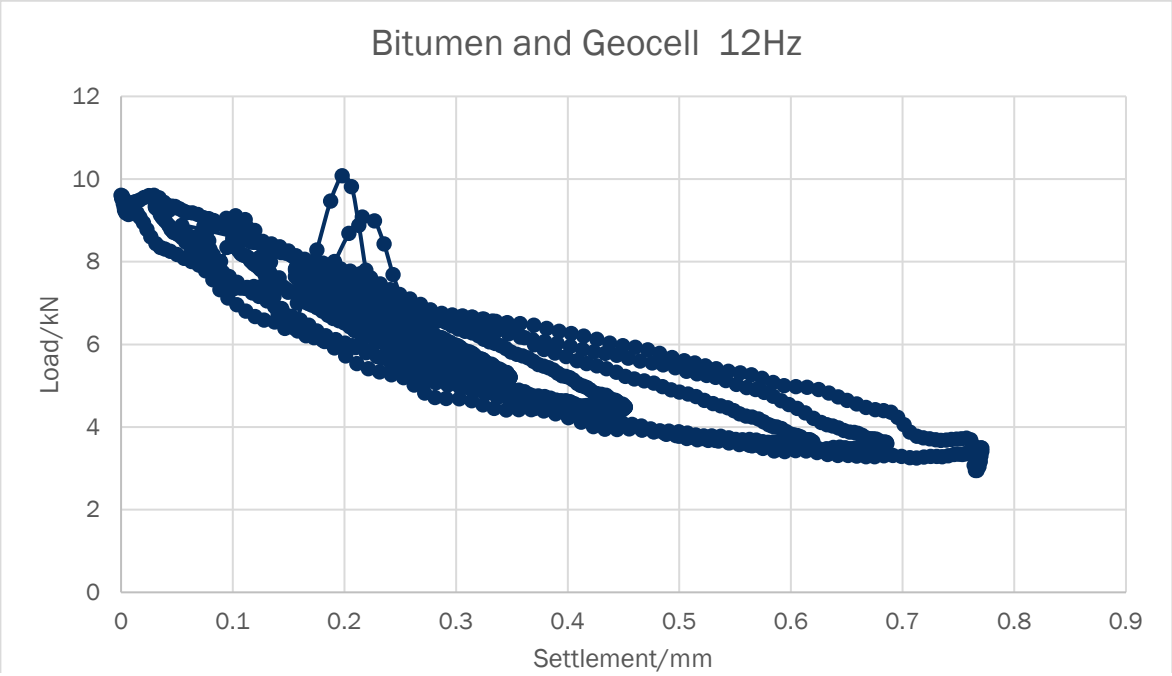


Figure A.32: Box test results for sample reinforced with geocell and bitumen at 12Hz

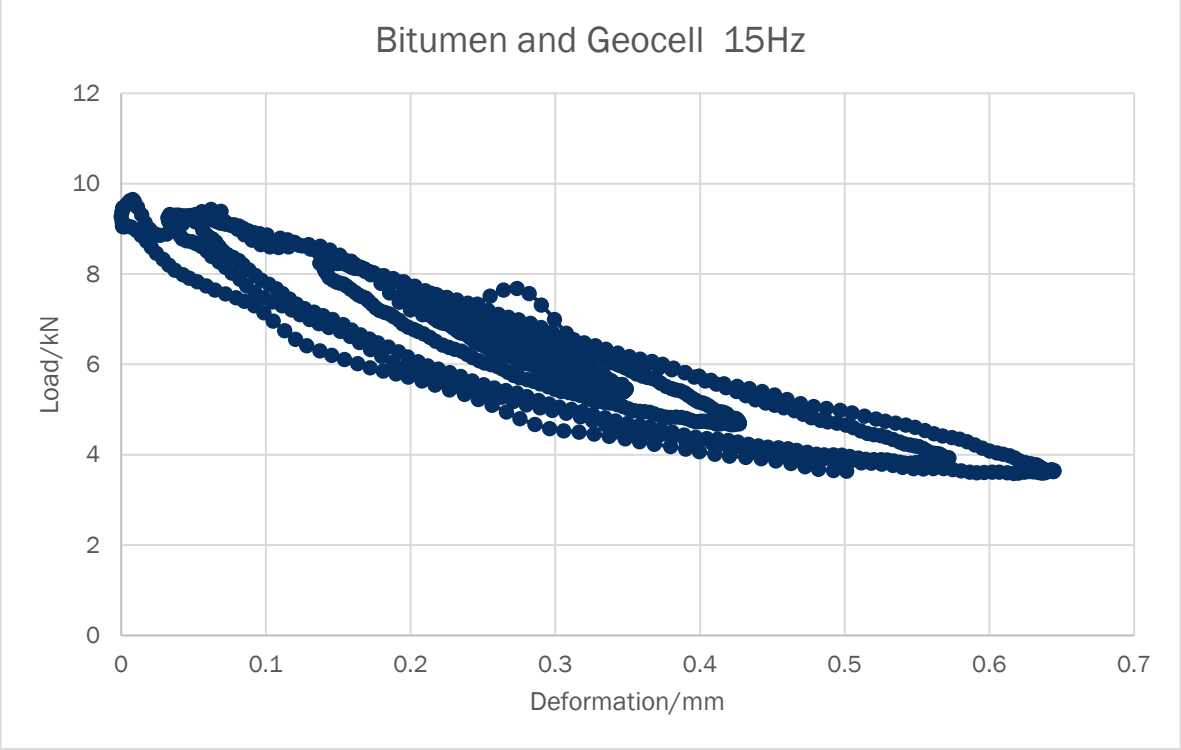


Figure A.33: Box test results for sample reinforced with geocell and bitumen at 15Hz

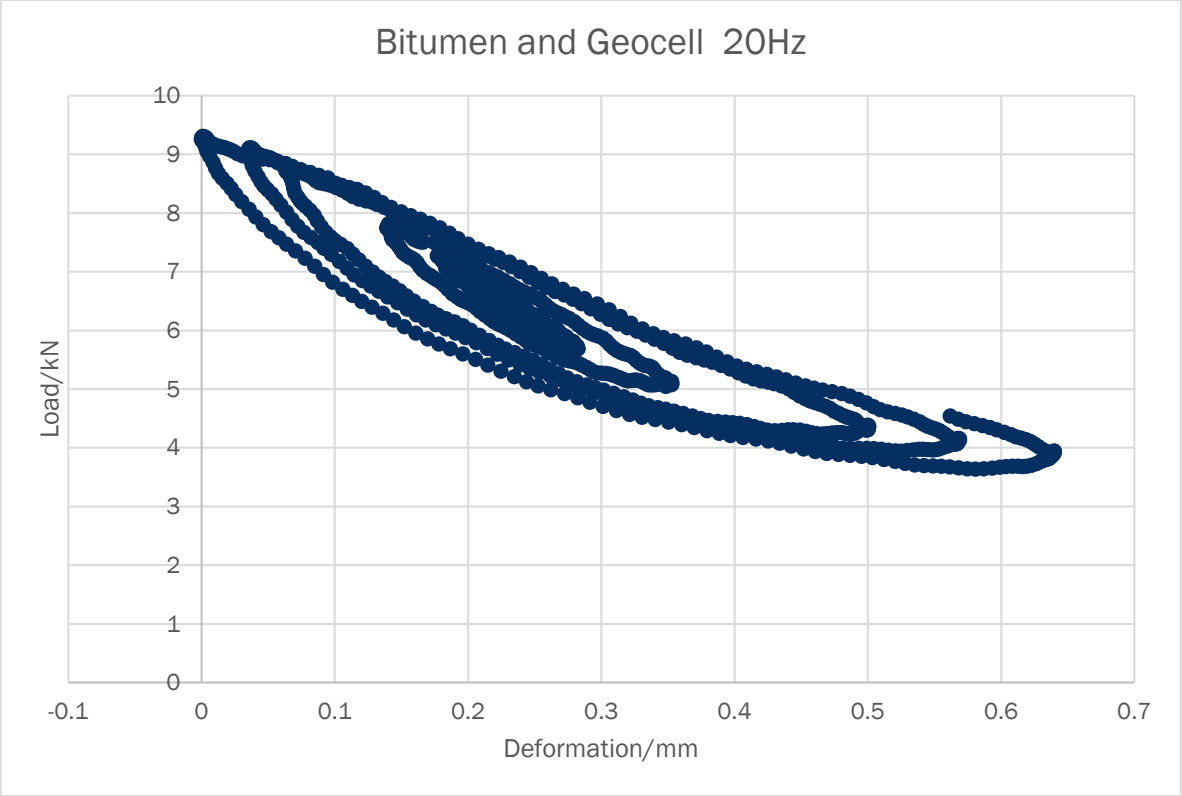
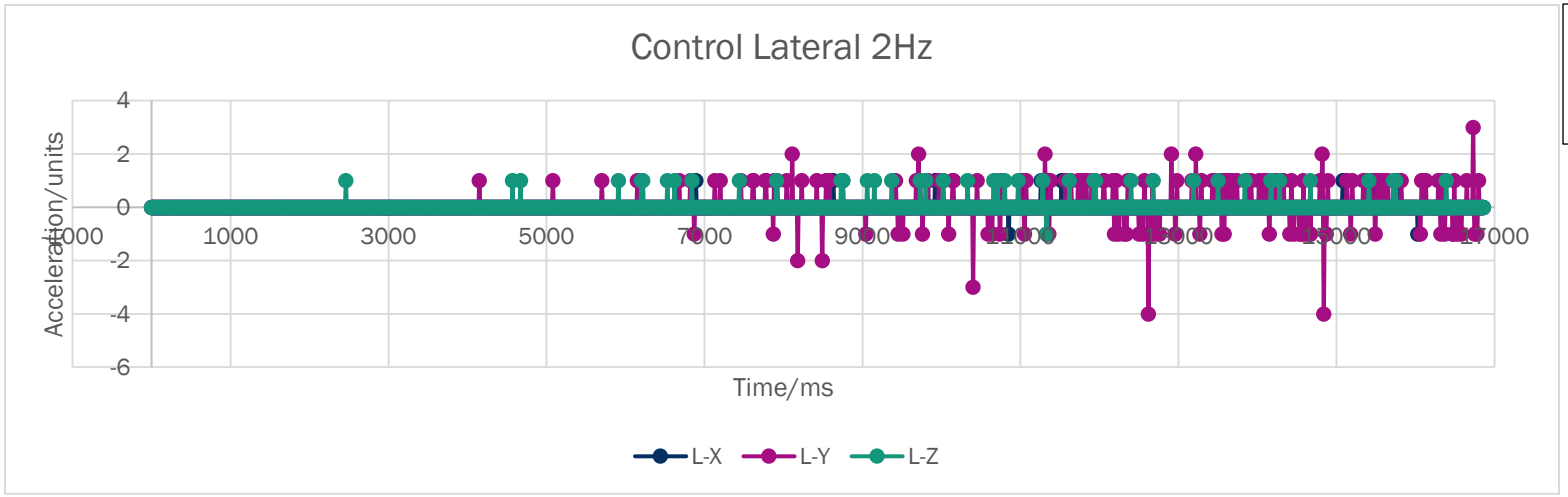


Figure A.34: Box test results for sample reinforced with geocell and bitumen at 20Hz

A.10.2 ACCELEROMETERS RESULTS



Calibration:

6units=1m/s^2

Figure A.35: Accelerometer 1 results for control at 2Hz

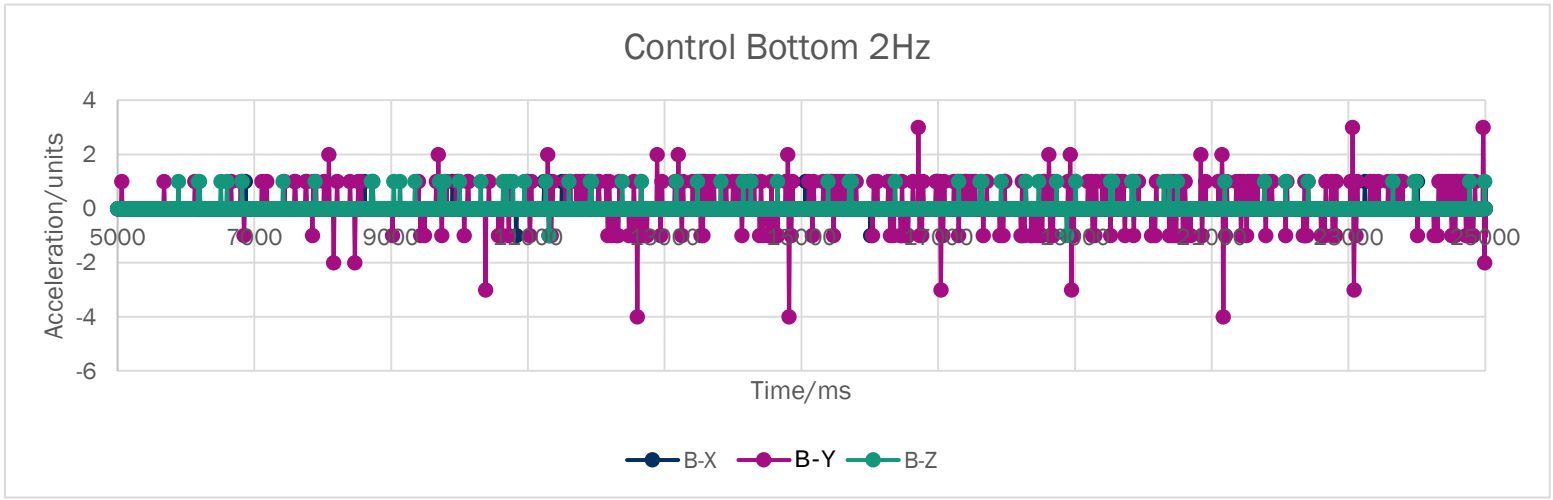


Figure A.36: Accelerometer 2 results for control at 2Hz

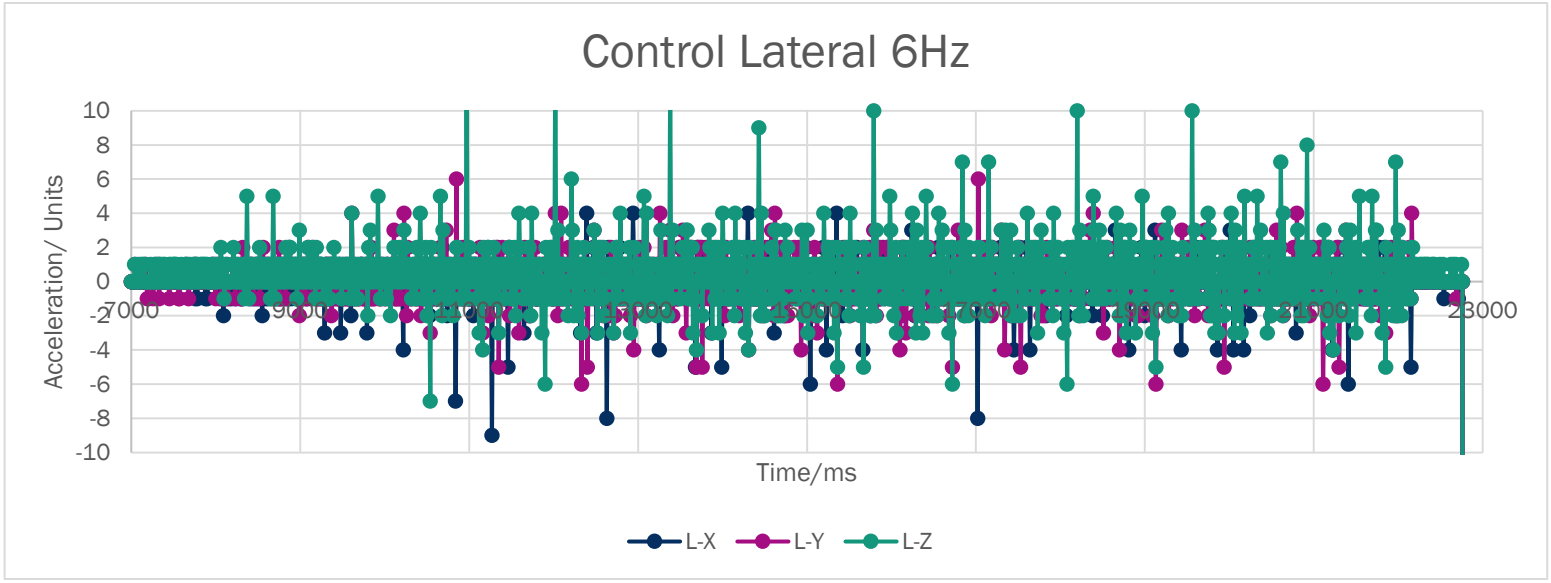


Figure A.37: Accelerometer 1 results for control at 6Hz

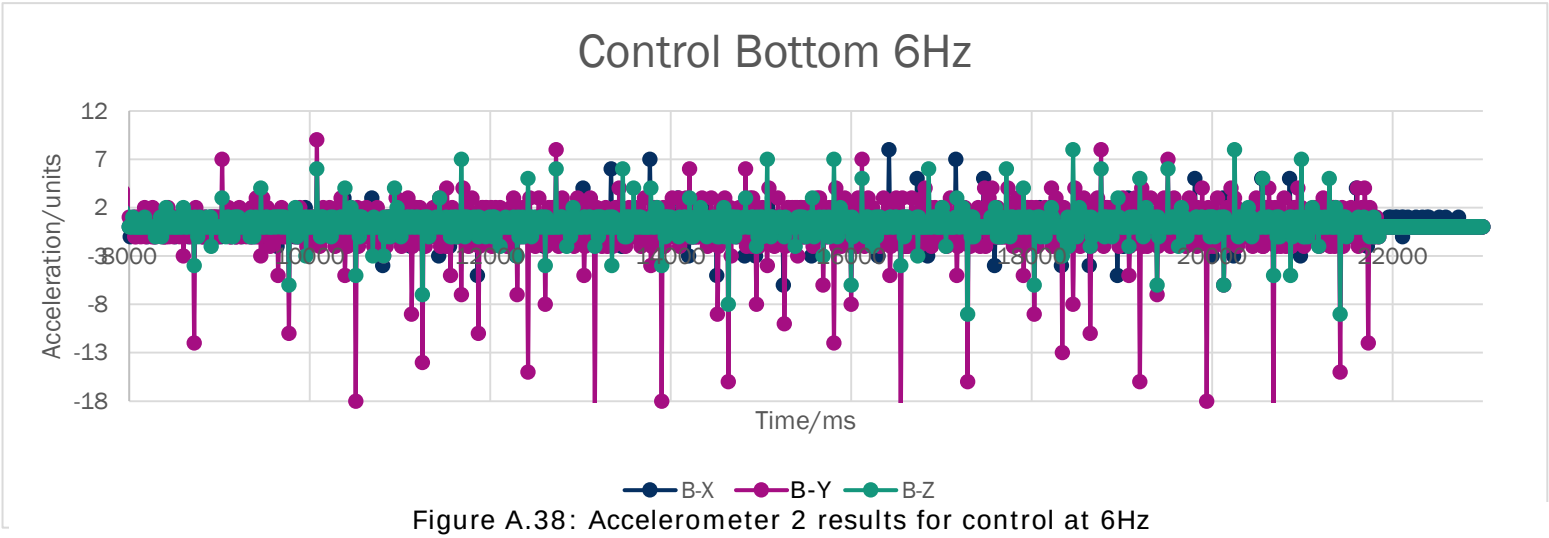


Figure A.38: Accelerometer 2 results for control at 6Hz

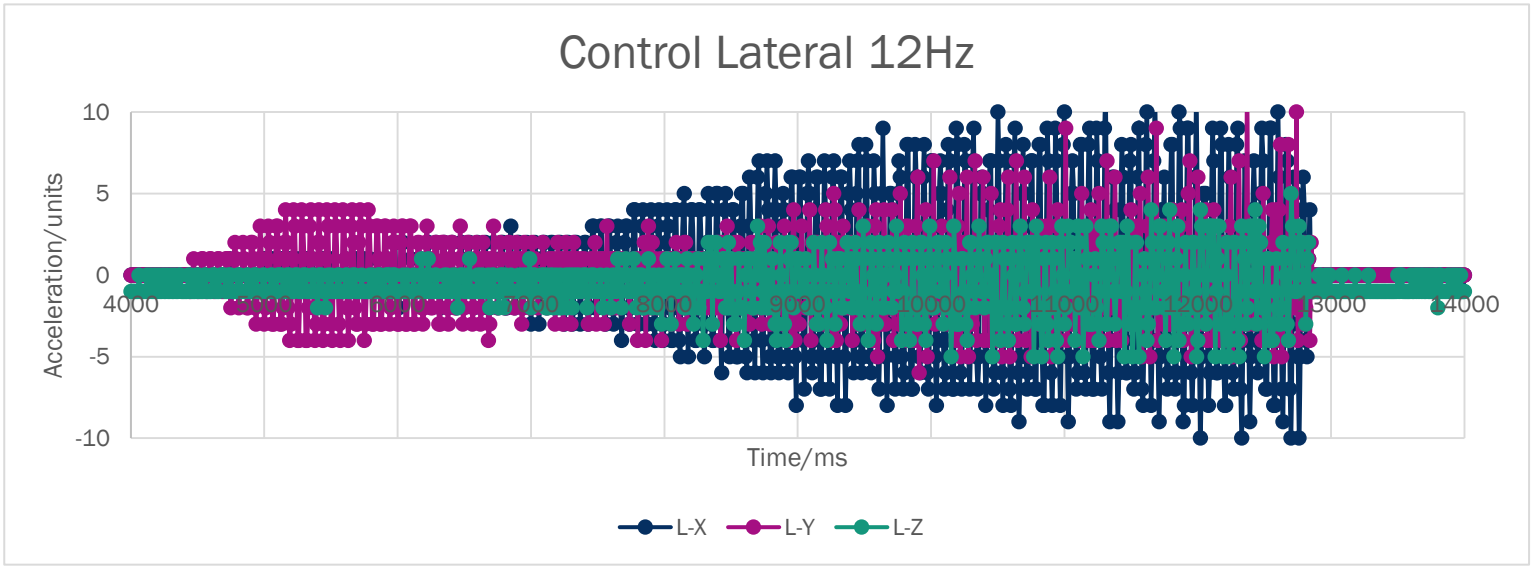


Figure A.39: Accelerometer 1 results for control at 12Hz

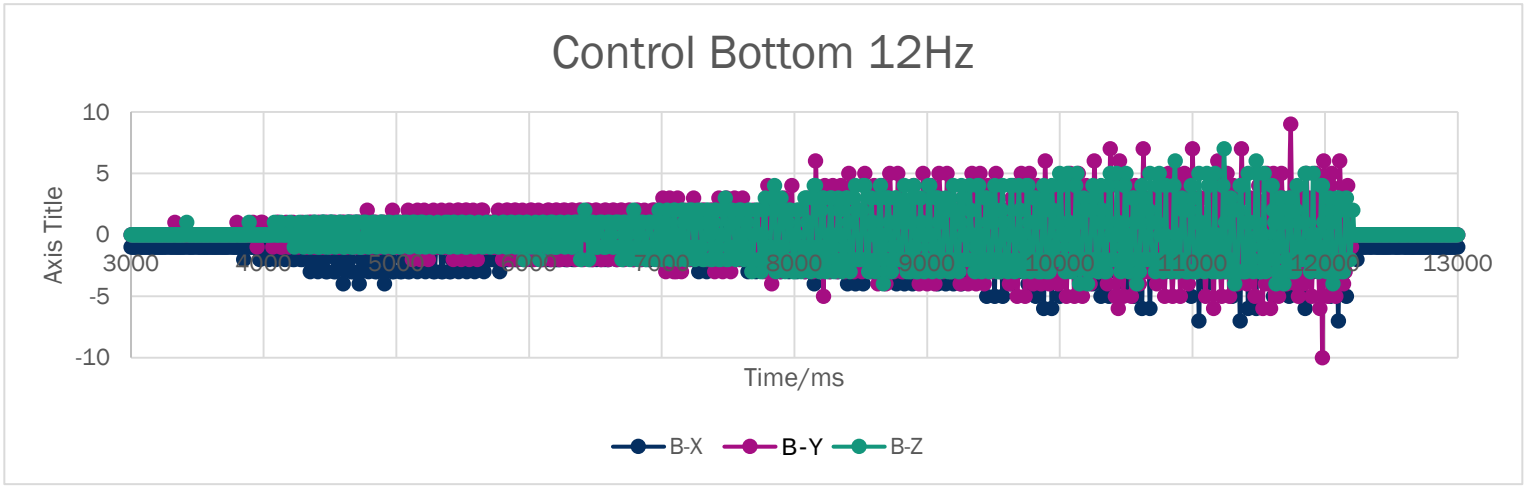


Figure A.40: Accelerometer 2 results for control at 12Hz

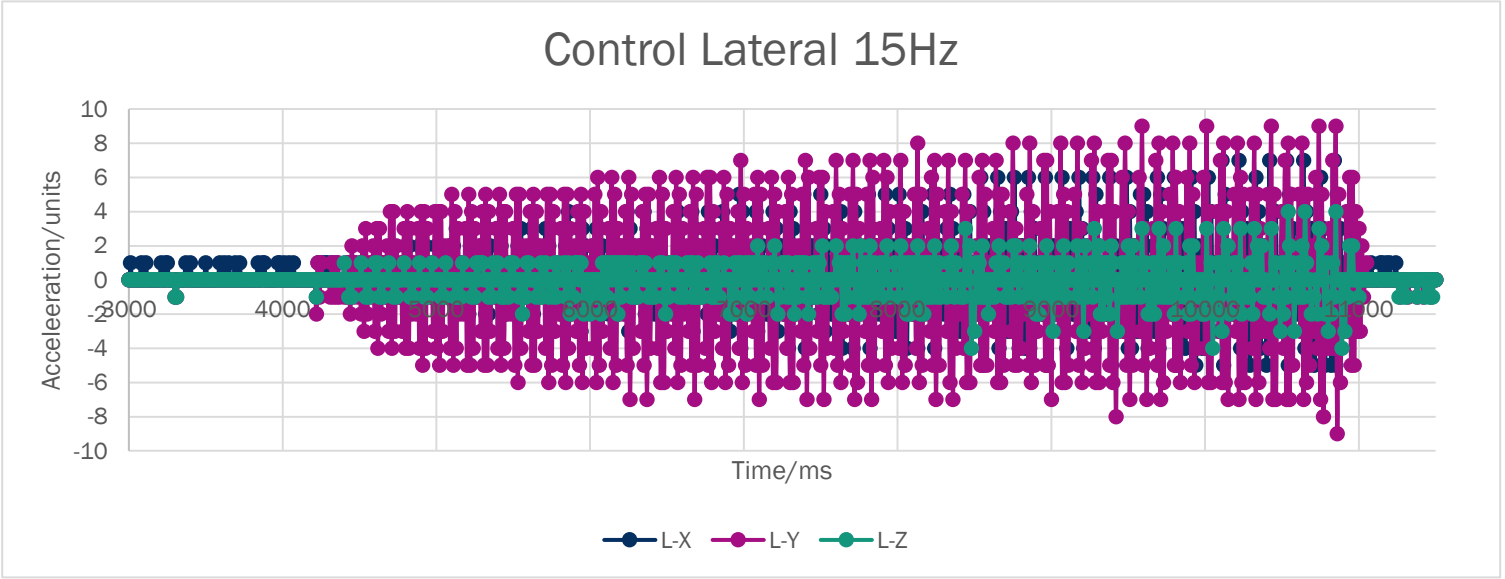


Figure A.41: Accelerometer 1 results for control at 15Hz

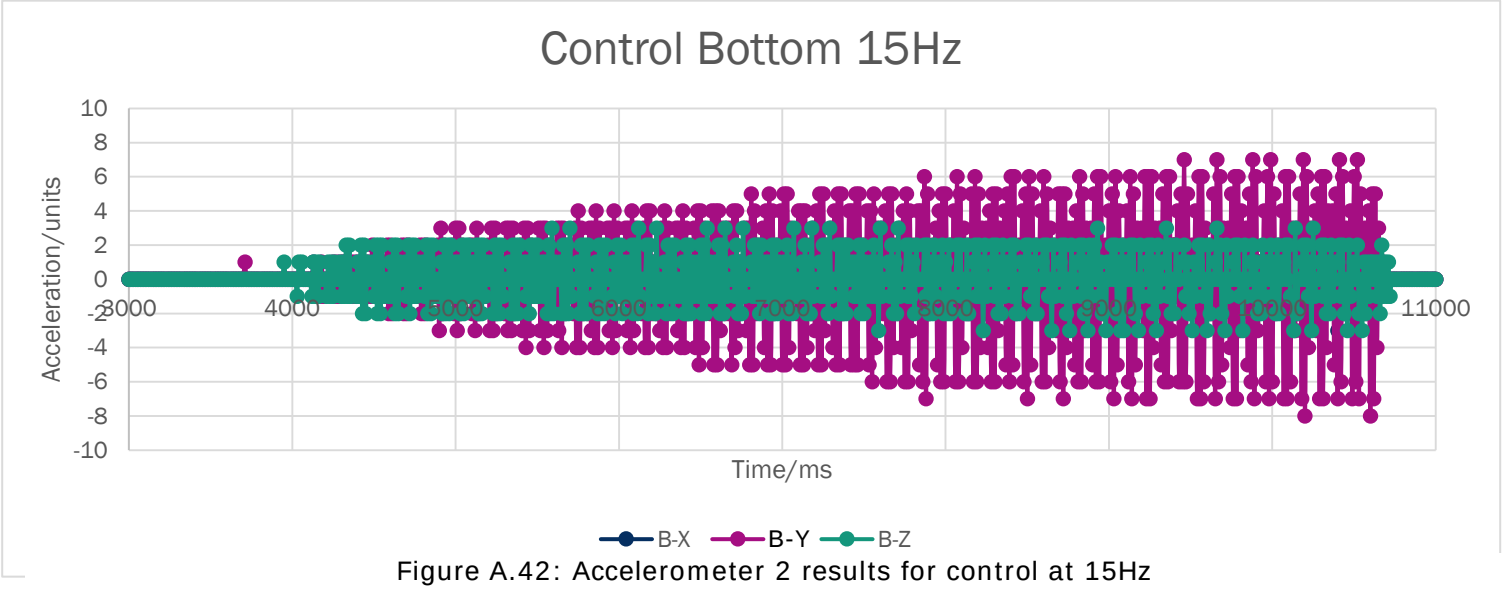


Figure A.42: Accelerometer 2 results for control at 15Hz

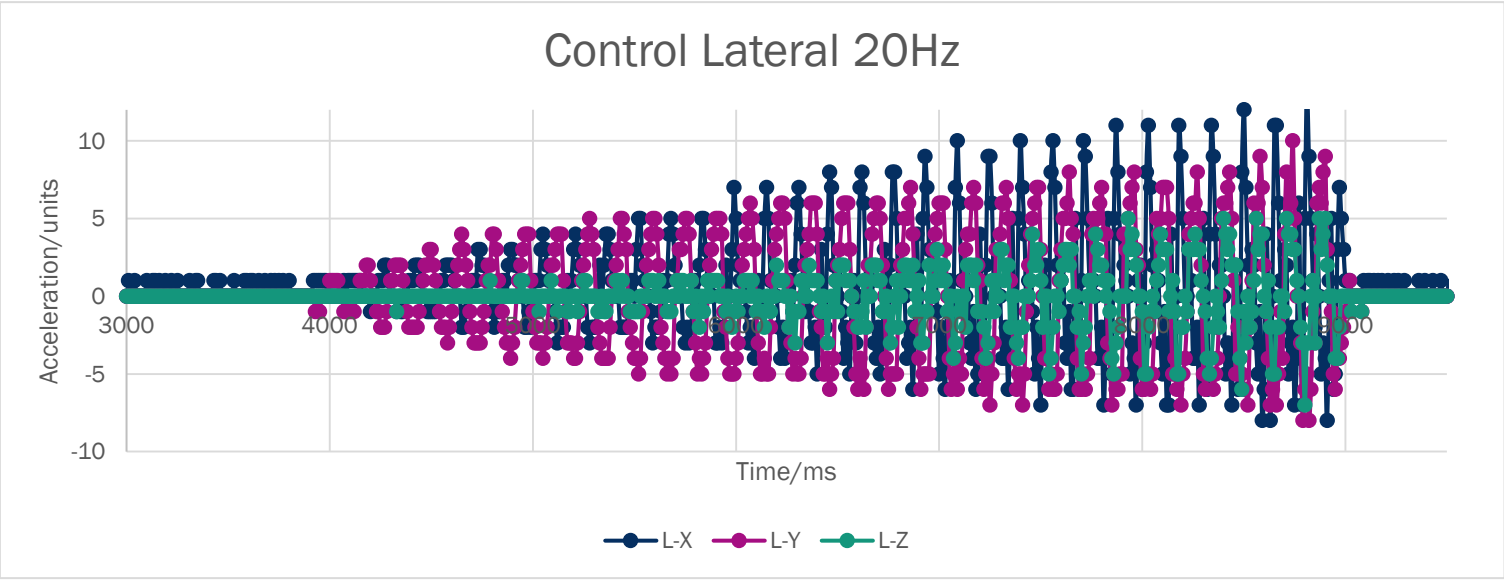


Figure A.43: Accelerometer 1 results for control at 20Hz

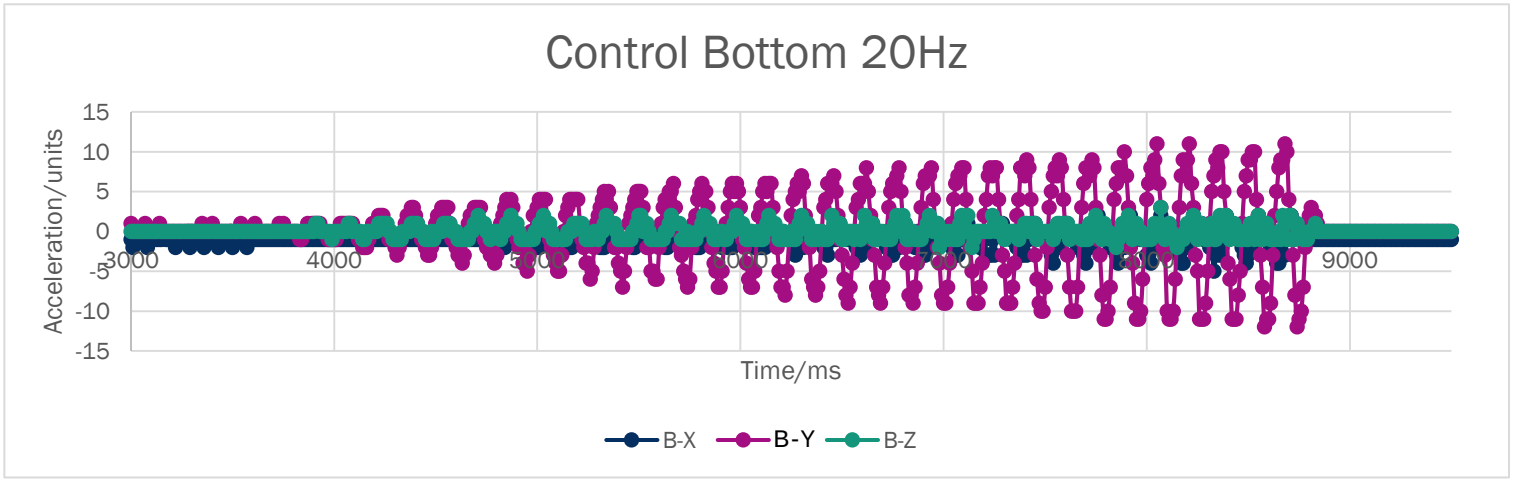


Figure A.44: Accelerometer 2 results for control at 20Hz

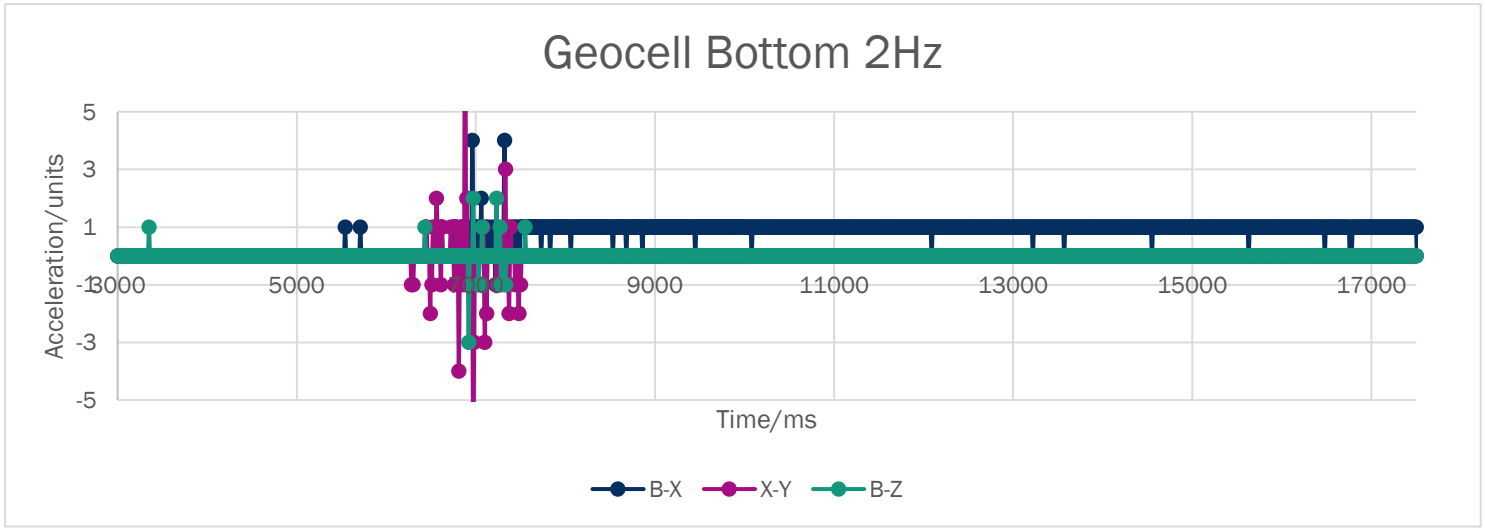


Figure A.45: Accelerometer 1 results for geocell reinforcement at 2Hz

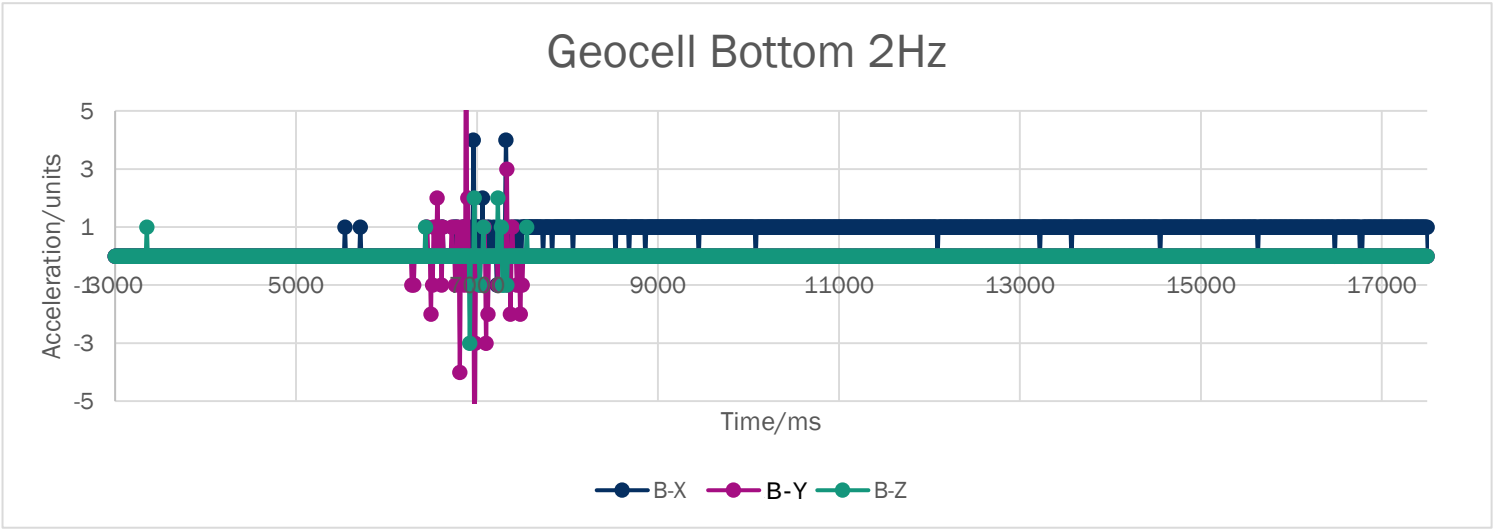


Figure A.46: Accelerometer 2 results for geocell reinforcement at 2Hz

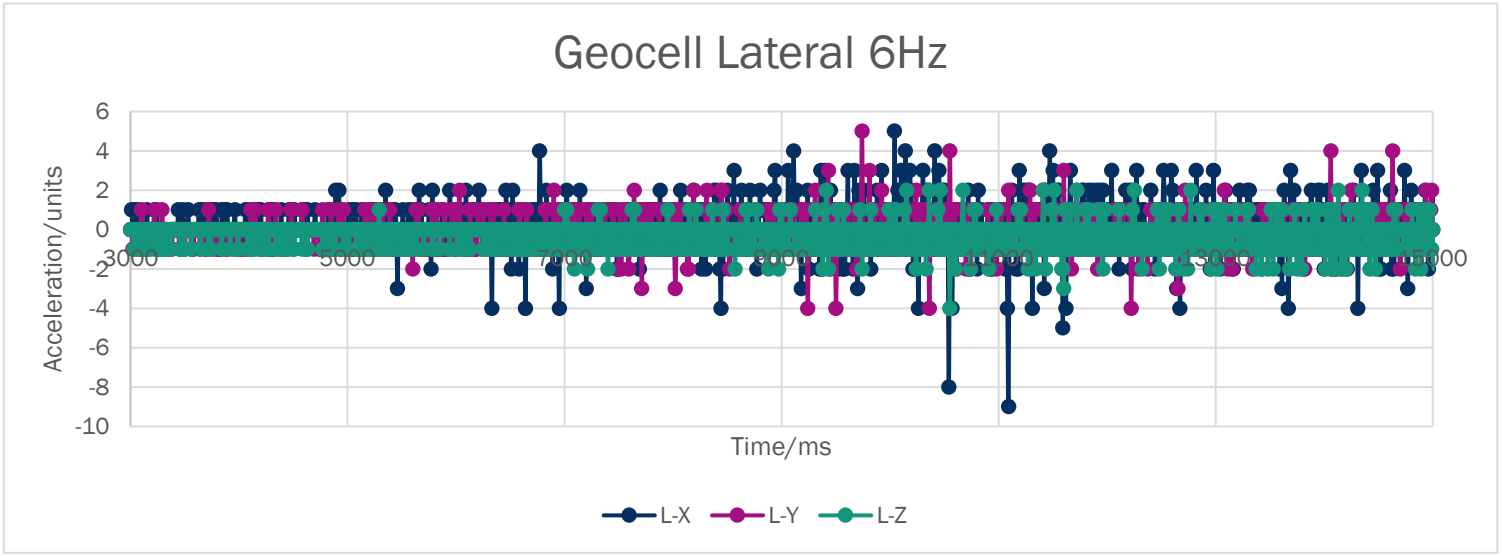


Figure A.47: Accelerometer 1 results for geocell reinforcement at 6Hz

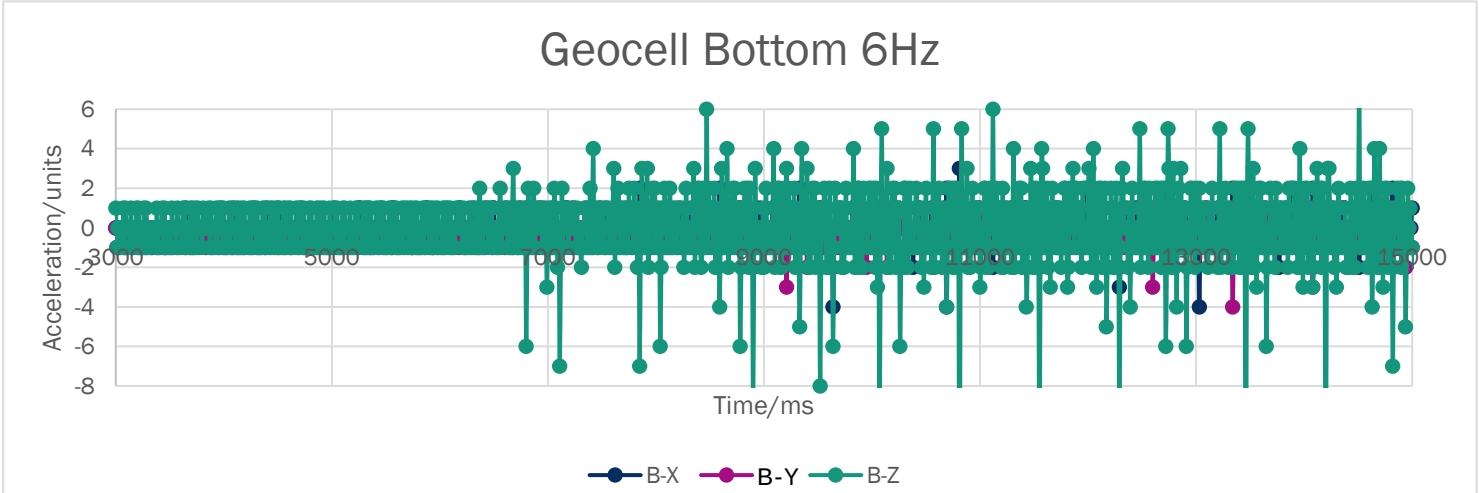


Figure A.48: Accelerometer 2 results for geocell reinforcement at 6Hz

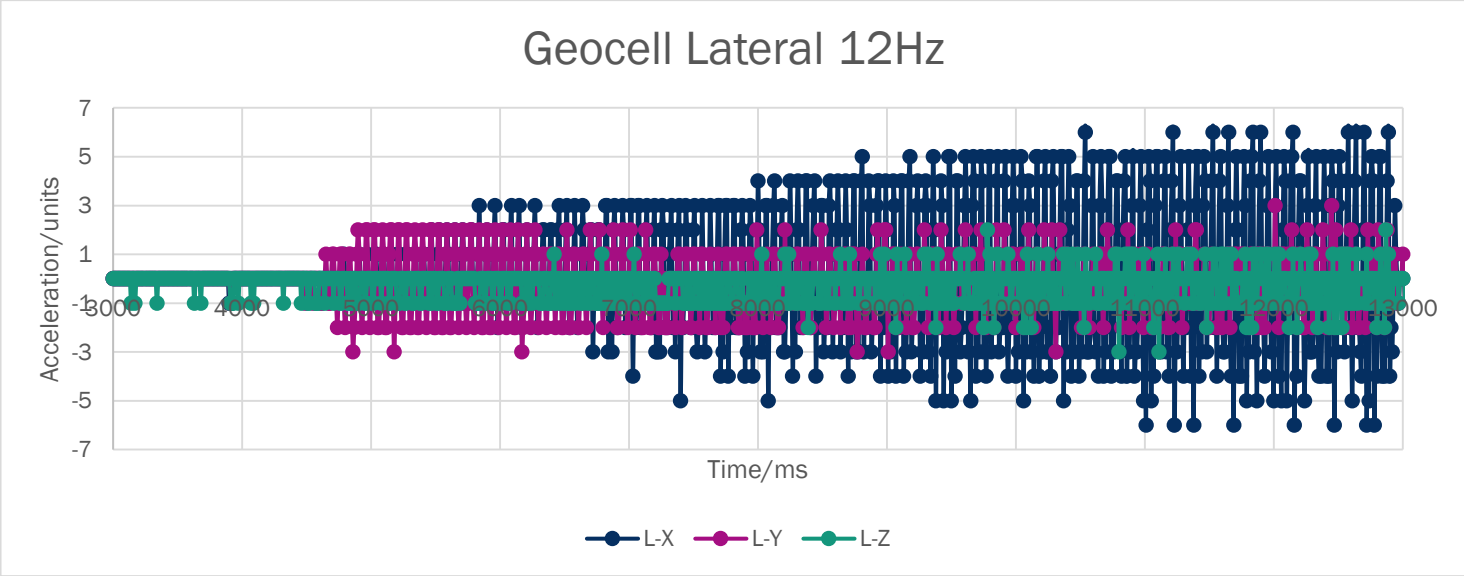


Figure A.49: Accelerometer 1 results for geocell reinforcement at12Hz

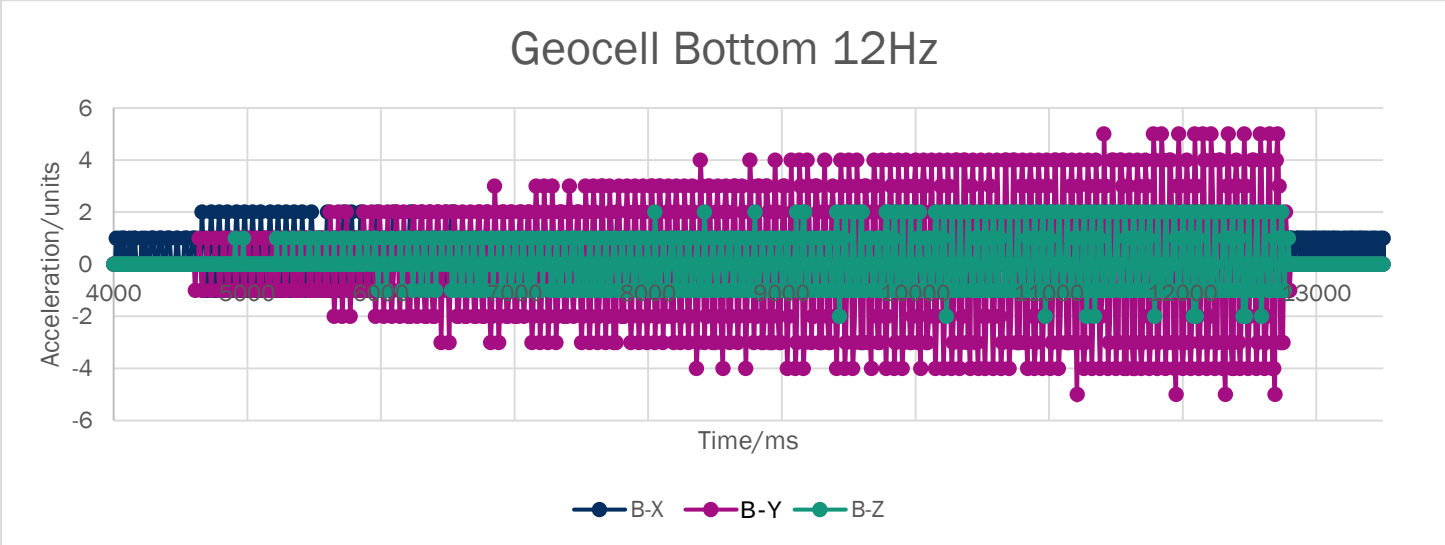


Figure A.50: Accelerometer 2 results for geocell reinforcement at12Hz

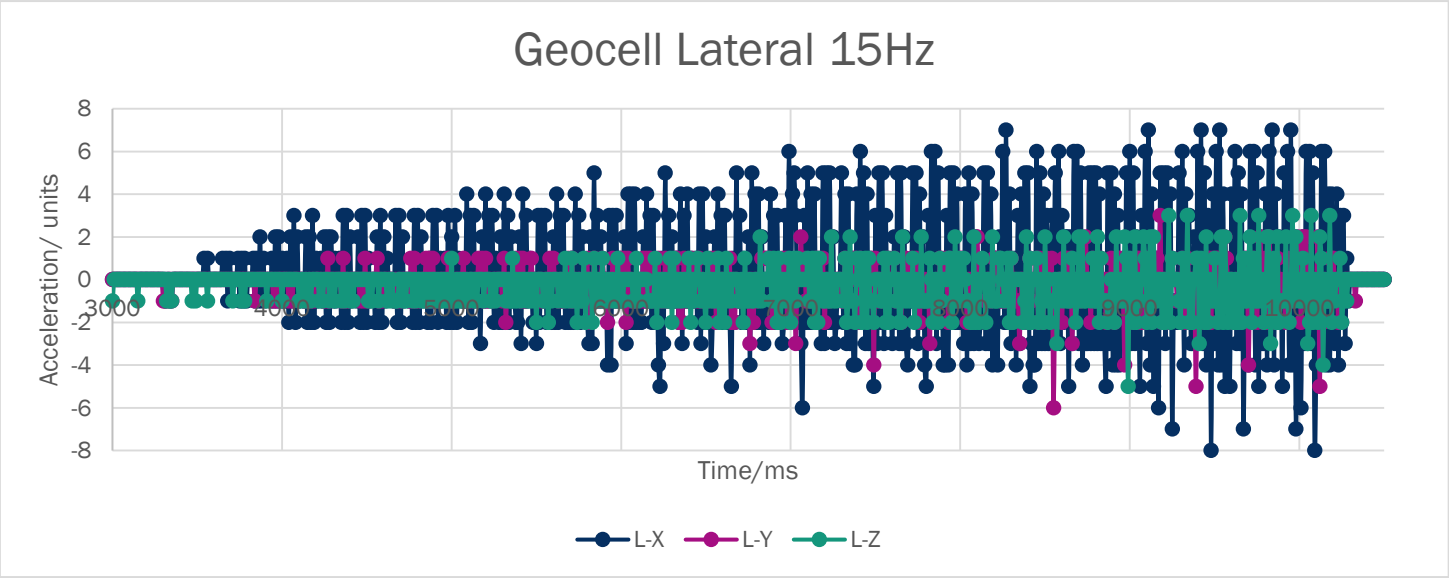


Figure A.51: Accelerometer 2 results for geocell reinforcement at 15Hz

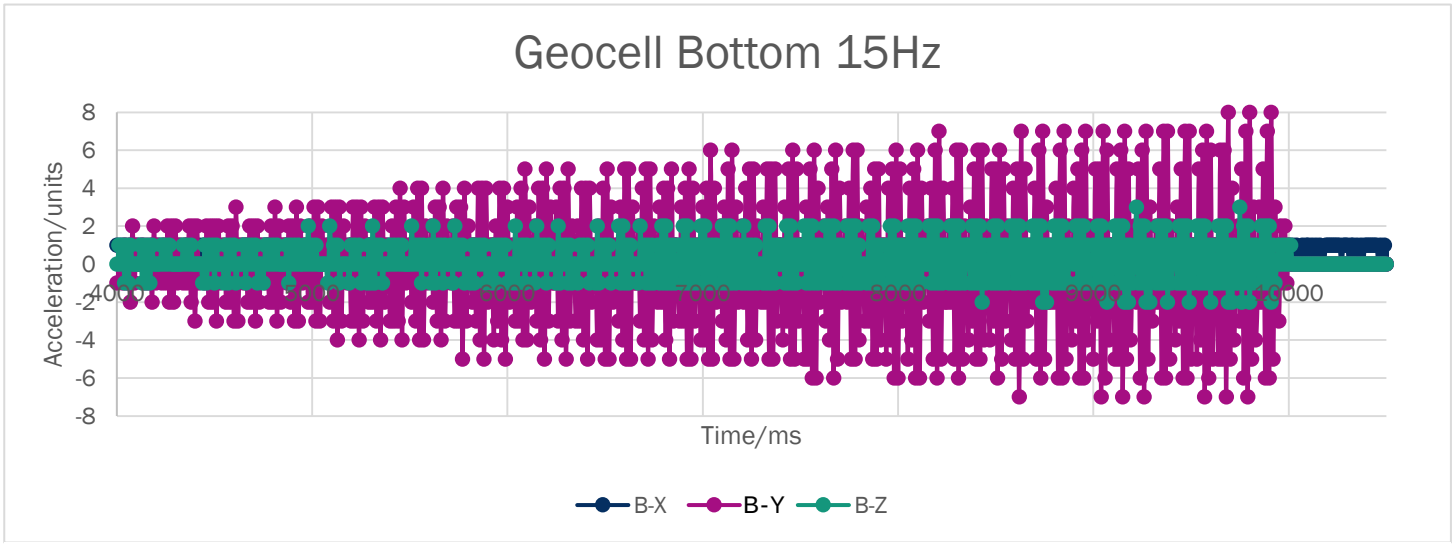


Figure A.52: Accelerometer 2 results for geocell reinforcement at 15Hz

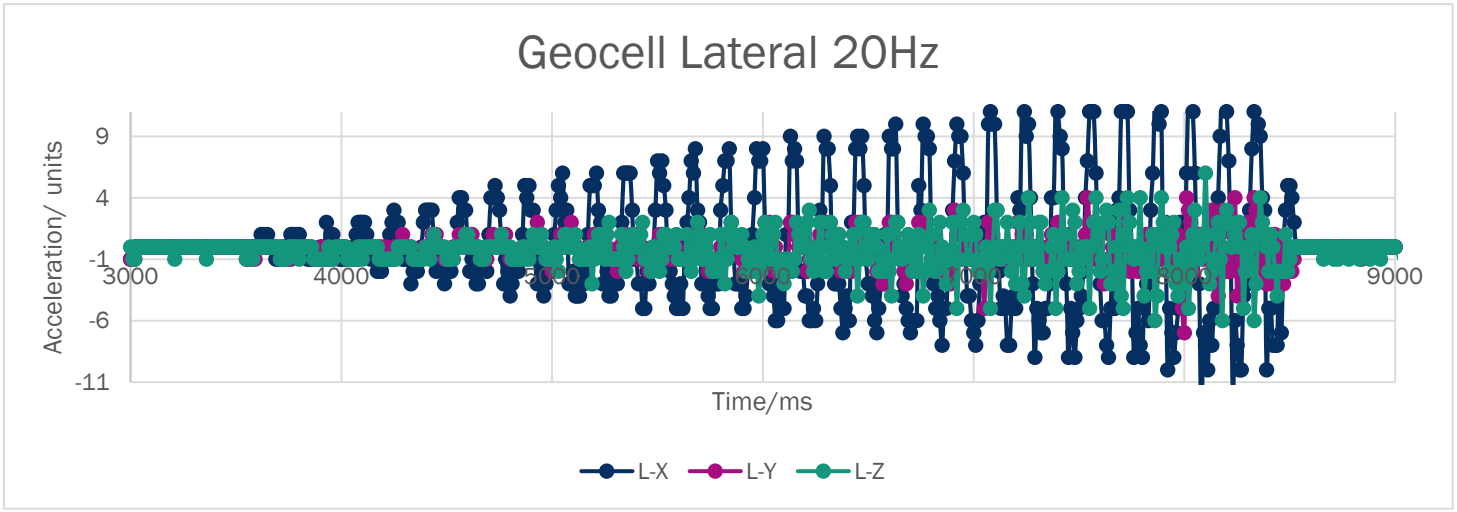


Figure A.53: Accelerometer 1 results for geocell reinforcement at20Hz

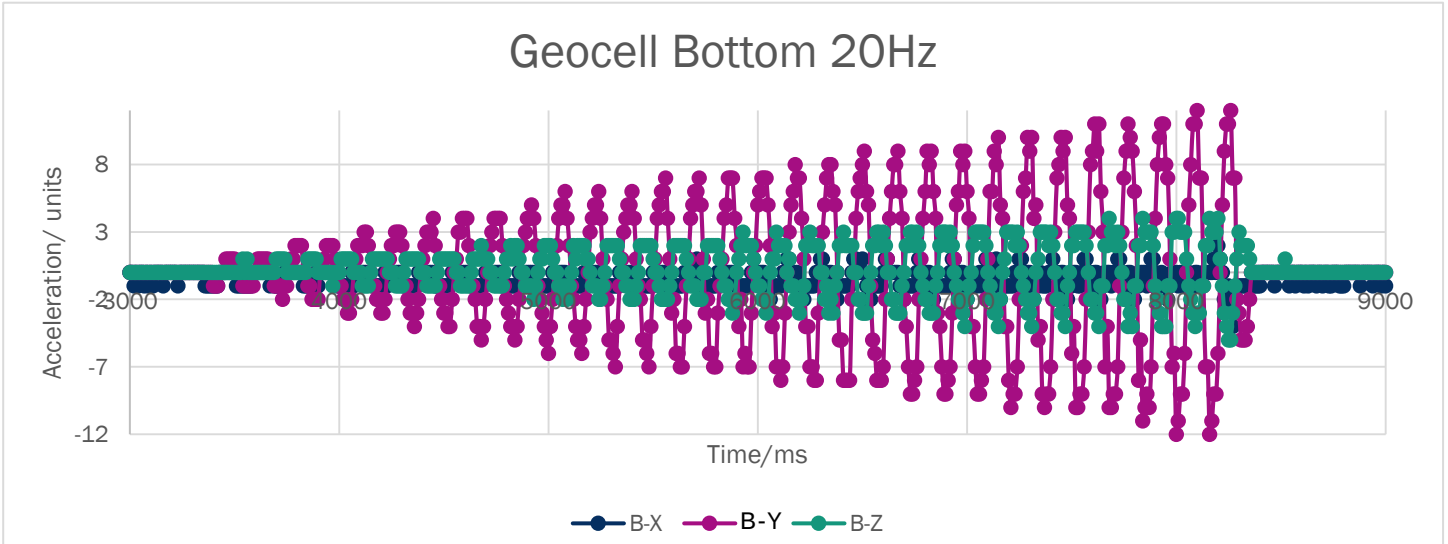


Figure A.54: Accelerometer 2 results for geocell reinforcement at 20Hz

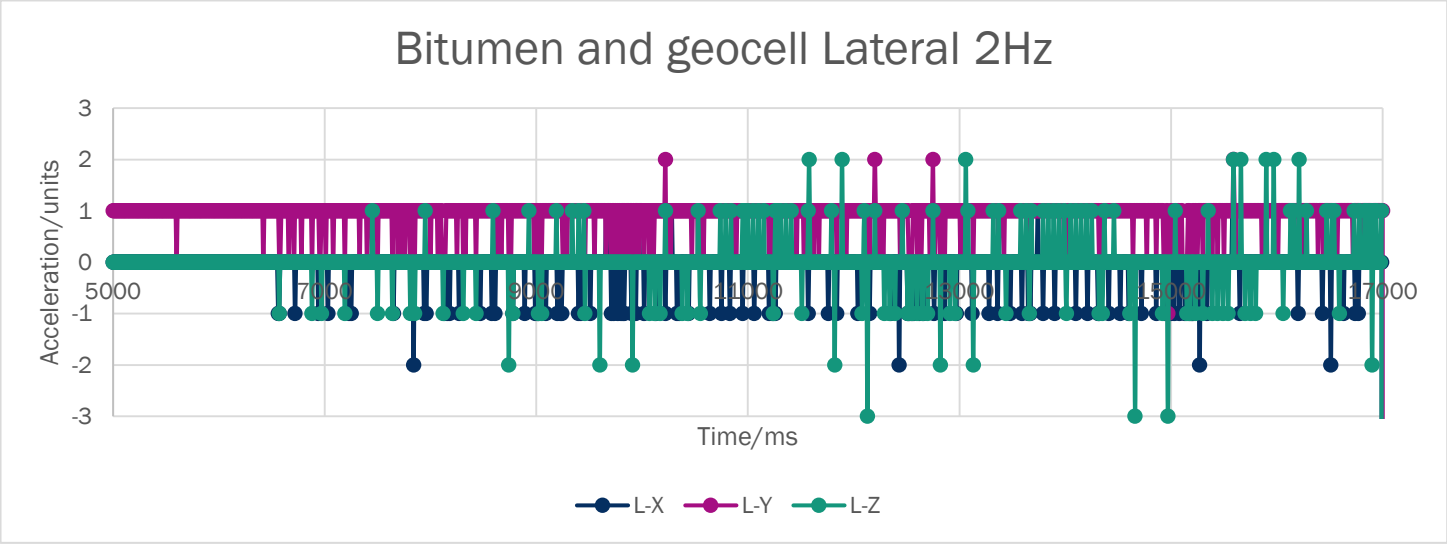


Figure A.55: Accelerometer 1 results for geocell and bitumen reinforcement at 2Hz

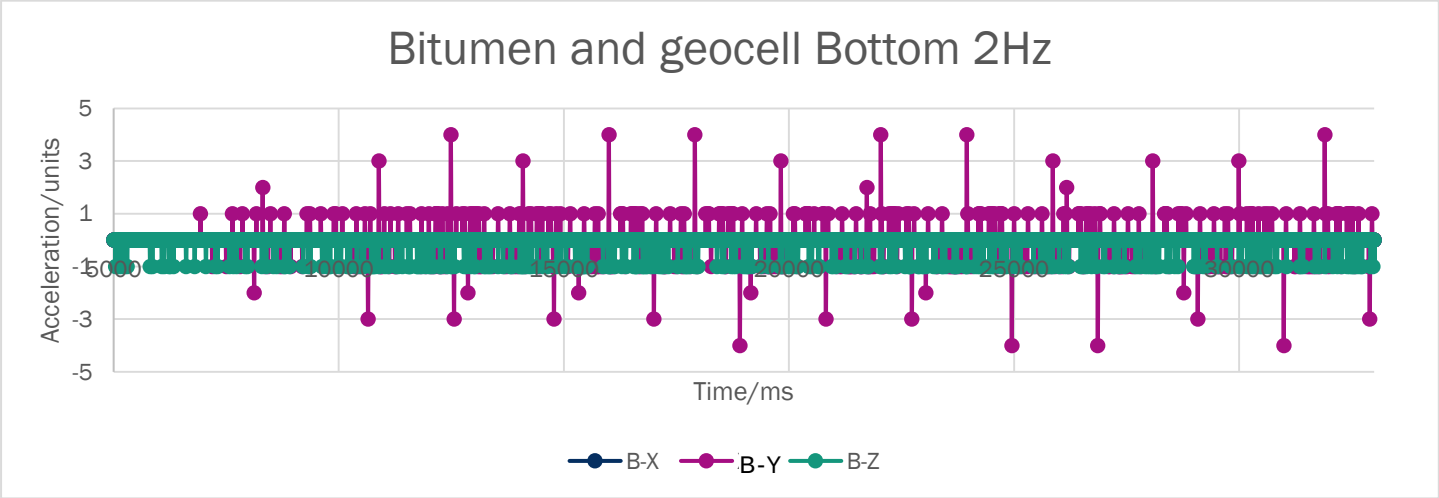


Figure A.56: Accelerometer 2 results for geocell and bitumen reinforcement at 2Hz

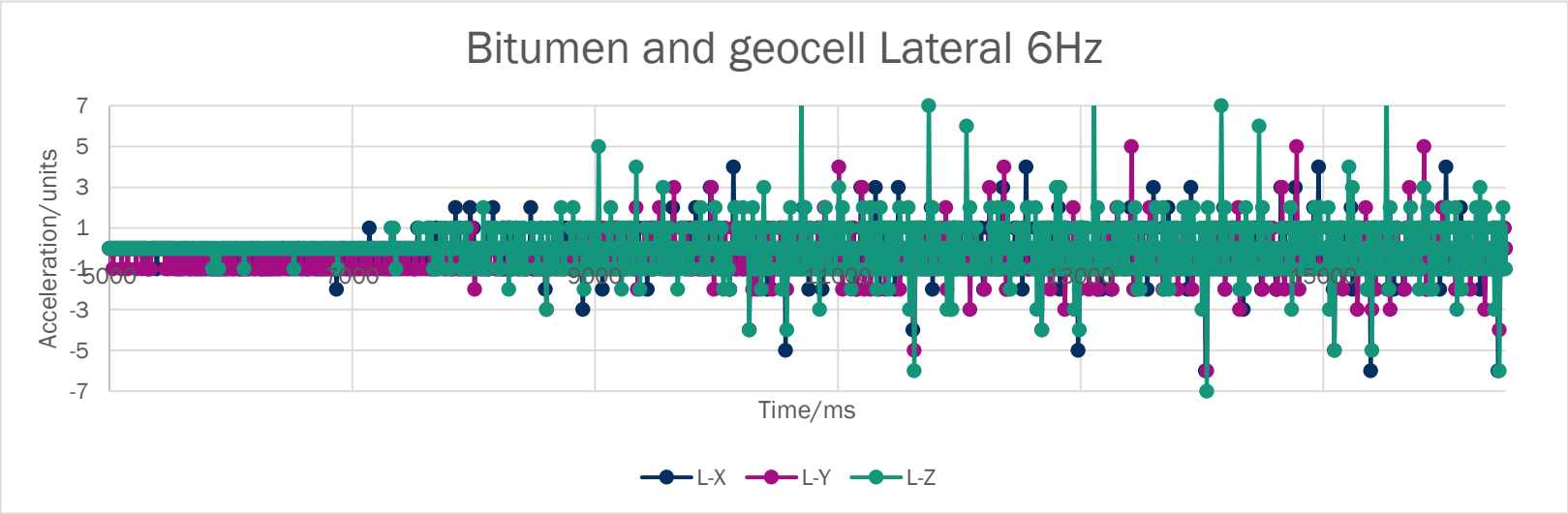


Figure A.57: Accelerometer 1 results for geocell and bitumen reinforcement at 6Hz

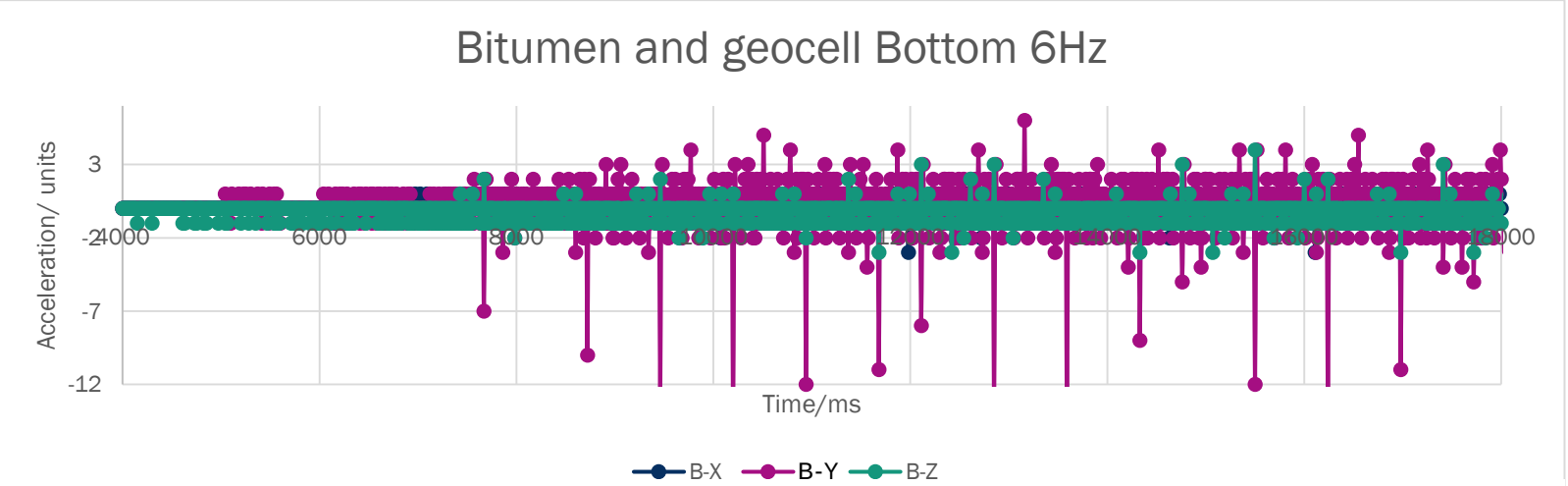


Figure A.58: Accelerometer 2 results for geocell and bitumen reinforcement at 6Hz

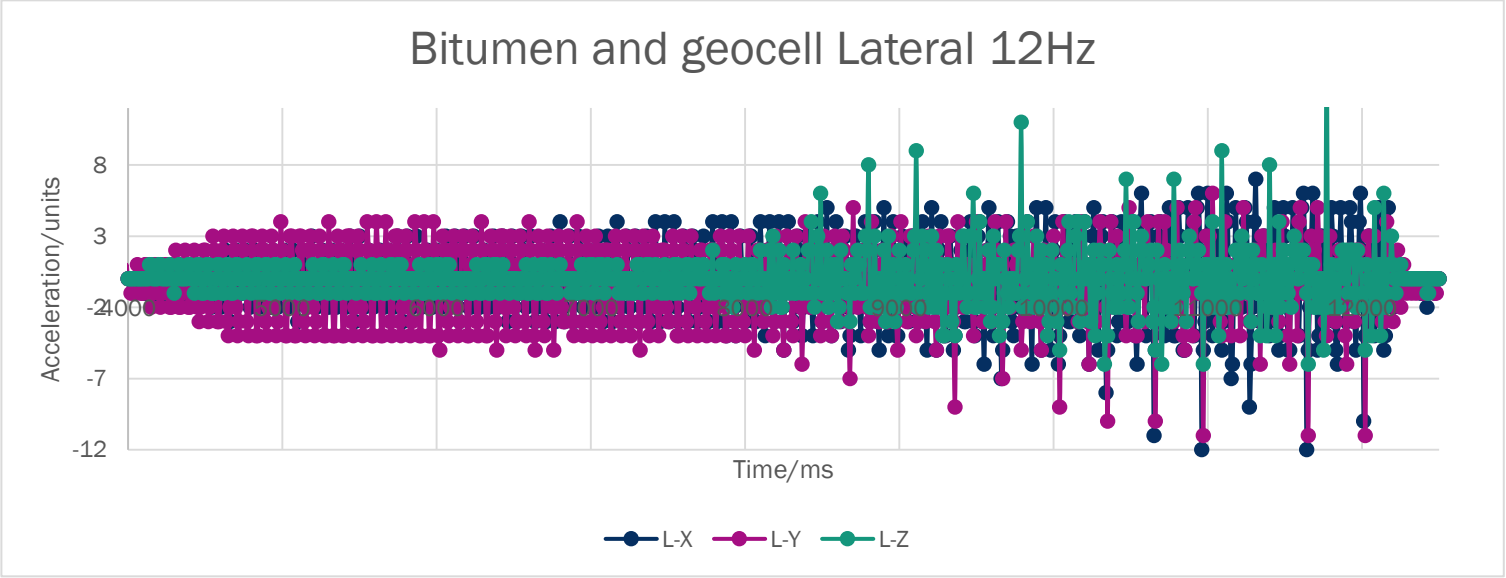


Figure A.59: Accelerometer 1 results for geocell and bitumen reinforcement at 12Hz

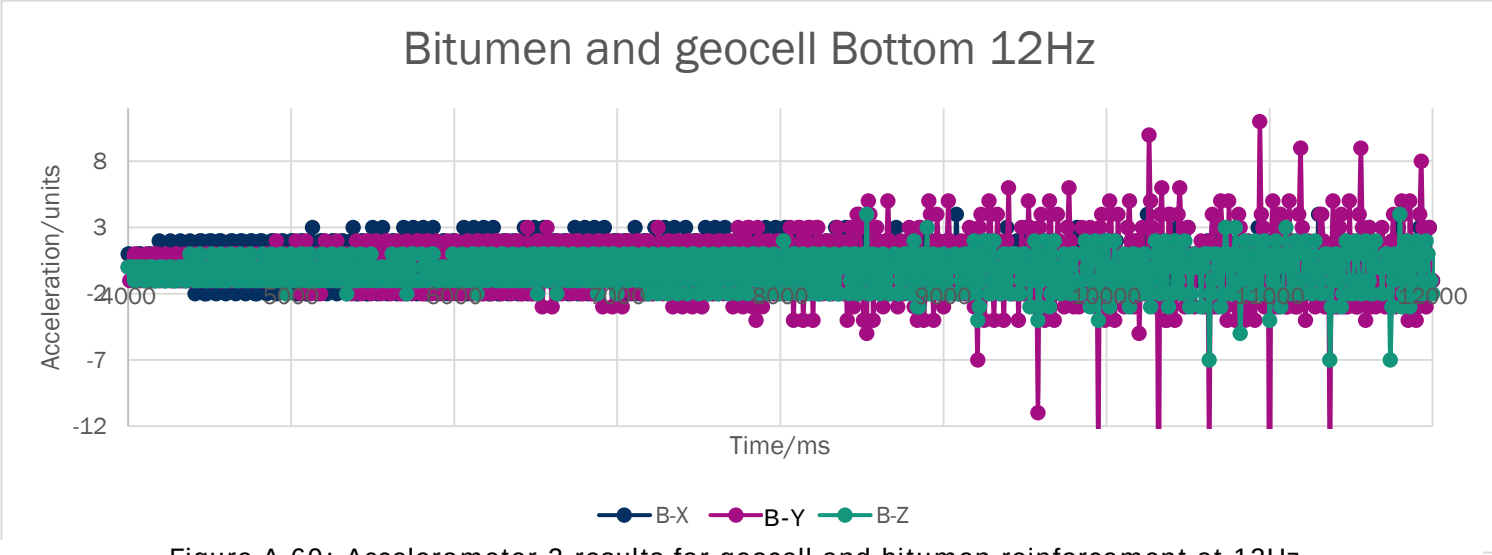


Figure A.60: Accelerometer 2 results for geocell and bitumen reinforcement at 12Hz

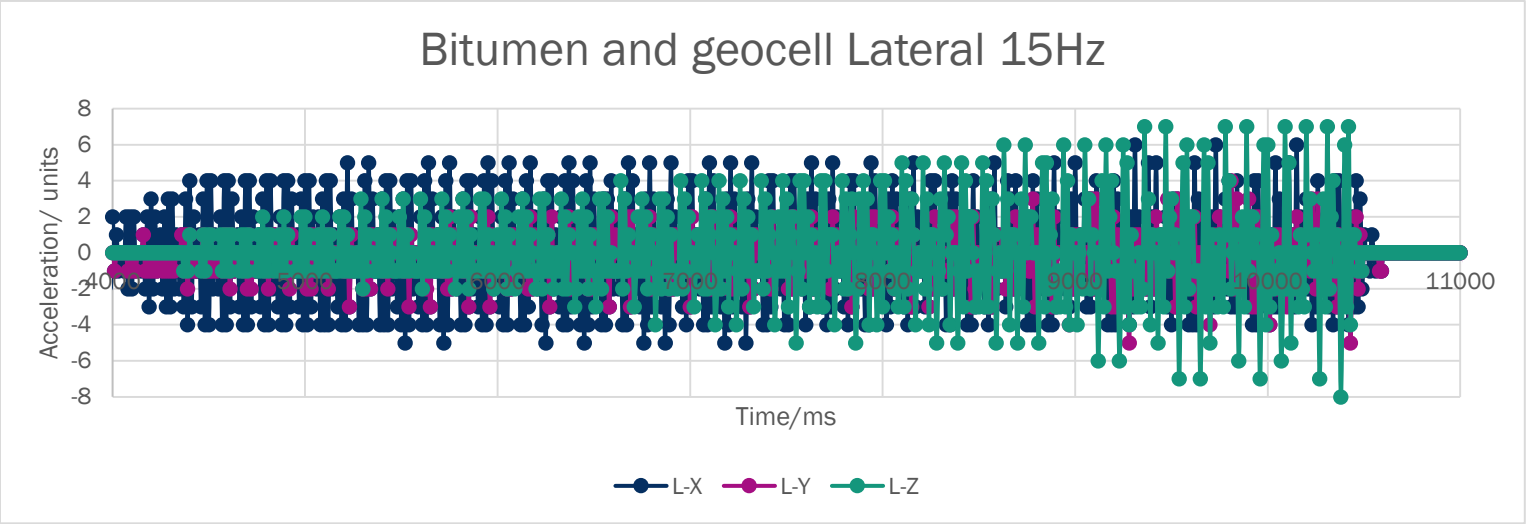


Figure A.61: Accelerometer 1 results for geocell and bitumen reinforcement at15Hz

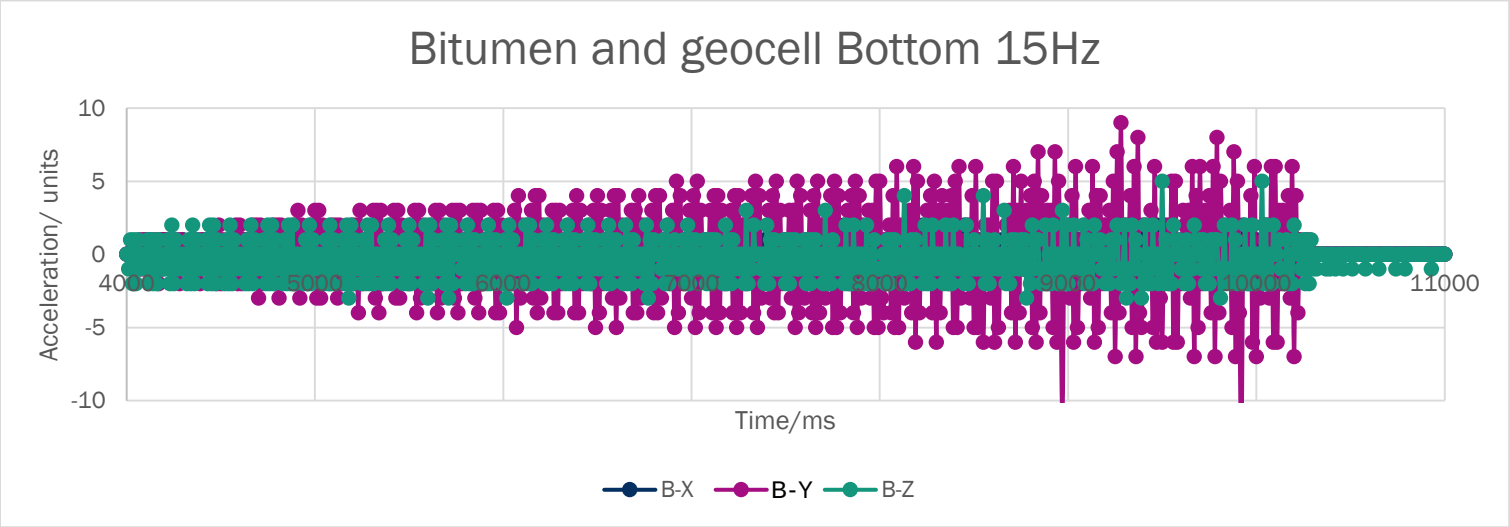


Figure A.62: Accelerometer 2 results for geocell and bitumen reinforcement at15Hz

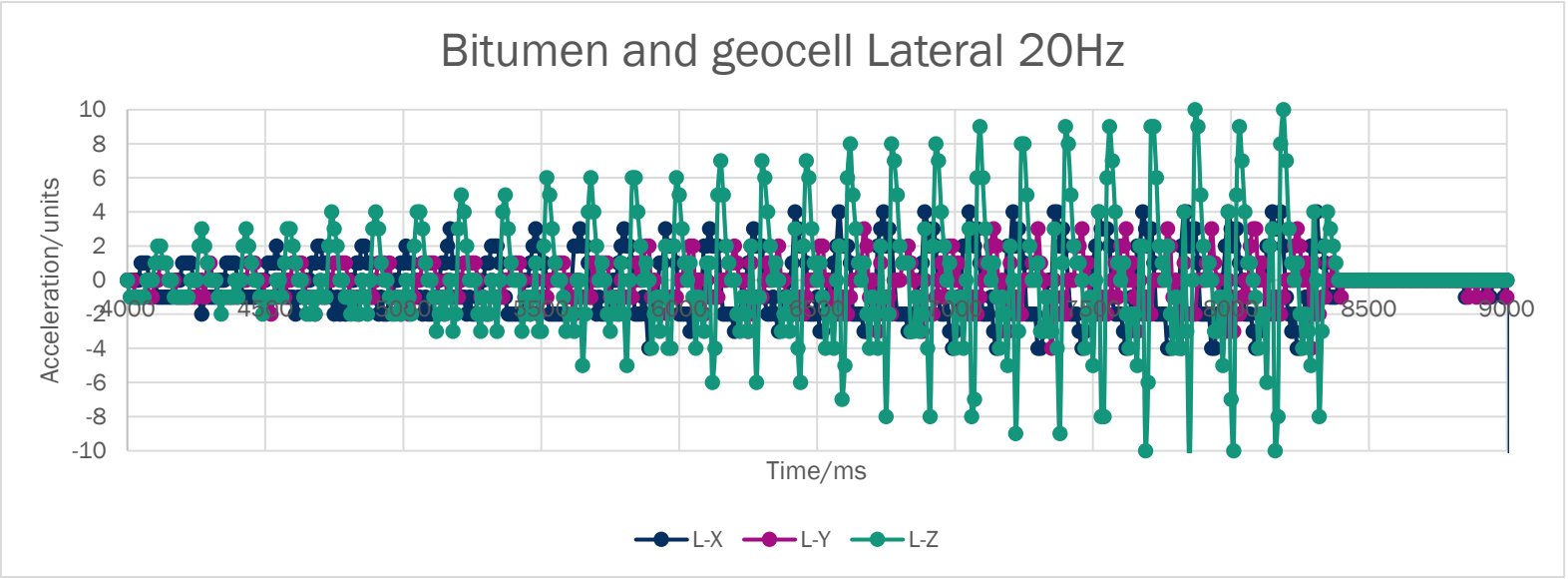


Figure A.63: Accelerometer 1 results for geocell and bitumen reinforcement at20Hz

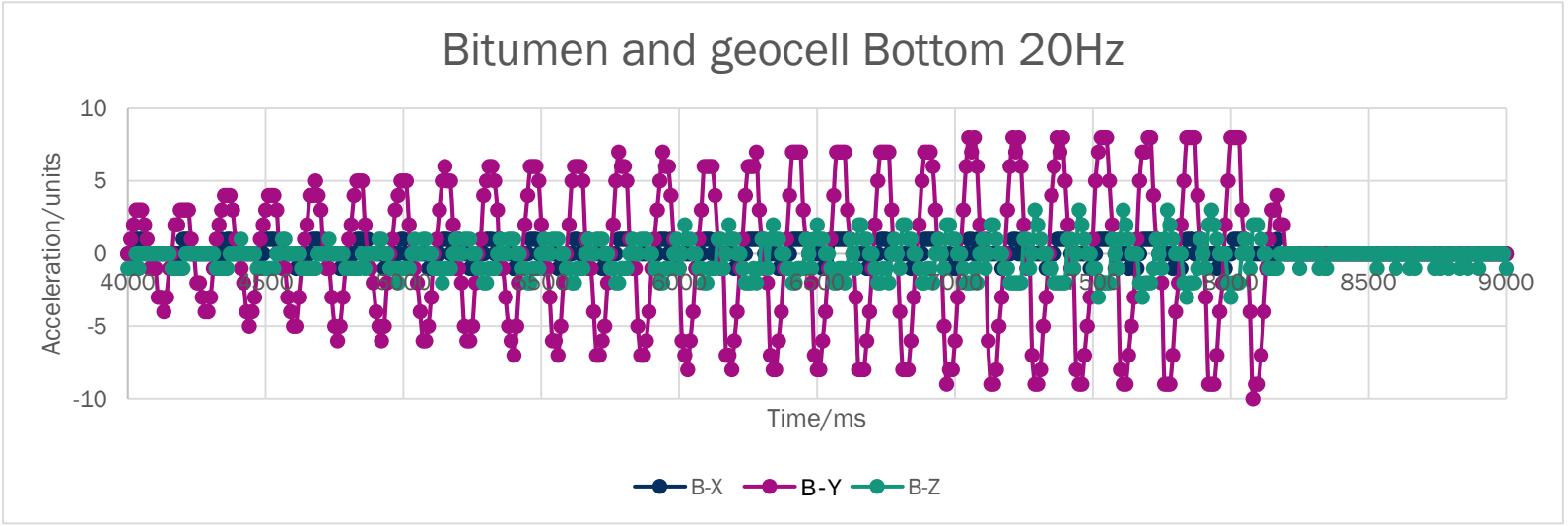


Figure A.64: Accelerometer 2 results for geocell and bitumen reinforcement at20Hz